

**NEGATIVE ION PHOTOELECTRON SPECTROSCOPY:
ELECTRONIC STRUCTURES, CHEMICAL BONDING, MOLECULAR
ACTIVATION, AND ELECTRON-MOLECULE INTERACTIONS**

by
Gaoxiang Liu

A dissertation submitted to Johns Hopkins University in conformity with the
requirements for the degree of Doctor of Philosophy

Baltimore, Maryland
October 2019

© 2019 Gaoxiang Liu
All rights reserved

Abstract

Negative ion photoelectron spectroscopy has been applied to address a broad range of fundamental problems in chemistry. Major topics that have been studied are related to electronic structures, chemical bonding, molecular activation, and electron-molecule interactions. New phenomena have been discovered, including but not limited to, the fine-tunability of the electronic spectra in superatoms, realization of Lewis basic sodium anion, halogen-bond stabilized anions, selective methane activation by single atomic anions, and excess electrons tethered by weak attractive interactions. The insight acquired from negative ion photoelectron spectroscopy has provided understanding into the above-mentioned topics at a molecular level.

Dissertation readers:

Prof. Kit H. Bowen (Committee Chair)

Prof. Lan Cheng

Prof. Joel R. Tolman

Acknowledgement

I would first like to thank my thesis advisor, Prof. Kit Bowen. Kit has been offering me his consistent support at a level that is beyond my imagination. He is always there when I am in need. He is willing to drop his urgent tasks to help me turn things around. I have also received invaluable guidance from Kit. This guidance is not only about science and academy, but also about the multifaceted reality of being the principal investigator of a lab. Such knowledge would make me more prepared if I were to establish my own lab.

I want to thank my parents, who have been providing me their unconditional support for every decision I make. It is their selfless support that ensures me a decent life which exceeds most of my peers, helping me concentrate on my career without too much financial concern.

I want to thank my colleagues whom I have the honor to work with. For those who have graduated from the group, I am grateful to Dr. Xinxing Zhang and Dr. Jacob Graham, who taught me a great deal on science and instrument when I was new to this group, and to Dr. Evan Collins, who was helpful under all kinds of situations. I feel blessed to work with a great team of researchers, Dr. Zachary Hicks, Sandy Ciborowski, Nic Blondo, Mary Marshall, Linjie Wang, Zhaoguo Zhu, Mike Denchy, Rachel Harris, Moritz Blankenhorn, Marica Dipalo, Lucas Hansen, and many visiting scholars. There is no way I can

accomplish this much without the great teamwork.

I am also very grateful to other professors and scientists whom we have collaborated with.

I am thankful for Prof. Joel Tolman and Prof. Lan Cheng to be on my thesis committee. I would also like to thank Prof. Robert Compton, Prof. Shiv Khanna, and Prof. Vincent Ortiz for their support during my postdoc search.

I want to thank my friends, who have helped keep me sane when I face up and down.

Lastly, and most importantly, I want to thank my wife, Shuiqing Liu, who has been, and will always be, the greatest discovery of my life. *You are all my reasons.*

Table of Contents

ABSTRACT	II
ACKNOWLEDGEMENT	III
LIST OF TABLES	VIII
LIST OF FIGURES.....	X
I. INTRODUCTION.....	1
II. ELECTRONIC STRUCTURES	3
II.1 TUNING THE ELECTRONIC PROPERTIES OF HEXANUCLEAR COBALT SULFIDE SUPERATOMS VIA LIGAND SUBSTITUTION	4
II.2 LIGAND EFFECT ON THE ELECTRONIC STRUCTURE OF COBALT SULFIDE CLUSTERS: A COMBINED EXPERIMENTAL AND THEORETICAL STUDY	25
III. CHEMICAL BONDING	47
III.1 PHOTOELECTRON SPECTROSCOPIC AND COMPUTATIONAL STUDY OF PYRIDINE-LIGATED GOLD CLUSTER ANIONS	48
III.2 STABILIZING OTHERWISE UNSTABLE ANIONS WITH HALOGEN BONDING.....	67
III.3 MYSTERY OF THREE BORIDES: DIFFERENTIAL METAL–BORON BONDING GOVERNING SUPERHARD STRUCTURES	79
III.4 SPECTROSCOPIC MEASUREMENT OF A HALOGEN BOND ENERGY	94
III.5 REALIZATION OF LEWIS BASIC SODIUM ANION IN THE NaBH_3^- CLUSTER	108

IV. MOLECULAR ACTIVATION	124
IV.1 CO ₂ ACTIVATION AND HYDROGENATION BY PTH _N ⁻ CLUSTER ANIONS	125
IV.2 COMMUNICATION: WATER ACTIVATION AND SPLITTING BY SINGLE METAL-ATOM ANIONS	139
IV.3 ACTIVATION OF HYDROXYLAMINE BY SINGLE GOLD ATOMIC ANIONS	159
IV.4 THE METALLO-FORMATE ANIONS, M(CO ₂) ⁻ , M = Ni, Pd, Pt, FORMED BY ELECTRON-INDUCED CO ₂ ACTIVATION	171
IV.5 SELECTIVE ACTIVATION OF THE C–H BOND IN METHANE BY SINGLE PLATINUM ATOMIC ANIONS 188	
V. ELECTRON-MOLECULE INTERACTIONS	202
V.1 DIPOLE-BOUND ANIONS OF INTRAMOLECULAR COMPLEXES	203
V.2 DIPOLE-BOUND ANIONS: FORMED BY RYDBERG ELECTRON TRANSFER (RET) AND STUDIED BY VELOCITY MAP IMAGING–ANION PHOTOELECTRON SPECTROSCOPY (VMI–APES).....	221
V.3 THE GROUND STATE, QUADRUPOLE-BOUND ANION OF SUCCINONITRILE REVISITED	235
V.4 THE CORRELATION-BOUND ANION OF <i>P</i> -CHLOROANILINE.....	249
V.5 OBSERVATION OF THE DIPOLE- AND QUADRUPOLE-BOUND ANIONS OF 1,4- DICYANOCYCLOHEXANE	259
VI. APPENDIX.....	276
VI.1 HMoO AND H ₂ MoO: MOLECULAR MIMICS FOR RHODIUM AND PLATINUM	276
VI.2 CO ₂ HYDROGENATION BY THE HYDRIDE OF PLATINUM MIMIC	278
VI.3 LIGATED LOW OXIDATION STATE ALUMINUM CLUSTER ANIONS AL _N L ⁻ (<i>N</i> = 1-14, L = N[Si(Me) ₃] ₂)	

VI.4	TWO NEW DOUBLE-RYDBERG ANIONS: $\text{Li}(\text{OH})_{1,2}^-$	289
VI.5	ON THE EXISTENCE OF TRIPLE RYDBERG ANIONS	312
VI.6	SUPERATOMIC CLUSTERS WITH FOUR DIFFUSE RYDBERG ELECTRONS	315
VI.7	DIRECT MAPPING OF THE ELECTRONIC STRUCTURES OF HEXAVALENT URANIUM COMPLEX....	319
VI.8	CO_2 HYDROGENATION TO FORMATE AND FORMIC ACID BY BIMETALLIC PALLADIUM-COPPER HYDRIDE CLUSTERS	322
VI.9	CO_2 HYDROGENATION TO FORMATE BY PALLADIUM HYDRIDE CLUSTERS	329
VI.10	TERTIARY SYSTEMS: TANDEM MOLECULAR ACTIVATION BY SINGLE ATOMIC ANIONS	333
VI.11	DECOMPOSITION OF HYDROXYLAMINE BY IRIIDIUM CLUSTER ANIONS	345
VI.12	PHOTOELECTRON SPECTROSCOPIC STUDY OF DIPOLE-BOUND AND VALENCE-BOUND NITROMETHANE ANIONS FORMED BY RYDBERG ELECTRON TRANSFER	348
VI.13	EXCESS ELECTRONS BOUND TO H_2S TRIMER AND TETRAMER CLUSTERS.....	359
VI.14	SOLVATED ELECTRONS IN FORMIC ACID TRIMER AND TETRAMER	380
VI.15	METHANE SOLVATED CYANIDE: THE TITAN CLUSTERS	381
VI.16	ELECTRON INDUCED PROTON TRANSFER.....	383
VI.17	XENON CLUSTER ANIONS	389
VI.18	VMI IMAGING DATA ANALYSIS SOFTWARE UPDATE	395
VII.	CURRICULUM VITAE	402

List of Tables

TABLE II.1.2	THEORETICAL AND EXPERIMENTAL ADIABATIC AND VERTICAL DETACHMENT ENERGIES (1 ST AND 2 ND PEAK) OF CO ₆ S ₈ (PET ₃) _{6-X} (CO) _X ⁻ (X = 0–3) CLUSTERS. THE SUPERSCRIPTS T AND E INDICATE THEORETICAL AND EXPERIMENTAL VALUES, RESPECTIVELY.....	18
TABLE II.2.2	THEORETICAL AND EXPERIMENTAL ADIABATIC AND 1 ST AND 2 ND VERTICAL DETACHMENT ENERGIES (VDE AND VDE*) OF CO ₆ S ₈ (PET ₃) _X ⁻ (X = 0–5) CLUSTERS.	38
TABLE III.1.2	OPTIMIZED STRUCTURES, RELATIVE ENERGIES, EXPERIMENTAL/THEORETICAL EA VALUES OF NEUTRAL AU _N (PY), AND EXPERIMENTAL/THEORETICAL VDE VALUES OF AU _N (PY) ⁻	62
TABLE III.2.2	EXPERIMENTAL AND THEORETICAL EAS OF PZ(BRPH) _N AND VDES OF PZ(BRPH) _N ⁻ . ALL VALUES ARE IN EV. (M=0,-).....	71
TABLE III.2.3	COMPUTED THERMODYNAMIC PROPERTIES (KCAL MOL ⁻¹) FOR GAS-PHASE COMPLEX FORMATION AT 298 K. THE THRESHOLD TEMPERATURES (K) FOR THE REACTIONS TO OCCUR ARE ALSO LISTED.	76
TABLE III.3.2	EXPERIMENTAL AND CALCULATED PHOTOELECTRON SPECTRA OF TIB ₂ ⁻ AND REB ₂ ⁻ (IN EV)	82
TABLE III.3.3	BADER CHARGES OF METALS IN BOTH NATURAL AND FOREIGN CRYSTAL STRUCTURES (OPTIMIZED TO THE NEAREST STATIONARY POINT).....	85
TABLE III.3.4	CHARGE DENSITIES (IN E ⁻) AT THE BOND CPS FOR BOTH RE AND OS IN THE	

BOAT AND CHAIR STRUCTURES 87

TABLE IV.5.2 EXPERIMENTAL AND CALCULATED VERTICAL PHOTODETACHMENT

TRANSITION ENERGY VALUES FOR THE GM STRUCTURE, H-PT-CH₃⁻ 194

List of Figures

FIGURE I.1.1	SCHEMATIC OF NEGATIVE ION PHOTOELECTRON SPECTROSCOPY.....	2
FIGURE II.1.1	(A) STRUCTURE OF $\text{CO}_6\text{S}_8(\text{PET}_3)_{6-x}(\text{CO})_x$. (B) ANION MASS SPECTRUM OF $\text{CO}_6\text{S}_8(\text{PET}_3)_{6-x}(\text{CO})_x^-$ GENERATED USING IR/PE ANION SOURCE. THIS WORK FOCUSES ON THE RED PEAKS IN THE MASS SPECTRUM.....	12
FIGURE II.1.2	NEGATIVE ION PHOTOELECTRON SPECTRA OF $\text{CO}_6\text{S}_8(\text{PET}_3)_{6-x}(\text{CO})_x^-$ ($X = 0-3$) ANIONS COLLECTED USING 355 NM (3.49 EV) PHOTONS FROM A ND:YAG LASER. THE ARROWS POINT TO THE EXPERIMENTAL VALUES OF AEA AND VDE; THE RED LINES CORRESPOND TO THEORETICAL AEA, AND THE BLUE LINES CORRESPOND TO VERTICAL TRANSITIONS FROM THE ANION TO THE SINGLET AND TRIPLET NEUTRAL STATES.	14
FIGURE II.1.3	OPTIMIZED GROUND STATE STRUCTURE OF ANIONIC $\text{CO}_6\text{S}_8(\text{PET}_3)_{6-x}(\text{CO})_x^-$ ($X = 0-3$) CLUSTERS. THE RED SUPERScript INDICATES THE SPIN MULTIPLICITY ($2S+1$) OF EACH CLUSTER.	16
FIGURE II.1.1	(A) THE ABSOLUTE ENERGY VALUES OF THE HOMO AND LUMO FOR NEUTRAL $\text{CO}_6\text{S}_8(\text{PET}_3)_{6-x}(\text{CO})_x$ ($X = 0-3$). (B) INCREMENTAL DIFFERENCES IN THE EXPERIMENTAL AEA VALUES, THE THEORETICAL AEA VALUES, AND THE LUMO VALUES OF $\text{CO}_6\text{S}_8(\text{PET}_3)_{6-x}(\text{CO})_x$, EACH WITH RESPECT TO $\text{CO}_6\text{S}_8(\text{PET}_3)_6$. (C) MOLECULAR ORBITAL ISO-SURFACES OF THE HOMO AND LUMO IN $\text{CO}_6\text{S}_8(\text{PET}_3)_{6-x}(\text{CO})_x$ ($X=0-3$) CLUSTERS.....	19
FIGURE II.2.1	ANION MASS SPECTRUM OF $\text{CO}_6\text{S}_8(\text{PET}_3)_x^-$ GENERATED USING IR/PE ANION	

SOURCE. 32

FIGURE II.2.2 NEGATIVE ION PHOTOELECTRON SPECTRA OF $\text{CO}_6\text{S}_8(\text{PET}_3)_X^-$ ($X = 2 - 5$) ANIONS COLLECTED USING 355 NM (3.49 EV) PHOTONS FROM A ND:YAG LASER. THE RED ARROWS INDICATE THE AEA, THE BLUE ARROWS INDICATE THE VDE AND THE VDE* 35

FIGURE II.2.3 OPTIMIZED GROUND STATE GEOMETRY OF ANIONIC $\text{CO}_6\text{S}_8(\text{PET}_3)_X$ ($X = 0-5$) CLUSTERS. SUPERSCRIPITS IN RED TEXT SHOW THE MULTIPLICITY OF THE CLUSTERS. 35

FIGURE II.2.4 THE EXPERIMENTAL AND THEORETICAL ADIABATIC AND VERTICAL DETACHMENT ENERGY OF $\text{CO}_6\text{S}_8(\text{PET}_3)_X$ ($X = 0 - 6$) CLUSTERS. THE PLUS SYMBOL (+) INDICATES THE AEA^T AND VDE^T VALUES OF CLUSTER'S ISOMERS AT X =2, 3, AND 5. THE RESULTS OF $\text{CO}_6\text{S}_8(\text{PET}_3)_6$ ARE TAKEN FROM REF. 38. 38

FIGURE II.2.1 ONE ELECTRON-ENERGY LEVELS OF $\text{CO}_6\text{S}_8(\text{PET}_3)_X$ ($X = 0-5$) CLUSTERS. THE SOLID BLUE AND RED BARS REPRESENT THE SINGLY AND DOUBLY OCCUPIED ENERGY LEVELS, RESPECTIVELY. UNOCCUPIED ENERGY LEVELS ARE SHOWN BY DASHED GRAY LINES. THE ENERGY OF LUMO (IN EV) IS INDICATED FOR EACH CLUSTER. THE A-SPIN AND B-SPIN CHANNEL ARE REPRESENTED BY UP AND DOWN ARROWS..... 40

FIGURE II.2.2 (A) ONE-ELECTRON ENERGY LEVELS WITH THEIR SYMMETRY LABELS FOR CO_6S_8 IN OCTAHEDRON SYMMETRY. THE SOLID AND DASHES LINES REPRESENT OCCUPIED AND UNOCCUPIED ENERGY LEVELS. (B) ONE-ELECTRON ENERGY LEVELS ALONG WITH THEIR ISO-SURFACES FOR $\text{CO}_6\text{S}_8(\text{PET}_3)$. THE SOLID BLUE AND RED BARS REPRESENT THE SINGLY AND DOUBLY OCCUPIED ENERGY LEVELS, RESPECTIVELY. UNOCCUPIED ENERGY LEVELS ARE

SHOWN BY DASHED GRAY LINES. THE <i>A</i> -SPIN AND <i>B</i> -SPIN CHANNEL REPRESENTED BY UP AND DOWN ARROWS.....	42
FIGURE III.1.1 SCHEMATIC OF THE LASER VAPORIZATION HOUSING COUPLED WITH A LIGATION CELL.	53
FIGURE III.1.2 THE MASS SPECTRA OF (A) Au_N^- CLUSTER ANIONS AND (B) PYRIDINE-LIGATED GOLD CLUSTER ANIONS $Au_N(PY)^-$	56
FIGURE III.1.3 PHOTOELECTRON SPECTRA OF (A-C) Au_N^- AND (D-F) $Au_N(PY)^-$ ($N = 2-4$).	57
FIGURE III.2.1 PHOTOELECTRON SPECTRA OF $PZ(BRPH)_N^-$ ($N=1,2$) TAKEN WITH A 355 NM (3.49 EV) LASER. 71	
FIGURE III.2.1 CALCULATED STRUCTURES OF $PZ(BRPH)_N^M$ ($M=0,-$). THE XB LENGTHS ARE IN Å. THE HIGHEST OCCUPIED MOLECULAR ORBITALS (HOMO) ARE ALSO PRESENTED.....	72
FIGURE III.2.2 ELECTROSTATIC POTENTIAL SURFACES OF PZ , PZ^- , $PZ(BRPH)_1^-$, AND $PZ(BRPH)_2^-$. THE INDUCED POSITIVE (BLUE), NEGATIVE (RED), AND NEUTRAL (GREEN) POTENTIALS ARE MAPPED ON THE 0.04 E/BOHR ³ SURFACES OF THE CLUSTERS.....	74
FIGURE III.3.1 STRUCTURES OF THE THREE BORIDES: TiB_2 FEATURING A FLAT B-SHEET AND ReB_2 AND OsB_2 WHERE THE B-SHEET IS BENT IN CHAIR AND BOAT CONFORMATIONS, RESPECTIVELY.(1) THE UPPER IMAGES DISPLAY SUPERCELLS TO MAKE APPARENT THE STRUCTURAL ANALOGIES WHILE THE LOWER IMAGES SHOW A SINGLE UNIT CELL.	80
FIGURE III.3.2 EXPERIMENTAL PHOTOELECTRON SPECTRA OF ReB_2^- (TOP) AND	

TIB₂⁻ (BOTTOM) AND THE THEORETICAL ASSIGNMENT OF SPECTRAL FEATURES..... 82

FIGURE III.3.1 LEFT: KOHN-SHAM ORBITALS OF REB₂, OSB₂, AND TIB₂, TRUNCATED SET; NBO CHARGES ON ATOMS. THE D → Σ_{2PX} M → B₂ BACKBONDS ARE OUTLINED IN RED, AND D → Π* IN BLUE. RIGHT: D → Π* STATE OCCUPIED IN SOLID OSB₂ (HIGHEST OCCUPIED AT GAMMA, HOS), CORRESPONDING TO THE DONATION FROM OS TO THE ACTIVATED AND ELONGATED B-B BONDS. 83

FIGURE III.3.1 ELECTRON DENSITY PLOTS OF REB₂ (LEFT) AND OSB₂ (RIGHT). QTAIM CPS ARE INDICATED: BOND CPS, BLUE; RING CPS, GREEN; CAGE CPS, YELLOW. I, M-B CP; II AND III, B-B CPS. 87

FIGURE III.3.1 (A) ENERGIES OF THE CLUSTERS AS A FUNCTION OF (A) COMPRESSION ALONG THE B-B BOND AND (B) SHEAR DISTORTION COORDINATE. CYAN, TIB₂²⁺; RED, REB₂⁺; PURPLE, OSB₂; DASHED BLACK, ISOLATED B₂ FOR A REFERENCE..... 89

FIGURE III.4.1 THE PHOTOELECTRON SPECTRA OF BR⁻ AND BR⁻(CCL₃BR) TAKEN WITH 266 NM (4.66 EV) PHOTONS AND BR⁻(CCL₃BR)₂ TAKEN WITH 193 NM (6.42 EV) PHOTONS..... 98

FIGURE III.4.2 CALCULATED GEOMETRIES AND HIGHEST OCCUPIED MOLECULAR ORBITALS (HOMO) OF BR^{0/-}(CCL₃BR)_{1,2}..... 100

FIGURE III.4.3 ELECTROSTATIC POTENTIAL (ESP) SURFACES FOR THE ANIONIC CL₃CBR-BR⁻, CL₃CBR-BR⁻-BRCCl₃(LEFT) AND NEUTRAL CCL₃BR, CLCCL₂BR-BR AND CLCCL₂BR-BR-BRCL₂CCL (RIGHT). THE INDUCED POSITIVE (BLUE), NEGATIVE (RED) POTENTIALS ARE MAPPED ON THE

0.04 E/BOHR³ SURFACES OF THE MOLECULES..... 103

FIGURE III.5.1 POTENTIAL ENERGY SURFACE OF (NA-BH₃)⁻ ALONG THE NA-B COORDINATE (BLUE CURVE) AND THE MULLIKEN CHARGE ON NA AT CORRESPONDING R(NA-B) (RED DOTTED CURVE). 117

FIGURE III.5.2 ADNDP AND QTAIM CHEMICAL BONDING PATTERNS. A) ADNDP FULL BONDING PICTURE OF (NA-BH₃)⁻, B) ADNDP RECOVERED S-TYPE LONE ELECTRON PAIR ON NA, C) QTAIM RESULTS OF (NA-BH₃)⁻, AND D) QTAIM RESULTS OF H₃N-BH₃. NA IS PURPLE, B IS DARK GREEN, N IS ORANGE, H IS BLUE. QTAIM CALCULATED BCPS ARE REPRESENTED BY LIGHT GREEN SPHERES. THE NUMBERS IN BLUE BESIDES BCPS ARE THE LAPLACIANS OF ELECTRON DENSITY, ∇^2P , IN E⁻ Å⁻⁵. 120

FIGURE IV.1.1 THE MASS SPECTRA OF PTH_N⁻ CLUSTER ANIONS A) WITHOUT AND B) WITH CO₂ INJECTION INTO THE CELL..... 128

FIGURE IV.1.2 PHOTOELECTRON SPECTRUM OF PTCO₂H₃⁻ TAKEN AT MASS 245 WITH 355 NM (3.496 EV) PHOTONS..... 129

FIGURE IV.1.3 PHOTOELECTRON SPECTRA OF A) PT⁻ (•) TAKEN AT MASS=194; B) PT⁻ (•) AND PTH⁻ (•) TAKEN AT MASS=195; C) PTH⁻ (•) AND PTCO₂H⁻ (•) TAKEN AT MASS=239..... 131

FIGURE IV.1.4 A) OPTIMIZED STRUCTURES OF PTCO₂H₃⁻ AND B) PTCO₂H⁻. BOND LENGTHS (Å). 133

FIGURE IV.1.5 CALCULATED REACTION PATHWAY FOR CO₂ HYDROGENATION BY PTH₃⁻..... 136

FIGURE IV.1.6 CALCULATED REACTION PATHWAY FOR CO₂ ACTIVATION AND THWARTED HYDROGENATION BY PTH⁻. THE PHOTODISSOCIATION PROCESS OF PTCO₂H⁻ IS ALSO PRESENTED. 136

FIGURE IV.2.1 THE TOP LEFT PANEL PRESENTS A STICK MASS SPECTRUM SHOWING THE SIMULATED ISOTOPIC MASS DISTRIBUTION OF [PT(H₂O)]⁻. THE PANELS BELOW IT SHOW THE MASS SPECTRA OF [PT(H₂O)]⁻ SPECIES FORMED UNDER THREE DIFFERENT LASER VAPORIZATION POWER SOURCE CONDITIONS; MASS SPECTRUM A WAS RECORDED UNDER LOW VAPORIZATION LASER POWER, B UNDER MODERATE VAPORIZATION LASER POWER, AND C UNDER HIGH VAPORIZATION LASER POWER. IN ALL CASES, LASER VAPORIZATION WAS CARRIED OUT USING THE SECOND HARMONIC (2.33 EV/PHOTON) OF A ND:YAG LASER. THE TOP RIGHT PANEL PRESENTS THE ANION PHOTOELECTRON SPECTRUM OF THE PT⁻ ATOMIC ANION. THE PANELS BELOW IT SHOW THE ANION PHOTOELECTRON SPECTRA OF [PT(H₂O)]⁻ SPECIES A, B, AND C, WHERE IN EACH CASE THE [PT(H₂O)]⁻ ANIONS HAD BEEN GENERATED UNDER THE SAME LASER VAPORIZATION POWER CONDITIONS USED TO RECORD THEIR CORRESPONDING MASS SPECTRA A, B, AND C, RESPECTIVELY. IN ALL CASES, THE ANION PHOTOELECTRON SPECTRA WERE MEASURED USING THE FOURTH HARMONIC (4.66 EV/PHOTON) OF A ND:YAG LASER..... 145

FIGURE IV.2.2 POSITIVE ION, ELECTRON BOMBARDMENT IONIZATION MASS SPECTRA OF THE SPECIES MADE UNDER LOW VAPORIZATION LASER POWER (A) AND HIGH VAPORIZATION LASER POWER (B). 148

FIGURE IV.2.3 PHOTOELECTRON SPECTRA OF THE ATOMIC METAL ANIONS, M^- , (IN THE UPPER PANELS) AND THEIR CORRESPONDING $[M(H_2O)]^-$ ANIONS (IN THE LOWER PANELS), WHERE $M =$ NI AND PD. ALL OF THESE ANION PHOTOELECTRON SPECTRA WERE MEASURED USING THE THIRD HARMONIC (3.49 EV/PHOTON) OF A ND:YAG LASER. DOTTED TIE-LINES LINK M^- PEAKS TO THE CORRESPONDING BLUE-SHIFTED PEAKS IN THEIR $M^-(H_2O)$ ANION-MOLECULE COMPLEXES. ADDITIONAL STRUCTURAL ISOMERS ARE MARKED BY RED DOTS. 150

FIGURE IV.2.4 THE CALCULATED POTENTIAL ENERGY PATHWAYS AND STATIONARY POINTS INVOLVED IN THE REACTIONS OF NI^- , PD^- , AND PT^- WITH A SINGLE WATER MOLECULE, H_2O . ZERO-POINT VIBRATIONAL AND SPIN-ORBIT CORRECTIONS ARE ALSO INCLUDED. 154

FIGURE IV.3.1 THE MASS SPECTRA OF AU^- ANIONS WITHOUT AND WITH THE ADDITION OF HA/H_2O MIXED VAPOR..... 164

FIGURE IV.3.2 THE PHOTOELECTRON SPECTRUM OF $[AU(HA)]^-$ TAKEN BY 3RD HARMONIC OUTPUT OF A ND:YAG LASER (3.496 EV). THE STICK SPECTRUM REPRESENTS THE CALCULATED VDE VALUE..... 165

FIGURE IV.3.3 OPTIMIZED STRUCTURES FOR $[AU(HA)]^-$ AND THEIR RELATIVE ENERGIES. 166

FIGURE IV.3.4 CALCULATED REACTION PATHWAY FOR HA ACTIVATION BY AU^- . THE NUMBERS DENOTE THE RELATIVE ENERGIES OF DIFFERENT STRUCTURES..... 167

FIGURE IV.4.1 ANION PHOTOELECTRON SPECTRA OF NI^- AND $NICO_2^-$, PD^- AND $PDCO_2^-$, AND PT^- AND $PTCO_2^-$. THE VERTICAL LINES IN THE $PDCO_2^-$ SPECTRUM REPRESENT FRANCK-

CONDON SIMULATED VIBRATIONAL PROGRESSION. 178

FIGURE IV.4.2 CALCULATED STRUCTURES OF NiCO_2^- , PdCO_2^- , PtCO_2^- (FIRST ROW) AND NiCO_2 , PdCO_2 , PtCO_2 (SECOND ROW). THE HOMOS OF THE ANIONIC COMPLEXES ARE ALSO PRESENTED. 181

FIGURE IV.4.3 THE POTENTIAL ENERGY SURFACES OF NEUTRAL NiCO_2 AND PtCO_2 WITH RESPECT TO THE M-C BOND LENGTH. THE RED CROSSES REPRESENT THE M-C BOND LENGTH OF OPTIMIZED ANIONIC NiCO_2^- AND PtCO_2^- 183

FIGURE IV.4.4 SELECTED MOLECULAR ORBITALS OF NEUTRAL (A) PtCO_2 AND (B) PdCO_2 . THE OVERLAP BETWEEN THE METAL ATOMIC ORBITALS AND THE CO_2 MOLECULAR ORBITALS IS BARELY PRESENT IN NEUTRAL PtCO_2 , BUT IS SIGNIFICANT IN NEUTRAL PdCO_2 184

FIGURE IV.5.1 THE MASS SPECTRA OF Pt^- WITHOUT METHANE (A), WITH METHANE (B), AND WITH DEUTERATED METHANE (C). 191

FIGURE IV.5.2 PHOTOELECTRON SPECTRA OF Pt^- (A), $[\text{PtCH}_4]^-$ (B), AND $[\text{PtCD}_4]^-$ (C), ALL MEASURED WITH 355 NM (3.496 EV) PHOTONS. 193

FIGURE IV.5.1 OPTIMIZED STRUCTURES FOR $[\text{PtCH}_4]^-$ AND THEIR RELATIVE ENERGIES COMPARED TO ITS GM. THE RELATIVE ENERGIES OF $[\text{PtCD}_4]^-$ ARE SHOWN IN PARENTHESIS. ENERGIES ARE GIVEN IN EV. BOND LENGTHS ARE GIVEN IN Å. 196

FIGURE IV.5.2 CALCULATED REACTION PATHWAY FOR METHANE ACTIVATION BY Pt^- . ZERO-POINT ENERGY CORRECTED ENERGIES ARE GIVEN IN EV. BOND LENGTHS OF THE TRANSITION

STATES ARE GIVEN IN Å. 199

FIGURE IV.5.3 SELECTED MOLECULAR ORBITALS OF THE GM H-PT-CH₃⁻ DEPICTING THE

PT-C AND PT-H BONDS AND THE NEARLY INTACT VALENCE PT ORBITALS. 199

I. Introduction

Negative ion photoelectron spectroscopy (NIPS) is among the ideal tools to study chemistry strictly at the molecular level. Since NIPS is conducted in the gas phase, it probes the physical and chemical properties of the negative ions of atoms, molecules, and clusters which are aggregates of atoms and molecules, unperturbed by environmental factors or averaging effects. NIPS allows us to access the rich energetic information about both the anions and the neutrals. The knowledge one can directly obtain from a negative ion photoelectron spectrum is the electronic structure related information, such as the HOMO-LUMO gap, the energy levels of vibrational and electronic excited states, etc. (Figure 1). Since the electronic structure has an integral relationship to chemical bonding, we can also acquire insight into the nature of the chemical bonds in the studied systems from NIPS results. The ability of NIPS to study electronic structures and chemical bonding makes it a powerful tool to investigate gas phase reactions and molecular activations, as reactions are essentially changes of electronic structures, and breakage and formation of chemical bonds. Finally, negative ions are the outcome of the electron-molecule interactions; therefore, NIPS is the natural probe for investigating such interactions.

The isolated, finite-size systems studied by NIPS offers an ideal playground for

quantum chemistry, as the state-of-the-art level of theoretical approaches which are too demanding for larger systems can be routinely applied to our systems. On the one hand, theoretical calculations can help interpret experimental results. On the other hand, the experimental results can provide benchmarks and validation to theory.

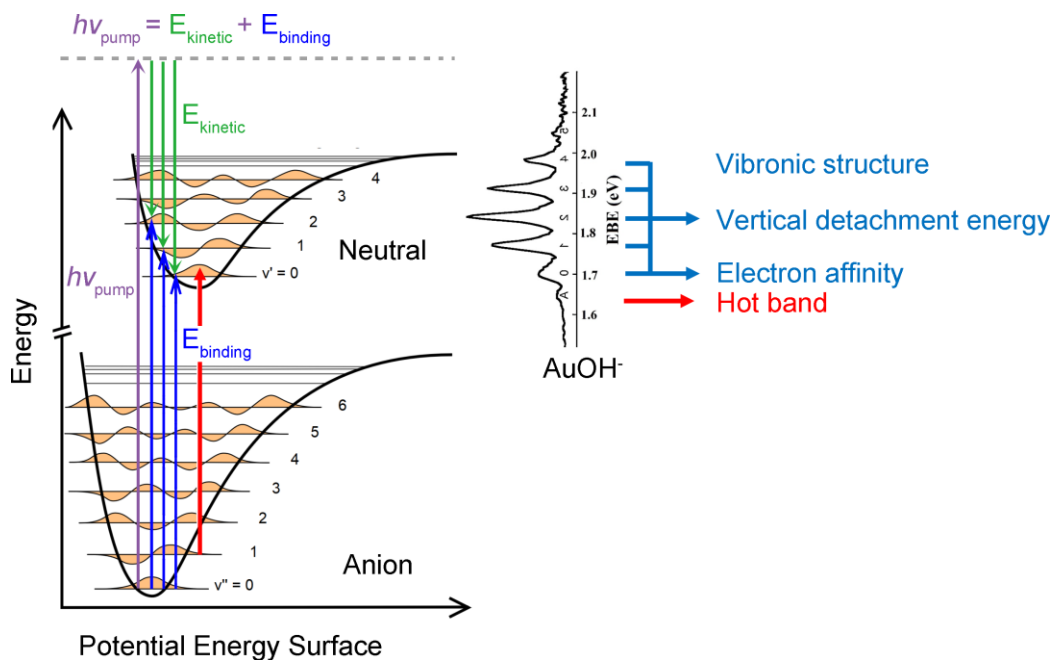


Figure I.1.1 Schematic of negative ion photoelectron spectroscopy.

Chapter II to **Chapter V** is mainly a collection of my published work on applying NIPS to study electronic structures (**Chapter II**), chemical bonding (**Chapter III**), molecular activation (**Chapter IV**), and electron-molecule interactions (**Chapter V**). The appendix contains majorly unpublished results. By the way, the list of figures and tables are not complete. I just made partial lists for passing the “beauty check”.

II. Electronic Structures

For a system of interest, its electronic structure refers to the atomic/molecular orbitals and the configuration of the electrons occupying these orbitals. Negative ion photoelectron spectroscopy (NIPS) is among the most appropriate experimental techniques for studying the electronic structures of atoms, molecules, and clusters. There are several advantages of NIPS over other spectroscopic approaches. Firstly, NIPS is performed in the gas phase under a high vacuum. Therefore, the systems being measured are isolated, that is, they interact with neither the neighboring systems nor the environment. As a result, NIPS can be regarded as a single atom/molecule spectroscopy in the gas phase. This makes NIPS advantageous over conventional photoelectron spectroscopy such as ultraviolet photoelectron spectroscopy (UPS), as NIPS results are not perturbed due to assembly averaging or environmental effects. Secondly, the electronic structure information acquired by NIPS reflects the properties of the frontier orbitals, such as the HOMO-LUMO gap, the vibrationally and electronic excited states, etc., which govern the chemistry and are thus of central interest to chemists.

II.1 Tuning the Electronic Properties of Hexanuclear Cobalt Sulfide Superatoms via Ligand Substitution

Gaoxiang Liu^a, Andrew Pinkard^b, Sandra M. Ciborowski^a, Vikas Chauhan^c, Zhaoguo Zhu^a, Alexander P. Ayt^b, Shiv N. Khanna^{*c}, Xavier Roy^{*b} and Kit H. Bowen^{*a}

^a *Department of Chemistry, Johns Hopkins University, Baltimore, Maryland 21218, USA.*

^b *Department of Chemistry, Columbia University, New York, New York 10027, USA.*

^c *Department of Physics, Virginia Commonwealth University, 701 W. Grace St., Richmond, Virginia 23284, USA.*

Abstract

Molecular clusters are attractive superatomic building blocks for creating materials with tailored properties due to their unique combination of atomic precision, tunability and functionality. The ligands passivating these superatomic clusters offer an exciting opportunity to control their electronic properties while preserving their closed shells and electron counts, which is not achievable in conventional atoms. Here we demonstrate this concept by measuring the anion photoelectron spectra of a series of hexanuclear cobalt sulfide superatomic clusters with different ratios of electron-donating and electron-withdrawing ligands, $\text{Co}_6\text{S}_8(\text{PEt}_3)_{6-x}(\text{CO})_x$ ($x = 0-3$). We find that $\text{Co}_6\text{S}_8(\text{PEt}_3)_6$ has a low electron affinity (EA) of 1.1 eV, and that the successive

replacement of PEt_3 ligands with CO gradually shifts its electronic spectrum to lower energy and increases its EA to 1.8 eV. Density functional theory calculations reveal that the increase of EA results from a monotonic lowering of the cluster highest occupied and lowest unoccupied molecular orbitals (HOMO and LUMO). Our work provides unique insights into the electronic structure and tunability of superatomic building blocks.

Introduction

Electron affinity and ionization energy are fundamental properties of the elements. Together they govern the interactions and bonding of close-contacting atoms and control the collective properties of solids. Because they are intrinsic to each element, however, the electron affinity and ionization energy of a given atom cannot be altered. This presents an immense synthetic challenge for the design of tunable materials as substituting atoms often leads to entirely new structures, interactions and collective behaviors.

By analogy to “atomic” building blocks, certain clusters can be used as “superatomic” building blocks for the assembly of novel materials.^{1–22} Within this context, the family of metal chalcogenide molecular clusters has recently received renewed attention for the creation of functional solids with tunable properties, including ferromagnetism,

electrical conductivity, tunable optical gaps and thermal switching.^{1,7,23–32} One of the key advantages of this approach over traditional atomic solids is that the characteristics of the building blocks can be tuned pre-assembly without changing the total electron count of the superatom. Using the molecular cluster $\text{Co}_6\text{Te}_8\text{L}_6$ (L = passivating ligand) as a model system, Khanna *et al.* recently predicted theoretically that changing L from PEt_3 to CO would increase its electron affinity, in effect transforming the cluster from a superatomic alkali metal toward a superatomic halogen.^{33,34} The potential to alter the donor/acceptor property of these superatomic clusters sheds light on assembling superatomic materials with fine-tuned properties. Experimentally demonstrating this concept by measuring the electron affinity and/or ionization energy of metal chalcogenide clusters is challenging, however, because it requires bringing the charged clusters into the gas phase without damaging the inorganic core or dissociating the ligands.

In this work, we use anion photoelectron spectroscopy to probe the electron affinity (EA) and electronic structure of a series of cobalt sulfide clusters, whose ligand shells consist of differing combinations of PEt_3 and CO. The clusters $\text{Co}_6\text{S}_8(\text{PEt}_3)_{6-x}(\text{CO})_x$ are synthesized from the parent compound $\text{Co}_6\text{S}_8(\text{PEt}_3)_6$ by ligand substitution with CO. These clusters are then brought into the gas phase, where electrons are attached to form anions, using a unique infrared desorption/photoelectron-emission/supersonic helium

expansion source. Mass spectrometry confirms the existence of carbonylated products with x up to 3 (*i.e.* $\text{Co}_6\text{S}_8(\text{PEt}_3)_5(\text{CO})^-$, $\text{Co}_6\text{S}_8(\text{PEt}_3)_4(\text{CO})_2^-$, and $\text{Co}_6\text{S}_8(\text{PEt}_3)_3(\text{CO})_3^-$). We find that the electron affinity and vertical detachment energy increase with the number of CO ligands, demonstrating the electronic spectral tunability of this family of superatoms. These results are further examples of the superatom concept, and an important step towards designing materials from programmable building blocks.

Methods

Synthesis

Dicobalt octacarbonyl and sulfur were purchased from Strem Chemicals. Triethylphosphine was purchased from Alfa Aesar. All other reagents and solvents were purchased from Sigma Aldrich. Dry and deoxygenated solvents were prepared by elution through a dual-column solvent system. Unless otherwise stated, all reactions and sample preparations were carried out under inert atmosphere using standard Schlenk techniques or in a N_2 -filled glovebox. While a multi-step synthesis of $\text{Co}_6\text{S}_8(\text{PEt}_3)_6$ has been previously reported,³⁵ we have developed an alternative one-pot approach detailed below.

$\text{Co}_6\text{S}_8(\text{PEt}_3)_6$. Sulfur (1.16 g, 36.25 mmol) was suspended in ~30 mL of toluene in a 200 mL Schlenk flask under N_2 atmosphere. In two separate flasks, $\text{Co}_2(\text{CO})_8$ (4.12 g, 12.05 mmol) and PEt_3 (4.27 g, 36.14 mmol) were dissolved in ~20 mL of toluene. The

$\text{Co}_2(\text{CO})_8$ solution was added to the S suspension, followed by quick addition of the PEt_3 solution. The reaction mixture was refluxed under N_2 for 2 days. The reaction mixture was then opened to air, and hot filtered through Celite. The filtrate was cooled to room temperature and left to stand for ~ 3 h. Black crystals formed during that period; the resulting suspension was filtered through a fine frit and the solid was washed with toluene, and diethyl ether. The dark, black crystals were collected, dried *in vacuo*, and stored under N_2 . Yield: 2.2 g (42%). MS-MALDI m/z^+ calculated 1317.92; found, 1317.95.

$\text{Co}_6\text{S}_8(\text{PEt}_3)_{6-x}(\text{CO})_x$. Safety note: CO is a toxic gas; this reaction can only be performed in a well-ventilated fumehood. Sulfur (0.15 g, 4.68 mmol) and $\text{Co}_6\text{S}_8(\text{PEt}_3)_6$ (1.00 g, 0.76 mmol) were combined in ~ 75 mL of toluene in a 200 mL Schlenk flask. An external bubbler was attached to the system, and the mixture was sparged with CO for 30 min. The mixture was heated to 100 °C and stirred under a CO atmosphere for 16 h. The reaction mixture was cooled to room temperature, sparged with N_2 , and the solvent was removed *in vacuo*. The resulting solid was used directly without further purification.

Anion photoelectron spectroscopy

Anion photoelectron spectroscopy was conducted by crossing a mass-selected negative ion beam with a fixed energy photon beam and analyzing the energies of the resultant

photodetached electrons. This technique is governed by the well-known energy-conserving relationship, $h\nu = \text{EBE} + \text{EKE}$, where $h\nu$, EBE, and EKE are the photon energy, electron binding energy (photodetachment transition energy), and the electron kinetic energy, respectively. The details of our apparatus have been described elsewhere.³⁶ Briefly, the photoelectron spectra were collected on an apparatus consisting of an ion source, a linear time-of-flight mass spectrometer for mass analysis and selection, and a magnetic-bottle photoelectron spectrometer for electron energy analysis (resolution ~ 35 meV at 1 eV EKE). The third harmonic (355 nm, 3.49 eV per photon) of a Nd:YAG was used to photodetach electrons from the cluster anion of interest. Photoelectron spectra were calibrated against the well-known atomic lines of the copper anion, Cu^- .

To make the parent anions $\text{Co}_6\text{S}_8(\text{PEt}_3)_{6-x}(\text{CO})_x^-$ in the gas phase, a specialized infrared desorption/laser photoemission (IR/PE) supersonic helium expansion source is employed.³⁷ Briefly, a low power IR pulse (1064 nm) from a Nd:YAG laser hits a translating graphite bar thinly coated with the $\text{Co}_6\text{S}_8(\text{PEt}_3)_{6-x}(\text{CO})_x$ sample. Because the graphite absorbs most of the energy, a localized thermal shock lasting a few nanoseconds propels the clusters into the gas phase. Almost simultaneously, a high power pulse of 532 nm light from a second Nd:YAG laser strikes a close-by photoemitter (Hf wire), creating a shower of electrons that attach to the evaporated neutral clusters. Also, almost

simultaneously, a plume of ultrahigh purity helium gas rapidly expands from a pulsed valve located slightly upstream, cooling the nascent anions and directing them into the mass spectrometer, where they are analyzed. Because the $\text{Co}_6\text{S}_8(\text{PET}_3)_{6-x}(\text{CO})_x$ clusters are slightly sensitive to air and moisture, they are coated onto the graphite bar in a N_2 -filled glove box. The graphite bar is then enclosed inside an air-tight “suitcase” container, which is only opened under high vacuum after being transferred to the vacuum chamber.

Theoretical calculations

First-principles electronic structure calculations on the anion and neutral forms of $\text{Co}_6\text{S}_8(\text{PET}_3)_{6-x}(\text{CO})_x$ ($x = 0-3$) clusters were carried out within density functional theory formalism. The ADF set of codes were used to perform the calculations where a PBE0 hybrid functional comprised of the PBE generalized gradient functional and 25% Hartree–Fock exchange, as proposed by Ernzerhof *et al.*, is used to incorporate exchange and correlation effects.³⁸⁻⁴⁰ The atomic wave functions are expressed in terms of Slater-type orbitals (STO) located at the atomic sites and the cluster wave functions are constructed from a linear combination of these atomic orbitals.⁴¹ A TZ2P basis set and a large frozen electron core was used. The zero-order regular approximation (ZORA) is used to include scalar-relativistic effect.^{42,43} The trial structures of the clusters were taken from the previously optimized structure of the $\text{Co}_6\text{Te}_8(\text{PET}_3)_6$ where the Te sites were replaced by S atoms.³³ The quasi-Newton method without any symmetry restriction

is used to determine the lowest energy arrangement for each trial structure of the clusters. The calculations also covered the several possible spin states for all the clusters during optimization. The adiabatic electron affinity (AEA) is calculated as the total energy difference between the anion in its ground state geometry and the neutral cluster in its ground state geometry, while the vertical detachment energy (VDE) is given by the total energy difference between the anion in its ground state and the neutral cluster in the geometry of the anion.

Results and discussions

Fig. 1a depicts the structure of $\text{Co}_6\text{S}_8(\text{PEt}_3)_{6-x}(\text{CO})_x$. Our strategy to synthesize these clusters begins by preparing the parent compound $\text{Co}_6\text{S}_8(\text{PEt}_3)_6$ on a multigram scale. To achieve this, we have developed a new approach detailed in the Methods section. Briefly, under a CO atmosphere, $\text{Co}_6\text{S}_8(\text{PEt}_3)_6$ is reacted with six equivalents of S in toluene at ~ 100 °C to partially substitute CO for PEt_3 , which is trapped as SPEt_3 . Using the mass spectrometry technique described below, we observe a mixture of clusters in which up to three CO ligands have been substituted for PEt_3 . It is possible to separate these different species using column chromatography,³⁰ but for this study we can use the mixture of clusters without further purification.

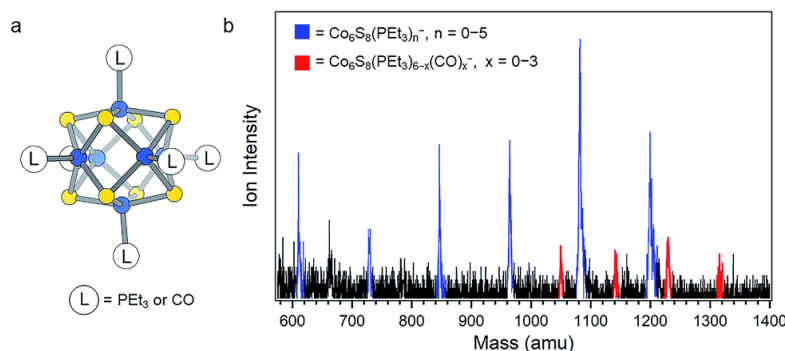


Figure II.1.1 (a) Structure of $\text{Co}_6\text{S}_8(\text{PET}_3)_{6-x}(\text{CO})_x$. (b) Anion mass spectrum of $\text{Co}_6\text{S}_8(\text{PET}_3)_{6-x}(\text{CO})_x^-$ generated using IR/PE anion source. This work focuses on the red peaks in the mass spectrum.

Measuring the electron affinity and electronic structure of $\text{Co}_6\text{S}_8(\text{PET}_3)_{6-x}(\text{CO})_x$ requires a negative ion photoelectron spectroscopic study on their parent anions, $\text{Co}_6\text{S}_8(\text{PET}_3)_{6-x}(\text{CO})_x^-$, in the gas phase. Common ionization methods (*e.g.* electrospray ionization and matrix-assisted laser desorption/ionization), however, fail to generate the parent anions $\text{Co}_6\text{S}_8(\text{PET}_3)_{6-x}(\text{CO})_x^-$ in the gas phase due to the effect of the solvent/matrix on neutral $\text{Co}_6\text{S}_8(\text{PET}_3)_{6-x}(\text{CO})_x$ clusters: the obtained anions are either dissociated or tagged by the solvent/matrix molecules. To make the parent anions in the gas phase, we instead employ a unique infrared desorption/photoemission (IR/PE) source as described in the Methods section. A typical anion mass spectrum of $\text{Co}_6\text{S}_8(\text{PET}_3)_{6-x}(\text{CO})_x^-$ obtained with the IR/PE source is shown in Fig. 1b. The spectrum contains two major series of anions: $\text{Co}_6\text{S}_8(\text{PET}_3)_n^-$ ($n = 0-5$) and $\text{Co}_6\text{S}_8(\text{PET}_3)_{6-x}(\text{CO})_x^-$ ($x = 0-3$). The $\text{Co}_6\text{S}_8(\text{PET}_3)_n^-$ clusters are from the sequential

dissociation of PEt_3 from $\text{Co}_6\text{S}_8(\text{PEt}_3)_6$ during infrared desorption, while the $\text{Co}_6\text{S}_8(\text{PEt}_3)_{6-x}(\text{CO})_x^-$ clusters are the anions of interest in this study. Though the $\text{Co}_6\text{S}_8(\text{PEt}_3)_{6-x}(\text{CO})_x^-$ signals are weaker, their high photodetachment cross-sections allow us to collect their anion photoelectron spectra.

Fig. 2 presents the anion photoelectron spectra of $\text{Co}_6\text{S}_8(\text{PEt}_3)_{6-x}(\text{CO})_x^-$ ($x = 0-3$) from which the adiabatic electron affinity (AEA) and vertical detachment energy (VDE) of each cluster are determined. The value of the AEA is taken to be the onset of the lowest electron binding energy (EBE) peak in the photoelectron spectrum. The VDE is the vertical transition energy from the ground state of the anion to the neutral state at the anion geometry. It is determined as the EBE value at the intensity maximum of the peak of interest, *i.e.* typically the first EBE peak. Based on the anion photoelectron spectra, the AEA values of $\text{Co}_6\text{S}_8(\text{PEt}_3)_{6-x}(\text{CO})_x$ are 1.1, 1.3, 1.7 and 1.8 eV for $x = 0, 1, 2, 3$, respectively, while the corresponding anion VDE values are 1.30, 1.51, 1.95 and 2.09 eV, respectively. By sequentially substituting half of the PEt_3 ligands with CO, the AEA of this superatom increases from 1.1 eV to 1.8 eV, all while maintaining the same oxidation state for the Co_6S_8 core. As a reference, the reducing agent SO_2 and oxidizing agent SO_3 have AEA values of 1.11 eV and 1.90 eV,^{44,45} respectively, where the increase in AEA is the result of the change in the S atom oxidation state. Thus, the observed changes in AEA values for the ligated superatoms are significant, given that the

oxidation state of the Co_6S_8 core does not change across the ligation series: these results underscore the remarkable characteristics of the superatoms. The observed unambiguous trend of increasing AEA and VDE values with ligand substitution is a direct evidence that the electronic properties of this superatom can be tuned effectively in this way.

The tuning of the electronic properties can be further demonstrated through the spectral features located at higher electron binding energies than that of the first EBE peak. These higher EBE peaks arise from transitions from the anion ground state to various excited electronic states of the neutral cluster. The shape of these features relates to the electronic structure of the neutral clusters. While the photoelectron spectra of $\text{Co}_6\text{S}_8(\text{PET}_3)_{6-x}(\text{CO})_x^-$

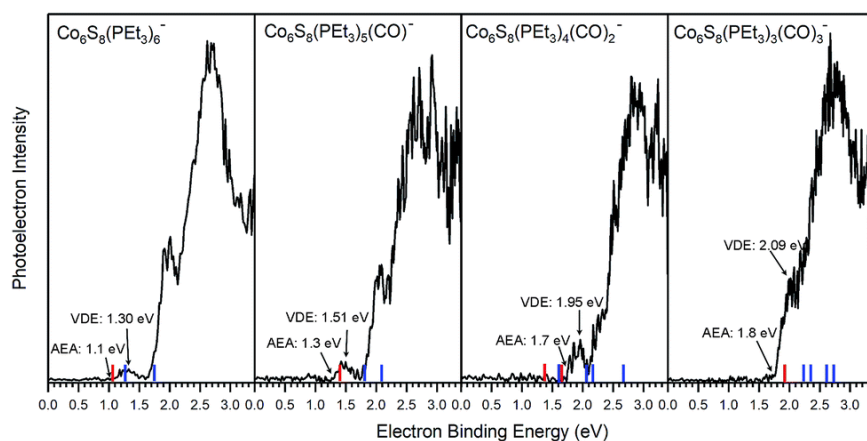


Figure II.1.2 Negative ion photoelectron spectra of $\text{Co}_6\text{S}_8(\text{PET}_3)_{6-x}(\text{CO})_x^-$ ($x = 0-3$) anions collected using 355 nm (3.49 eV) photons from a Nd:YAG laser. The arrows point to the experimental values of AEA and VDE; the red lines correspond to theoretical AEA, and the blue lines correspond to vertical transitions from the anion to the singlet and triplet neutral states.

shift to higher electron binding energy as x increases, the overall spectral shapes are remarkably similar, confirming that the sequential exchange of PEt_3 with CO ligand leaves the essential electronic structure of $\text{Co}_6\text{S}_8(\text{PEt}_3)_{6-x}(\text{CO})_x$ superatoms largely unchanged. What is changing with sequential ligation, however, is a monotonic decrease in the energies of the highest occupied and lowest unoccupied molecular orbital (HOMO and LUMO) levels, even though the gap between them remains relatively constant. This is discussed further below.

To support these experimental observations, we modeled the ground state structures of $\text{Co}_6\text{S}_8(\text{PEt}_3)_{6-x}(\text{CO})_x^-$, and calculated their AEA and VDE using density functional theory formalism (Fig. 3). In agreement with previous calculations of the $\text{Co}_6\text{Te}_8(\text{PEt}_3)_{6-x}(\text{CO})_x$ system,³³ we find that the anionic clusters $\text{Co}_6\text{S}_8(\text{PEt}_3)_{6-x}(\text{CO})_x^-$ have doublet spin ground states, while the neutral species have singlet spin states. For $\text{Co}_6\text{S}_8(\text{PEt}_3)_4(\text{CO})_2^-$, there are two possible structures: *trans*- $\text{Co}_6\text{S}_8(\text{PEt}_3)_4(\text{CO})_2^-$ and *cis*- $\text{Co}_6\text{S}_8(\text{PEt}_3)_4(\text{CO})_2^-$, with the latter lower in energy by 0.20 eV. The replacement of three PEt_3 ligands with CO leads to *fac*- $\text{Co}_6\text{S}_8(\text{PEt}_3)_3(\text{CO})_3^-$ and *mer*- $\text{Co}_6\text{S}_8(\text{PEt}_3)_3(\text{CO})_3^-$ isomers, with the latter isomer lower in energy by 0.07 eV. The small energy difference between the $\text{Co}_6\text{S}_8(\text{PEt}_3)_3(\text{CO})_3^-$ isomers suggests their co-existence in the experimental beam. Table S1† contains more calculation results on neutral and anionic species.

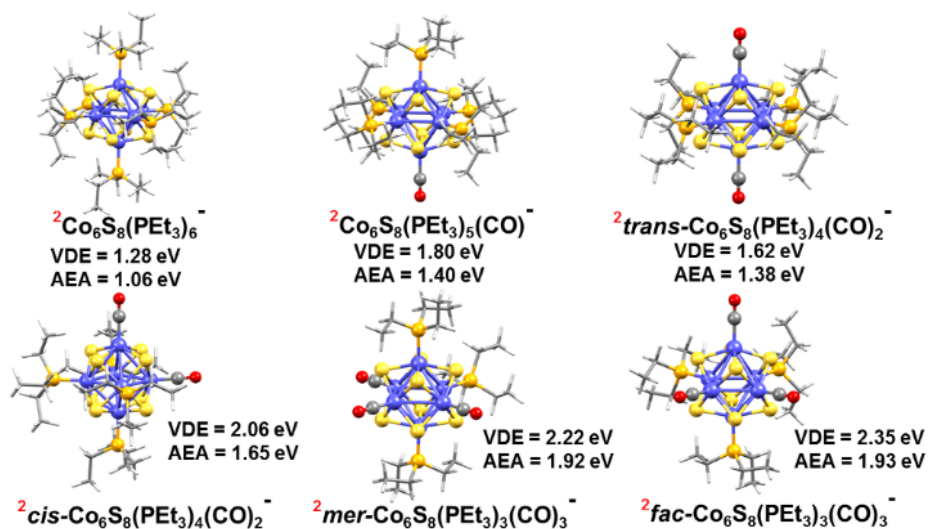


Figure II.1.3 Optimized ground state structure of anionic $\text{Co}_6\text{S}_8(\text{PET}_3)_{6-x}(\text{CO})_x^-$ ($x = 0-3$) clusters. The red superscript indicates the spin multiplicity ($2S+1$) of each cluster.

We modeled the electronic structure of the superatoms using the anion photoelectron spectra as fingerprints of the ground state geometry and electronic states of both the neutral and anionic clusters.⁴⁶ Three points of comparison are used to establish the theoretical ground state of the system: AEA, VDE and VDE*. VDE and VDE* are the vertical transitions from the anion ground state to the neutral with singlet and triplet spin multiplicity, respectively. Experimentally, VDE and VDE* correspond to the electron binding energies of the first (lowest EBE) and second (next highest EBE) peaks in the photoelectron spectra.

Table 1 presents both theoretical and experimental values of AEA, VDE and VDE* for all the superatoms considered here. Using AEA, VDE and VDE* as references to validate

the computation, we observe close agreement between experimental and calculated values. The agreement between experiments and calculations is further demonstrated by including the computed values in the anion photoelectron spectra in Figure 2. The key result is that the AEA and both VDE values increase as PEt_3 ligands are successively replaced with CO. Starting with $\text{Co}_6\text{S}_8(\text{PEt}_3)_6^-$, the calculated AEA, VDE, and VDE^* values of 1.06, 1.28, and 1.74 eV are close to the experimental values of 1.1, 1.30 eV, and 1.91 eV, respectively. Experimentally, the replacement of one PEt_3 with a CO ligand results in a ~ 0.2 eV increase in the AEA (1.3 eV) and VDE values (1.51 and 2.05 eV), whereas the calculated AEA (1.40 eV) and VDE values (1.80 and 2.08 eV) for $\text{Co}_6\text{S}_8(\text{PEt}_3)_5\text{CO}^-$ are only slightly higher. For *cis*- $\text{Co}_6\text{S}_8(\text{PEt}_3)_4(\text{CO})_2^-$ and *trans*- $\text{Co}_6\text{S}_8(\text{PEt}_3)_4(\text{CO})_2^-$, the computed ground states have AEA values of 1.65 and 1.38 eV, VDE values of 2.06 and 1.62 eV, and VDE^* values of 2.66 and 2.16 eV, respectively. A comparison between the experimental and theoretical results for $\text{Co}_6\text{S}_8(\text{PEt}_3)_4(\text{CO})_2^-$ confirms that this cluster is primarily the *cis*-isomer: the experimental values AEA = 1.7 eV, VDE = 1.95 eV, and $\text{VDE}^* = 2.51$ eV all agree very well with the *cis*-isomer calculations. We note that the small shoulder at 2.19 eV in the spectrum (Figure 2) matches the calculated VDE^* of the *trans*-isomer, raising the possibility that a small amount of the *trans*-isomer is also present. For $n = 3$, both the *mer*- $\text{Co}_6\text{S}_8(\text{PEt}_3)_3(\text{CO})_3^-$ and *fac*- $\text{Co}_6\text{S}_8(\text{PEt}_3)_3(\text{CO})_3^-$ have similar computed AEA and VDE values that are consistent with the experimental data. Because the *mer*- and *fac*-clusters are close in

energy in their neutral and anionic forms, it is very likely that they both exist in the ion beam, and that the $\text{Co}_6\text{S}_8(\text{PEt}_3)_3(\text{CO})_3^-$ photoelectron spectrum contains transitions from both isomers.

Table II.1.2 Theoretical and experimental adiabatic and vertical detachment energies (1st and 2nd peak) of $\text{Co}_6\text{S}_8(\text{PEt}_3)_{6-x}(\text{CO})_x^-$ ($x = 0-3$) clusters. The superscripts T and E indicate theoretical and experimental values, respectively.

Anionic clusters	AEA ^T (eV)	VDE ^T (eV)		AEA ^E (eV)	VDE ^E (eV)	
		VDE	VDE*		VDE	VDE*
$\text{Co}_6\text{S}_8(\text{PEt}_3)_6^-$	1.06	1.28	1.74	1.1	1.30	1.91
$\text{Co}_6\text{S}_8(\text{PEt}_3)_5(\text{CO})^-$	1.40	1.80	2.08	1.3	1.51	2.05
<i>cis</i> - $\text{Co}_6\text{S}_8(\text{PEt}_3)_4(\text{CO})_2^-$	1.65	2.06	2.66	1.7	1.95	2.51
<i>trans</i> - $\text{Co}_6\text{S}_8(\text{PEt}_3)_4(\text{CO})_2^-$	1.38	1.62	2.16			
<i>mer</i> - $\text{Co}_6\text{S}_8(\text{PEt}_3)_3(\text{CO})_3^-$	1.92	2.22	2.71	1.8	2.09	2.67
<i>fac</i> - $\text{Co}_6\text{S}_8(\text{PEt}_3)_3(\text{CO})_3^-$	1.93	2.35	2.60			

^a The superscripts T and E indicate theoretical and experimental values, respectively.

The replacement of PEt_3 ligands by CO concurrently lowers the energies of the HOMO and LUMO, with the result that the HOMO-LUMO gap is essentially unchanged across the cluster series. Figure 4a illustrates this trend for the neutral species while their absolute energy values are given in Table S1. The lowering of the HOMO and LUMO can be in part understood in terms of the vastly different ligand field effect of the cluster surface passivation: PEt_3 is a strong σ -donor that increases the electron density in the core while CO is a strong π -acceptor that removes electron density from the core, thus lowering the energy of the electronic spectrum.³³ This behavior can be seen in the Figures S1 and S2 which show the one-electron energy levels of $\text{Co}_6\text{S}_8(\text{PEt}_3)_{6-x}(\text{CO})_x$ (x

= 0–3). The change in the AEA closely tracks the change in the LUMO as the electron is attached to the LUMO of the neutral. This is illustrated in Figure 4b, which shows the changes in the energy of the LUMO (Δ LUMO), theoretical AEA (Δ AEA^T)

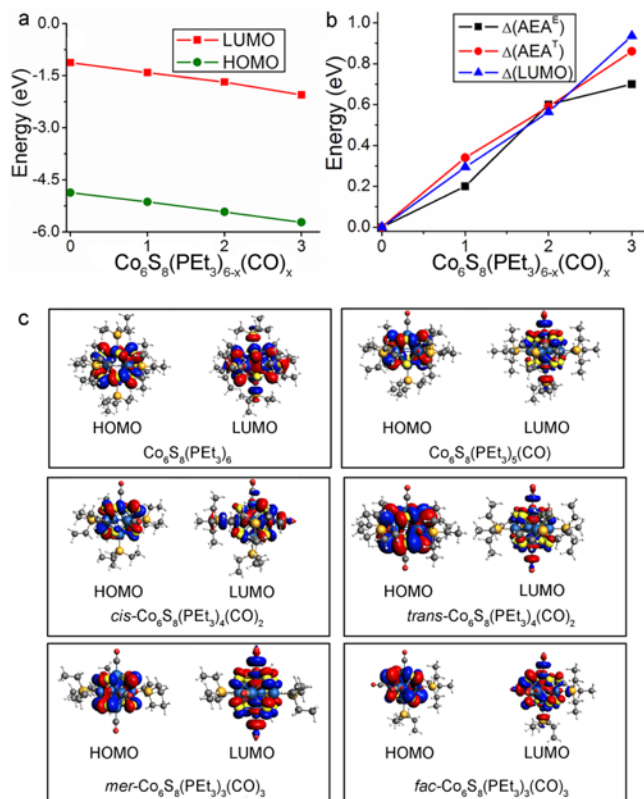


Figure II.1.1 (a) The absolute energy values of the HOMO and LUMO for neutral $\text{Co}_6\text{S}_8(\text{PET}_3)_{6-x}(\text{CO})_x$ ($x = 0-3$). (b) Incremental differences in the experimental AEA values, the theoretical AEA values, and the LUMO values of $\text{Co}_6\text{S}_8(\text{PET}_3)_{6-x}(\text{CO})_x$, each with respect to $\text{Co}_6\text{S}_8(\text{PET}_3)_6$. (c) Molecular orbital iso-surfaces of the HOMO and LUMO in $\text{Co}_6\text{S}_8(\text{PET}_3)_{6-x}(\text{CO})_x$ ($x=0-3$) clusters.

And experimental AEA (Δ AEA^E) of $\text{Co}_6\text{S}_8(\text{PET}_3)_{6-x}(\text{CO})_x$ as x increases from 0 to 3. The

molecular orbital iso-surfaces of the HOMO and LUMO in $\text{Co}_6\text{S}_8(\text{PET}_3)_{6-x}(\text{CO})_x$ are shown in Figure 4c. A Mulliken population analysis of the molecular orbitals reveals that hybridization between the p-states of S and the 3d-states of Co forms the HOMO in each cluster, while the LUMO is an antibonding state comprising the $3d_z^2$ -orbital of Co and the lone pair of the ligand (PET₃/CO). An additional phenomenon combines with the traditional ligand field effect to explain the changes in AEA and VDE: PET₃ and CO form charge transfer complexes, and the induced dipoles at the cluster surface play a critical role in changing the electronic properties. As a reference, surface dipoles can either increase or decrease the work function of metals.^{47,48} In this case, as PET₃ ligands are replaced by CO, the sign of the dipole changes and hence AEA increases as more CO are bound to the core.

Lastly, though the ionization energy of $\text{Co}_6\text{S}_8(\text{PET}_3)_{6-x}(\text{CO})_x$ is not directly measured, the successive rise in AEA and lowering of HOMO are evidence of a trend of increasing ionization energy as PET₃ is replaced by CO.

Conclusions

By combining cluster synthesis, gas-phase anion photoelectron spectroscopy, and electronic structure calculations, we have demonstrated that the electronic properties of metal chalcogenide superatomic clusters can be tuned by varying their capping ligands.

While the total electron count of the closed-shell core remains unchanged, substitution of the ligands leads to a simultaneous rise or fall of the HOMO and LUMO levels, resulting in a change of the cluster donor/acceptor behavior.

These results are significant because such drastic change in the cluster properties is rarely observed in other superatomic systems. Besides changes of electron affinity and ionization potential, ligand substitution of a ligated cluster almost always results in changes of other core chemical properties such as the HOMO-LUMO gap, electron configuration, and electronic structure. For example, in phosphine-passivated gold clusters approximated by the confined nearly free electron gas model, charge transfer from the phosphine ligands results in significant changes to the core electron count and HOMO-LUMO gap.⁴⁹ The unpredictable outcome of ligand substitution can impose important challenges in designing programmable cluster building blocks. In this context, the metal chalcogenide cluster presented in this work is unique: ligand substitution can be used to tune its electron affinity and ionization potential while maintaining its HOMO-LUMO gap, electronic structure and effective electron count, thus enabling us to control its oxidative and reductive properties. Such tunability may prove crucial for applications as catalysts, semiconductor dopants, and superatomic building blocks for cluster-assembled materials. In one example, we recently showed that related clusters can be used as electron-donating or electron-accepting surface dopants for two-

dimensional semiconductors, where the band structures can be controlled by the choice of ligands.^{32,50} Such dopants could also be made magnetic because of their finite spin moments.⁵¹ More broadly, our results open the door to the design of tunable functional materials from superatomic building blocks.

References

- A. Pinkard, A. M. Champsaur and X. Roy, *Acc. Chem. Res.*, 2018, **51**, 919-929.
- S. A. Claridge, A. W. Castleman, S. N. Khanna, C. B. Murray, A. Sen and P. S. Weiss, *ACS Nano.*, 2009, **3**, 244-255.
- E. G. Tulsky and J. R. Long, *Chem. Mater.*, 2001, **13**, 1149-1166.
- S. A. Baudron, P. Batail, C. Coulon, R. Clerac, E. Canadell, V. Laukhin, R. Melzi, P. Wzietek, D. Jerome, P. Auban-Senzier and S. Ravy, *J. Am. Chem. Soc.*, 2005, **127**, 11785-11797.
- B. Yoon, W. D. Luedtke, R. N. Barnett, J. Gao, A. Desireddy, B. E. Conn, T. Bigioni and U. Landman, *Nat. Mater.*, 2014, **13**, 807-811.
- J. F. Corrigan, O. Fuhr and D. Fenske, *Adv. Mater.*, 2009, **21**, 1867-1871.
- X. Roy, C.-H. Lee, A. C. Crowther, C. L. Schenck, T. Besara, R. A. Lalancette, T. Siegrist, P. W. Stephens, L. E. Brus, P. Kim, M. L. Steigerwald and C. Nuckolls, *Science*, 2013, **341**, 157-160.
- S. N. Khanna and P. Jena, *Phys. Rev. B.*, 1995, **51**, 13705-13716.
- A. W. Castleman and S. N. Khanna, Clusters, *J. Phys. Chem. C*, 2009, **113**, 2664-2675.
- A. C. Reber and S. N. Khanna, *Acc. Chem. Res.*, 2017, **50**, 255-263.
- C.-H. Lee, L. Liu, C. Bejger, A. Turkiewicz, T. Goko, C. J. Arguello, B. A. Frandsen, S. C. Cheung, T. Medina, T. J. S. Munsie, R. D'Ortenzio, G. M. Luke, T. Besara, R. A. Lalancette, T. Siegrist, P. W. Stephens, A. C. Crowther, L. E. Brus, Y. Matsuo, E. Nakamura, Y. J. Uemura, P. Kim, C. Nuckolls, M. L. Steigerwald and X. Roy, *J. Am. Chem. Soc.*, 2014, **136**, 16926-16931.
- X. Roy, C. L. Schenck, S. Ahn, R. A. Lalancette, L. Venkataraman, C. Nuckolls and M. L. Steigerwald, *Angew. Chem., Int. Ed.*, 2012, **51**, 12473-12476.
- M. T. Trinh, A. Pinkard, A. B. Pun, S. N. Sanders, E. Kumarasamy, M. Y. Sfeir, L. M. Campos, X. Roy and X.-Y. Zhu, *Sci. Adv.* 2017, **3**, e1700241
- V. Chauhan, S. Sahoo and S. N. Khanna, *J. Am. Chem. Soc.* 2016, **138**, 1916-1921.
- S. N. Khanna and A. C. Reber, *Nat. Chem.*, 2017, **9**, 1151-1152.
- D. A. Tomalia and S. N. Khanna, *Chem. Rev.*, 2016, **116**, 2705-2774.
- Z. Zheng, J. R. Long and R. H. Holm, *J. Am. Chem. Soc.*, 1997, **119**, 2163-2171.
- M. Cargnello, A. C. Johnston-Peck, B. T. Diroll, E. Wong, B. Datta, D. Damodhar, V. V. T.

Doan-Nguyen, A. A. Herzing, C. R. Kagan and C. B. Murray, *Nature*, 2015, **524**, 450–453.

M. N. O’Brien, M. R. Jones, B. Lee and C. A. Mirkin, *Nat. Mater.*, 2015, **14**, 833–839.

M. A. Boles and D. V. Talapin, *J. Am. Chem. Soc.*, 2015, **137**, 4494.

C. L. Poyser, T. Czerniuk, A. Akimov, B. T. Diroll, E. A. Gaudling, A. S. Salasyuk, A. J. Kent, D. R. Yakovlev, M. Bayer and C. B. Murray, *ACS Nano.*, 2016, **10**, 1163–1169.

W.-L. Ong, S. M. Rupich, D. V. Talapin, A. J. H. McGaughey and J. A. Malen, *Nat. Mater.*, 2013, **12**, 410–415.

A. Voevodin, L. M. Campos and X. Roy, *J. Am. Chem. Soc.*, 2018, **140**, 5607–5611.

A. M. Champsaur, J. Yu, X. Roy, D. W. Paley, M. L. Steigerwald, C. Nuckolls and C. M. Bejger, *ACS Cent. Sci.*, 2017, **3**, 1050–1055.

A. M. Champsaur, C. Mézière, M. Allain, D. W. Paley, M. L. Steigerwald, C. Nuckolls and P. Batail, *J. Am. Chem. Soc.*, 2017, **139**, 11718–11721.

E. S. O’Brien, M. T. Trinh, R. L. Kann, J. Chen, G. A. Elbaz, A. Masurkar, T. L. Atallah, M. V. Paley, N. Patel, D. W. Paley, I. Kymissis, A. C. Crowther, A. J. Millis, D. R. Reichman, X.-Y. Zhu and X. Roy, *Nat. Chem.*, 2017, **9**, 1170–1174.

G. Lovat, B. Choi, D. W. Paley, M. L. Steigerwald, L. Venkataraman and X. Roy, *Nat. Nanotechnol.*, 2017, **12**, 1050–1054.

W.-L. Ong, E. S. O’Brien, P. S. M. Dougherty, D. W. Paley, C. Fred Higgs Iii, A. J. H. McGaughey, J. A. Malen and X. Roy, *Nat. Mater.*, 2017, **16**, 83–88.

B. Choi, J. Yu, D. W. Paley, M. Tuan Trinh, M. V. Paley, J. M. Karch, A. C. Crowther, C. H. Lee, R. A. Lalancette, X. Zhu, K. Kim, M. L. Steigerwald, C. Nuckolls and X. Roy, *Nano Lett.*, 2016, **16**, 1445–1449.

A. M. Champsaur, A. Velian, D. W. Paley, B. Choi, X. Roy, M. L. Steigerwald and C. Nuckolls, *Nano Lett.*, 2016, **16**, 5273–5277.

A. Turkiewicz, D. W. Paley, T. Besara, G. Elbaz, A. Pinkard, T. Siegrist and X. Roy, *J. Am. Chem. Soc.*, 2014, **136**, 15873–15876.

J. Yu, C. H. Lee, D. Bouilly, M. Han, P. Kim, M. L. Steigerwald, X. Roy and C. Nuckolls, *Nano Lett.*, 2016, **16**, 3385–3389.

V. Chauhan, A. C. Reber and S. N. Khanna, *J. Am. Chem. Soc.*, 2017, **139**, 1871–1877.

V. Chauhan and S. N. Khanna, *J. Phys. Chem. A*, 2018, **122** (28), 6014–6020.

F. Cecconi, C. A. Ghilardi, S. Midollini and A. Orlandini, *Inorg. Chimica Acta*, 1983, **76**, 183–184.

X. Zhang, G. Liu, G. Gantefoer, K. H. Bowen and A. N. Alexandrova, *J. Phys. Chem. Lett.*, 2014, **5**, 1596–1601.

A. Grubisic, H. Wang, X. Li, Y. J. Ko, S. Kocak, M. R. Pederson, K. H. Bowen and B. W. Eichhorn, *PNAS*. 2011, **108**, 14757–14762.

J. P. Perdew and W. Yue, *Phys. Rev. B*, 1986, **33**, 8800–8802.

M. Ernzerhof and G. E. Scuseria, *J. Chem. Phys.* 1999, **110**, 5029.

C. Adamo, *J. Chem. Phys.*, 1999, **110**, 6158.

E. van Lenthe and E. J. Baerends, *J. Comput. Chem.*, 2003, **24**, 1142–1156.

E. van Lenthe, R. van Leeuwen, E. J. Baerends and J. G. Snijders, *Int. J. Quantum Chem.*,

1996, **57**, 281-293.

E. van Lenthe, A. Ehlers and E. J. Baerends, *J. Chem. Phys.*, 1999, **110**, 8943.

M. R. Nimlos and G. B. Ellison, *J. Phys. Chem.*, 1986, **90**, 2574-2580.

E. W. Rothe, S. Y. Tang, G. P. Reck, *J. Chem. Phys.*, 1975, **62**, 3829.

P. J. Robinson, G. Liu, S. Ciborowski, C. Martinez-Martinez, J. R. Chamorro, X. Zhang, T.

M. McQueen, K. H. Bowen and A. N. Alexandrova, *Chem. Mater.*, 2017, **29**, 9892-9896.

P. C. Rusu and G. Brocks, *J. Phys. Chem. B*, 2006, **110**, 22628-22634.

V. Chauhan, A. C. Reber and S. N. Khanna, *Nature Comm.*, 2018, **9**, 2357.

D. Mollenhauer and N. Gaston, *Phys. Chem. Chem. Phys.*, 2016, **18**, 29686.

A. C. Reber and S. N. Khanna, *npj Computational Material*, 2018, **4**, 33.

V. Chauhan, A. C. Reber and S. N. Khanna, *Phys. Chem. Chem. Phys.*, 2017, **19**, 31940-31948.

II.2 Ligand Effect on the Electronic Structure of Cobalt Sulfide Clusters: A Combined Experimental and Theoretical Study

Gaoxiang Liu^a, Vikas Chauhan^b, Alexander P. Ayt^c, Sandra M. Ciborowski^a, Andrew Pinkard,^c Zhaoguo Zhu^a, Xavier Roy^{c,*}, Shiv N. Khanna,^{b,*} and Kit H. Bowen^{a,*}

^a Department of Chemistry, Johns Hopkins University, Baltimore, Maryland 21218, USA.

^b Department of Physics, Virginia Commonwealth University, 701 W. Grace St., Richmond, Virginia 23284, USA.

^c Department of Chemistry, Columbia University, New York, New York 10027, USA.

Abstract

Recent studies have shown that capping ligands offer a new dimension for fine tuning the properties of clusters. Here we investigate this concept by measuring the anion photoelectron spectra of a series of hexanuclear cobalt sulfide clusters, Co_6S_8 , passivated by different numbers of triethylphosphine ligands, PET_3 . We find that the addition of PET_3 gradually shifts the electronic spectrum of the cluster to higher energy, leading to a decrease in its electron affinity. Density functional theory calculations reveal that adding ligands demagnetize the Co_6S_8 core. The decrease in electron affinity results from a monotonic increase in the energy of the cluster lowest

unoccupied molecular orbitals (LUMO). This effect is attributed to the electron donation from the ligands to the cluster core, which increases the charge density in the core region.

Introduction

Quantum confinement in small symmetric clusters can result in a grouping of electronic states into shells, leading to the formation of stable clusters with a well-defined valence. The resemblance to atomic shells has prompted the description of such entities as superatoms.¹ Utilizing these clusters as the “superatomic” building blocks for the assembly of novel materials represents a frontier in material science.¹⁻²² Within this context, the family of metal chalcogenide molecular clusters has recently received renewed attention for fabricating functional materials with tunable properties including ferromagnetism, electrical conductivity, optical gaps and thermal conductivity switching.^{2,7,23-32} One of the key advantages of such materials over traditional atomic solids is that the properties of the superatomic building blocks can be tailored pre-assembly. While the composition and structure of the cluster are traditionally used to control the behavior of the superatomic building unit, the capping ligands have recently received attention as valuable knobs for fine tuning.^{33,34} Capping ligands can modulate the electronic characteristics of the cluster core, and direct the assembly into solid state materials.

Recently, Khanna and coworkers theoretically predicted a variety of properties that can be tuned by modifying the capping ligands of metal chalcogenide clusters. Using $\text{Co}_6\text{Te}_8\text{L}_6$ (L = capping ligand) as a model system, they have shown that changing L from PEt_3 to CO increases the electron affinity of the cluster, in effect transforming it from a superatomic alkali metal to a superatomic halogen.¹⁴ Such an ability to alter the donor/acceptor behavior of the building blocks offers unique opportunity for creating materials with fine-tuned properties.³⁴ In a related study, it was predicted that the ionization energy of the Co_6Se_8 cluster can be gradually decreased by sequentially coordinating PEt_3 capping ligands to its surface metal atoms.³⁵ Binding carbon monoxide (CO) ligands to the Co_6Se_8 cluster, on the other hand, results in the gradual demagnetization of the core, thus stabilizing it.³⁶ Experimentally demonstrating these predictions by measuring the electronic structures of metal chalcogenide clusters is challenging, however, because it requires bringing the charged clusters with a controlled number of ligands into the gas phase without damaging the inorganic core. Common ionization methods (e.g., electrospray ionization and matrix-assisted laser desorption/ionization) fail to generate the desirable anions in the gas phase due to the effect of the solvent/matrix on charged clusters: the obtained anions are either dehydrogenated or tagged by the solvent/matrix molecules.

We recently reported an experimental study supported by theoretical calculations establishing the tunability of the electronic properties of the cluster $\text{Co}_6\text{S}_8(\text{PET}_3)_{6-n}(\text{CO})_n$ by altering the ligand ratio.³⁸ The unique infrared desorption/laser photoemission (IR/PE) supersonic expansion source used in that work serves as the ideal tool to bring the cluster into the gas phase with different number of ligands while maintaining the core structure. Here we employ this method to investigate a series of cobalt sulfide clusters passivated with varying numbers of PET_3 ligands. The cluster $\text{Co}_6\text{S}_8(\text{PET}_3)_6$ is synthesized and then brought into the gas phase, where ligands are sequentially dissociated and electrons are attached to form anions, using the IR/PE source. Mass spectrometry confirms the existence of $\text{Co}_6\text{S}_8(\text{PET}_3)_x^-$ with x ranging from 0 to 6. We find that the electron affinity and vertical detachment energy decrease with increasing ligation, demonstrating the electronic spectral tunability of this family of superatoms.

Methods

Synthesis

Dicobalt octacarbonyl and sulfur were purchased from Strem Chemicals. PET_3 was obtained from Alfa Aesar. All other reagents and solvents were purchased from Sigma Aldrich. Dry and deoxygenated solvents were prepared by elution through a dual-column solvent system (MBraun). Unless otherwise stated, all reactions and sample

preparations were carried out under inert atmosphere using standard Schlenk techniques or in a N₂-filled glovebox. While a multi-step synthesis of Co₆S₈(PEt₃)₆ has been previously reported,³⁷ we have developed an alternative one-pot approach detailed below.³⁸

Co₆S₈(PEt₃)₆. Sulfur (1.16 g, 36.25 mmol) was suspended in 30 mL of toluene in a 200 mL Schlenk flask. In two separate flasks, Co₂(CO)₈ (4.12 g, 12.05 mmol) and PEt₃ (4.27 g, 36.14 mmol) were dissolved in 20 mL of toluene. The Co₂(CO)₈ solution was added to the S suspension, followed by quick addition of the PEt₃ solution. The reaction mixture was refluxed under N₂ for 2 days. The reaction mixture was then opened to air, and hot filtered through Celite. The filtrate was cooled to room temperature and left to stand for ~3 h. Black crystals formed during that period; the resulting suspension was filtered through a fine frit and the solid was washed with toluene, and diethyl ether. The dark, black crystals were collected, dried *in vacuo*, and stored under N₂. Yield: 2.2 g (42%). The characterization data are as previously published. MS-MALDI *m/z*⁺ calculated 1317.92; found, 1317.95.

Anion photoelectron spectroscopy

Anion photoelectron spectroscopy was conducted by crossing a mass-selected negative ion beam with a fixed energy photon beam and analyzing the energies of the

resultant photodetached electrons. This technique is governed by the well-known energy-conserving relationship, $h\nu = \text{EBE} + \text{EKE}$, where $h\nu$, EBE, and EKE are the photon energy, electron binding energy (photodetachment transition energy), and the electron kinetic energy, respectively. The details of our apparatus have been described elsewhere.^{39,40} Briefly, the photoelectron spectra were collected on an apparatus consisting of an ion source, a linear time-of-flight mass spectrometer for mass analysis and selection, and a magnetic-bottle photoelectron spectrometer for electron energy analysis (resolution ~ 35 meV at 1 eV EKE). The third harmonic (355 nm, 3.49 eV per photon) of a Nd:YAG was used to photodetach electrons from the cluster anion of interest. Photoelectron spectra were calibrated against the well-known atomic lines of the copper anion, Cu^- .

To make $\text{Co}_6\text{S}_8(\text{PEt}_3)_x^-$ in the gas phase, a specialized infrared desorption/laser photoemission (IR/PE) supersonic helium expansion source was employed.^{38,41} Briefly, a low power IR pulse (1064 nm) from a Nd:YAG laser hit a translating graphite bar thinly coated with the $\text{Co}_6\text{S}_8(\text{PEt}_3)_6$ sample. Because the graphite absorbed most of the energy, a localized thermal shock lasting a few nanoseconds propelled the clusters into the gas phase. Almost simultaneously, a high power pulse of 532 nm light from a second Nd:YAG laser struck a close-by photoemitter (Hf wire), creating a shower of electrons that attached to the evaporated

neutral clusters. Also, almost simultaneously, a plume of ultrahigh purity helium gas rapidly expanded from a pulsed valve located slightly upstream, cooling the nascent anions and directing them into the mass spectrometer, where they were analyzed. The $\text{Co}_6\text{S}_8(\text{PEt}_3)_6$ cluster was coated onto a graphite bar in a N_2 -filled glove box, which was then enclosed inside an air-tight “suitcase” container and opened under high vacuum after being transferred to the vacuum chamber.

Theoretical calculations

Electronic structure modeling of the anion and neutral $\text{Co}_6\text{S}_8(\text{PEt}_3)_x$ ($x = 1-5$) were carried out to understand the variation in the adiabatic and vertical detachment energies at the microscopic level. The exchange-correlation effects are included via a generalized gradient functional PBE detailed by Perdew et al.⁴² The cluster wave function is formed from a linear combination of atomic orbitals constructed from Slater-type orbitals located on the atomic sites.⁴³ A TZ2P basis set and a large frozen electron core (S: $1s^22s^2p^6$, Co: $1s^22s^2p^63s^2p^6$, P: $1s^22s^2p^6$, C: $1s^2$) are used. The calculations incorporate a zero-order regular approximation (ZORA) to include scalar-relativistic effect.^{44,45} The trial structures of the clusters are taken from the previously optimized structure of the $\text{Co}_6\text{Se}_8(\text{PEt}_3)_x$ where the Se sites are replaced by S. A quasi-Newton method without any symmetry restriction allowed a determination of the ground state of the clusters. During optimization, we investigated all possible spin states. The positive vibrational frequencies of neutral and anionic clusters

established the true ground states of the clusters. Also, none of the clusters in their ground states has the spin-contamination. The adiabatic electron affinity (AEA) is calculated as the difference between the total energy between the anion in its ground state geometry and the neutral cluster in its ground state geometry, while the vertical detachment energy (VDE) is given by the total energy difference between the anion in its ground state and the neutral cluster in the geometry of the anion.

Results and discussions

Figure 1 presents a typical mass spectrum of $\text{Co}_6\text{S}_8(\text{PEt}_3)_x^-$ obtained with the IR/PE source. The ultrashort thermal shock induced by IR laser irradiation caused the sequential dissociation of the PEt_3 ligand during the vaporization of the solid $\text{Co}_6\text{S}_8(\text{PEt}_3)_6$ sample into gas phase. $\text{Co}_6\text{S}_8(\text{PEt}_3)_x^-$ with x ranging from 0 to 6 were generated and investigated by anion photoelectron spectroscopy.

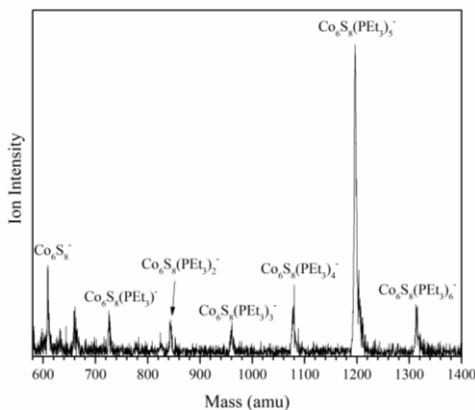


Figure II.2.1 Anion mass spectrum of $\text{Co}_6\text{S}_8(\text{PEt}_3)_x^-$ generated using IR/PE anion source.

Figure 2 presents the anion photoelectron spectra of $\text{Co}_6\text{S}_8(\text{PEt}_3)_x^-$ ($x = 2-5$) collected

with 355 nm (3.49 eV) 3rd harmonic laser. The spectrum of $\text{Co}_6\text{S}_8(\text{PEt}_3)_6^-$ has been published in a previous report.³⁸ Our attempts to measure the photoelectron spectra of Co_6S_8^- and $\text{Co}_6\text{S}_8(\text{PEt}_3)^-$ ($x = 0$ and 1) with a 355 nm laser were for the most part unsuccessful: for Co_6S_8^- , no photoelectron signal was observed, i.e., its AEA and VDE are above 3.49 eV, while for $\text{Co}_6\text{S}_8(\text{PEt}_3)^-$, only a small portion of its spectrum could be collected because the majority of its photoelectron spectrum lies beyond the photon energy (Figure S1). The AEA and VDE of each cluster are determined from the photoelectron spectra. The value of the AEA is taken to be the onset of the lowest electron binding energy (EBE) peak in the photoelectron spectrum. The VDE is the vertical transition energy from the ground state of the anion to the neutral ground electronic state at the anion geometry. It is determined as the EBE value at the intensity maximum of the peak of interest. Here, however, due to the large number of electronic states that can be accessed during the photodetachment process, the photoelectron spectra are convoluted. We therefore determine the VDE as the EBE of the first noticeable peak in each spectrum. Based on the anion photoelectron spectra, the AEA values of $\text{Co}_6\text{S}_8(\text{PEt}_3)_x$ are 3.0, 2.6, 2.2, 2.0 and 1.8 eV for $x = 1, 2, 3, 4,$ and 5, respectively, while the corresponding anion VDE values are 3.22, 2.71, 2.44, 2.31, and 2.05 eV, respectively. We also report the VDE* values, which correspond to the transition from the anion ground state to the first electronic excited state of the neutral, as the EBE of the second noticeable peak. Their values are 3.35, 2.85, 2.45, 2.29 and

2.16 eV for $x = 1, 2, 3, 4,$ and $5,$ respectively. By sequentially adding PEt_3 ligands to the Co_6S_8 core, the AEA and VDE of this superatom decrease systematically, which is consistent with the electron-donating nature of the PEt_3 ligands.

Changes in the electronic properties of the cluster are evident in high energy spectral features above the first EBE peak. These higher EBE peaks arise from transitions from the anion ground state to excited electronic states of the neutral cluster and the shape of these features relates to the electronic structure of the neutral clusters. As x increases, the photoelectron spectra of $\text{Co}_6\text{S}_8(\text{PEt}_3)_x^-$ shifts to lower electron binding energy and the overall spectral shapes change significantly. Such observation suggests a change in the electronic structure of $\text{Co}_6\text{S}_8(\text{PEt}_3)_x^-$ as x changes. Note that this is different from the previous study of $\text{Co}_6\text{S}_8(\text{PEt}_3)_{6-n}(\text{CO})_n^-$ where the photoelectron spectra shift to higher electron binding energy as the CO ratio increases, but the overall spectral shapes are maintained, indicating that the essential electronic structure of $\text{Co}_6\text{S}_8(\text{PEt}_3)_{6-n}(\text{CO})_n$ superatoms are largely unchanged.³⁸

The structures of the anionic and neutral $\text{Co}_6\text{S}_8(\text{PEt}_3)_x$ clusters were investigated by theoretical calculations. Figure 3 shows the optimized ground state geometries of $\text{Co}_6\text{S}_8(\text{PEt}_3)_x^-$, while those of the neutral species are in Figure S2. For $x = 2$ and $x = 4,$ the clusters can either be *cis* or *trans* isomers. In both cases, the *trans* isomers are

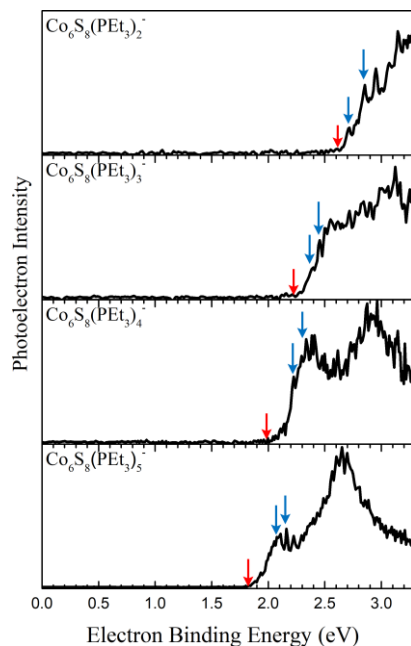


Figure II.2.2 Negative ion photoelectron spectra of $\text{Co}_6\text{S}_8(\text{PEt}_3)_x^-$ ($x = 2 - 5$) anions collected using 355 nm (3.49 eV) photons from a Nd:YAG laser. The red arrows indicate the AEA, the blue arrows indicate the VDE and the VDE*.

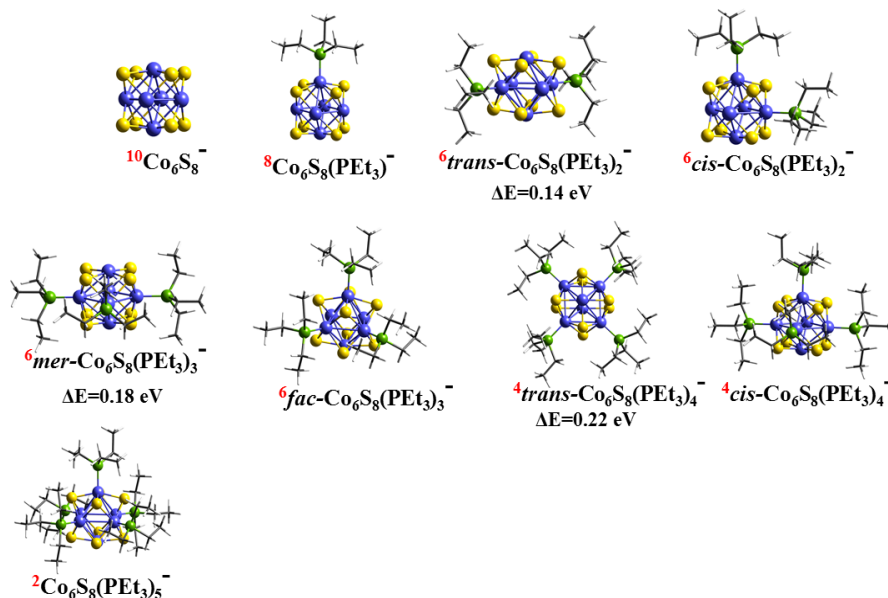


Figure II.2.3 Optimized ground state geometry of anionic $\text{Co}_6\text{S}_8(\text{PEt}_3)_x^-$ ($x = 0-5$) clusters. Superscripts in red text show the multiplicity of the clusters.

higher in energy, by ~ 0.14 and ~ 0.22 eV, respectively. A similar situation arises for

the corresponding neutral clusters: the *trans* isomers are ~ 0.01 and ~ 0.25 eV higher in energy for $x = 2$ and $x = 4$ respectively. For $\text{Co}_6\text{S}_8(\text{PET}_3)_3$, the cluster can adopt *fac* and *mer* configurations. We find that the *fac* isomer is the ground state for both anionic and neutral clusters, being lower in energy by ~ 0.18 and ~ 0.04 eV, respectively. In addition to the ligated clusters, we optimize the anionic and neutral naked Co_6S_8 core in order to complete the analysis although no photoelectron spectrum could be measured as the transitions are outside the range of measurable energies.

The key experimental finding in Figure 2 is that the bonding of PET_3 to the Co_6S_8 core leads to a change in the peak position and the leading edge of the spectrum. To provide insight into these variations, we calculate the VDE by taking the energy difference between the ground state of the anion and neutral cluster with the same geometry as the anion. The VDE corresponds to the first peak maximum in the photodetachment spectra and provides the most direct comparison with the experiment while an estimation of 2nd VDE is obtained by a vertical transition from the anion ground state to the neutral with next higher spin multiplicity. We also calculated the AEA, which are determined by the onset of the experimental spectra and corresponds to the energy difference between the ground states of the anion and neutral species. Finally, we examine the excited states of the neutral cluster in the anionic geometry that correspond to the spectral features beyond the first peak. Figure 4 compares the

experimental and theoretical AEA and VDE values while Table 1 lists the values of both the theoretical and calculated AEA and VDE. The calculated AEA and VDE of the Co₆S₈ core are 3.55 and 3.59 eV, respectively, which are in accordance with the absence of photoelectron signal when using 355 nm (3.49 eV) photon. The AEA^T for Co₆S₈(PEt₃) is 2.94 eV, agreeing with the AEA^E of 3.0 eV, while VDE^E is 3.22 eV compared to the calculated VDE^T of 2.98 eV. The *cis*-Co₆S₈(PEt₃)₂ isomer has an AEA^T of 2.49 eV, which is slightly closer to the AEA^E of 2.6 eV than that of *trans*-Co₆S₈(PEt₃)₂ (2.35 eV). Both Co₆S₈(PEt₃)₂ isomers have VDE^T around 2.60 eV that are close to the VDE^E of 2.71 eV, suggesting the possible presence of both isomers. The AEA^T and VDE^T of *fac*-Co₆S₈(PEt₃)₃ are 2.26 and 2.32 eV, in very good agreement with corresponding experimental values of AEA^E (2.2 eV) and VDE^E (2.39 eV), while the AEA^T and VDE^T for *mer*-Co₆S₈(PEt₃)₃ are 2.10 eV and 2.16 eV. Both *trans*- and *cis*-Co₆S₈(PEt₃)₄ have AEA^T around 2.0 eV, matching the experimental value of 2.0 eV, while the corresponding VDE^T (2.15 and 2.11 eV) are slightly smaller than the experimental value of 2.31 eV. In order to evaluate the dispersion effect on the calculated AEA^T and VDE^T, we also carried out calculations with Grimme dispersion corrected PBE functional.⁴⁶ Similar calculated AEA^T and VDE^T were obtained (Table S1). Overall, the calculated values are in excellent agreement with

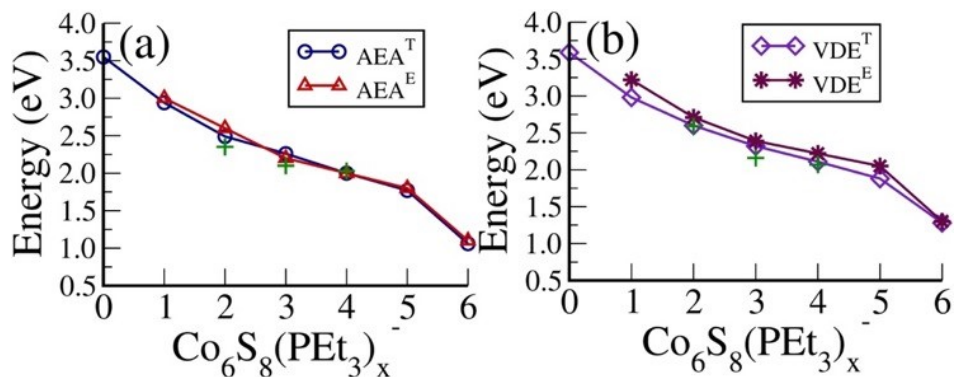


Figure II.2.4 The experimental and theoretical adiabatic and vertical detachment energy of $\text{Co}_6\text{S}_8(\text{PEt}_3)_x$ ($x = 0 - 6$) clusters. The plus symbol (+) indicates the AEA^T and VDE^T values of cluster's isomers at $x=2, 3$, and 5 . The results of $\text{Co}_6\text{S}_8(\text{PEt}_3)_6$ are taken from Ref. 38.

experimental results, thus validating the calculations. Since the photoelectron spectra are fingerprint of the electronic structures of neutral clusters, the agreement indicates that the calculated atomic structures and the multiplicities match the ones observed experimentally.

Table II.2.2 Theoretical and experimental adiabatic and 1st and 2nd vertical detachment energies (VDE and VDE*) of $\text{Co}_6\text{S}_8(\text{PEt}_3)_x^-$ ($x = 0-5$) clusters.

Cluster	VDE ^E (eV)				VDE ^T (eV)			
	AEA ^E (eV)	VDE	VDE*	Isomers	ΔE (eV)	AEA ^T (eV)	VDE	VDE*
Co_6S_8^-	>3.49	>3.49				3.55	3.59	3.96
$\text{Co}_6\text{S}_8(\text{PEt}_3)^-$	3.0		3.22			2.94	2.98	3.37
	3.35							

$\text{Co}_6\text{S}_8(\text{PEt}_3)_2^-$	2.6	2.71	<i>trans</i>	0.14	2.35	2.59	2.88
	2.85		<i>cis</i>		2.49	2.60	2.92
$\text{Co}_6\text{S}_8(\text{PEt}_3)_3^-$	2.2	2.39	<i>mer</i>	0.18	2.10	2.16	2.32
	2.45		<i>fac</i>		2.26	2.32	2.33
$\text{Co}_6\text{S}_8(\text{PEt}_3)_4^-$	2.0	2.22	<i>trans</i>	0.22	2.03	2.07	2.15
	2.29		<i>cis</i>		2.00	2.11	2.21
$\text{Co}_6\text{S}_8(\text{PEt}_3)_5^-$	1.8	2.05					2.09
	2.16				1.77	1.88	

The main result is a monotonic decrease in the AEA and VDE as ligands are successively attached to the Co_6S_8 core. Such a decrease is attributed to the fact that PEt_3 ligands are electron donors and thus increase the charge density in the core region. To support this hypothesis, we performed a Hirshfeld charge analysis (Figure S3). The cumulative charge donated from the ligands to the Co_6S_8 core gradually increases, from ~ 0.32 e in $\text{Co}_6\text{S}_8(\text{PEt}_3)$ to ~ 0.90 e in $\text{Co}_6\text{S}_8(\text{PEt}_3)_5$. The added charge affects the one-electron levels of the clusters, in particular, the HOMO and LUMO energies, which control the ionization and electron affinity. Figure 5 presents the one-electron levels of the neutral clusters. The values of the HOMO, LUMO and HOMO-LUMO gap for anionic and neutral clusters are given in Table S2. Note that the addition of successive ligands raises the one-electron levels, as marked by the position of the LUMO. As the position of the LUMO is raised in energy, the electron affinity of the

cluster decreases since the extra electron occupies the LUMO of the neutral cluster. The largest increase in the LUMO energy occurs with the attachment of the 1st and 2nd PEt₃. Beyond x = 2, each additional ligand increases the LUMO by around 0.3 eV. Remarkably, we find that the ligands are not bound strongly to the cluster core: the binding energy of the first PEt₃ to Co₆S₈ is 1.53 eV, and decreases to 1.38 eV for the 5th ligand.

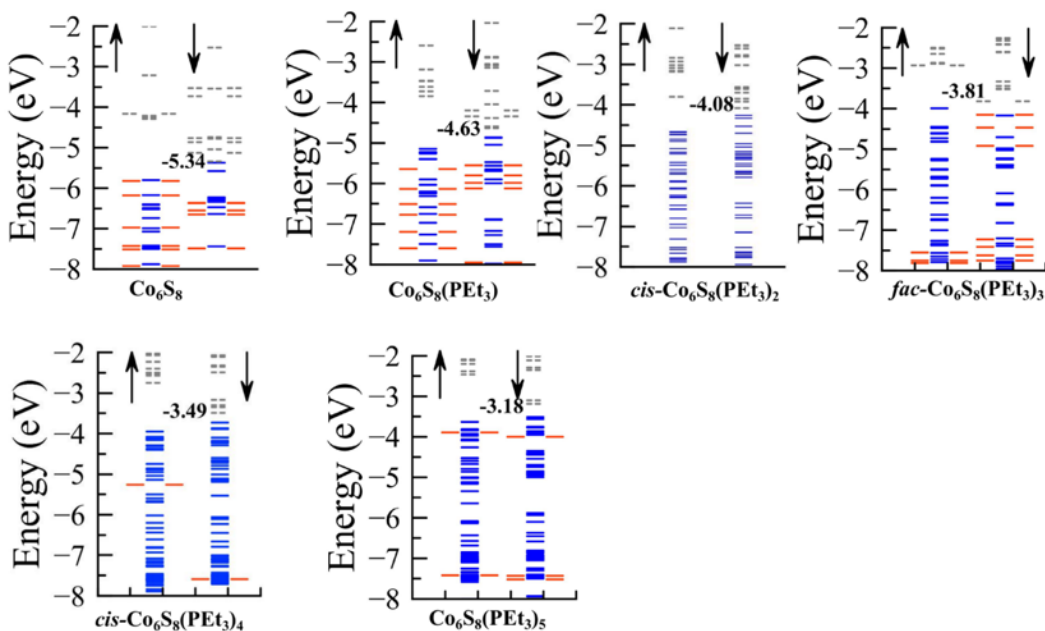


Figure II.2.1 One electron-energy levels of Co₆S₈(PEt₃)_x (x = 0–5) clusters. The solid blue and red bars represent the singly and doubly occupied energy levels, respectively. Unoccupied energy levels are shown by dashed gray lines. The energy of LUMO (in eV) is indicated for each cluster. The α -spin and β -spin channel are represented by up and down arrows.

Our earlier studies have shown that a complete ligation with either PEt₃ or a mixture

of PEt_3 and CO ligands produces the lowest spin state for the $\text{Co}_6\text{S}_8(\text{PEt}_3)_{6-n}(\text{CO})_n$ clusters. This contrasts drastically with the partially ligated cluster in this study: starting from the bare anionic Co_6S_8 core, with a spin multiplicity of $M = 10$, the multiplicity is reduced by 2 upon addition of a PEt_3 ligand, leading to $\text{Co}_6\text{S}_8(\text{PEt}_3)^-$ in an octet state. The attachment of the 2nd and 3rd PEt_3 ligands produces a sextet spin state, while the bonding of the 4th and 5th ligands generates a quartet ground state. To support these results, Figure 6a shows the one-electron energy levels of Co_6S_8 in an octahedral symmetry. In the energy range -20 to -18 eV, there are 16 electrons accommodated in A_{1g} , T_{1u} , T_{2g} , and A_{2u} orbitals formed by s -states of S and Co sites. The remaining 86 electrons are accommodated in $T_{2g/2u}$, T_{1g}/T_{1u} , $E_{g/u}$, A_{2u} , and $A_{1g/2g}$ states in the energy range from -10 to -2 eV. A set of unoccupied T_{1g} (d_{xz} , d_{yz} , d_{xy}), T_{2u} (d_{xz} , d_{yz} , $d_{x^2-y^2}$), T_{1u} (d_{xz} , d_{yz} , d_z^2), and E_g (d_z^2) states in β -spin channel lead to a spin multiplicity $M = 11$. In addition, the E_g ($d_{x^2-y^2}$) in β -spin channel is occupied. As the LUMO is a minority spin state, addition of an electron leads to an anion with a spin multiplicity of 10. The d -orbitals in the parentheses with italics text are localized on the Co site along z -axis. Note that two d_z^2 orbitals form a bonding E_g -type and an anti-bonding T_{1u} -type orbitals with a node along z axis. Figure 6b shows the one-electron energy levels of Co_6S_8 with PEt_3 ligand along the z -axis. Addition of PEt_3 ligand breaks the octahedral symmetry and the sp -states of P combine primarily with d -states of Co to stabilize the E_g (d_z^2) and T_{1g} (d_{xz} , d_{yz}) states while E_g ($d_{x^2-y^2}$) state is

destabilized and becomes a part (MO^β-70) of unoccupied states in the β-spin channel. The $E_g(d_z^2)$ states form the occupied bonding (MO^α-49, MO^β-44) states with lone pair of electrons of PET₃ while corresponding unoccupied anti-bonding (MO^α-78, MO^β-78) states are higher in energy. The remaining $T_{2u}(d_{xz}, d_{yz}, d_{x^2-y^2})$, $T_{1u}(d_{xz}, d_{yz}, d_z^2)$ also lose their degeneracy and turn into MO^β-(75,76,72) and MO^β-(73,74,71), respectively. These six states along with MO^β-70 and MO^β-77 ($T_{1g}(d_{xy})$) lead to a reduced multiplicity M = 9 in the ground state of Co₆S₈(PET₃). Further addition of ligands leads to a similar mixing with reduction in multiplicity.

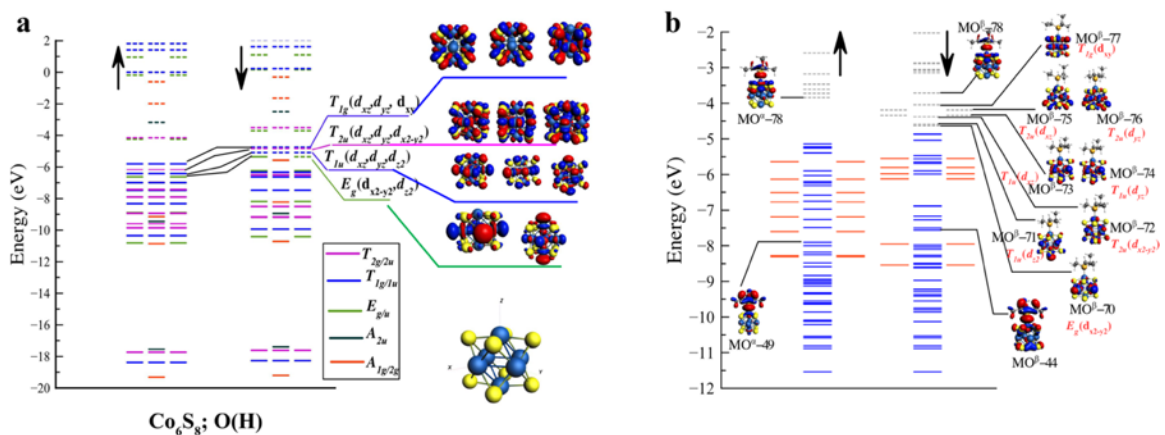


Figure II.2.2 (a) One-electron energy levels with their symmetry labels for Co₆S₈ in octahedron symmetry. The solid and dashed lines represent occupied and unoccupied energy levels. (b) One-electron energy levels along with their iso-surfaces for Co₆S₈(PET₃). The solid blue and red bars represent the singly and doubly occupied energy levels, respectively. Unoccupied energy levels are shown by dashed gray lines. The α-spin and β-spin channel represented by up and down arrows.

Summary

By combining inorganic cluster synthesis, gas-phase anion photoelectron spectroscopy, and electronic structure calculations, we have demonstrated that the electronic properties of metal chalcogenide clusters can be tuned by varying the number of phosphine capping ligands. The sequential addition of PEt_3 to the Co_6S_8 core results in a gradual decrease of its electron affinity and a shift of its electronic spectrum to lower energy. Density functional theory calculations reveal that addition of PEt_3 ligands gradually demagnetizes the Co_6S_8 core and increases its charge density. These effects stabilize the core and lift the energy of the LUMO.

References

1. Reber, A. C.; Khanna, S. N. Superatoms: Electronic and Geometric Effects on Reactivity. *Acc. Chem. Res.* **2017**, *50*, 255–263.
2. Pinkard, A.; Champsaur, A. M.; Roy, X. Molecular Clusters: Nanoscale Building Blocks for Solid-State Materials. *Acc. Chem. Res.* **2018**, *51*, 919–929.
3. Claridge, S. A.; Castleman, A. W.; Khanna, S. N.; Murray, C. B.; Sen, A.; Weiss, P. S. Dimensional Reduction: A Practical Formalism for Manipulating Solid Structures. *ACS Nano*. 2009, *3*, 244–255.
4. Tulsy, E. G.; Long, J. R. Dimensional Reduction: A Practical Formalism for Manipulating Solid Structures. *Chem. Mater.* **2001**, *13*, 1149–1166.
5. Baudron, S. A.; Batail, P.; Coulon, C.; Clerac, R.; Canadell, E.; Laukhin, V.; Melzi, R.; Wzietek, P.; Jerome, D.; Auban-Senzier, P.; Ravy, S. $(\text{EDT-TTF-CONH}_2)_6[\text{Re}_6\text{Se}_8(\text{CN})_6]$, a Metallic Kagome-Type Organic–Inorganic Hybrid Compound: Electronic Instability, Molecular Motion, and Charge Localization. *J. Am. Chem. Soc.* **2005**, *127*, 11785–11797.
6. Yoon, B.; Luedtke, W. D.; Barnett, R. N.; Gao, J.; Desireddy, A.; Conn, B. E.; Bigioni, T.; Landman, U. Hydrogen-bonded structure and mechanical chiral response of a silver nanoparticle superlattice. *Nat. Mater.* **2014**, *13*, 807–811.
7. Corrigan, J. F.; Fuhr, O.; Fenske, D. Metal Chalcogenide Clusters on the Border between Molecules and Materials. *Adv. Mater.* **2009**, *21*, 1867–1871.
8. Roy, X.; Lee, C. H.; Crowther, A. C.; Schenck, C. L.; Besara, T.; Lalancette, R. A.; Siegrist, T.; Stephens, P. W.; Brus, L. E.; Kim, P.; Steigerwald, M. L.; Nuckolls, C. Nanoscale Atoms in Solid-State Chemistry. *Science*, **2013**, *341*, 157–160.

9. Khanna, S. N.; Jena, P. Atomic clusters: Building Blocks for a Class of Solids. *Phys. Rev. B.* **1995**, *51*, 13705-13716.
10. Castleman, A. W.; Khanna, S. N. Clusters, Superatoms, and Building Blocks of New Materials. *J. Phys. Chem. C* **2009**, *113*, 2664–2675.
11. Lee, C. H.; Liu, L.; Bejger, C.; Turkiewicz, A.; Goko, T.; Arguello, C. J.; Frandsen, B. A.; Cheung, S. C.; Medina, T.; Munsie, T. J. S.; D’Ortenzio, R.; Luke, G. M.; Besara, T.; Lalancette, R. A.; Siegrist, T.; Stephens, P. W.; Crowther, A. C.; Brus, L. E.; Matsuo, Y.; Nakamura, E.; Uemura, Y. L.; Kim, P.; Nuckolls, C.; Steigerwald, M. L.; Roy, X. Ferromagnetic Ordering in Superatomic Solids. *J. Am. Chem. Soc.* **2014**, *136*, 16926–16931.
12. Roy, X.; Schenck, C. L.; Ahn, S.; Lalancette, R. A.; Venkataraman, L.; Nuckolls, C.; Steigerwald, M. L. Quantum Soldering of Individual Quantum Dots. *Angew. Chem., Int. Ed.* **2012**, *51*, 12473–12476.
13. Trinh, M. T.; Pinkard, A.; Pun, A. B.; Sanders, S. N.; Kumarasamy, E.; Sfeir, M. Y.; Campos, L. M.; Roy, X.; Zhu, X. Y. Distinct Properties of the Triplet Pair State from Singlet Fission. *Sci. Adv.* **2017**, *3*, e1700241
14. Chauhan, V.; Sahoo, S.; Khanna, S. N. Ni₉Te₆(PEt₃)₈C₆₀ Is a Superatomic Superalkali Superparamagnetic Cluster Assembled Material (S³-CAM). *J. Am. Chem. Soc.* **2016**, *138*, 1916–1921.
15. Khanna, S. N.; Reber, A. C. Intercalation without Altercation. *Nat. Chem.* **2017**, *9*, 1151–1152.
16. Tomalia, D. A.; Khanna, S. N. A Systematic Framework and Nanoperiodic Concept for Unifying Nanoscience: Hard/Soft Nanoelements, Superatoms, Meta-Atoms, New Emerging Properties, Periodic Property Patterns, and Predictive Mendeleev-like Nanoperiodic Tables. *Chem. Rev.* **2016**, *116*, 2705–2774.
17. Zheng, Z.; Long, J. R.; Holm, R. H. A Basis Set of Re₆Se₈ Cluster Building Blocks and Demonstration of Their Linking Capability: Directed Synthesis of an Re₁₂Se₁₆ Dicluster. *J. Am. Chem. Soc.*, **1997**, *119*, 2163–2171.
18. Cargnello, M.; Johnston-Peck, A. C.; Diroll, B. T.; Wong, E.; Datta, B.; Damodhar, D.; Doan-Nguyen, V. V. T.; Herzing, A. A.; Kagan, C. R.; Murray, C. B. Substitutional Doping in Nanocrystal Superlattices. *Nature*, **2015**, *524*, 450–453.
19. O’Brien, M. N.; Jones, M. R.; Lee, B.; Mirkin, C. A. Anisotropic Nanoparticle Complementarity in DNA-mediated Co-crystallization. *Nat. Mater.* **2015**, *14*, 833–839.
20. Boles, M. A.; Talapin, D. V. Many-Body Effects in Nanocrystal Superlattices: Departure from Sphere Packing Explains Stability of Binary Phases. *J. Am. Chem. Soc.* **2015**, *137*, 4494.
21. Poyser, C. L.; Czerniuk, T.; Akimov, A.; Diroll, B. T.; Gaudling, E. A.; Salasyuk, A. S.; Kent, A. J.; Yakovlev, D. R.; Bayer, M.; Murray, C. B. Coherent Acoustic Phonons in Colloidal Semiconductor Nanocrystal Superlattices. *ACS Nano*. **2016**, *10*, 1163–1169.
22. Ong, W. L.; Rupich, S. M.; Talapin, D. V.; McGaughey, A. J. H.; Malen, J. A. Surface Chemistry Mediates Thermal Transport in Three-dimensional Nanocrystal Arrays. *Nat.*

- Mater.* **2013**, *12*, 410–415.
23. Voevodin, A.; Campos, L. M.; Roy, X. Multifunctional Vesicles from a Self-assembled Cluster-Containing Diblock Copolymer. *J. Am. Chem. Soc.* **2018**, *140*, 5607–5611.
 24. Champsaur, A. M.; Yu, J.; Roy, X.; Paley, D. M.; Steigerwald, M. L.; Nuckolls, C.; Bejger, C. M. Two-Dimensional Nanosheets from Redox-Active Superatoms. *ACS Cent. Sci.* **2017**, *3*, 1050–1055.
 25. Champsaur, A. M.; Mézière, C.; Allain, M.; Paley, D. W.; Steigerwald, M. L.; Nuckolls, C.; Batail, P. Weaving Nanoscale Cloth through Electrostatic Templating. *J. Am. Chem. Soc.* **2017**, *139*, 11718–11721.
 26. O'Brien, E. S.; Trinh, M. T.; Kann, R. L.; Chen, J.; Elbaz, G. A.; Masurkar, A.; Atallah, T. L.; Paley, M. V.; Patel, N.; Paley, D. W.; Kymissis, I.; Crowther, A. C.; Millis, A. J.; Reichman, D. R.; Zhu, X. Y.; Roy, X. Single-crystal-to-single-crystal Intercalation of a Low-bandgap Superatomic crystal. *Nat. Chem.* **2017**, *9*, 1170–1174.
 27. Lovat, G.; Choi, B.; Paley, D. W.; Steigerwald, M. L.; Venkataraman, L.; Roy, X. Room-temperature Current Blockade in Atomically Defined Single-cluster Junctions. *Nat. Nanotechnol.* **2017**, *12*, 1050–1054.
 28. Ong, W. L.; O'Brien, E. S.; Dougherty, P. S. M.; Paley, D. W.; Fred Higgs Iii, C.; McGaughey, A. J. H.; Malen, J. A.; Roy, X. Orientational Order Controls Crystalline and Amorphous Thermal Transport in Superatomic Crystals. *Nat. Mater.* **2017**, *16*, 83–88.
 29. Choi, B.; Yu, J.; Paley, D. W.; Tuan Trinh, M.; Paley, M. V.; Karch, J. M.; Crowther, A. C.; Lee, C. H.; Lalancette, R. A.; Zhu, X.; Kim, K.; Steigerwald, M. L.; Nuckolls, C.; Roy, X. van der Waals Solids from Self-Assembled Nanoscale Building Blocks. *Nano Lett.* **2016**, *16*, 1445–1449.
 30. Champsaur, A. M.; Velian, A.; Paley, D. W.; Choi, B.; Roy, X.; Steigerwald, M. L.; Nuckolls, C. Building Diatomic and Triatomic Superatom Molecules. *Nano Lett.* **2016**, *16*, 5273–5277.
 31. Turkiewicz, A.; Paley, D. W.; Besara, T.; Elbaz, G.; Pinkard, A.; Siegrist, T.; Roy, X. Assembling Hierarchical Cluster Solids with Atomic Precision. *J. Am. Chem. Soc.* **2014**, *136*, 15873–15876.
 32. Yu, J.; Lee, C. H.; Bouilly, D.; Han, M.; Kim, P.; Steigerwald, M. L.; Roy, X.; Nuckolls, C. Patterning Superatom Dopants on Transition Metal Dichalcogenides. *Nano Lett.* **2016**, *16*, 3385–3389.
 33. Walter, M.; Akola, J.; Lopez-Acevedo, O.; Jadzinsky, P. D.; Calero, G.; Ackerson, C. J.; Whetten, R. L.; Grönbeck, H.; Häkkinen, H. A Unified View of Ligand-protected Gold Clusters as Superatom Complexes. *Proc. Natl. Acad. Sci. U. S. A.* **2008**, *105*, 9157–916.
 34. Aikens, C. M. Electronic and Geometric Structure, Optical Properties, and Excited State Behavior in Atomically Precise Thiolate-Stabilized Noble Metal Nanoclusters. *Acc. Chem. Res.* **2018**, *51*, 3065–3073
 35. Reber, A. C.; Khanna, S. N. Co₆Se₈(PEt₃)₆ Superatoms as Tunable Chemical Dopants for Two-Dimensional Semiconductors. *npj Comput. Mater.* **2018**, *4*, 33.
 36. Chauhan, V.; Khanna, S. N. Strong Effect of Organic Ligands on the Electronic Structure

- of Metal-Chalcogenide Clusters. *J. Phys. Chem. A* **2018**, *122*, 6014–6020.
37. Cecconi, F.; Ghilardi, C. A.; Midollini, S.; Orlandini, A. One Electron Reduction of a Cobalt-sulfur Cluster. Synthesis and Molecular Structure of $[\text{Co}_6(\mu_3\text{-S})_8(\text{PEt}_3)_6] \cdot \text{nthf}$. *Inorg. Chimica Acta* **1983**, *76*, 183-184.
38. Liu, G.; Pinkard, A.; Ciborowski, S. M.; Chauhan, V.; Zhu, Z.; Aydt, A. P.; Khanna, S. N.; Roy, X.; Bowen, K. H. Tuning the Electronic Properties of Hexanuclear Cobalt Sulfide Superatoms via Ligand Substitution. *Chem. Sci.* **2019**, *10*, 1760-1766.
39. Zhang, X.; Liu, G.; Gantefoer, G.; Bowen, K. H.; Alexandrova, A. N. PtZnH_5^- , A σ -Aromatic Cluster. *J. Phys. Chem. Lett.* **2014**, *5*, 1596 -1601.
40. Liu, G.; Ciborowski, S. C.; Bowen, K. Photoelectron Spectroscopic and Computational Study of PyridineLigated Gold Cluster Anions. *J. Phys. Chem. A* **2017**, *121*, 5817-5822.
41. Grubisic, A.; Wang, H.; Li, X.; Ko, Y. J.; Kocak, S.; Pederson, M. R.; Bowen, K. H.; Eichhorn, B. W. Photoelectron Spectroscopic and Computational Studies of the Pt@Pb_{10}^{1-} and $\text{Pt@Pb}_{12}^{1-/2-}$ Anions. *Proc. Nat. Acad. Sci.* **2011**, *108*, 14757-14762.
42. Perdew, J. P.; Yue, W. Accurate and Simple Density Functional for the Electronic Exchange Energy: Generalized Gradient Approximation. *Phys. Rev. B* **1986**, *33*, 8800–8802.
43. van Lenthe, E.; Baerends, E. J. Optimized Slate-type basis sets for the elements 1-118. *J. Comput. Chem.* **2003**, *24*, 1142–1156.
44. van Lenthe, E.; van Leeuwen, R.; Baerends, E. J.; Snijders, J. G. Relativistic Regular Two-component Hamiltonians. *Int. J. Quantum Chem.* **1986**, *57*, 281–293.
45. van Lenthe, E.; Ehlers, A.; Baerends, E. J. Geometry Optimizations in the Zero-order Regular Approximation for Relativistic Effects. *J. Chem. Phys.* **1999**, *110*, 8943–8953.
46. Grimme, S.; Ehrlich, S.; Goerigk, L. Effect of the Damping Function in Dispersion Corrected Density Functional Theory. *J. Comp. Chem.* **2011**, *32*, 1456-1465.

III. Chemical Bonding

Chemical bonding is at the heart of chemistry. Because the electronic structure information revealed by negative ion photoelectron spectroscopy (NIPS) is directly correlated to the bonding scenario in the investigated systems, NIPS has been widely applied for the study of chemical bonding in gas-phase molecules and clusters. On the one hand, the isolated systems studied by NIPS allows the highest level of theory to be applied. On the other hand, the variety of ion sources utilized in our lab grants access to novel clusters that are not easily synthesized in solution or solid phase. This advantage enables NIPS to push the boundary in revealing the nature and discovering new concepts of chemical bonding.

III.1 Photoelectron Spectroscopic and Computational Study of Pyridine-Ligated Gold Cluster Anions

Gaoxiang Liu, Sandra M. Ciborowski, and Kit H. Bowen*

Department of Chemistry, Johns Hopkins University, 3400 N. Charles Street, Baltimore, Maryland 21218, USA

Abstract

Pyridine-ligated gold cluster anions were studied through a combination of negative ion photoelectron spectroscopy and density functional theory calculations. Small gold cluster anions ligated by pyridine, $Au_n(py)^-$ were generated with a ligation cell coupled to a laser vaporization source (LVS). We showed that pyridine is weakly bound (physisorbed) to the Au_2^- moiety of $Au_2(py)^-$ by interactions between its gold atoms and either the hydrogen atoms or the π -ring of pyridine. We also found that pyridine's lone electron pair strongly binds (chemisorbs) to both $Au_3(py)^-$ and $Au_4(py)^-$ through single gold atoms on each of these clusters. Bonding analysis of two isomers of $Au_4(py)^-$ supported the presence of two different ligand binding motifs, these differing in terms of the gold atom to which pyridine binds.

Introduction

The synthesis of sub-nanometer gold clusters with a precise number of metal atoms

and organic ligands has been the subject of intensive research.¹ The size-dependent physical and chemical properties of these nanoclusters have made them promising materials for a broad range of applications including catalysis²⁻⁵, chemical sensing^{6,7}, optical imaging^{8,9} and biomedicine¹⁰⁻¹². Particular compositions are often achieved by solution-phase reduction syntheses, including size-focusing methodologies¹³ or ligand-exchange-induced size/structure transformation processes¹⁴. Organic ligands such as thiols¹⁵, phosphines¹⁶ and alkynes¹⁷ are used to control the growth of gold clusters to specific sizes and to stabilize the prepared nanoclusters¹³. The bonding and interaction between specific organic ligands and gold cluster cores play a critical role in determining the structure, stability and functionality of gold nanoclusters.¹⁸ Metal-ligand interactions are also relevant to metal-protein recognition at a molecular level, with these guiding the synthesis of metalloproteins having desirable properties.¹⁹

Extensive theoretical work has investigated the effect of ligation on the structures and energetics of various size gold cluster cores.²⁰⁻²² Examining how certain ligands can stabilize gold clusters of specific size has provided insight into the growth mechanism of atomically precise ligated gold clusters.²⁰⁻²² For example, density functional theory (DFT) calculations were performed on the absorption of methylthiol onto various gold cores Au_n^Z ($n = 1-8, 12, 13, 20$; $Z = 0, -1, +1$).²¹ In another study, DFT was employed to analyze the binding energies of small Au_n clusters ($n = 1-7, 11$) with various lone-

pair ligands ($L = \text{SH}_2, \text{NH}_3, \text{PCl}_3, \text{PMe}_3, \text{etc.}$).²³ For even-sized gold clusters, it was found that covalent $\text{Au}_n\text{-L}$ bonds were formed when the ligands' (L) lone pairs interacted with the Au_n moiety's lowest unoccupied molecular orbital (LUMO). For odd-sized gold clusters, the bonding was found to be dominated by the interaction between the ligands' lone pairs and the Au_n core's singly-occupied molecular orbital (SOMO).²³ While many theoretical studies have been conducted on the nature of the bonding interactions between gold cluster cores and their ligands, direct experimental measurements pertaining to those interactions have been limited. Ligated gold clusters are commonly characterized by electrospray ionization mass spectrometry (ESI-MS)²⁴, X-ray diffraction (XRD)²⁵ and UV-Vis spectroscopy²⁶, which yield information on the clusters' sizes, crystal structures, and optical properties, respectively. These, however, provide little insight into the nature of binding between ligands and gold clusters.

Recently, gas-phase experiments which couple ESI-MS with techniques, such as collision induced dissociation (CID) and surface induced dissociation (SID), have been used to characterize the ligand-core interactions and binding energies of ligated gold clusters.²⁷ Johnson, Laskin, and co-workers investigated fragmentation patterns and binding energies of mass-selected triphenylphosphine (TPP) ligated gold cluster cations using ESI-MS-SID and found that the $\text{Au}_8(\text{TPP})_6^+$ ion is remarkably stable

towards dissociation, likely due to its large ligand binding energy.²⁸ Their strategy, however, required that ligated gold clusters first be synthesized in solution and then introduced into the gas phase using ESI. The choices of ligated gold clusters that could be studied in the gas phase by this approach were limited to those that could be synthesized in solution.²⁹⁻³¹ Since most of the ligands used in solution synthesis are thiols and phosphines, only a limited number of interaction motifs between ligands and gold cores have been explored using these methods.^{1,27} Thus, an experimental approach which affords an opportunity to investigate interactions between a wider variety of ligands and different size gold clusters may help to sample a broader range of interactions.

In this work, a cluster beam source was used to prepare pyridine-ligated gold cluster anions, $\text{Au}_n(\text{pyridine})^-$. This source comprises a laser vaporization source (LVS) and a ligation cell. Pyridine (py) was chosen as a ligand for these experiments because of its simplicity and its binding flexibility; it can interact via its lone pair or its π -ring. Moreover, pyridine-ligated gold clusters are not easily synthesized in solution. The $\text{Au}_n(\text{py})^-$ cluster anions formed by this source were identified and mass-selected by mass spectrometry (MS), their excess electrons were photodetached and energy-analyzed by anion photoelectron spectroscopy (PES), and the resulting spectra were analyzed and interpreted through density functional theory (DFT) calculations. This

combination of experiment and theory led to insight into the nature of the interactions between the gold cluster cores and their pyridine ligand.

Experimental and Computational Methods

Anion photoelectron spectroscopy is conducted by crossing a beam of mass-selected negative ions with a fixed-frequency photon beam and energy-analyzing the resultant photodetached electrons. The photodetachment process is governed by the energy-conserving relationship: $h\nu = EBE + EKE$, where $h\nu$ is the photon energy, EBE is the electron binding energy, and EKE is the electron kinetic energy. Our apparatus consists of a laser vaporization cluster anion source with an attached ligation cell, a time-of-flight mass spectrometer, a Nd:YAG photodetachment laser, and a magnetic bottle electron energy analyzer³². The photoelectron spectrometer resolution is ~ 35 meV at 1 eV EKE. The third (355 nm) and fourth (266 nm) harmonic outputs of a Nd:YAG laser were used to photodetach electrons from mass-selected Au_n^- and $Au_n(py)^-$ clusters. Photoelectron spectra were calibrated against the well-known atomic transitions of atomic Cu^- .³³

A schematic of our LVS-coupled ligation cell source is shown in Figure 1. Gold cluster anions were generated by laser vaporization of a pure gold foil wrapped around an aluminum rod. The resultant plasma was cooled with helium gas delivered by a pulsed

valve (PV1) having a backing pressure of a 100 psig. The resulting gold cluster anions then traveled through a ligation cell (4-mm diameter), where they mixed with pyridine vapor. The pyridine vapor was introduced into the ligation cell by a second pulsed valve (PV2). The resulting $Au_n(py)^-$ anionic clusters were mass-analyzed by the time-of-flight mass spectrometer and their photoelectron spectra recorded.

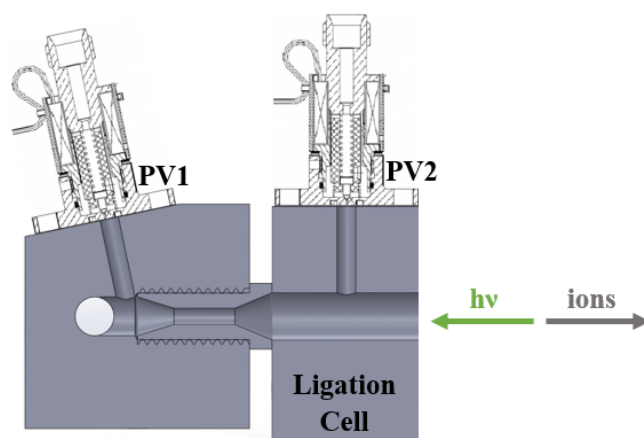


Figure III.1.1 Schematic of the laser vaporization housing coupled with a ligation cell.

Density functional theory calculations were performed with the ORCA computational chemistry software package.³⁴ All calculations were carried out with the Becke Perdew (BP86) functional³⁵ with the D3 dispersion correction³⁶ and the RIJCOSX approximation³⁷. The Ahlrichs Def2 basis sets were used throughout our calculations³⁸. For geometry optimization, Def2-SVP and auxiliary Def2-SVP/J basis sets were chosen for hydrogen, nitrogen, and carbon atoms; the Stuttgart effective core potential SDD³⁹ and ECP basis set Def2-TZVP|Def2-TZVP/J were used for gold

atoms. Single-point calculations were then improved with larger basis sets: Def2-TZVP|Def2-TZVP/J for hydrogen, nitrogen, and carbon atoms, and SDD|Def2-QZVPP|Def2-QZVPP/J for gold atoms. Vertical detachment energies (VDE) were computed from the energetic difference between the relaxed anionic complex and its corresponding neutral species at the geometry of the relaxed anion. Electron affinities (EA) were calculated from the energy differences between the relaxed anionic complex and its relaxed neutral counterpart. Frequency calculations were performed to verify that no imaginary frequencies existed and all optimized structures were minima.

Results

A. Experimental

The mass spectra, with and without pyridine (py) pulsed into the ligation cell, are shown in Figure 2. This work focuses on relatively small gold-pyridine clusters. With no pyridine in the ligation cell, Au_n^- cluster anions ($n = 2-5$) are observed in the mass spectrum; when pyridine is added to the cell, a new series of $\text{Au}_n(\text{py})^-$ complexes appears. While $\text{Au}_n(\text{py})^-$ and Au_n^- show comparable ion intensities for $n = 2-5$, $\text{Au}(\text{py})^-$ has a very low ion intensity despite the abundance of Au^- . The mass spectra clearly show that pyridine binds to gold cluster anions.

Photoelectron spectra of Au_n^- and $\text{Au}_n(\text{py})^-$ were recorded for $n = 2-4$, and these are displayed in Figure 3. The photoelectron spectra for Au_n^- agree well with those measured in previous studies.⁴⁰ For $\text{Au}_2(\text{py})^-$, its lowest EBE spectral band covers EBE = 1.7 to 2.5 eV, and it exhibits two distinct features. These comprise a relatively broad peak centered at EBE = 2.11 eV and a sharp peak centered at EBE = 2.34 eV. These spectral features suggest the coexistence of two $\text{Au}_2(\text{py})^-$ isomers, in which their pyridine molecules are weakly bound (physisorbed) to their Au_2^- moieties in both cases. There, the gold dimer anion moieties act as the chromophores for photodetachment, and for that reason the resulting spectra look like Au_2^- spectra, just shifted to slightly higher EBE values by their ion-molecule interaction energies.⁴¹ The electron affinities (EA) for the neutral counterparts of these two isomers, obtained by extrapolating the lower EBE edges of their peaks to baseline, are estimated to be 1.7 eV and 2.3 eV. (The band at EBE \sim 3 eV may be due to excited electronic states or to a chemisorbed isomer, but that feature was not pursued in this study.)

For $\text{Au}_3(\text{py})^-$ and $\text{Au}_4(\text{py})^-$, broad spectral features appear at lower EBE values than those of the relatively narrow peaks of Au_3^- and Au_4^- . This means that they are not weakly bound (physisorbed) anion-molecule complexes. In fact, it implies that the energetics of the molecular orbitals (MO) of the Au_3^- and Au_4^- cores are substantially modified by interaction with pyridine, indicating strong, chemisorbed interactions in

these anionic complexes. For $\text{Au}_3(\text{py})^-$, transitions with maximum spectral intensities at 2.93 and 3.43 eV are identified, with corresponding EA values of 2.5 and 3.2 eV. For $\text{Au}_4(\text{py})^-$, the EBE peaks with maxima at 2.03 and 2.36 eV are likely due to different isomers, and the EA values of their neutral counterparts are determined as 1.9 and 2.2 eV. (The higher EBE features in both of these cases may again be due to excited electronic states or to a chemisorbed isomer, but we did not pursue them in this study.)

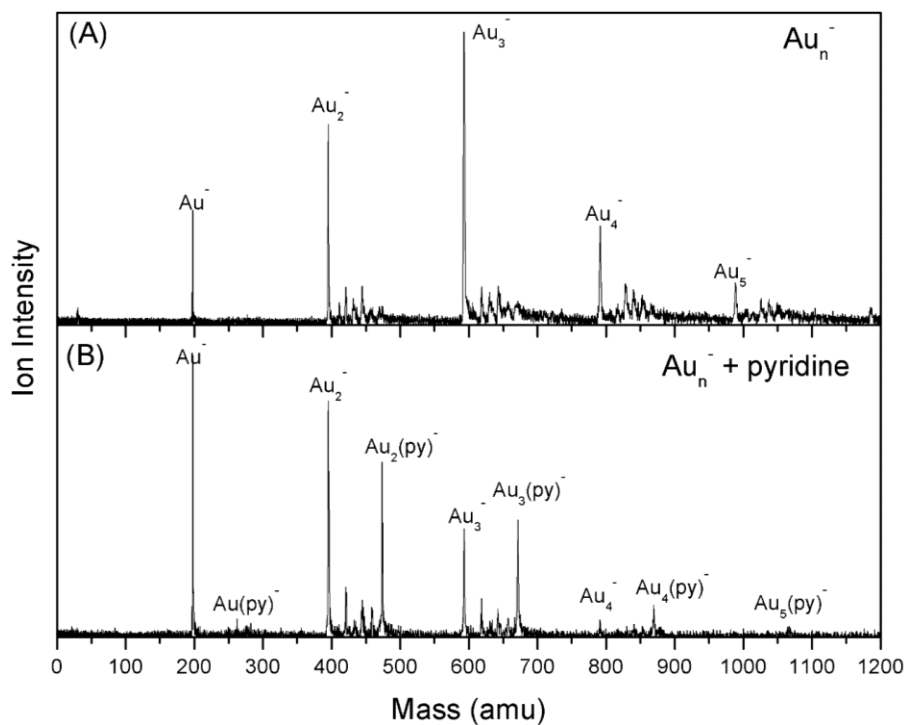


Figure III.1.2 The mass spectra of (A) Au_n^- cluster anions and (B) pyridine-ligated gold cluster anions $\text{Au}_n(\text{py})^-$.

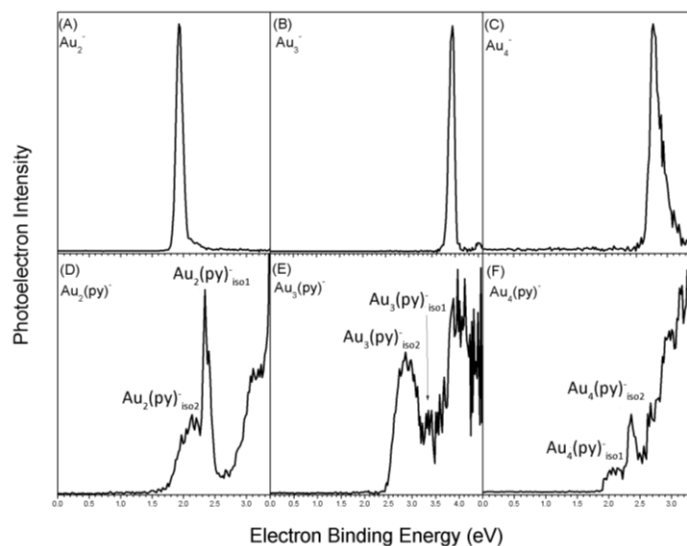


Figure III.1.3 Photoelectron spectra of (A-C) Au_n^- and (D-F) $Au_n(py)^-$ ($n = 2-4$).

B. Computational

DFT calculations were performed to account for the multiple features observed in the photoelectron spectra of $Au_n(py)^-$. The optimized structures, relative energies, experimental/theoretical VDE values of $Au_n(py)^-$ and experimental/theoretical EA values of their neutral molecule counterparts, $Au_n(py)$, are presented in Table 1. The lowest energy structure for $Au_2(py)^-$ is a complex, where the anionic Au_2^- moiety weakly interacts with the hydrogen atoms of pyridine (see $Au_2(py)^-_{iso1}$ in Table 1). The distances between Au and H are around 2.7 Å which is typical for hydrogen-bond like interaction, i.e., solvation effect. In $Au_2(py)^-_{iso2}$, the Au_2^- moiety is predicted to interact strongly with pyridine, i.e., a pyridine-ligated Au_2^- , and to exhibit a VDE value of 1.16 eV. There is, however, no feature there in our spectrum. For $Au_2(py)^-_{iso3}$, however, the

prediction of a weakly bound complex (VDE = 1.96 eV) is in agreement with the observed feature at VDE = 2.11 eV (see $\text{Au}_2(\text{py})^-_{\text{iso3}}$ in Table 1). For $\text{Au}_3(\text{py})^-$, two stable products were identified. For both isomers, the gold trimer moieties adopted linear geometries. Pyridine ligated the Au_3^- moieties either through the end gold atom (see $\text{Au}_3(\text{py})^-_{\text{iso1}}$ in Table 1) or through the middle gold atom (see $\text{Au}_3(\text{py})^-_{\text{iso2}}$). Two of the three calculated $\text{Au}_4(\text{py})^-$ cluster anion isomers exhibit corresponding features in the $\text{Au}_4(\text{py})^-$ spectrum, and both of these are chemisorbed systems, i.e., pyridine-ligated gold clusters. The Au_4 moieties in $\text{Au}_4(\text{py})^-_{\text{iso1}}$ and in $\text{Au}_4(\text{py})^-_{\text{iso2}}$ exhibit Y-shaped structures. There is no evidence for $\text{Au}_4(\text{py})^-_{\text{iso3}}$ in the photoelectron spectrum; its Au_4 moiety is predicted to have a diamond-shape.

Discussion

Table 1 presents comparisons between experimentally-determined and theoretically-calculated VDE and EA values. Experimental VDE values are generally more reliable measurements than experimental EA values, since the former are simply peak locations, while the latter involve extrapolations. Due to differences in the structures of anions and their neutral counterparts, the EA-determining origin transition may not always correspond to the extrapolated lowest EBE side of the spectral band. Table 1 shows excellent agreement between experimental and theoretical VDE values is observed, although for the reasons stated the agreement between experimental and

theoretical EA values is not as good.

To understand why the $\text{Au}(\text{py})^-$ ion intensity in the mass spectrum is so weak, we calculated the potential energy between a gold anion, Au^- , and a pyridine molecule. As shown in Figure S2, the interaction is largely repulsive. As described above, both the broad peak at $\text{EBE} = 2.11$ eV and the sharp peak at $\text{EBE} = 2.34$ eV in the $\text{Au}_2(\text{py})^-$ spectrum are due to weakly bound complexes, where pyridine is physisorbed to the Au_2^- moiety. These VDE values agree relatively well with the calculated VDE values. Moreover, the calculated structures for these isomers are consistent with this interpretation. Since no spectral feature was seen in the vicinity of $\text{EBE} = 1.16$ eV in the photoelectron spectrum, the predicted strongly ligated (chemisorbed) isomer, $\text{Au}_2(\text{py})^-_{\text{iso}2}$ was not present in the experiment. Its absence may be explained by examining the relaxed potential energy scan shown in Figure S3. There, one sees a 0.62 eV high barrier between $\text{Au}_2(\text{py})^-_{\text{iso}2}$ and the “weakly-ligated” $\text{Au}_2(\text{py})^-_{\text{iso}3}$. This barrier may keep $\text{Au}_2(\text{py})^-_{\text{iso}3}$ from converting to $\text{Au}_2(\text{py})^-_{\text{iso}2}$, even though the latter is lower in energy. Physically, the barrier is understandable in terms of electrostatic repulsion, i.e., the interaction between pyridine’s lone pair and the negatively-charged Au_2^- moiety.

The two isomers of the $\text{Au}_3(\text{py})^-$ cluster are due to pyridine being chemisorbed

(strongly bound) to its gold trimer moiety. The two EBE peaks exhibited in the photoelectron spectrum of $\text{Au}_3(\text{py})^-$ correspond to the calculated VDE values of $\text{EBE} = 2.84 \text{ eV}$ and $\text{EBE} = 3.50 \text{ eV}$. The gold tetramer moieties in $\text{Au}_4(\text{py})^-_{\text{iso1}}$ and $\text{Au}_4(\text{py})^-_{\text{iso2}}$ are Y-shaped, and both isomers are chemisorbed (ligated) clusters. The two EBE peaks exhibited in the photoelectron spectrum of $\text{Au}_4(\text{py})^-$ correspond to the calculated VDE values of $\text{EBE} = 1.92 \text{ eV}$ and $\text{EBE} = 2.22 \text{ eV}$. Since no spectral feature was seen in the vicinity of $\text{EBE} = 1.70 \text{ eV}$ in the photoelectron spectrum of $\text{Au}_4(\text{py})^-$, the predicted chemisorbed isomer, $\text{Au}_4(\text{py})^-_{\text{iso3}}$, with its diamond-shaped gold tetramer moiety was not present in the experiment.

The differing bonding motifs in $\text{Au}_{1,2}(\text{py})^-$ versus $\text{Au}_{3,4}(\text{py})^-$ may be due to different negative charge densities on $\text{Au}_{1,2}^-$ versus $\text{Au}_{3,4}^-$. While the excess negative charge is highly localized in the cases of $\text{Au}_{1,2}^-$, it is likely to be somewhat delocalized in the cases of $\text{Au}_{3,4}^-$. Diffuse electron distributions may have the effect of reducing electrostatic repulsion between $\text{Au}_{3,4}^-$ and pyridine and with it the type of barrier seen in Figure S3, making it easier to form chemisorbed (ligated) cluster anions.

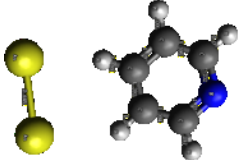
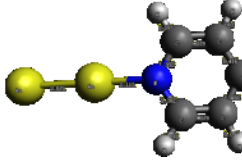
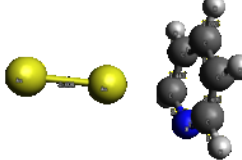
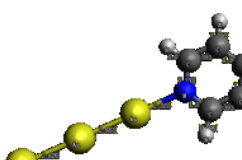
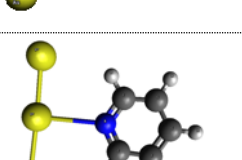
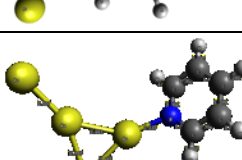
To gain more insight into the interaction between pyridine and gold cluster anions, the two isomers of $\text{Au}_4(\text{py})^-$ observed in the experiment were selected as candidates for molecular orbital (MO) and charge analyses. The frontier orbitals of $\text{Au}_4(\text{py})^-_{\text{iso1}}$,

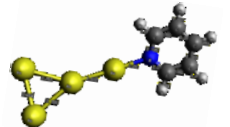
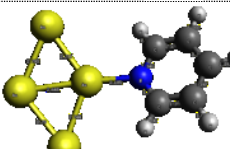
$\text{Au}_4(\text{py})^-_{\text{iso}2}$ and pyridine are presented in Chart 1. The Au_4 moieties in $\text{Au}_4(\text{py})^-_{\text{iso}1}$ and $\text{Au}_4(\text{py})^-_{\text{iso}2}$ have net charges of $-0.87e$ and $-1.07e$, respectively. Orbital analysis indicates that the bonding motif differs depending on which gold atom interacts with pyridine. For $\text{Au}_4(\text{py})^-_{\text{iso}1}$, while its SOMO-1 and SOMO-2 are mostly the MOs of Au_4 , its SOMO shows a strong participation of the LUMO of pyridine. The SOMO likely includes strong electron back-bonding from the Au_4 metal core to pyridine. The back-bonding is also manifested by a decrease of the negative charge on Au_4 moiety from $-1e$ to $-0.87e$. Such back-bonding effects strengthen the interactions between pyridine and the gold cluster, resulting in a shorter, 2.13 \AA Au-N bond, compared to the 2.26 \AA bond in $\text{Au}_4(\text{py})^-_{\text{iso}2}$ (Figure S1). The back-bonding also helps to stabilize the anionic complex, making $\text{Au}_4(\text{py})^-_{\text{iso}1}$ 0.18 eV lower in energy than $\text{Au}_4(\text{py})^-_{\text{iso}2}$ (Table 1). For $\text{Au}_4(\text{py})^-_{\text{iso}2}$, its SOMO is mainly the combination of gold atomic orbitals; thus, electron detachment from this orbital should resemble electron detachment from Au_4^- . This is consistent with the sharp transition in the photoelectron spectrum [Figure 3(F)]. The SOMO-1 for $\text{Au}_4(\text{py})^-_{\text{iso}2}$ shows that the ligand-metal interaction is primarily between the metal core and the lone-pair of pyridine.

To summarize this work, a source which couples LVS and a ligation cell was used to make pyridine-ligated gold cluster anions, $\text{Au}_n(\text{py})^-$. A combined anion photoelectron spectroscopic and DFT study confirmed the structures of stable $\text{Au}_n(\text{py})^-$ ($n = 2-4$) and explored the nature of their bonding interactions. The excess electrons on the gold

cores had significant effects on the structures of the ligated gold cluster anions and thus on their binding motifs.

Table III.1.2 Optimized Structures, Relative Energies, Experimental/Theoretical EA Values of Neutral $Au_n(py)$, and Experimental/Theoretical VDE Values of $Au_n(py)^-$

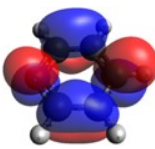
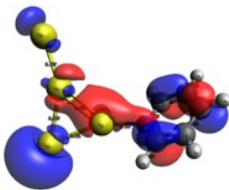
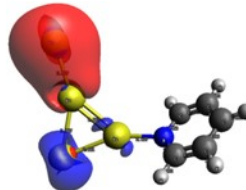
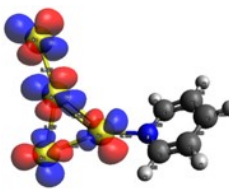
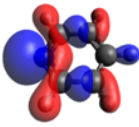
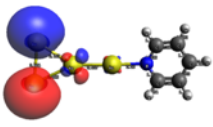
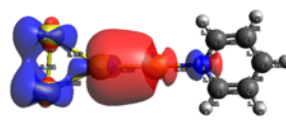
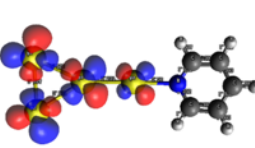
Anion	Optimized Structure	ΔE	Expt. EA	Theo. EA	Expt. VDE	Theo. VDE
$Au_2(py)^-_{iso1}$		0	2.3	2.36	2.34	2.47
$Au_2(py)^-_{iso2}$		0.06	N/A	0.94	N/A	1.16
$Au_2(py)^-_{iso3}$		0.15	1.7	1.40	2.11	1.96
$Au_3(py)^-_{iso1}$		0	2.5	2.68	2.93	2.84
$Au_3(py)^-_{iso2}$		0.19	3.2	2.20	3.43	3.50
$Au_4(py)^-_{iso1}$		0	1.9	1.41	2.03	1.92

$\text{Au}_4(\text{p})\text{y}^-_{\text{iso}2}$		0. 18	2.2	2.1 3	2.3 6	2.2 2
$\text{Au}_4(\text{p})\text{y}^-_{\text{iso}3}$		0. 21	N/ A	1.5 0	N/ A	1.7 0

The unit of energy is eV. N/A indicates the corresponding isomer was not observed in the experiment.

Chart 1. Frontier Molecular Orbitals of Pyridine and $\text{Au}_4(\text{py})^-$ Cluster Anions

Observed in Experiments

Pyridine	$\text{Au}_4(\text{py})^-_{\text{iso}1}$ (net charge on Au_4 moiety is $-0.87e$)			
				
LUMO	SOMO	SOMO-1	SOMO-2	
	$\text{Au}_4(\text{py})^-_{\text{iso}2}$ (net charge on Au_4 moiety is $-1.07e$)			
				
HOMO	SOMO	SOMO-1	SOMO-2	

References

- ¹ Jin, R.; Zeng, C.; Zhou, M.; Chen, Y. Atomically Precise Colloidal Metal Nanoclusters and Nanoparticles: Fundamentals and Opportunities. *Chem. Rev.* **2016**, *116*, 10346-10413.
- ² Zhu, Y.; Qian, H.; Zhu, M.; Jin, R. Thiolate-Protected Au_n Nanoclusters as Catalysts for Selective Oxidation and Hydrogenation Processes. *Adv. Mat.* **2010**, *22*, 1915-1920.
- ³ Gaur, S.; Wu, H.; Stanley, G. G.; More, K.; Kumar, C. S. S. R.; Spivey, J. J. CO Oxidation Studies over Cluster-Derived Au/TiO₂ and AUROLite™ Au/TiO₂ Catalysts using DRIFTS. *Catalysis Today* **2013**, *208*, 72-81.
- ⁴ Chen, W.; Chen, S. Oxygen Electroreduction Catalyzed by Gold Nanoclusters: Strong Core Size Effects. *Angew. Chem.* **2009**, *48*, 4386-4389.
- ⁵ Yu, C.; Li, G.; Kumar, S.; Kawasaki, H.; Jin, R. Stable Au₂₅(SR)₁₈/TiO₂ Composite Nanostructure with Enhanced Visible Light Photocatalytic Activity. *J. Phys. Chem. Lett.* **2013**, *4*, 2847-2852; Oliver-Meseguer, J.; Cabrero-Antonino, J. R.; Domínguez, I.; Leyva-Pérez, A.; Corma, A. Small Gold Clusters Formed in Solution Give Reaction Turnover Numbers of 10⁷ at Room Temperature. *Science* **2012**, *338*, 1452-1455.
- ⁶ Muhammed, M. A. H.; Verma, P. K.; Pal, S. K.; Kumar, R. C. A.; Paul, S.; Omkumar, R. V.; Pradeep, T. Bright, NIR-Emitting Au₂₃ from Au₂₅: Characterization and Applications Including Biolabeling. *Chem. Eur. J.* **2009**, *15*, 10110-10120.
- ⁷ Wu, Z.; Wang, M.; Yang, J.; Zheng, X.; Cai, W.; Meng, G.; Qian, H.; Wang, H.; Jin, R. Fluorescent Probes: Well-Defined Nanoclusters as Fluorescent Nanosensors: A Case Study on Au₂₅(SG)₁₈ (Small 13/2012). *Small* **2012**, *8*, 2027.
- ⁸ Ramakrishna, G.; Varnavski, O.; Kim, J.; Lee, D.; Goodson, T. Quantum-Sized Gold Clusters as Efficient Two-Photon Absorbers. *J. Am. Chem. Soc.* **2008**, *130*, 5032-5033.
- ⁹ Philip, R.; Chantharasupawong, P.; Qian, H.; Jin, R.; Thomas, J. Evolution of Nonlinear Optical Properties: From Gold Atomic Clusters to Plasmonic Nanocrystals. *Nano Lett.* **2012**, *12* 4661-4667.
- ¹⁰ George, A.; Shibu, E. S.; Maliyekkal, S. M.; Bootharaju, M. S.; Pradeep, T. Luminescent, Freestanding Composite Films of Au₁₅ for Specific Metal Ion Sensing. *ACS Appl. Mater. Interfaces* **2012**, *4*, 639-644.
- ¹¹ Xiaohong, T.; Rongchao, J. Ultrasmall Metal Nanoclusters for Bio-Related Applications. *WIREs Nanomed. Nanobiotechnol.* **2013**, *5*, 569-581.
- ¹² Wong, O. A.; Hansen, R. J.; Ni, T. W.; Heinecke, C. L.; Compel, W. S.; Gustafson, D. L.; Ackerson, C. J. Structure-Activity Relationships for Biodistribution, Pharmacokinetics, and Excretion of Atomically Precise Nanoclusters in a Murine Model. *Nanoscale* **2013**, *5*, 10525-10533.
- ¹³ Jin, R.; Qian, H.; Wu, Z.; Zhu, Y.; Zhu, M.; Mohanty, A.; Garg, N. Size Focusing: A Methodology for Synthesizing Atomically Precise Gold Nanoclusters. *J. Phys. Chem. Lett.* **2010**, *1*, 2903-2910.
- ¹⁴ Zeng, C.; Chen, Y.; Das, A.; Jin, R. Transformation Chemistry of Gold Nanoclusters: From One Stable Size to Another. *J. Phys. Chem. Lett.* **2015**, *6*, 2976-2986.
- ¹⁵ Negishi, Y.; Nobusada, K.; Tsukuda, T. Glutathione-Protected Gold Clusters Revisited: Bridging the Gap between Gold(I)-Thiolate Complexes and Thiolate-Protected Gold

- Nanocrystals. *J. Am. Chem. Soc.* **2005**, *127*, 5261-5270.
- ¹⁶ Wan, X.-K.; Lin, Z.-W.; Wang, Q.-M. Au₂₀ Nanocluster Protected by Hemilabile Phosphines. *J. Am. Chem. Soc.* **2012**, *134*, 14750-14752.
- ¹⁷ Maity, P.; Tsunoyama, H.; Yamauchi, M.; Xie, S.; Tsukuda, T. Organogold Clusters Protected by Phenylacetylene. *J. Am. Chem. Soc.* **2011**, *133*, 20123-20125.
- ¹⁸ Walter, M.; Akola, J.; Lopez-Acevedo, O.; Jadzinsky, P. D.; Calero, G.; Ackerson, C. J.; Whetten, R. L.; Grönbeck, H.; Häkkinen. A Unified View of Ligand-Protected Gold Clusters as Superatom Complexes. *PNAS* **2008**, *105*, 9157-9162.
- ¹⁹ Dudev, T.; Lim, C. Metal Binding Affinity and Selectivity in Metalloproteins: Insights from Computational Studies. *Annu. Rev. Biophys.* **2008**, *37*, 97-116.
- ²⁰ Shafai, G.; Hong, S.; Bertino, M.; Rahman, T. S. Effect of Ligands on the Geometric and Electronic Structure of Au₁₃ Clusters. *J. Phys. Chem. C* **2009**, *113*, 12072-12078.
- ²¹ Barngrover, B. M.; Aikens, C. M. Oxidation of Gold Clusters by Thiols. *J. Phys. Chem. A* **2013**, *117*, 5377-5384.
- ²² Jiang, D. The Expanding Universe of Thiolated Gold Nanoclusters and Beyond. *Nanoscale* **2013**, *5*, 7149-7160.
- ²³ Rajský, T.; Urban, M. Au_n (*n* = 1, 11) Clusters Interacting with Lone-Pair Ligands. *J. Phys. Chem. A* **2016**, *120*, 3938-3949.
- ²⁴ Black, D. M.; Bhattarai, N.; Whetten, R. L.; Bach, S. B. H. Collision-Induced Dissociation of Monolayer Protected Clusters Au₁₄₄ and Au₁₃₀ in an Electrospray Time-of-Flight Mass Spectrometer. *J. Phys. Chem. A* **2014**, *118*, 10679-10687.
- ²⁵ Crasto, D.; Malola, S.; Brososky, G.; Dass, A.; Häkkinen, H. Single Crystal XRD Structure and Theoretical Analysis of the Chiral Au₃₀S(S-*t*-Bu)₁₈ Cluster. *J. Am. Chem. Soc.* **2014**, *136*, 5000-5005.
- ²⁶ Zeng, C.; Liu, C.; Pei, Y.; Jin, R. Thiol Ligand-Induced Transformation of Au₃₈(SC₂H₄Ph)₂₄ to Au₃₆(SPh-*t*-Bu)₂₄. *ACS Nano* **2013**, *7*, 6138-6145.
- ²⁷ Johnson, G. E.; Laskin, J. Understanding Ligand Effects in Gold Clusters using Mass Spectrometry. *Analyst* **2016**, *141*, 3573-3589.
- ²⁸ Johnson, G. E.; Priest, T.; Laskin, J. Size-Dependent Stability toward Dissociation and Ligand Binding Energies of Phosphine Ligated Gold Cluster Ions. *Chem. Sci.* **2014**, *5*, 3275-3286.
- ²⁹ Johnson, G. E.; Olivares, A.; Hill, D.; Laskin, J. Cationic Gold Clusters Ligated with Differently Substituted Phosphines: Effect of Substitution on Ligand Reactivity and Binding. *Phys. Chem. Chem. Phys.* **2015**, *17*, 14636-14646.
- ³⁰ Johnson, G. E.; Priest, T.; Laskin, J. Synthesis and Characterization of Gold Clusters Ligated with 1,3-Bis(dicyclohexylphosphino)propane. *ChemPlusChem* **2013**, *78*, 1033-1039.
- ³¹ Chakraborty, P.; Baksi, A.; Khatun, E.; Nag, A.; Ghosh, A.; Pradeep, T. Dissociation of Gas Phase Ions of Atomically Precise Silver Clusters Reflects Their Solution Phase Stability. *J. Phys. Chem. C* **2017**, *121*, 10971-10981.
- ³² Zhang, X.; Liu, G.; Ganteför, G.; Bowen, K. H.; Alexandrova, A. N. PtZnH₅⁻, A σ -Aromatic Cluster. *J. Phys. Chem. Lett.* **2014**, *5*, 1596-1601.

- ³³ Ho, J.; Ervin, K. M.; Lineberger, W. C. Photoelectron Spectroscopy of Metal Cluster Anions: Cu_n^- , Ag_n^- , and Au_n^- . *J. Chem. Phys.* **1990**, *93*, 6987-7002.
- ³⁴ Neese, F. The ORCA Program System. *WIREs Comput. Mol. Sci.* **2012**, *2*, 73-78.
- ³⁵ Becke, A. D. Density-Functional Exchange-Energy Approximation with Correct Asymptotic Behavior. *Phys. Rev. A* **1988**, *38*, 3098-3100; Perdew, J. P. Density-Functional Approximation for the Correlation Energy of the Inhomogeneous Electron Gas. *Phys. Rev. B* **1986**, *33*, 8822-8824.
- ³⁶ Grimme, S.; Antony, J.; Ehrlich, S.; Krieg, H. A Consistent and Accurate *Ab Initio* Parametrization of Density Functional Dispersion Correction (DFT-D) for the 94 Elements H-Pu. *J. Chem. Phys.* **2010**, *132*, DOI: 10.1063/1.3382344.
- ³⁷ Neese, F.; Wennmohs, F.; Hansen, A.; Becker, U. Efficient, Approximate and Parallel Hartree-Fock and Hybrid DFT Calculations. A 'Chain-of-Spheres' Algorithm for the Hartree-Fock Exchange. *Chem. Phys.* **2008**, *356*, 98-109.
- ³⁸ Weigend, F.; Ahlrichs, R. Balanced Basis Sets of Split Valence, Triple Zeta Valence and Quadruple Zeta Valence Quality for H to Rn: Design and Assessment of Accuracy. *Phys. Chem. Chem. Phys.* **2005**, *7*, 3297-3305, DOI: 10.1039/B508541A; Weigend, F. Accurate Coulomb-Fitting Basis Sets for H to Rn. *Phys. Chem. Chem. Phys.* **2006**, *8*, 1057-1065.
- ³⁹ Andrae, D.; Häußermann, U.; Dolg, M.; Stoll, H.; Preuß, H. Energy-Adjusted *Ab Initio* Pseudopotentials for the Second and Third Row Transition Elements. *Theor. Chim. Acta* **1990**, *77*, 123-141.
- ⁴⁰ Häkkinen, H.; Yoon, B.; Landman, U.; Li, X.; Zhai, H.-J.; Wang, L.-S. On the Electronic and Atomic Structures of Small Au_N^- ($N = 4-14$) Clusters: A Photoelectron Spectroscopy and Density-Functional Study. *J. Phys. Chem. A* **2003**, *107*, 6168-6175.
- ⁴¹ Zhang, X.; Lim, E.; Kim, S. K.; Bowen, K. H. Photoelectron Spectroscopic and Computational Study of $(\text{M-CO}_2)^-$ Anions, $\text{M} = \text{Cu}, \text{Ag}, \text{Au}$. *J. Chem. Phys.* **2015**, *143*, 174305/1-6.

III.2 Stabilizing Otherwise Unstable Anions with Halogen Bonding

Xinxing Zhang, *Gaoxiang Liu*, Sandra Ciborowski, Kit Bowen

*Department of Chemistry, Johns Hopkins University, 3400N. Charles Street,
Baltimore, MD 21218(USA)*

Abstract

Both hydrogen bonding (HB) and halogen bonding (XB) are essentially electrostatic interactions, but whereas hydrogen bonding has a well-documented record of stabilizing unstable anions, little is known about halogen bonding's ability to do so. Herein, we present a combined anion photoelectron spectroscopic and density functional theory study of the halogen bond-stabilization of the pyrazine (Pz) anion, an unstable anion in isolation due to its neutral counterpart having a negative electron affinity (EA). The halogen bond formed between the σ -hole on bromobenzene (BrPh) and the lone pair(s) of Pz significantly lowers the energies of the $\text{Pz}(\text{BrPh})_1^-$ and $\text{Pz}(\text{BrPh})_2^-$ anions relative to the neutral molecule, resulting in the emergence of a positive EA for the neutral complexes. As seen through its charge distribution and electrostatic potential analyses, the negative charge on Pz^- is diluted due to the XB. Thermodynamics reveals that the low temperature of the supersonic expansion plays a key role in forming these complexes.

Being electron-withdrawing, covalently bonded halogens are often negatively charged in character. Surprisingly, they can interact attractively and directionally with nucleophiles such as lone pairs and anions.^{1,2} This noncovalent interaction was first called halogen bonding (XB) by Dumas and co-workers.^{3,4} The nature of XB was not resolved until 1992; covalently bonded, polarizable halogen atoms have positive electrostatic potential regions on the opposite end of the covalent bond and the equatorial sides of these atoms are negative.^{5,6} XB is therefore attributed to the electrostatic attraction between this positive region and nucleophiles. The positive site was termed the σ -hole by Politzer et al. in 2007.⁷ The size of the σ -hole depends on the polarizability of the halogen, that is, $I > Br > Cl > F$, but can also be tuned by other electron-withdrawing groups.^{2, 13}

Once its enigmatic nature was understood, XB was widely applied in supramolecular chemistry and crystal engineering as a driving force for self-assembly.⁸⁻¹³ Gas phase experimental investigations of XB are scarce; they are limited to a handful of experiments using techniques such as molecular beam scattering,¹⁴ rotational spectroscopy,¹⁵⁻¹⁷ and blackbody infrared radiative dissociation.¹⁸ Theoretical calculations, on the other hand, have been very fruitful.^{1, 2, 19-23} According to Politzer, thermodynamics accounts for the rarity of gas phase studies;^{1, 24} that is, the Gibbs free energy, $\Delta G = \Delta H - T\Delta S$, has to be negative. The enthalpy change, ΔH , is usually

negative, yet due to entropy changes (loss of rotational and translational degrees of freedom) that occur upon forming a halogen bond, the $T\Delta S$ term often has a large negative value, resulting in a positive ΔG . Therefore, to construct XB in the gas phase, one needs to have an exothermic reaction at low temperatures.

Herein, we present a gas phase photoelectron spectroscopic study of the pyrazine anion (Pz^-)-bromobenzene (BrPh) complexes. Pz is an *N*-heterocyclic molecule with two nitrogen atoms at the *para* positions of a six-membered ring, and it has been determined to have a negative electron affinity (EA) of -0.01 eV,^{25,26} implying that Pz^- is unstable and difficult to form in isolation. Hydrogen bonding (HB) with water is a well-known means of stabilizing unstable anions.²⁶⁻³¹ Upon forming HB, the potential energy of the anion is lowered relative to the neutral species. This is due to a stronger interaction between water molecules and the anion than between water molecules and the anion's corresponding neutral species. As a result, the EA value switches from negative to positive. In this work, we have provided evidence that XB is formed between Pz^- and BrPh, stabilizing unstable Pz^- and rendering the EAs of neutral $\text{Pz}(\text{BrPh})_n$ ($n=1,2$) positive. Density functional theory (DFT) calculations were performed for comparison with the experimental findings.

The details of experimental/computational methods are provided in the Supporting

Information. The M06-2x functional³² used is parameterized for dispersion and regarded as a standard method for describing non-covalent interactions such as XB.³³

The mass spectra of $\text{Pz}(\text{BrPh})_n^-$ ($n=1,2$) are provided in the Supporting Information. The photoelectron spectra of $\text{Pz}(\text{BrPh})_n^-$ taken with a 355 nm (3.49 eV) laser are presented in Figure 1. For $\text{Pz}(\text{BrPh})_1^-$, the major electron binding energy (EBE) band ranges from 0.1 eV to 1.2 eV and peaks at 0.48 eV. For $\text{Pz}(\text{BrPh})_2^-$, it ranges from 0.3 eV to 1.5 eV and peaks at 0.69 eV. If there is sufficient Franck–Condon overlap between the ground state of the anion and the ground state of the neutral species and there is not much vibrational hot band intensity, the threshold of the EBE band is the EA. We extrapolate the lower EBE side of the band to zero, and the EBE values there, 0.15 eV and 0.32 eV, are taken as the experimental EA values of $\text{Pz}(\text{BrPh})_1$ and $\text{Pz}(\text{BrPh})_2$, respectively. The EA of $\text{Pz}(\text{BrPh})_1$ is not much above zero, suggesting that one BrPh molecule (one XB) is the threshold number that barely pulls the EA from negative to positive. The peak positions of the two spectra, 0.48 eV and 0.69 eV, are the experimental vertical detachment energies (VDE) for $\text{Pz}(\text{BrPh})_1^-$ and $\text{Pz}(\text{BrPh})_2^-$, respectively. The VDE is the photodetachment transition energy at which the Franck–Condon overlap between the wave functions of the anion and its neutral counterpart is maximal. These experimental results are tabulated in Table 1 for comparison with those obtained from calculations, and excellent agreement is observed. Gaussian

fittings of these two spectra are provided in the Supporting Information.

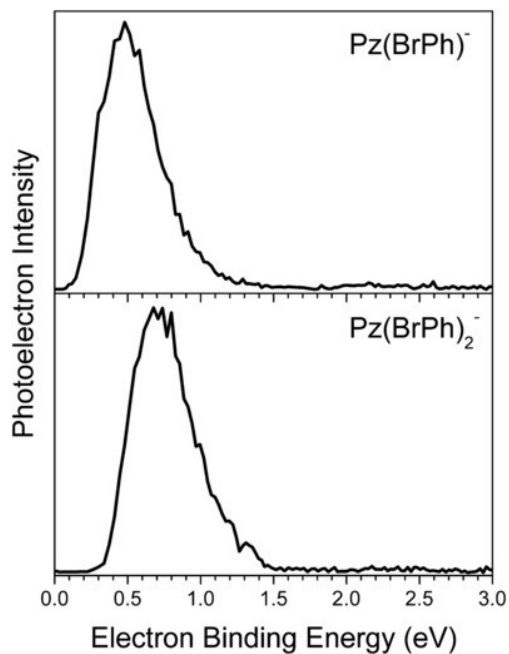


Figure III.2.1 Photoelectron spectra of $\text{Pz}(\text{BrPh})_n^-$ ($n=1,2$) taken with a 355 nm (3.49 eV) laser.

Table III.2.2 Experimental and theoretical EAs of $\text{Pz}(\text{BrPh})_n$ and VDEs of $\text{Pz}(\text{BrPh})_n^-$. All values are in eV. ($m=0,-$)

	EA (Exp./Theo.)	VDE (Exp./Theo.)
$\text{Pz}(\text{BrPh})^m$	0.15/0.164	0.48/0.432
$\text{Pz}(\text{BrPh})_2^m$	0.32/0.331	0.69/0.664

The calculated 3D coordinates of all the species are provided in the Supporting Information. Figure 2 presents the structures of $\text{Pz}(\text{BrPh})_n^m$ ($m=0,-$).

$\text{Pz}(\text{BrPh})_1^m$ possess C_{2v} symmetries with the Pz plane perpendicular to the BrPh plane. The bromine atom in BrPh and one of the nitrogen atoms of Pz form a XB. The XB length in the neutral complex is 3.00 Å, significantly longer than the 2.71 Å in the anion, indicating that the XB in the anion is stronger than in the neutral species. This is because the higher negative charge in the anion leads to stronger electrostatic attraction. $\text{Pz}(\text{BrPh})_2^m$, on the other hand, have D_{2h} symmetries. Each of the nitrogen atoms of Pz forms a XB with one BrPh molecule. The XB length in the anion (2.72 Å) is also shorter than that in the neutral species (2.98 Å). These bond lengths fall within the range of typical XB lengths.^{1,2} The highest occupied molecular orbitals (HOMO) of $\text{Pz}(\text{BrPh})_n^-$ have the excess electron occupying the π^* orbital of the Pz ring, indicating that the Pz moieties are indeed negatively charged.

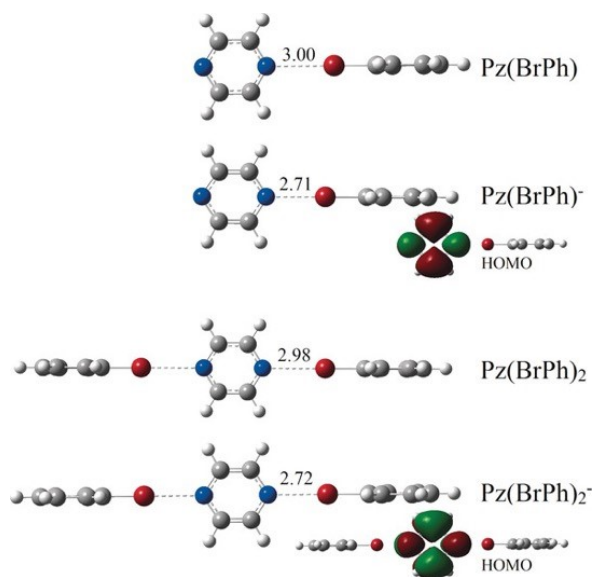


Figure III.2.1 Calculated structures of $\text{Pz}(\text{BrPh})_n^m$ ($m=0,-$). The XB lengths are in Å. The highest occupied molecular orbitals (HOMO) are also presented.

Natural population analysis (NPA) provides another perspective for understanding the stabilization of Pz^- by XB. NPA shows that the net charge on the Pz ring is -0.93 e in Pz^- , -0.86 e in $\text{Pz}(\text{BrPh})_1^-$ and -0.88 e in $\text{Pz}(\text{BrPh})_2^-$. Therefore, the first XB decreases the charge by -0.07 e, and the second further decreases the charge by -0.05 e. To better visualize the XB, Figure 3 shows the electrostatic potential (ESP) surfaces of Pz, Pz^- and $\text{Pz}(\text{BrPh})_n^-$. The induced neutral (green), positive (blue), and negative (red) electrostatic potentials are mapped on the 0.04 e/bohr³ surfaces in the range of ± 44 kcal mol⁻¹. In neutral Pz, only the small ends of the nitrogen atoms show a negative potential due to their higher electronegativity. Upon electron attachment, the ESP of Pz^- has mostly negative potentials. In $\text{Pz}(\text{BrPh})_1^-$, in which one XB is present, the negative potentials (red) on the Pz^- ring decreases compared to bare Pz^- . When two XBs are formed in $\text{Pz}(\text{BrPh})_2^-$, the negative potential on Pz^- further decreases. These observations are consistent with the charge distribution change revealed by NPA. The positive σ -holes at the end of the Br atom (blue) and the negative equatorial side (yellow) can be clearly observed. The σ -holes directionally point towards the most negative (red) regions on the Pz^- ring, that is, the nitrogen atoms, forming the XB. Our theoretical effort in searching for other possible isomers, especially the π - σ hole interaction, did not end in any stable local minima; this might be because the negative charge on the ring is mainly localized on the nitrogen atom in Pz^- (-0.65 e).

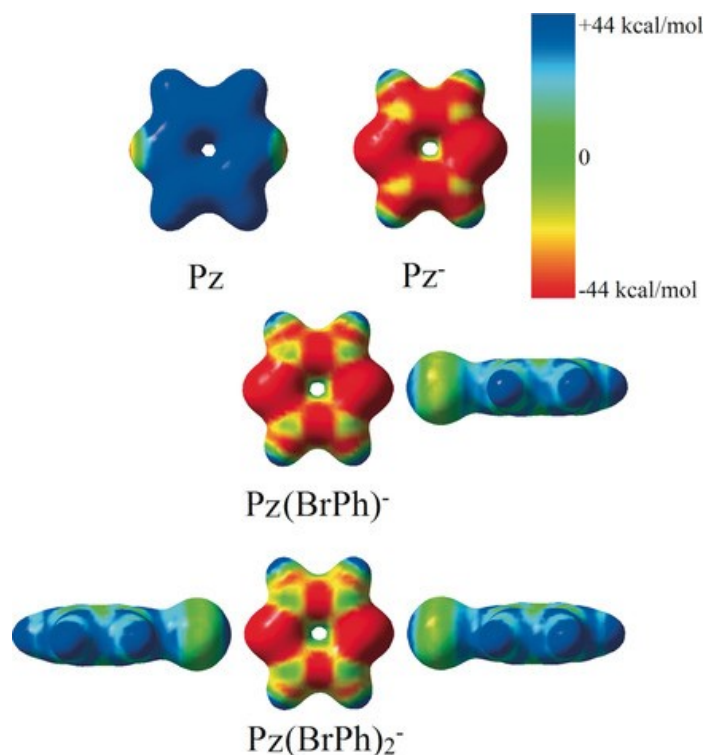


Figure III.2.2 Electrostatic potential surfaces of Pz, Pz⁻, Pz(BrPh)₁⁻, and Pz(BrPh)₂⁻. The induced positive (blue), negative (red), and neutral (green) potentials are mapped on the 0.04 e/bohr³ surfaces of the clusters.

To quantify the stabilization effect of XB, the binding energies of the first and second XB of the neutral and anionic complexes, $D_0[\text{Pz}(\text{BrPh})_n^m]$, are given by: $D_0[\text{Pz}(\text{BrPh})^m] = E[\text{Pz}^m] + E[\text{BrPh}] - E[\text{Pz}(\text{BrPh})^m]$ and $D_0[\text{Pz}(\text{BrPh})_2^m] = E[\text{Pz}(\text{BrPh})^m] + E[\text{BrPh}] - E[\text{Pz}(\text{BrPh})_2^m]$ where E refers to the calculated energies with the zero-point energy corrected. In this case, $D_0[\text{Pz}(\text{BrPh})^0]$ is 0.055 eV, $D_0[\text{Pz}(\text{BrPh})^-]$ is 0.226 eV, $D_0[\text{Pz}(\text{BrPh})_2^0]$ is 0.051 eV and $D_0[\text{Pz}(\text{BrPh})_2^-]$ is 0.218 eV. The binding energies of the anions are higher than those of the neutral species, suggesting that upon forming the XB, the energy of the

anions are lowered more than those of the neutral species, which switches the EA value from negative to positive. The higher negative charge on Pz^- compared to Pz causes stronger electrostatic attractions and shorter XBs in the anions.

Additionally, since $D_0[\text{Pz}(\text{BrPh})^-] - D_0[\text{Pz}(\text{BrPh})^0] = \text{EA}[\text{Pz}(\text{BrPh})^0] - \text{EA}[\text{Pz}] = 0.171 \text{ eV}$, and the calculated $\text{EA}[\text{Pz}(\text{BrPh})^0]$ is 0.164 eV , we deduce that $\text{EA}[\text{Pz}] = -0.007 \text{ eV}$, which is consistent with the previously reported experimental value, -0.01 eV .²⁵ Since accurate prediction of slightly negative EA values is difficult, this excellent agreement gives us confidence in the reliability of the theoretical methods used.

Finally, we discuss the thermodynamics of forming $\text{Pz}(\text{BrPh})_n^m$. Computed at 298 K, the internal energy change (ΔE^0), enthalpy change (ΔH^0), entropy change (ΔS^0), and Gibbs free energy change (ΔG^0) are tabulated in Table 2. Anion formation is more exothermic than that of the neutral species, which is consistent with the binding energy differences. At room temperature, none of these four complexes can form due to the positive ΔG^0 . Thus, we calculated the threshold temperature for each reaction to occur. Forming $\text{Pz}(\text{BrPh})$ needs a temperature lower than 2.9 K, and the formation of $\text{Pz}(\text{BrPh})_2$ is thermodynamically forbidden due to both the entropy loss and endothermicity. The formation of $\text{Pz}(\text{BrPh})_1^-$ and $\text{Pz}(\text{BrPh})_2^-$ needs temperatures

lower than 124.3 K and 114.1 K, respectively. Gas phase supersonic expansion can usually cool the molecules to several tens of Kelvin,^{34,35} which justifies our observation of the anions, although the neutral complexes will fall apart into Pz and BrPh molecules after photodetachment. This implies the mechanism of forming the anions. Two pathways could be present: 1) The neutral Pz reacts with BrPh to form neutral complexes, which then attach electrons to form the anions. 2) The anionic Pz^- reacts with BrPh to form the anionic complexes. The first pathway is not realistic due to the very low temperatures needed to form the neutral complexes, hence, we speculate that even though Pz has a slightly negative EA, there are short-lived Pz^- anions formed in the ion source, which are then stabilized by forming the XB.

Table III.2.3 Computed thermodynamic properties (kcal mol^{-1}) for gas-phase complex formation at 298 K. The threshold temperatures (K) for the reactions to occur are also listed.

Reactions	ΔE^0	ΔH^0	$T\Delta S^0$	ΔG^0	Threshold T
$\text{Pz} + \text{BrPh} \rightarrow \text{Pz}(\text{BrPh})$	-0.1	-0.7	-10.2	9.5	2.9
$\text{Pz}^- + \text{BrPh} \rightarrow \text{Pz}(\text{BrPh})^-$	-4.1	-4.7	-10.5	5.8	124.3
$\text{Pz}(\text{BrPh}) + \text{BrPh} \rightarrow \text{Pz}(\text{BrPh})_2$	0.15	-0.45	-10.1	9.6	Won't occur
$\text{Pz}(\text{BrPh})^- + \text{BrPh} \rightarrow \text{Pz}(\text{BrPh})_2^-$	-3.8	-4.4	-10.4	6.1	114.1

In general, HB and XB are considered to be two parallel worlds,^{36,37} so the binding

circumstances of HB should be largely applicable to XB. However, there are still many missing pieces in studies of XB compared to HB. For example, we recently designed anionic, metallic XB acceptors, which have long been known to exist for HB but have been unknown for XB.³⁸ In this work, we for the first time extend XB to stabilizing gas-phase unstable anions, which is already well-known in the case of HB.²⁶⁻³¹

References

1. P. Politzer, J. S. Murray, T. Clark, *Phys. Chem. Chem. Phys.* 2013, **15**, 11178– 11189.
2. P. Politzer, P. Lane, M. C. Concha, Y. Ma, J. S. Murray, *J. Mol. Model.* 2007, **13**, 305– 311
3. J. M. Dumas, M. Kern, J. L. Janier-Dubry, *Bull. Soc. Chim. Fr.* 1976, 1785– 1787.
4. J. M. Dumas, H. Peurichard, M. Gomel, *J. Chem. Res. Synop.* 1978, 54– 57.
5. T. Brinck, J. S. Murray, P. Politzer, *Int. J. Quantum Chem.* 1992, **44**, 57– 64.
6. T. Brinck, J. S. Murray, P. Politzer, *Int. J. Quantum Chem.* 1993, **48**, 73– 88.
7. T. Clark, M. Hennemann, J. S. Murray, P. Politzer, *J. Mol. Model.* 2007, **13**, 291– 296.
8. P. Metrangolo, G. Resnati, *Chem. Eur. J.* 2001, **7**, 2511– 2519.
9. A. De Santis, A. Forni, R. Liantonio, P. Metrangolo, T. Pilati, G. Resnati, *Chem. Eur. J.* 2003, **9**, 3974– 3983.
10. B. Amico, S. V. Meille, E. Corradi, M. T. Messina, G. Resnati, *J. Am. Chem. Soc.* 1998, **120**, 8261– 8262.
11. T. Imakubo, H. Sawa, R. Kato, *Synth. Met.* 1995, **73**, 117– 122.
12. J. Xu, X. Liu, T. Lin, J. Huang, C. He, *Macromolecules* 2005, **38**, 3554– 3557.
13. P. Auffinger, F. A. Hays, E. Westhof, P. S. Ho, *Proc. Natl. Acad. Sci. USA* 2004, **101**, 16789– 16794.
14. D. Cappelletti, P. Candori, F. Pirani, L. Belpassi, F. Tarantelli, *Cryst. Growth Des.* 2011, **11**, 4279– 4283.
15. S. L. Stephens, N. R. Walker, A. C. Legon, *J. Chem. Phys.* 2011, **135**, 224309.
16. H. I. Bloemink, J. H. Holloway, A. C. Legon, *Chem. Phys. Lett.* 1996, **254**, 59– 68.
A. Domene, P. W. Fowler, A. C. Legon, *Chem. Phys. Lett.* 1999, **309**, 463– 470.
17. E. A. L. Gillis, M. G. Chudzinski, M. Demireva, M. S. Taylor, M. G. Sarwar, E. R. Williams, T. D. Fridgen, *Phys. Chem. Chem. Phys.* 2013, **15**, 7638– 7647.
18. M. Jabłoński, M. Palusiak, *J. Phys. Chem. A* 2012, **116**, 2322– 2332.

19. Y. Lu, J. Zou, Y. Wang, Y. Jiang, Q. Yu, *J. Phys. Chem. A* 2007, **111**, 10781– 10788.
20. S. H. Jungbauer, S. Schindler, E. Herdtweck, S. Keller, S. M. Huber, *Chem. Eur. J.* 2015, **21**, 13625– 13636.
21. R. Li, Q. Li, J. Cheng, Z. Liu, W. Li, *ChemPhysChem* 2011, **12**, 2289– 2295.
A. Bauzá, I. Alkorta, A. Frontera, J. Elguero, *J. Chem. Theory Comput.* 2013, **9**, 5201– 5210.
22. P. Politzer, J. S. Murray, *CrystEngComm* 2013, **15**, 3145– 3150.
23. J. K. Song, N. K. Lee, S. K. Kim, *J. Chem. Phys.* 2002, **117**, 1589.
24. Y. Wang, X. Zhang, S. Lyapustina, M. M. Nilles, S. Xu, J. D. Graham, K. H. Bowen, J. T. Kelly, G. S. Tschumper, N. I. Hammer, *Phys. Chem. Chem. Phys.* 2015, **18**, 704– 712.
25. J. T. Kelly, S. Xu, J. Graham, J. M. Nilles, D. Radisic, A. M. Buonaugurio, K. H. Bowen, N. I. Hammer, G. S. Tschumper, *J. Phys. Chem. A* 2014, **118**, 11901– 11907.
26. S. Eustis, D. Wang, S. Lyapustina, K. H. Bowen, *J. Chem. Phys.* 2007, **127**, 224309.
27. S. Xu, J. M. Nilles, K. H. Bowen, *J. Chem. Phys.* 2003, **119**, 10696– 10701.
28. J. K. Song, S. Y. Han, I. Chu, J. H. Kim, S. K. Kim, S. A. Lyapustina, S. J. Xu, J. M. Nilles, K. H. Bowen, *J. Chem. Phys.* 2002, **116**, 4477– 4481.
29. S. A. Lyapustina, S. J. Xu, M. Nilles, K. H. Bowen, *J. Chem. Phys.* 2000, **112**, 6643– 6648.
30. Y. Zhao, D. G. Truhlar, *J. Phys. Chem. A* 2006, **110**, 51215129.
31. S. Kozuch, J. M. L. Martin, *J. Chem. Theory Comput.* 2013, **9**, 1918– 1931.
A. Ding, J. Hesslich, *Chem. Phys. Lett.* 1983, **94**, 54– 57.
B. T. Droege, P. C. Engelking, *Chem. Phys. Lett.* 1983, **96**, 316– 318.
32. P. Metrangolo, H. Neukirch, T. Pilati, G. Resnati, *Acc. Chem. Res.* 2005, **38**, 386– 395.
33. Z. P. Shields, J. S. Murray, P. Politzer, *Int. J. Quantum Chem.* 2010, **110**, 2823– 2832.
34. X. Zhang, K. Bowen, *Chem. Eur. J.* 2017, **23**, 5439– 5442.

III.3 Mystery of Three Borides: Differential Metal–Boron Bonding Governing Superhard Structures

Paul J. Robinson[†], Gaoxiang Liu[‡], Sandra Ciborowski[‡], Chalynette Martinez-Martinez[‡], Juan R. Chamorro[‡], Xinxing Zhang[‡], Tyrel M. McQueen[‡], Kit H. Bowen^{*‡}, Anastassia N. Alexandrova^{*†§}

[†] *Department of Chemistry & Biochemistry, University of California, Los Angeles, Los Angeles, California 90095, United States*

[‡] *Department of Chemistry and Materials Science, Johns Hopkins University, 3400 N. Charles Street, Baltimore, Maryland 21218, United States*

[§] *California NanoSystems Institute, Los Angeles, California 90095, United States*

Ultrahard materials have been of interest to human kind since prehistoric times. Borides of certain transition metals form a new class of hard materials.(1-4) Being metals, these borides are easily cut with electric discharge machining and thus appear as an attractive alternative to diamond. The governing principles for the design of ultrahard borides have been proposed to be the combination of high electron density at the Fermi level (E_F) coming from the metal, making borides incompressible, and a rigid covalent boron skeleton resisting the shear stress.(5-10) The metal and boron sublattices in this model are seen independently. Here, we challenge these old principles and show that only with the inclusion of specific metal–boron bonding can

we explain and design for the structure and hardness of borides.

We zoom in to a set of three diborides, which are stoichiometrically identical and structurally related yet distinct: TiB_2 , ReB_2 , and OsB_2 (Figure 1). Among these three, only ReB_2 is ultrahard.(11-13) In all three cases, the boron sublattice is a sheet: planar in TiB_2 and corrugates as a “chair” in ReB_2 and as a “boat” in OsB_2 , by analogy with the conformations of cyclohexane. These diborides demonstrate how boron, a metalloid, is capable of many different kinds of bonds to metals, and this promiscuity strongly dictates hardness.

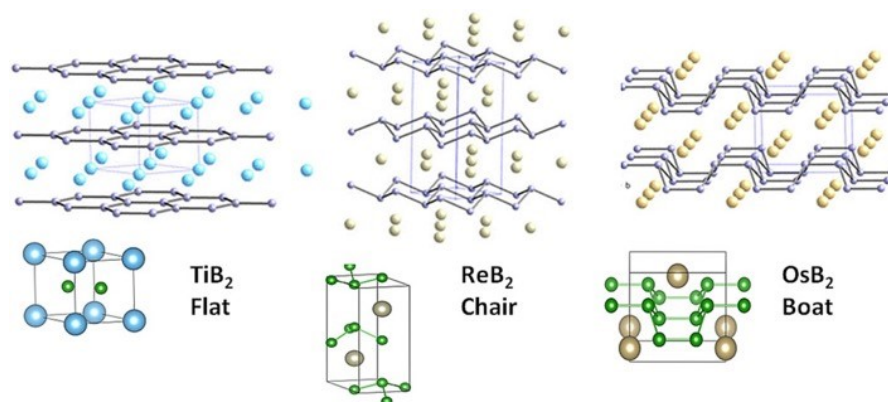


Figure III.3.1 Structures of the three borides: TiB_2 featuring a flat B-sheet and ReB_2 and OsB_2 where the B-sheet is bent in chair and boat conformations, respectively.(1) The upper images display supercells to make apparent the structural analogies while the lower images show a single unit cell.

Our approach links the chemical bonding in materials to that in relevant small cluster fragments, which can be studied in great detail using state-of-the-art theory and

experiment. The identified critical elements in the electronic structure of the cluster are mapped back onto the solid for property rationalization and design.(14, 15)

The most elementary motif that can be observed in the solids is MB_2 , and thus, we begin from the $MB_2^{0/-}$ clusters (ions being included for experimental characterization with anion photoelectron spectroscopy). All clusters have C_{2v} symmetry, with the metal coordinating to the center of the B–B bond. However, they have markedly different B–B and M–B distances (see Supporting Information), indicating that metals affect the B–B bonding in different ways. TiB_2^- (2A_1) has a short $R(B-B)$ of 1.56 Å; ReB_2^- has three competing configurations: 3B_2 , $R(B-B) = 1.75$ Å; 3B_1 , $R(B-B) = 1.66$ Å (2.51 kcal/mol above 3B_2); and 3A_2 , $R(B-B) = 1.76$ Å (3.14 kcal/mol above 3B_2). OsB_2^- (4A_2) has $R(B-B)$ of 1.66 Å. Note that these calculations are large-active-space multireference with dynamic electron correlation (see Supporting Information). This tour de force theoretical approach appeared to be required to reproduce experimental spectra for these seemingly simple systems.(16) The close proximity and mixing of many electronic states can be linked to the promiscuity of metal–boron bonding. Table 1 and Figure 2 show the experimental and theoretical photoelectron spectra (OsB_2^- was not done experimentally due to the high toxicity of Os). The good agreement between theory and experiment signifies that theory can adequately describe these clusters and provide an electronic structure insight.

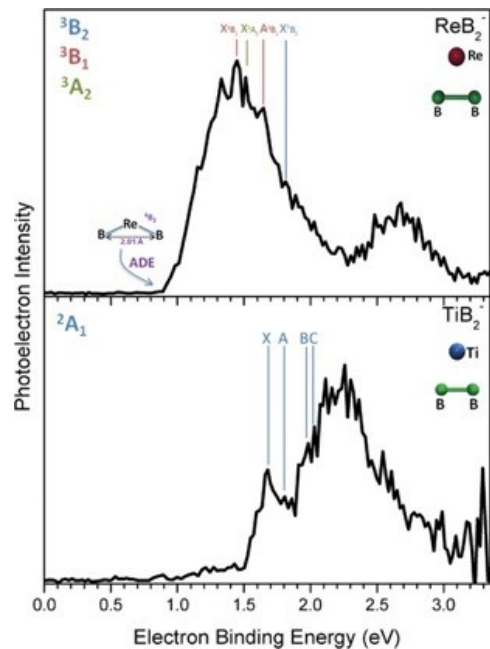


Figure III.3.2 Experimental photoelectron spectra of ReB_2^- (top) and TiB_2^- (bottom) and the theoretical assignment of spectral features.

Table III.3.2 Experimental and Calculated Photoelectron Spectra of TiB_2^- and ReB_2^- (in eV)

feature	expt. E	transition	calc. E
ReB_2^-			
ADE	0.9 ± 0.1	${}^3\text{A}_2 \rightarrow {}^4\text{B}_1$	1.21
X^1B_3	1.45 ± 0.1	${}^3\text{B}_1 \rightarrow {}^4\text{B}_1$ (${}^2\text{B}_1$ VDE)	1.51
X^3A_2	1.52 ± 0.1	${}^3\text{A}_2 \rightarrow {}^4\text{B}_1$ (${}^2\text{A}_2$ VDE)	1.58
A^3B_1	1.65 ± 0.1	${}^3\text{B}_1 \rightarrow {}^2\text{B}_1$	1.70
X^3B_2	1.76 ± 0.1	${}^3\text{B}_2 \rightarrow {}^4\text{B}_1$ (${}^2\text{B}_2$ VDE)	1.76
TiB_2^-			
ADE	1.4 ± 0.1	${}^2\text{A}_1 \rightarrow {}^1\text{A}_1$	1.09
X	1.68 ± 0.1	${}^2\text{A}_1 \rightarrow {}^1\text{A}_1$ (${}^2\text{A}_1$ VDE)	1.49
A	1.80 ± 0.1	${}^2\text{A}_1 \rightarrow {}^3\text{A}_1$	1.63
B	1.96 ± 0.1	${}^2\text{A}_1 \rightarrow {}^1\text{A}_1$	1.86
C	2.07 ± 0.1	${}^2\text{A}_1 \rightarrow {}^3\text{A}_1$	2.02

The chemical bonding in the three neutral clusters (Figure 3) reveals peculiarities of metal–boron interactions and differences between the three clusters. When transition metals interact with B₂, the back-donation first happens to the LUMO of B₂, which is a bonding σ_{2p_x} -MO. The d-AO \rightarrow LUMO(B₂) back-donation thus strengthens the B–B bond. The resulting MO falls deep below the HOMO–LUMO gap in ReB₂ and OsB₂,

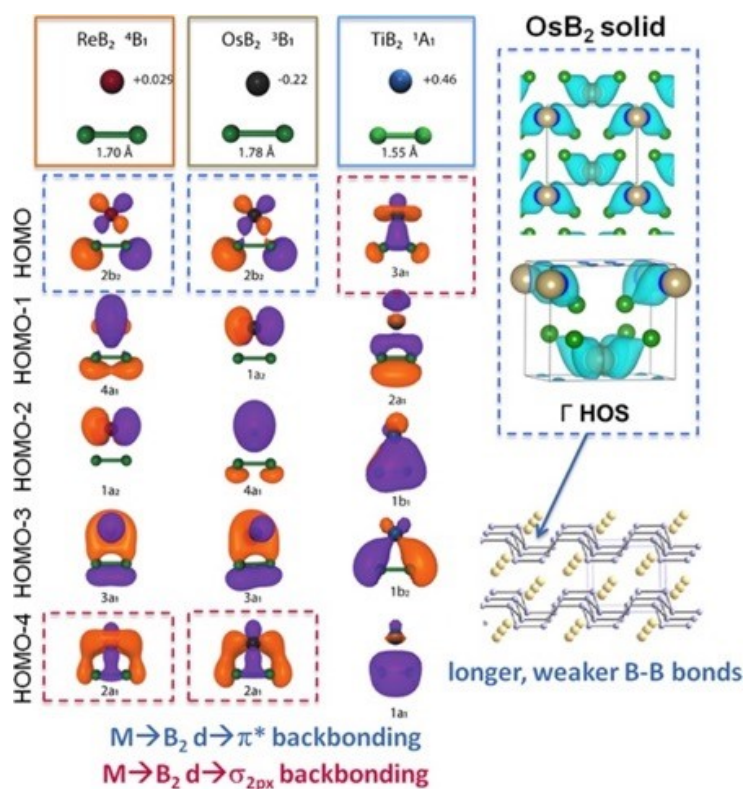


Figure III.3.1 Left: Kohn–Sham orbitals of ReB₂, OsB₂, and TiB₂, truncated set; NBO charges on atoms. The d \rightarrow σ_{2p_x} M \rightarrow B₂ backbonds are outlined in red, and d \rightarrow π^* in blue. Right: d \rightarrow π^* state occupied in solid OsB₂ (highest occupied at gamma, HOS), corresponding to the donation from Os to the activated and elongated B–B bonds.

while in TiB_2 it is the HOMO. In addition, Re and Os are capable of back-donation to the LUMO+1 (π^*) of B_2 , in the clusters' HOMOs. $d \rightarrow \pi^*$ is bonding between the metal and B_2 and B–B π -antibonding. Due to this MO, R(B–B) in ReB_2 and OsB_2 is elongated. Both back bonds are lower in energy in OsB_2 than in ReB_2 , and while this makes little difference for clusters, it will become profoundly important in the corresponding solids. Both types of back bonds are covalent in nature, as seen also from the partial charges on atoms (Figure 3). The ionic M- B_2 bonding component is the strongest in TiB_2 . Thus, clusters give us a simple representation of the fundamental M- B_2 interactions possible in the three systems.

In the bulk, the dangling valencies present in clusters are saturated, and so some cluster electronic states become unoccupied. The $d \rightarrow \sigma_{2px}$ HOMO in $\text{TiB}_2^{0/-}$ does not have an analogue among the valent states in the bulk TiB_2 . The material thus exhibits no covalent Ti–B interactions, and the only bonding present is ionic, as is also clear from the charge of +2 on Ti, corresponding to a typical d^2 configuration (Table 2). Furthermore, the +2 charge persists when Ti is substituted into the boat or chair structures. The TiB_2 structure type is also characteristic of other diborides including those of Mg, V, Cr, Mn, Sc, Zr, Nb, and Mo.⁽¹⁷⁾ The common electronic origin is the presence of a 2+ metal. M^{+2} means that the boron sublattice receives one electron per B. B^- is isoelectronic to neutral C, and the flat hexagonal boron sheet is therefore

isoelectronic and isostructural to graphene. In fact, it has many attributes of graphene, such as the Dirac points.(18)

Both ReB_2 and OsB_2 retain the $d \rightarrow \sigma_{2px}$ states in the bulk, in line with their low energies in the cluster models. These states strengthen both M–B and B–B bonding. However, the $d \rightarrow \pi^*$ state exists only in OsB_2 and specifically in the longer B–B

Table III.3.3 Bader Charges of Metals in Both Natural and Foreign Crystal Structures (optimized to the nearest stationary point)

	Os	Re	Ti
boat	<u>+0.04</u>	+0.44	+2.02
chair	+0.07	<u>+0.39</u>	+1.89
flat	+0.60	+0.93	<u>+1.98</u>

bonds within the asymmetric “boat” structure (Figure 3). Os has enough electrons to give only half of the B–B bonds a π^* character. Thus, the “boat” structure of OsB_2 is dictated by the antibonding M–B₂ interactions, which makes half of the B–B bonds longer and weaker, while in ReB_2 all B–B bonds are strengthened by M–B interactions. The M–B bonds are stronger in OsB_2 . Increased covalent character in Re and Os borides reflects in greatly reduced partial charges as compared to those in TiB_2 , particularly in the Os systems (Table 2). Hence we see the chemical bonding origin of

the structural differences of the three borides.

We further quantify the degree of covalency and relative bond strengths in the solids via the quantum theory of atoms in molecules (QTAIM) (Figure 4, Table 3), which analyzes the total rather than per-MO charge density.(19, 20) QTAIM detects the presence of critical points (CPs) in the charge density. In the “boat” configuration, there are three bond CPs, labeled i (M–B CP), ii (B–B CP), and iii (the second B–B CP). The “chair” structure has two distinct bond CPs, i and ii. The amount of charge at bond CPs correlates with bond strength.(21, 22)Both the “boat” and “chair” structures have stronger M–B bonds when containing Os rather than Re. Furthermore, while in general B–B bonds are stronger than M–B bonds, the B–B bonds in the OsB₂ systems are of comparable strength to the Os–B bonds in contrast to the more differentiated ReB₂ systems. Thus, the covalent character of Re/Os–B bonds is confirmed, and it is additionally seen that half of the B–B bonds in OsB₂ are weakened by the interaction with Os, with the charge density flowing from B–B to Os–B bonds.

As a confirmation of the QTAIM analysis, we employed the COHP method to directly measure the bond strengths between the different atoms (see Supporting Information). The integrated COHP values indicate that in ReB₂ Re–B bonds are much weaker than the corresponding B–B bonds, while in OsB₂ Os–B bonds are stronger than the

lengthened B–B bonds. This corroborates the QTAIM picture.

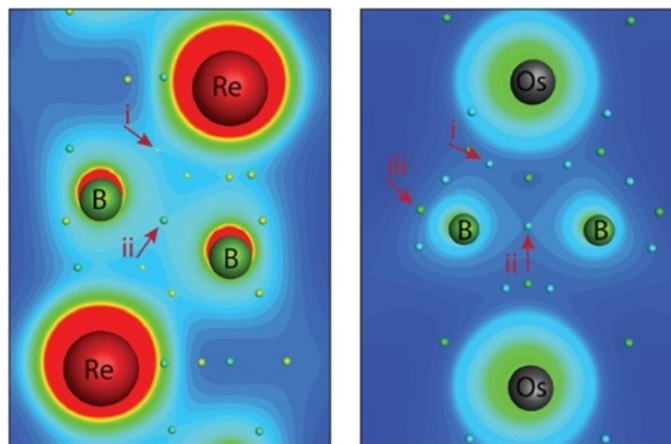


Figure III.3.1 Electron density plots of ReB_2 (left) and OsB_2 (right). QTAIM CPs are indicated: bond CPs, blue; ring CPs, green; cage CPs, yellow. i, M–B CP; ii and iii, B–B CPs.

Table III.3.4 Charge Densities (in e^-) at the Bond CPs for Both Re and Os in the Boat and Chair Structures

	i	ii	iii
ReB_2 boat	0.608	0.740	0.697
OsB_2 boat	0.656	0.732	0.618
ReB_2 chair	0.590	0.713	X
OsB_2 chair	0.629	0.668	X

There transpires a correlation between the relative strengths of the M–B and B–B bonding and the materials' hardness. In order to pin it down, we depart from the static bonding picture constructed at equilibrium. Hardness is a response to external force,

and the effect of pressure is comprised of the combination of two types of distortion: compression and shear. High incompressibility and shear modulus are both necessary but not alone sufficient for hardness.(5-10) We examine the materials' response to these two types of stimuli independently, again relying on the cluster models for clarity.

Because the π^* back bond is not present in the ReB_2 and TiB_2 solids, at this point, the clusters were charged +1 and +2, respectively, in order to unoccupy the $d \rightarrow \pi^*$ states. To mimic the effects of compression and shear stress, the B–B compression and M–B₂ shift were applied, and the clusters' responses were monitored (Figure 5).(23) Response to compression should primarily report on the strength of the B–B bonding, whereas that to shear should report on the M–B bonding. The force constants corresponding to the B₂ compression (Figure 5A) show bond stiffening in order of covalent to ionic character. TiB_2^{2+} has the stiffest B–B bond, because it is compact, and electrons confined to the smaller space resist the deformation, while the stable $d^2 \text{Ti}^{2+}$ is not willing to relieve the stress by taking electrons back. ReB_2^+ , with its $d \rightarrow \sigma_{2px}$ back bond, has a strengthened B–B bond and some charge flow toward M–B bonds allowing for the flexibility in charge distribution. Thus, B–B bonds are slightly less stiff than in TiB_2^{2+} . Being the most covalent, Os is the other extreme: the B–B bond activation by the $d \rightarrow \pi^*$ donation leads to charge redistribution toward the covalent Os–B bonds. The system is further capable of relieving the stress by shifting

electrons toward Os upon the B–B bond compression as if having a shock absorber both in the cluster and in every unit cell in the solid. This reduces the material’s stiffness upon compression.

The clusters’ ordering of resistance to shearing is exactly the opposite from that to compressing (Figure 5B). The M–B₂ bonding is the most covalent in OsB₂, intermediate in ReB₂⁺, and purely ionic in TiB₂²⁺. Hence, Ti in TiB₂²⁺ easily slides along B₂, ReB₂⁺ resists the slip more, and OsB₂ is the most resilient because the slip disrupts the strong Os–B bonds. OsB₂ has a force constant 5 times higher than that of TiB₂²⁺ for this mode of deformation. To bridge our understanding to the solids, we

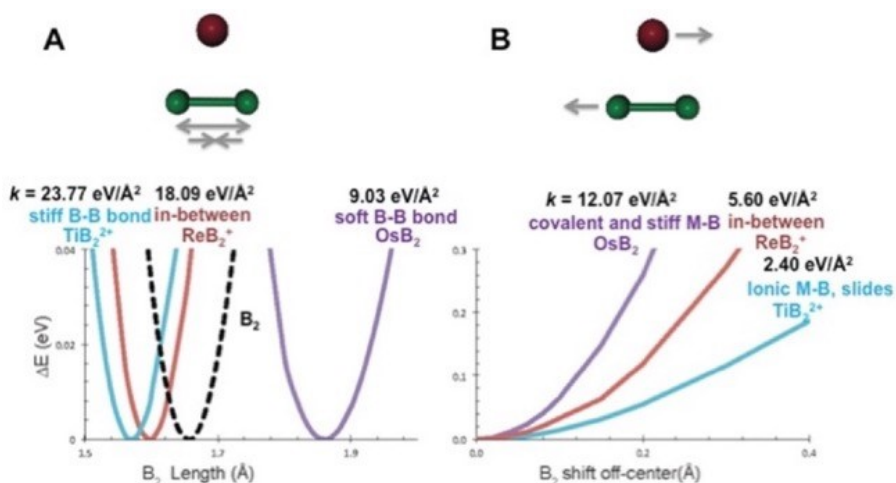


Figure III.3.1 (A) Energies of the clusters as a function of (A) compression along the B–B bond and (B) shear distortion coordinate. Cyan, TiB₂²⁺; red, ReB₂⁺; purple, OsB₂; dashed black, isolated B₂ for a reference.

examine stiffness tensors (Supporting Information Tables 7–11). Starting with

compression of the boron network (C_{11}), we see $\text{ReB}_2 \approx \text{TiB}_2 > \text{OsB}_2$. This shows the same distinction we had in the clusters: Re and Ti stiffen B the same amount, and Os weakens it. Shearing the metal against the B sheet shows $\text{ReB}_2 (C_{55}) > \text{TiB}_2(C_{44}) > \text{OsB}_2 (C_{66})$. This is not the same as the cluster model, but we must consider that there are other interactions in real distortions. The cluster model is Os bound to a long B_2 , but in the solid there are also shorter, more slippery B_2 bonds. Still, it should be hardest to shear on that long B_2 bond in $\text{OsB}_2 (C_{66})$, and that is the case ($C_{66} > C_{44} \gg C_{55}$). In TiB_2 the shear across the B layer is the easiest ($C_{44} < C_{66}$). Thus, we can explain slip-plane strength in solids.

Finally, we computed the geometries and shear moduli of Re and Os in both boat and chair configurations (Table 4). The consequence of more covalent Os–B bonding is a lengthening of the B_2 bonds in the chair structure. This, in turn, lowers the shear modulus. Similarly, Re added to the boat structure causes B_2 bonds to move toward uniformly short, losing the antibonding π^* character, and increasing in the shear modulus. Os in the chair structure is significantly harder than its boat counterpart. This results from forcing the B-lattice to be uniform—no B_2 bond becomes overly covalent, but all are weakened. The moduli thus have full support from the cluster bonding models.

Table 4. Calculated Properties of Re and Os in Both the Boat and Chair Structures.

	B ₂ -1 (Å)	B ₂ -2 (Å)	G (GPa)
OsB₂, boat	1.80	1.88	166
ReB₂, boat	1.84	1.81	244
OsB₂, chair	1.86	X	187
ReB₂, chair	1.82	X	276

^a G is the shear modulus. X indicates that the structure only has one B₂ bond length.

In conclusion, a metal that is too covalent with boron will lower the incompressibility, while a metal that is too ionic with boron will lower the shear strength. A “goldilocks metal” would be intermediate, i.e., having only the bonding $d \rightarrow \sigma_{2px}$ and no antibonding $d \rightarrow \pi^*$ B–M bonds. Re within the given family of diborides has just the right electron count to fulfill this requirement; as a result ReB₂ is the only ultrahard boride. This constitutes a new bonding model for ultrahard borides, which is based on promiscuous metal–boron bonding, previously unrecognized as one of the crucial aspects of superhard structures. The model reveals the origin of the structural differences in the TiB₂, ReB₂, and OsB₂ borides and explains their differences in hardness. Beyond the three borides, a chemical bonding based design principle for hard materials is a step toward designing novel materials that rival diamond’s hardness.

References

1. Chung, H. Y.; Weinberger, M. B.; Levine, J. B.; Kavner, A.; Yang, J. M.; Tolbert, S. H.; Kaner, R. B. Synthesis of Ultra-Incompressible Superhard Rhenium Diboride at Ambient Pressure *Science* 2007, 316, 436– 439

2. Cumberland, R. W.; Weinberger, M. B.; Gilman, J. J.; Clark, S. M.; Tolbert, S. H.; Kaner, R. B. Osmium Diboride, an Ultra-Incompressible, Hard Material *J. Am. Chem. Soc.* 2005, 127, 7264–7265
3. Kaner, R. B.; Gilman, J. J.; Tolbert, S. H. Designing Superhard Materials *Science* 2005, 308, 1268–1269
4. Lech, A. T.; Turner, C. L.; Mohammadi, R.; Tolbert, S. H.; Kaner, R. B. Structure Of Superhard Tungsten Tetraboride: A Missing Link Between MB_2 And MB_{12} Higher Borides *Proc. Natl. Acad. Sci. U. S. A.* 2015, 112, 3223–3228
5. Levine, J. B.; Tolbert, S. H.; Kaner, R. B. Advancements in the Search for Superhard Ultra-Incompressible Metal Borides *Adv. Funct. Mater.* 2009, 19, 3519–3533
6. Gilman, J. J.; Cumberland, R. W.; Kaner, R. B. Design of Hard Crystals *Int. J. Refract. Hard Met.* 2006, 24, 1–5
7. Brazhkin, V. V.; Lyapin, A. G.; Hemley, R. J. Harder Than Diamond: Dreams and Reality *Philos. Mag. A* 2002, 82, 231–253
8. Haines, J.; Léger, J. M.; Bocquillon, G. Synthesis and Design of Superhard Materials *Annu. Rev. Mater. Res.* 2001, 31, 1–23
9. Leger, J. M.; Djemia, P.; Ganot, F.; Haines, J.; Pereira, A. S.; da Jornada, J. A. H. Hardness and Elasticity in Cubic Ruthenium Dioxide *Appl. Phys. Lett.* 2001, 79, 2169–2171
10. Harrison, W. A. *Electronic Structure and the Properties of Solids*; Freeman: San Francisco, 1980.
11. Yeung, M. T.; Mohammadi, R.; Kaner, R. B. Ultraincompressible, Superhard Materials *Annu. Rev. Mater. Res.* 2016, 46, 465–485
12. Gu, Q.; Krauss, G.; Steurer, W. Transition Metal Borides: Superhard Versus Ultra-incompressible *Adv. Mater.* 2008, 20, 3620–3626
13. Munro, R. G. Material Properties of Titanium Diboride *J. Res. Natl. Inst. Stand. Technol.* 2000, 105, 709–720
14. Hoffmann, R. *Solids and surfaces: a chemist's view of bonding in extended structures*; VCH Publishers: 1988.
15. Hoffmann, R.; Zheng, C. Making and Breaking Bonds in the Solid State: The $ThCr_2Si_2$, Structure *J. Phys. Chem.* 1985, 89, 4175–4181
16. Robinson, P. J.; Zhang, X.; McQueen, T.; Bowen, K. H.; Alexandrova, A. N. SmB_6^- Cluster Anion: Covalency Involving f Orbitals *J. Phys. Chem. A* 2017, 121, 1849–1854
17. Akopov, G.; Yeung, M. T.; Kaner, R. B. Rediscovering the Crystal Chemistry of Borides *Adv. Mater.* 2017, 29, 1604506
18. Feng, X.; Yue, C.; Song, Z.; Wu, Q.; Wen, B. Topological Dirac Nodal-net Fermions in AlB_2 -type TiB_2 and ZrB_2 . *arXiv:1705.00511*, 2017.
19. Morgenstern, A.; Wilson, T.; Miorelli, J.; Jones, T.; Eberhart, M. E. In Search of an Intrinsic Chemical Bond *Comput. Theor. Chem.* 2015, 1053, 31–37
20. Bader, R. F. *Atoms in Molecules*; John Wiley & Sons: 1990.

21. Matta, C. F.; Boyd, R. J. *The Quantum Theory of Atoms in Molecules: From Solid State to DNA and Drug Design*; John Wiley & Sons: 2007.
22. Grabowski, S. J. Ab Initio Calculations on Conventional and Unconventional Hydrogen Bonds—Study of the Hydrogen Bond Strength *J. Phys. Chem. A* 2001, 105, 10739– 10746
23. Robinson, P. J.; Alexandrova, A. N. Assessing the Bonding Properties of Individual Molecular Orbitals *J. Phys. Chem. A* 2015, 119, 12862– 12867.

III.4 Spectroscopic Measurement of a Halogen Bond Energy

Xinxing Zhang, *Gaoxiang Liu*, Sandra Ciborowski, Wei Wang, Chu Gong, Yifan Yao,
Kit Bowen

*Key Laboratory of Advanced Energy Materials Chemistry (Ministry of Education),
Renewable Energy Conversion and Storage Center (ReCAST), College of Chemistry,
Nankai University*

Departments of Chemistry, Johns Hopkins University Baltimore, MD 21218 (USA)

Abstract

Halogen bonding (XB) has emerged as an important bonding motif in supramolecules and biological systems. Although regarded as a strong noncovalent interaction, benchmark measurements of the halogen bond energy are scarce. Here, a combined anion photoelectron spectroscopy and density functional theory (DFT) study of XB in solvated Br^- anions is reported. The XB strength between the positively-charged σ -hole on the Br atom of the bromotrichloromethane (CCl_3Br) molecule and the Br^- anion was found to be 0.63 eV (14.5 kcal mol⁻¹). In the neutral complexes, $\text{Br}(\text{CCl}_3\text{Br})_{1,2}$, the attraction between the free Br atom and the negatively charged equatorial belt on the Br atom of CCl_3Br , which is a second type of halogen bonding, was estimated to have interaction strengths of 0.15 eV (3.5 kcal mol⁻¹) and 0.12 eV (2.8 kcal mol⁻¹).

Even though they are generally regarded as electron withdrawing groups, already covalently-bonded halogen atoms can in addition interact attractively and directionally by a non-covalent bond to neighbor nucleophiles such as lone pairs and anions.¹⁻⁴ This noncovalent interaction was first referred to as “halogen bonding” (XB) by Dumas and co-workers in 1976.^{5,6} Halogen atoms have positive electrostatic potential regions on the opposite end of their σ bond due to polarizability; moreover, the equatorial sides of these atoms exhibit negative electrostatic potential belts.^{7,8} The positive facial site was termed as “ σ -hole” by Politzer et al. in 2007,⁹ although, clearly it is only a positive partial charge present at this site and no full electron is missing in any orbital. The size of the σ -hole depends on the polarizability of the halogen atom, that is, $I > Br > Cl > F$, but it can also be tuned by other highly electron-withdrawing functional groups in the molecule.² While the positively-charged σ -hole interacts with nucleophiles, the negatively-charged equatorial belt interacts with electrophiles, resulting in two categories of XB interactions.¹ XB has rapidly expanded into applications such as crystal engineering.¹⁰⁻¹⁴ It also has provoked the survey of biological structures, where XB has been found to stabilize inter- and intramolecular interactions that can further affect ligand binding, protein folding, and enzymatic reactions.¹⁵ While presence of XB interactions in the condensed-phase materials and biological chemistry is well known, experimental investigations of XB in the gas phase have been scarce. Nevertheless, techniques such as molecular beam

scattering,¹⁶ rotational spectroscopy,¹⁷⁻¹⁹ blackbody infrared radiative dissociation²⁰ and ion-mobility mass spectrometry have provided significant insight.²¹ More recently, our group reported the stabilization of otherwise unstable anions by XB using gas-phase anion photoelectron spectroscopy.²²

Theoretical calculations have also been widely used to investigate the nature and applications of XB.^{1-4, 23-28} Even though many levels of theory have estimated the strength of a long list of XBs to be in the range of 0.04–1.20 eV,²⁹ they have hardly been investigated experimentally. There is a dearth of experimental determinations of halogen bond strengths. Gas-phase measurements of isolated systems has unique advantages to provide XB strengths that are in undisturbed local environments. In the current paper, we present a gas-phase, mass spectrometric and photoelectron spectroscopic study of the archetypical Br⁻-bromotrichloromethane complexes. In CCl₃Br, the Br atom exhibits a significant σ -hole, making it a good XB donor. The bromine anion is necessary to act as a negatively-charged non-covalent binding partner and to be able to apply the anion photoelectron spectroscopy. We measured the photoelectron spectra of Br⁻(CCl₃Br)₀₋₂, and utilized density functional theory (DFT) calculations to compare with our experimental values, to visualize the XBs, and to provide thermodynamic rationales to understand the formation of these complexes.

Details of the experimental and theoretical methods are provided in the Supporting Information. The photoelectron spectra of Br^- and $\text{Br}^-(\text{CCl}_3\text{Br})$ taken with 266 nm (4.66 eV) laser and $\text{Br}^-(\text{CCl}_3\text{Br})_2$ taken with 193 nm (6.42 eV) laser are presented in Figure 1. The two peaks of Br^- at 3.37 eV and 3.82 eV correspond to the $^2\text{P}_{3/2}$ and $^2\text{P}_{1/2}$ spin-orbit states of the Br atom after photodetachment; these perfectly match reported values.³⁰ While their features are broadened, the anion photoelectron spectra of $\text{Br}^-(\text{CCl}_3\text{Br})_{1,2}$ resemble the pattern seen in the spectrum of Br^- . This is because the Br^- moiety acts as the chromophore for photodetachment in both cases. Thus, $\text{Br}^-(\text{CCl}_3\text{Br})_{1,2}$ are “solvated” anions, where Br^- is “solvated” by one and two CCl_3Br molecules, respectively. The electron binding energies (EBE) of the observed spectra reflect the stabilization of the Br^- moiety's excess electron due to the solvation by CCl_3Br molecule(s). Their spectral broadening is likely due to vibrational motions that perturb the Br^- moiety. The persistence of the Br^- spectral pattern in the spectra of $\text{Br}^-(\text{CCl}_3\text{Br})_1$ and $\text{Br}^-(\text{CCl}_3\text{Br})_2$, even though the $^2\text{P}_{1/2}$ peak in the latter case is obscured by noise, implies good Franck–Condon overlap between the ground state of the anion and the ground state of the neutral. Ideally in such cases, the EBE threshold would provide the electron affinity (EA). Source conditions, however, often give rise to some degree of vibrational hot band intensity on the lowest EBE side of the origin peak. To account for this effect and thus to determine the EA

value, we extrapolated the leading edge of the low EBE side of the peaks to zero intensity. These EBE values are 3.87 eV and 4.22 eV, and we report them as the experimentally-determined EA values of $\text{Br}(\text{CCl}_3\text{Br})_{1,2}$, respectively. The EBE values of the intensity maxima in the main and lowest EBE peaks in these spectra correspond to their vertical detachment energies (VDE). Vertical detachment energies reflect the maximal Franck–Condon overlap between the anion and its neutral counterpart during photodetachment. The peak positions at $\text{EBE}=4.21$ eV and 4.71 eV are the experimentally-determined vertical detachment energies (VDE) of $\text{Br}^-(\text{CCl}_3\text{Br})_1$ and $\text{Br}^-(\text{CCl}_3\text{Br})_2$, respectively. As shown in Figure 1, the EA shifts between adjacent photoelectron spectra are 0.50 eV and 0.35 eV, respectively. These values are closely-related to the XB strength (see below). Table 1 presents both experimental and theoretical EA and VDE values for these systems. A high degree of consistency is seen there.

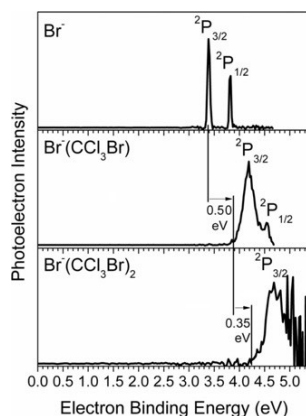


Figure III.4.1 The photoelectron spectra of Br^- and $\text{Br}^-(\text{CCl}_3\text{Br})$ taken with 266 nm (4.66 eV) photons and $\text{Br}^-(\text{CCl}_3\text{Br})_2$ taken with 193 nm (6.42 eV) photons.

Table 1. Experimental and theoretical EA values of $\text{Br}(\text{CCl}_3\text{Br})_{0-2}$ and VDE values of $\text{Br}^-(\text{CCl}_3\text{Br})_{1,2}$. All values are in eV.

	EA [Expt./Theo.]	VDE [Expt./Theo.]
$\text{Br}^{0/-}$	3.37/3.45	-
$\text{Br}^{0/-}(\text{CCl}_3\text{Br})$	3.87/3.93	4.21/4.28
$\text{Br}^{0/-}(\text{CCl}_3\text{Br})_2$	4.22/4.24	4.71/4.78

The calculated structures of $\text{Br}^{0/-}(\text{CCl}_3\text{Br})_{1,2}$ and their highest occupied molecular orbitals (HOMO) are presented in Figure 2, and the 3D coordinates of all calculated species are presented in the Supporting Information. $\text{Br}^-(\text{CCl}_3\text{Br})$ possesses a C_{3v} symmetry, where the Br atom in CCl_3Br and the Br^- kernel form a XB. Given this calculated structure, we write this complex as $\text{Cl}_3\text{CBr}-\text{Br}^-$. The XB length in $\text{Cl}_3\text{CBr}-\text{Br}^-$ is 2.90 Å, an indicator of a noncovalent bond. The HOMO of $\text{Cl}_3\text{CBr}-\text{Br}^-$, from which the photoelectron is detached, is mostly the *p*orbital of the Br^- kernel, consistent with the observed spectrum and its Br^- chromophore. For $\text{Br}^-(\text{CCl}_3\text{Br})_2$, with a C_1 symmetry, the Br^- kernel is equally shared by two 3.03 Å long XB's. Likewise, we write $\text{Br}^-(\text{CCl}_3\text{Br})_2$ as $\text{Cl}_3\text{CBr}-\text{Br}^--\text{BrCCl}_3$. Since the negative charge on Br^- is shared by two CCl_3Br molecules, the electrostatic attraction is weakened compared to that in $\text{Cl}_3\text{CBr}-\text{Br}^-$, resulting in longer XB bonds. The HOMO of $\text{Cl}_3\text{CBr}-\text{Br}^--\text{BrCCl}_3$ also shows a *p*orbital of Br^- . Interestingly, the two XBs exhibit a bond

angle of 144.8° , even though intuitively they should be linear (see below). The neutral complexes exhibit very different structures. Compared to nucleophilic Br^- , a free Br atom is highly in need of one electron to fulfill the octet rule. Hence, being electrophilic in nature, the Br atom cannot form a conventional XB with the σ -hole, but tends instead to interact with the negatively-charged equatorial belt of Br and Cl atoms in CCl_3Br , forming the second type of XB. $\text{Br}(\text{CCl}_3\text{Br})$ has a C_s symmetry, and $\text{Br}(\text{CCl}_3\text{Br})_2$ has a C_i symmetry. According to these structures, we write the neutrals as $\text{ClCCl}_2\text{Br}-\text{Br}$ and $\text{ClCCl}_2\text{Br}-\text{Br}-\text{BrCl}_2\text{CCl}$. The XB lengths in the neutrals are longer than those in the anions, implying that the binding energy is weaker in the neutrals than in the anions. The HOMO's of $\text{ClCCl}_2\text{Br}-\text{Br}$ and $\text{ClCCl}_2\text{Br}-\text{Br}-\text{BrCl}_2\text{CCl}$ clearly show the interaction between the p orbital of the free Br atom and the p orbital of the covalently bonded Br atom.

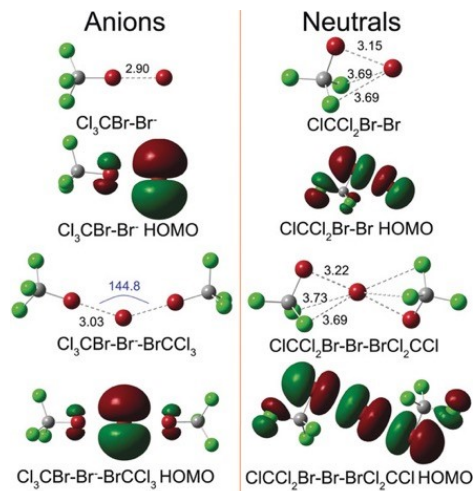


Figure III.4.2 Calculated geometries and highest occupied molecular orbitals (HOMO) of $\text{Br}^{0/-}(\text{CCl}_3\text{Br})_{1,2}$.

Natural population analysis (NPA) provides another perspective for understanding the solvation of the Br^- anion by BrCCl_3 molecule(s) via XB. The negative charge on the Br^- kernel is $-0.80 e$ for $\text{Cl}_3\text{CBr}-\text{Br}^-$ and $-0.77 e$ for $\text{Cl}_3\text{CBr}-\text{Br}^--\text{BrCCl}_3$. Hence, a single XB interaction lowers the electron density on Br^- by $-0.20 e$, while two XB interactions further lower the charge by $-0.03 e$.

In order to better visualize XB, Figure 3 shows the electrostatic potential (ESP) surfaces of the anions, $\text{Cl}_3\text{CBr}-\text{Br}^-$, $\text{Cl}_3\text{CBr}-\text{Br}^--\text{BrCCl}_3$ (left) and the neutrals, CCl_3Br , $\text{ClCCl}_2\text{Br}-\text{Br}$ and $\text{ClCCl}_2\text{Br}-\text{Br}-\text{BrCl}_2\text{CCl}$ (right). The induced positive (blue) and negative (red) electrostatic potentials are mapped on the $0.04 e/\text{bohr}^3$ surfaces. In order to better visualize potential differences between spatial regions, the potentials ranging from $-25 \text{ kcal mol}^{-1}$ to $+50 \text{ kcal mol}^{-1}$ are presented for the anions, and potentials from $-10 \text{ kcal mol}^{-1}$ to $+150 \text{ kcal mol}^{-1}$ are presented for the neutrals. For the anionic $\text{Cl}_3\text{CBr}-\text{Br}^-$ and $\text{Cl}_3\text{CBr}-\text{Br}^--\text{BrCCl}_3$, the XB between the σ -hole on the covalently-bonded Br atom (blue) and Br^- (red) can be clearly observed. On the equator of covalently-bonded Br and Cl atoms, there are negatively charged belts (red and yellow). To explore the $144.8^\circ \angle \text{BrBrBr}$ bond angle in $\text{Cl}_3\text{CBr}-\text{Br}^--\text{BrCCl}_3$, we mapped the ESP of $\text{Cl}_3\text{CBr}-\text{Br}^-$ on a different scale and from the axial perspective (lower left in Figure 3), where a less negatively-charged hole (yellow) on the non-XB side of Br^- is observed. The XB between Cl_3CBr and Br^- draws the negative charge

on Br^- toward the XB, resulting in a less negatively-charged hole on the other side of Br^- . We tentatively refer to this electrostatic hole as the “halogen bond-hole” (XB-hole). In order to obtain the optimal electrostatic interaction, the XB formed with a second CCl_3Br avoids direct contact with this XB-hole, resulting in a $\angle\text{BrBrBr}$ bond angle of 144.8° in $\text{Cl}_3\text{CBr}-\text{Br}^--\text{BrCCl}_3$. In neutral CCl_3Br (top right in Figure 3), even though all the Cl and Br atoms exhibit σ -holes, due to its lower electronegativity and higher polarizability, the σ -hole on Br is larger than that on Cl, thus supporting the XB between Br and Br^- but not between Cl and Br^- . The evidence presented above overwhelmingly implies that the interactions between the Br^- anion and the CCl_3Br molecule(s) in the $\text{Br}^-(\text{CCl}_3\text{Br})_{1,2}$ anion complexes are dominated by halogen bonding. While electrostatic ion-dipole interactions no doubt contribute, they are expected to be minor by comparison, given the calculated small dipole moment of the CCl_3Br molecule (0.046 D).

For neutral $\text{ClCCl}_2\text{Br}-\text{Br}$ and $\text{ClCCl}_2\text{Br}-\text{Br}-\text{BrCl}_2\text{CCl}$, the second type of halogen binding is observed, i.e., the interaction between the free electrophilic Br atom (see its blue region) and the negatively-charged equatorial belt of the covalently-bonded Br (reddish-yellow).

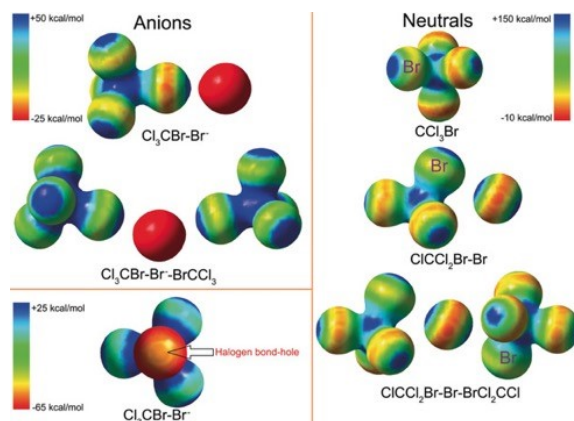


Figure III.4.3 Electrostatic potential (ESP) surfaces for the anionic $\text{Cl}_3\text{CBr-Br}^-$, $\text{Cl}_3\text{CBr-Br}^- \cdot \text{BrCCl}_3$ (left) and neutral CCl_3Br , $\text{ClCCl}_2\text{Br-Br}$ and $\text{ClCCl}_2\text{Br-Br-BrCl}_2\text{CCl}$ (right). The induced positive (blue), negative (red) potentials are mapped on the $0.04 e/\text{bohr}^3$ surfaces of the molecules.

Next, we discuss the XB strengths. The strength of the first and second XB of the neutral and anionic complexes, $D_0[\text{Br}^{0/-}(\text{CCl}_3\text{Br})_{1,2}]$, are calculated by

$$D_0[\text{Br}^{0/-}(\text{CCl}_3\text{Br})] = E[\text{Br}^{0/-}] + E[\text{CCl}_3\text{Br}] - E[\text{Br}^{0/-}(\text{CCl}_3\text{Br})]$$

and

$$D_0[\text{Br}^{0/-}(\text{CCl}_3\text{Br})_2] = E[\text{Br}^{0/-}(\text{CCl}_3\text{Br})] + E[\text{CCl}_3\text{Br}] - E[\text{Br}^{0/-}(\text{CCl}_3\text{Br})_2],$$

where E refers to the calculated absolute energy of species with zero-point energy corrected. Our calculations found $D_0[\text{Br}^0(\text{CCl}_3\text{Br})]=0.15$ eV, $D_0[\text{Br}^-(\text{CCl}_3\text{Br})]=0.63$ eV, $D_0[\text{Br}^0(\text{CCl}_3\text{Br})_2]=0.12$ eV and $D_0[\text{Br}^-(\text{CCl}_3\text{Br})_2]=0.43$ eV. The binding energies of the anions are higher than those of the neutrals, consistent with bond length differences between the anionic and neutral complexes. Further,

$$D_0[\text{Br}^-(\text{CCl}_3\text{Br})] - D_0[\text{Br}^0(\text{CCl}_3\text{Br})] = (E[\text{Br}^0(\text{CCl}_3\text{Br})] - E[\text{Br}^-(\text{CCl}_3\text{Br})]) - (E[\text{Br}^0] - E[\text{Br}^-]) = \text{EA}[\text{Br}^0(\text{CCl}_3\text{Br})] - \text{EA}[\text{Br}^0]$$

and

$$\begin{aligned} D_0[\text{Br}^-(\text{CCl}_3\text{Br})_2] - D_0[\text{Br}^0(\text{CCl}_3\text{Br})_2] &= (E[\text{Br}^0(\text{CCl}_3\text{Br})_2] \\ &- E[\text{Br}^-(\text{CCl}_3\text{Br})_2]) - (E[\text{Br}^0(\text{CCl}_3\text{Br})] \\ &- E[\text{Br}^-(\text{CCl}_3\text{Br})]) = \text{EA}[\text{Br}^0(\text{CCl}_3\text{Br})_2] - \text{EA}[\text{Br}^0(\text{CCl}_3\text{Br})], \end{aligned}$$

where EA denotes the electron affinity. Equations (3) and (4) show that the differences between the EAs of Br and Br(CCl₃Br), and between the EAs of Br(CCl₃Br) and Br(CCl₃Br)₂ are equal to the binding energy differences between the anions and their neutral counterparts. In our photoelectron spectra (Figure 1), the EA shifts between adjacent size anionic species are 0.50 eV and 0.35 eV, respectively, in excellent agreement with the calculated binding energy differences, 0.48 eV and 0.31 eV.

The Gibbs free energy ΔG , that is, $\Delta G = \Delta H - T\Delta S$, has to be negative for a XB to form. The enthalpy change, ΔH , is negative, yet due to entropy decrease (loss of rotational and translational degrees of freedom) upon forming a XB, the $T\Delta S$ term often has a large negative value.¹ For this reason, low temperatures are often required in order to form a XB in an isolated (gas-phase) environment. To better understand the formation of these complexes, the appropriate thermodynamic values computed at room temperature are tabulated in the first four columns of Table 2. The formation of the anions is more exothermic than the formation of the neutrals. At room temperature, only Br⁻(CCl₃Br) has a negative ΔG . The temperatures below which ΔG remains negative, T*, are also tabulated in Table 2. For Br⁻(CCl₃Br), ΔG is negative until the temperature reaches 688 K, this being largely due to the large enthalpy change despite

the entropy loss. Thus, the formation of $\text{Br}^-(\text{CCl}_3\text{Br})$ is favorable at temperatures below 688 K. The formation of $\text{Br}^-(\text{CCl}_3\text{Br})_2$, on the other hand, cannot occur above 289 K. Likewise, the neutral molecules, $\text{Br}(\text{CCl}_3\text{Br})_{1,2}$ can only be formed under 140 K and 50 K, respectively. Since supersonic expansions can form complexes with temperatures of several tens of degrees Kelvin,^{31,32} the formation of all these species is thermodynamically allowed under the experimental conditions that obtained in these experiments.

Table 2. Computed thermodynamic values (kcal mol^{-1}) for gas-phase XB complex formation. The maximum temperature (T^*) at which each reaction to occur is also listed in units of K.

Reactions	ΔE^0	ΔH^0	$T\Delta S^0$	ΔG^0	T^*
$\text{Br} + \text{CCl}_3\text{Br} \rightarrow \text{Br}(\text{CCl}_3\text{Br})$	-2.9	-3.5	-6.9	3.4	140
$\text{Br}^- + \text{CCl}_3\text{Br} \rightarrow \text{Br}^-(\text{CCl}_3\text{Br})$	-3.9	-4.5	-6.6	-7.9	688
$\text{Br}(\text{CCl}_3\text{Br}) + \text{CCl}_3\text{Br} \rightarrow \text{Br}(\text{CCl}_3\text{Br})_2$	-1.3	-1.9	-8.2	6.3	50
$\text{Br}^-(\text{CCl}_3\text{Br}) + \text{CCl}_3\text{Br} \rightarrow \text{Br}^-(\text{CCl}_3\text{Br})_2$	-8.4	-9.0	-9.3	0.3	289

To conclude, combined results from anion photoelectron spectroscopy and DFT calculations have shown the interaction between the Br^- anion and the CCl_3Br molecule(s) to be dominated by halogen bonding, XB. The halogen bonding

interaction energy between Br^- and CCl_3Br in $\text{Br}^-(\text{CCl}_3\text{Br})$ was determined to be 0.63 eV, thus providing a benchmark for the further exploration of halogen bonding in other systems.

References

1. P. Politzer, J. S. Murray, T. Clark, *Phys. Chem. Chem. Phys.* 2013, **15**, 11178– 11189.
2. P. Politzer, P. Lane, M. C. Concha, Y. Ma, J. S. Murray, *J. Mol. Model.* 2007, **13**, 305– 311.
3. G. Cavallo, P. Metrangolo, R. Milani, T. Pilati, A. Priimagi, G. Resnati, G. Terraneo, *Chem. Rev.* 2016, **116**, 2478– 2601.
4. M. H. Kolář, P. Hobza, *Chem. Rev.* 2016, **116**, 5155– 5187.
5. J.-M. Dumas, M. Kern, J. L. Janier-Dubry, *Bull. Soc. Chim. Fr.* 1976, 1785– 1787.
6. J.-M. Dums, H. Peurichard, M. J. Gomel, *J. Chem. Res. Synop.* 1978, 54– 57.
7. T. Brinck, J. S. Murray, P. Politzer, *Int. J. Quantum Chem.* 1992, **44**, 57– 64.
8. T. Brinck, J. S. Murray, P. Politzer, *Int. J. Quantum Chem.* 1993, **48**, 73– 88.
9. T. Clark, M. Hennemann, J. S. Murray, P. Politzer, *J. Mol. Model.* 2007, **13**, 291– 296.
10. B. Li, S. Q. Zang, L. Y. Wang, T. C. Mak, *Coord. Chem. Rev.* 2016, **308**, 1– 21.
11. R. Bertani, P. Sgarbossa, A. Venzo, F. Lelj, M. Amati, G. Resnati, T. Pilati, P. Metrangolo, G. Terraneo, *Coord. Chem. Rev.* 2010, **254**, 677– 695.
12. V. Amico, S. V. Meille, E. Corradi, M. T. Messina, G. Resnati, *J. Am. Chem. Soc.* 1998, **120**, 8261– 8262.
13. P. Metrangolo, F. Meyer, T. Pilati, G. Resnati, G. Terraneo, *Angew. Chem. Int. Ed.* 2008, **47**, 6114– 6127; *Angew. Chem.* 2008, **120**, 6206– 6220.
14. L. C. Gilday, S. W. Robinson, T. A. Barendt, M. J. Langton, B. R. Mullaney, P. D. Beer, *Chem. Rev.* 2015, **115**, 7118– 7195.
15. M. R. Scholfield, C. M. V. Zanden, M. Carter, P. S. Ho, *Protein Sci.* 2013, **22**, 139– 152.
16. D. Cappelletti, P. Candori, F. Pirani, L. Belpassi, F. Tarantelli, *Cryst. Growth Des.* 2011, **11**, 4279– 4283.
17. S. L. Stephens, N. R. Walker, A. C. Legon, *J. Chem. Phys.* 2011, **135**, 224309.
18. H. I. Bloemink, J. H. Holloway, A. C. Legon, *Chem. Phys. Lett.* 1996, **254**, 59– 68.
19. C. Domene, P. W. Fowler, A. C. Legon, *Chem. Phys. Lett.* 1999, **309**, 463– 470.
20. E. A. Gillis, M. Demireva, M. G. Sarwar, M. G. Chudzinski, M. S. Taylor, E. R. Williams, T. D. Fridgen, *Phys. Chem. Chem. Phys.* 2013, **15**, 7638– 7647.
21. A. C. Pearcy, K. A. Mason, M. S. El-Shall, *J. Phys. Chem. A* 2019, **123**, 1363– 1371.
21. X. Zhang, G. Liu, S. Ciborowski, K. Bowen, *Angew. Chem. Int. Ed.* 2017, **56**, 9897– 9900; *Angew. Chem.* 2017, **129**, 10029– 10032.

22. M. Jabłoński, M. Palusiak, *J. Phys. Chem. A* 2012, **116**, 2322– 2332.
23. Y. X. Lu, J. W. Zou, Y. H. Wang, Y. J. Jiang, Q. S. Yu, *J. Phys. Chem. A* 2007, **111**, 10781– 10788.
24. S. H. Jungbauer, S. Schindler, E. Herdtweck, S. Keller, S. M. Huber, *Chem. Eur. J.* 2015, **21**, 13625– 13636.
25. R. Li, Q. Li, J. Cheng, Z. Liu, W. Li, *ChemPhysChem* 2011, **12**, 2289– 2295.
26. A. Bauzá, I. Alkorta, A. Frontera, J. Elguero, *J. Chem. Theory Comput.* 2013, **9**, 5201– 5210.
27. P. Politzer, J. S. Murray, *CrystEngComm* 2013, **15**, 3145– 3150.
28. P. Politzer, J. S. Murray, *ChemPhysChem* 2013, **14**, 278– 294.
29. C. E. Moore, *Natl. Stand. Ref. Data Ser.* (U.S. Natl. Bur. Stand.) **1971**, *NSRDS-NBS 35*, 208.
30. A. Ding, J. Hesslich, *Chem. Phys. Lett.* 1983, **94**, 54– 57.
31. A. T. Droege, P. C. Engelking, *Chem. Phys. Lett.* 1983, **96**, 316– 318.

III.5 Realization of Lewis Basic Sodium Anion in the NaBH_3^- Cluster

Gaoxiang Liu, Nikita Fedik, Chalynette Martinez-Martinez, Sandra M. Ciborowski,

Xinxing Zhang, Alexander I. Boldyrev, Kit H. Bowen

Department of Chemistry, Johns Hopkins University Baltimore, MD 21218 (USA)

Department of Chemistry and Biochemistry Utah State University

Key Laboratory of Advanced Energy Materials Chemistry (Ministry of Education),

Renewable Energy Conversion and Storage Center (ReCAST), College of Chemistry,

Nankai University

Abstract

We report a $\text{Na}^- \rightarrow \text{B}$ dative bond in the NaBH_3^- cluster, which was designed on the principle of minimum-energy rupture, prepared by laser vaporization, and characterized by a synergy of anion photoelectron spectroscopy and electronic structure calculations. The global minimum of NaBH_3^- features a Na–B bond. Its preferred heterolytic dissociation conforms with the IUPAC definition of dative bond. The lone electron pair revealed on Na and the negative Laplacian of electron density at the bond critical point further confirm the dative nature of the Na–B bond. This study represents the first example of a Lewis adduct with an alkali as the Lewis base.

Metals normally act as Lewis acids (LA), given the prevalence of metal-ligand compounds in which the empty orbitals of the Lewis acidic metals accept pairs of electrons from Lewis basic ligands. Intriguingly, some transition metals can conversely provide their lone electron pairs and form directional dative bonds to electron deficient molecules, that is, act as Lewis bases. The concept of metal Lewis basicity was recognized by Shriver,¹ and developed as a synthetic methodology by Vaska, Werner, and others.² Later structural assignments, however, casted doubt on these complexes with negative results on metal-LA interaction.³ It was not until 1999 that the first structural confirmation of a M→B dative bond was reported.⁴ Then, metal Lewis basicity has seen a prosper of research activity, and numerous novel Lewis pairs have been prepared featuring the interaction between Lewis basic transition metals and Lewis acidic ligands.⁵ Compared to classic metal–ligand bond, this weak yet electronically reverse metal→LA interaction holds the promise for a novel type of metal–ligand cooperativity in catalytic reactions,⁶ and open doors to many applications involving H₂ storage and activation, olefin hydrogenation, CO₂ fixation, etc.⁷⁻¹⁶

The metal Lewis basicity, however, has only been demonstrated for transition metals.⁵ Main group metals have only shown Lewis acidity.^{5c} Intuitively, among all

main group metals, alkali metals are the least appropriate candidates for Lewis base. The lack of an electron pair requires them to form the extremely reducing alkalides (alkali metal anions) before forming dative bonds with LA. While alkalides have been found in a handful of examples, their interaction with the surroundings is ionic.¹⁷

Within this context, we aimed to design an unusual Lewis acid/base adduct in which the Lewis base is an alkalide. Two requirements are to be fulfilled: the alkalide needs to form a direct chemical bond with the LA, and this bond needs to be dative, i.e., the electron pair needs to derive from the alkalide. The latter requirement is better interpreted using the minimum-energy rupture principle,¹⁸ which is adapted by IUPAC as the standard for differentiating dative bond from covalent or ionic bond.¹⁹ Specifically, this principle analyses the energies of the homolytic and heterolytic bond breakage in the gas phase: if homolytic bond rupture requires less energy, the bond is considered covalent or ionic; if heterolytic bond rupture is energetically favored, the bond is considered dative. This implies a strategy for designing the alkalide→LA Lewis adduct: choose a weak LA whose electron affinity is much lower than alkali, and prepare an anionic alkali-LA complex where the alkali moiety forms a direct chemical bond with the LA moiety, i.e., (alkali-LA)⁻. Such (alkali-LA)⁻ complex would prefer a heterolytic bond rupture into alkalide and LA, fulfilling the above-mentioned requirements for being a Lewis adduct with an alkalide

as the base. The choice of LA is thus critical. Being electron deficient in nature, some LA have surprisingly low EA. For example, the EA of the prototype LA, BH_3 , is only 0.038 eV,²⁰ which is much lower than the EA of all alkali metals. Here, we show that the designer $(\text{Na-BH}_3)^-$ cluster possesses a unique $\text{Na}^- \rightarrow \text{BH}_3$ dative bond, representing the first observation of a Lewis pair in which the base is an alkali.

The $(\text{Na-BH}_3)^-$ was generated with a laser vaporization source by focusing an intense beam of Nd:YAG laser (532 nm, 60 mJ) onto a NaBH_4 coated rod. The laser caused dissociation of the B-H bond in NaBH_4 . The resulting mass spectrum is presented in Figure 1 A, along with the expected isotopic mass distribution of $(\text{Na-BH}_3)^-$ in its top panel. The overall agreement between the experimental and expected mass patterns verifies the existence of $(\text{Na-BH}_3)^-$. Dissociation of multiple B-H bonds is possible during the laser vaporization of borohydride.²¹ Thus, the small mass peak at 35 amu suggests the formation of NaBH_2^- via the breakage of two B-H bonds. The peak at 37 amu was selected for anion photoelectron spectroscopic study as it was solely comprised of $(\text{Na-BH}_3)^-$.

Anion photoelectron spectroscopy can interpret the bonding picture of $(\text{Na-BH}_3)^-$ via directly probing the electronic structure and intramolecular interaction.²² The photoelectron spectrum of $(\text{Na-BH}_3)^-$ (Figure 1 B) exhibits two fairly sharp

transitions peaked at electron binding energies (EBE) of 0.87 and 2.74 eV. The two EBE values are assigned as the vertical detachment energies (VDE), respectively corresponding to transitions with maximized Franck-Condon overlaps from the

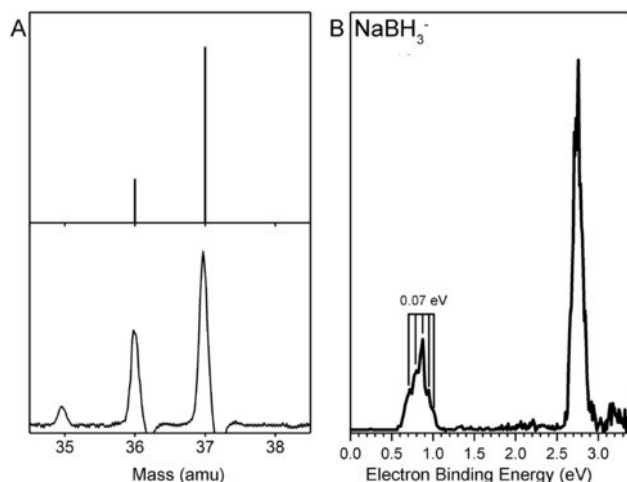


Figure 1 A) The expected (top panel) and experimental (bottom panel) mass spectra of $(\text{Na}-\text{BH}_3)^-$, and B) the anion photoelectron spectrum of NaBH_3^- taken with 355 nm (3.496 eV) photons.

ground state of anion, to the ground and to the first excited electronic state of neutral. Potentially, the Na moiety could exist in three different structures: (i) Na forms chemical bonds with multiple B and H atoms, (ii) Na^- weakly interacts with the H atoms in BH_3 molecule, that is, physically “solvated” by BH_3 , resulting in $\text{Na}^-(\text{BH}_3)$, and (iii) Na^- directly interacts with the electron-deficient B atom, forming a $[\text{Na}^-(\text{BH}_3)]$ complex. Only structure (iii) holds the promise for a Lewis adduct. The photoelectron spectrum of NaBH_3^- resembles that of Na^- ,²³ suggesting the existence

of a Na^- moiety in NaBH_3^- as the chromophore for photodetachment. Though the spectrum appears to be a shift of the Na^- spectrum to higher EBE, which is a common fingerprint of physical solvation effect,^{24, 25} two spectral features strongly suggest the formation of chemical bond between the Na^- and BH_3 moieties: a) the spacing between the two peaks, 1.87 eV, is smaller than the expected spacing for solvation complex, 2.10 eV (the Na D-line), implying a change in electronic structure induced by chemical interaction; b) the observed vibrational progression spaced at ≈ 0.07 eV in the lower EBE peak is not a characteristic frequency of BH_3 ; thus, this progression is likely due to a Na–B vibrational mode, implying the formation of a Na–B chemical bond.

Isolated and well-defined gas-phase systems are ideally suited for simulations employing state-of-the-art quantum theoretical methods. To find the most thermodynamically stable structure of $(\text{Na–BH}_3)^-$, which was expected to be the main contributor of the photoelectron spectrum, we performed an unbiased GM search of 5000 randomly generated structures on both singlet and triplet potential energy surfaces. All the geometries were initially optimized using DFT-level PBE0/6–31+G*.²⁶ The low-lying singlet and triplet structures were subsequently reoptimized with CCSD(T)/aug-cc-pVTZ.²⁷ Then single-point energy calculations were performed using CCSD(T)/aug-cc-pCVQZ accounting for full electron

correlation.²⁸ Structures were then ranked based on their relative energies. The GM of NaBH_3^- exhibits a C_{3v} structure, features a Na–B bond of 2.72 Å between Na and the slightly distorted BH_3 , and has a singlet electronic configuration of $1a_1^2 1e_1^4 2a_1^2$.

The B–H–B \angle is 119.4°, while the overall distortion measured as the \angle between $\text{H}_1\text{–H}_2\text{–H}_3$ plane and B atom is 8.7°. The most stable triplet structure has a C_s symmetry with a $1a'^2 1a''^2 3a'^2 4a'^1 5a'^1$ electronic configuration, and is less stable than the GM by 5.9 kcal mol⁻¹ (Figure 2).

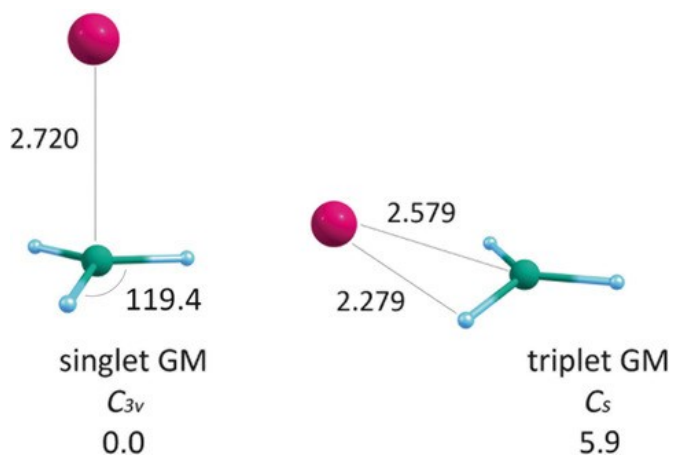


Figure 2 The lowest energy singlet and triplet structures of $(\text{Na-BH}_3)^-$. No other structures were found within 20 kcal mol⁻¹. Bond lengths are given in Å. Point groups are given in italic. Bottom values refer to the relative energy including ZPE correction at CCSD(T)/aug-cc-pCVQZ level.

Though being a simple cluster, pronounced multireference character in $(\text{Na-BH}_3)^-$ is revealed by CASSCF(8,14)/aug-cc-pwCVQZ.²⁹ To verify that the calculated GM of

(Na–BH₃)[−] describes the experimental spectrum, the VDEs were computed at the coupled cluster and CASSCF levels of theory. As shown in Table 1, for the singlet GM, the calculated VDEs are in excellent agreement with the experimental VDEs, validating the calculations for accurately describing the energetics of this system. An A1 symmetric umbrella inversion with a frequency of 0.078 eV (629 cm^{−1}) is also revealed (Supporting Information, Table S1), which is in accordance with the vibrational progression observed in the photoelectron spectrum. For the triplet (Na–BH₃)[−], however, while its 1st calculated VDE matches the experiment, the absence of the 2nd one in experimental spectrum makes its existence unlikely. This thus confirms the singlet GM structure of (Na–BH₃)[−], which possesses a Na–B chemical bond, as the major species observed in experiment.

Table 1. Experimental and calculated VDEs for lowest-energy singlet and triplet (Na–BH₃)[−] at different levels of theory. For all calculations aug-cc-pCVQZ basis set was used.

Anion state ∇	Neutral configuration	VDE [eV]		
		EXPT.	CC ^[a]	CAS(8,14)NEVPT2
Singlet GM	1a ₁ ² 1e ₁ ⁴ 2a ₁ ¹ 3a ₁ ⁰	0.87	0.88	0.81
	1a ₁ ² 1e ₁ ⁴ 2a ₁ ⁰ 3a ₁ ¹	2.74	2.64	– ^[b]
Triplet	1a ² 1a ² 3a ² 4a ¹ 5a ⁰	0.87	0.79	–
	1a ² 1a ² 3a ² 4a ¹ 5a ¹	2.74	1.54	–

[a] CC stands for coupled-cluster theory. For the first VDEs CCSD(T) method was used while the second ones were calculated with EOM-CCSD.³⁰ [b] This VDE cannot be obtained at this level of theory.

Since the EA of Na (12.64 kcal mol⁻¹) is significantly higher than that of BH₃ (0.88 kcal mol⁻¹), the heterolytic breakage of (Na-BH₃)⁻ into Na:⁻ and BH₃ should be favored by approximately (12.64-0.88=11.76) kcal mol⁻¹ over the homolytic breakage into Na· and ·BH₃⁻. As shown in Table 2, the calculated heterolytic bond dissociation energy (BDE) is 17.8 kcal mol⁻¹, while the calculated homolytic BDE is 30.1 kcal mol⁻¹. The calculated BDE difference, 12.3 kcal mol⁻¹, is close to the expected value, 11.76 kcal mol⁻¹, validating the calculated BDEs. For reference, the BDE of the prototype Lewis adduct, H₃N-BH₃, was also calculated. Our result is consistent with previous study.³¹ Dissociation into ionic fragments Na⁺ and :BH₃²⁻ is much less favored due to the instability of :BH₃²⁻. Therefore, the Na-B bond in (Na-BH₃)⁻ favors the heterolytic dissociation, making it satisfy the IUPAC definition of dative bond; (Na-BH₃)⁻ can be described as a Na:⁻→BH₃ Lewis acid/base adduct.

Table 2. BDEs calculated at the CCSD(T)/ aug-cc-pCVQZ level of theory including ZPE corrections. The energies are given in kcal mol⁻¹.

Dissociation pathway	BDE
(Na-BH ₃) ⁻ → Na: ⁻ + BH ₃	17.8
(Na-BH ₃) ⁻ → Na· + ·BH ₃ ⁻	30.1
(Na-BH ₃) ⁻ → Na ⁺ + :BH ₃ ²⁻	248.7
H ₃ N-BH ₃ → :NH ₃ + BH ₃	26.0

The Lewis adduct nature of $(\text{Na-BH}_3)^-$ is also demonstrated by the charge distribution change on the potential energy surface along the Na-B coordinate. Figure 3 shows that when Na and BH_3 moieties are completely separated, all the negative charge localizes on Na, that is, the formation of $(\text{Na-BH}_3)^-$ complex starts from Na^- and BH_3 . The charge on Na moiety gradually reduces as Na approaches BH_3 , suggesting charge transfer from Na to BH_3 when forming $\text{Na}^- \rightarrow \text{BH}_3$ bond. These curves comply with the classic picture of dative bond formation.

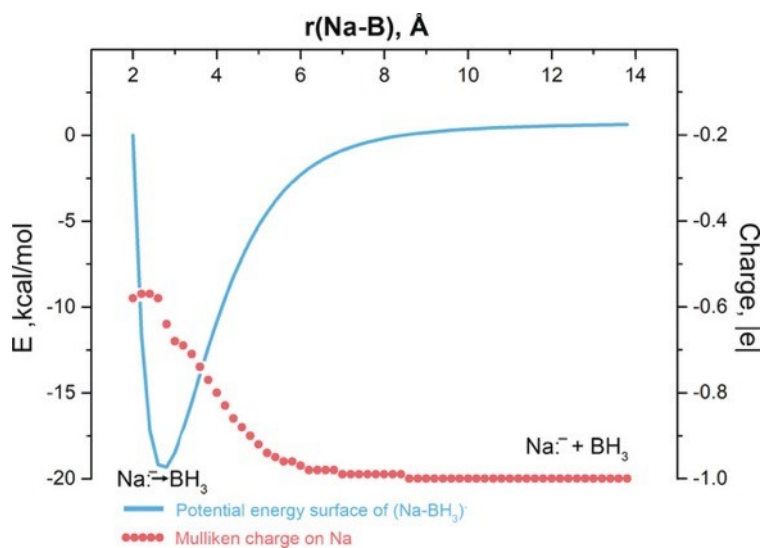


Figure III.5.1 Potential energy surface of $(\text{Na-BH}_3)^-$ along the Na-B coordinate (blue curve) and the Mulliken charge on Na at corresponding $r(\text{Na-B})$ (red dotted curve).

The nature of this $\text{Na}^- \rightarrow \text{BH}_3$ dative bond is further investigated using Adaptive Natural Density Partitioning (AdNDP), which analyses chemical bonding patterns based on the concept of electron pair,³² and the Quantum Theory of Atoms in

Molecules (QTAIM), which interprets chemical bonds based on topological analysis of electron density.³³ According to AdNDP, there are three fully localized 2c-2e B–H σ -bonds with an occupation number (ON) equal to $1.96|e|$. The $\text{Na}:\bar{\rightarrow}\text{BH}_3$ bond is a pure 2c-2e σ -bond with $\text{ON}=1.76|e|$ (Figure 4 A). AdNDP also allows us to locate an *s* lone pair on Na as an alternative to the 2c-2e Na–B bond in order to evaluate the Na contribution. The recovered lone pair has an ON of $1.28|e|$ (Figure 4 B), indicating that Na acquires extra electron and has doubly occupied orbital. Moreover, the ON value of the *s* lone pair suggests it the primary component of the Na–B bond. The QTAIM results for $(\text{Na-BH}_3)^-$ are shown in Figure 4 C. The negative $\nabla^2\rho$ values at the B–H bond critical points (BCPs) indicate shared interaction, in accordance with the covalent nature of the B–H bonds. The positive $\nabla^2\rho$ value at the Na–B BCP indicates closed shell interaction, which is one main feature of a dative bond. The electron density of Na–B bond is comparable to that of a strong hydrogen bond.³⁴ For comparison, we also performed QTAIM on $\text{H}_3\text{N-BH}_3$ as an example of a classic dative interaction³⁵ (Figure 4 D). The QTAIM results of $(\text{Na-BH}_3)^-$ and $\text{H}_3\text{N-BH}_3$ are similar: both dative Na–B and N–B bonds have positive $\nabla^2\rho_{(\text{BCP})}$ values, while the $\nabla^2\rho_{(\text{BCP})}$ of all covalent B–H bonds are negative. Therefore, the QTAIM results further corroborate the dative nature of the Na–B bond. These results comply with the AdNDP analysis.

Lastly, we analyzed an isolated hypothetical $[\text{Na-B(CN)}_3]^-$ complex, which derives from the solid-phase $\text{Na}_2\text{B(CN)}_3$, a salt comprised of Na^+ and B(CN)_3^{2-} dianion.³⁶ For $[\text{Na-B(CN)}_3]^-$, its homolytic dissociation into Na^\cdot and B(CN)_3^\cdot requires 60.3 kcal mol⁻¹ less in energy than the heterolytic dissociation into Na^\cdot and B(CN)_3 (Table S3). This is consistent with the high EA of B(CN)_3 (78.9 kcal mol⁻¹). Dissociation into Na^+ and $[\text{B(CN)}_3]^{2-}$ has a much higher BDE, because $[\text{B(CN)}_3]^{2-}$ is not a stable species when isolated. According to the IUPAC guidance, the Na-B bond in $[\text{Na-B(CN)}_3]^-$ can be characterized as covalent or ionic. AdNDP reveals that the Na moiety bears an ON of only 0.49|e|, while NBO suggests a positive charge of +0.23|e| on Na. These indicate a near-neutral configuration of Na, and that the Na-B bond is a polar covalent bond (Figure S1). The $[\text{Na-B(CN)}_3]^-$ can thus be written as $\text{Na}^0[\text{B(CN)}_3]^-$. While this result seems counter-intuitive to the condensed-phase characterization of $[\text{Na-B(CN)}_3]^-$ as $\text{Na}^+[\text{B(CN)}_3]^{2-}$, it is consistent with numerous studies on anions of isolated salts $(\text{M}^+\text{X}^-)^-$, which have shown that the excess electron goes to the cation to form M^0X^- .³⁷ Therefore, this hypothetical $[\text{Na-B(CN)}_3]^-$ serves as a contrasting example of $(\text{Na-BH}_3)^-$, emphasizing the importance of using weak Lewis acid for the design of alkalide \rightarrow LA Lewis adduct.

To summarize, we have designed a $(\text{Na-BH}_3)^-$ cluster featuring a non-trivial $\text{Na}^\cdot\rightarrow\text{BH}_3$ dative bond, representing the first example of a Lewis adduct with an

alkalide as the base. Anion photoelectron spectroscopy reveals a negatively charged Na moiety and its direct chemical bond with BH₃. The excellent agreement between the experimental and calculated VDEs confirms the optimized structure. The dative nature of the Na–B bond is confirmed by *minimum energy rupture*, AdNDP and

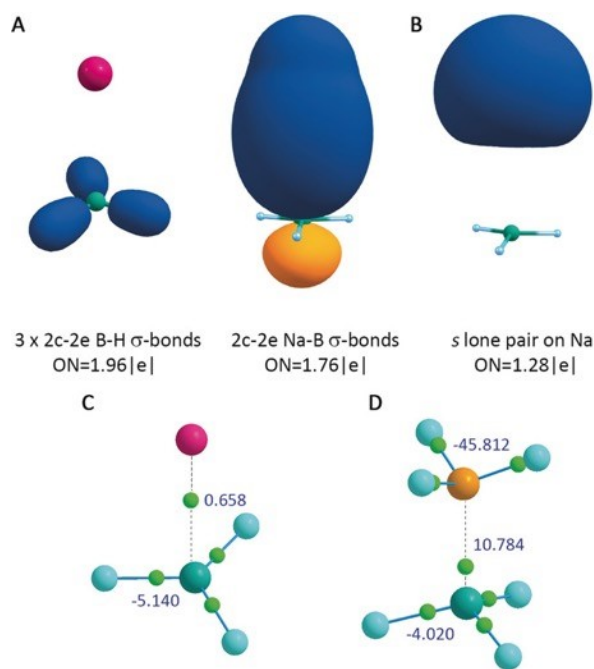


Figure III.5.2 AdNDP and QTAIM chemical bonding patterns. A) AdNDP full bonding picture of (Na–BH₃)[−], B) AdNDP recovered *s*-type lone electron pair on Na, C) QTAIM results of (Na–BH₃)[−], and D) QTAIM results of H₃N–BH₃. Na is purple, B is dark green, N is orange, H is blue. QTAIM calculated BCPs are represented by light green spheres. The numbers in blue besides BCPs are the Laplacians of electron density, $\nabla^2\rho$, in $e^- \text{Å}^{-5}$.

QTAIM analyses. The realization of this unprecedented Na:[−]→B dative bond, together with several recent studies showing alkali metals can form covalent bond as ligands³⁸ and electronically transmute Al to form Al–Al multiple

bonds,³⁹ demonstrates the unusual versatility of alkali metals in contributing to various types of chemical bonds. This study extends our understanding on Lewis acid/base, a fundamental concept in chemistry, and opens the door for synthesizing novel Lewis adducts.

References

1. D. F. Shriver, *Acc. Chem. Res.* 1970, **3**, 231–238.
2. (a) L. Vaska, *Acc. Chem. Res.* 1968, **1**, 335–344; (b) H. Werner, *Pure Appl. Chem.* 1982, **54**, 177–188.
3. (a) H. Braunschweig, T. Wagner, *Chem. Ber.* 1994, **127**, 1613–1614; (b) H. Braunschweig, T. Wagner, *Z. Naturforsch.* 1996, **51**, 1618–1620.
4. A. F. Hill, G. R. Owen, A. J. P. White, D. J. Williams, *Angew. Chem. Int. Ed.* 1999, **38**, 2759–2761; *Angew. Chem.* 1999, **111**, 2920–2923.
5. (a) H. Braunschweig, R. D. Dewhurst, A. Schneider, *Chem. Rev.* 2010, **110**, 3924–3957; (b) H. Braunschweig, R. D. Dewhurst, *Dalton Trans.* 2011, **40**, 549–558; (c) J. Bauer, H. Braunschweig, R. D. Dewhurst, *Chem. Rev.* 2012, **112**, 4329–4346; (d) G. Bouhadir, D. Bourissou, *Chem. Soc. Rev.* 2016, **45**, 1065–1079.
6. (a) H. Grützmacher, *Angew. Chem. Int. Ed.* 2008, **47**, 1814–1818; *Angew. Chem.* 2008, **120**, 1838–1842; (b) C. Gunanathan, D. Milstein, *Acc. Chem. Res.* 2011, **44**, 588–602.
7. M. Devillard, R. Declercq, E. Nicolas, A. W. Ehlers, J. Backs, N. Saffon-Merceron, G. Bouhadir, J. C. Sloatweg, W. Uhl, D. Bourissou, *J. Am. Chem. Soc.* 2016, **138**, 4917–4926.
8. D. L. M. Suess, J. C. Peters, *J. Am. Chem. Soc.* 2013, **135**, 12580–12583.
9. R. C. Cammarota, C. C. Lu, *J. Am. Chem. Soc.* 2015, **137**, 12486–12489.
10. Y. Li, C. Hou, J. Jiang, Z. Zhang, C. Zhao, A. J. Page, Z. Ke, *ACS Catal.* 2016, **6**, 1655–1662.
11. M. Devillard, G. Bouhadir, D. Bourissou, *Angew. Chem. Int. Ed.* 2015, **54**, 730–732; *Angew. Chem.* 2015, **127**, 740–742.
12. G. R. Owen, *Chem. Commun.* 2016, **52**, 10712–10726.
13. D. You, H. Yang, S. Sen, F. P. Gabbaï, *J. Am. Chem. Soc.* 2018, **140**, 9644–9651.
14. I. M. Riddlestone, N. A. Rajabi, J. P. Lowe, M. F. Mahon, S. A. Macgregor, M. K. Whittlesey, *J. Am. Chem. Soc.* 2016, **138**, 11081–11084.
15. J. Campos, *J. Am. Chem. Soc.* 2017, **139**, 2944–2947.
16. B. R. Barnett, M. L. Neville, C. E. Moore, A. L. Rheingold, J. S. Figueroa, *Angew. Chem.*

- Int. Ed.* 2017, **56**, 7195– 7199; *Angew. Chem.* 2017, **129**, 7301– 7305.
17. (a) J. L. Dye, J. M. Ceraso, M. L. Tak, B. L. Barnett, F. J. Tehan, *J. Am. Chem. Soc.* 1974, **96**, 608– 609; (b) J. L. Dye, *Angew. Chem. Int. Ed. Engl.* 1979, **18**, 587– 598; *Angew. Chem.* 1979, **91**, 613– 625; (c) J. Kim, A. S. Ichimura, R. H. Huang, M. Redko, R. C. Phillips, J. E. Jackson, J. L. Dye, *J. Am. Chem. Soc.* 1999, **121**, 10666– 10667; (d) M. Y. Redko, M. Vlassa, J. E. Jackson, A. W. Misiolek, R. H. Huang, J. L. Dye, *J. Am. Chem. Soc.* 2002, **124**, 5928– 5929.
 18. A. Haaland, *Angew. Chem. Int. Ed. Engl.* 1989, **28**, 992– 1007; *Angew. Chem.* 1989, **101**, 1017– 1032.
 19. International Union of Pure and Applied Chemistry, *Compendium of Chemical Terminology (Goldbook)*, Vol. 2.3.3, **2014**, pp. 374.
 20. A. T. Wickham-Jones, S. Moran, G. B. Ellison, *J. Chem. Phys.* 1989, **90**, 795– 806.
 21. X. Zhang, K. H. Bowen, *J. Chem. Phys.* 2016, **144**, 224311.
 22. E. F. Belogolova, G. Liu, E. P. Doronina, S. M. Ciborowski, V. F. Sidorkin, K. H. Bowen, *J. Phys. Chem. Lett.* 2018, **9**, 1284– 1289.
 23. A. L. Moores, D. W. Norcross, *Phys. Rev. A* 1974, **10**, 1646– 1657.
 24. G. Liu, E. Miliordos, S. M. Ciborowski, M. Tschurl, U. Boesl, U. Heiz, X. Zhang, S. S. Xantheas, K. H. Bowen, *J. Chem. Phys.* 2018, **149**, 221101.
 25. X. Zhang, G. Liu, S. Ciborowski, K. Bowen, *Angew. Chem. Int. Ed.* 2017, **56**, 9897– 9900; *Angew. Chem.* 2017, **129**, 10029– 10032.
 26. (a) G. D. Purvis III, R. J. Bartlett, *J. Chem. Phys.* 1982, **76**, 1910– 1918; (b) K. Raghavachari, G. W. Trucks, J. A. Pople, M. Head-Gordon, *Chem. Phys. Lett.* 1989, **157**, 479– 483; (c) T. H. Dunning, Jr., *J. Chem. Phys.* 1989, **90**, 1007– 1023.
 27. K. A. Peterson, *J. Chem. Phys.* 2002, **117**, 10548– 10560.
 28. (a) N. Yamamoto, T. Vreven, M. A. Robb, M. J. Frisch, H. B. Schlegel, *Chem. Phys. Lett.* 1996, **250**, 373– 378; (b) E. M. Siegbahn, *Chem. Phys. Lett.* 1984, **109**, 417– 423.
 29. (a) H. Koch, P. Jørgensen, *J. Chem. Phys.* 1990, **93**, 3333– 3344; (b) M. Kállay, J. Gauss, *J. Chem. Phys.* 2004, **121**, 9257– 9269; (c) J. J. Goings, M. Caricato, M. J. Frisch, X. Li, *J. Chem. Phys.* 2014, **141**, 164116.
 30. A. A. Dixon, M. Gutowski, *J. Phys. Chem. A* 2005, **109**, 5129– 5135.
 31. (a) D. Y. Zubarev, A. I. Boldyrev, *Phys. Chem. Chem. Phys.* 2008, **10**, 5207– 5217; (b) D. Yu. Zubarev, A. I. Boldyrev, *J. Org. Chem.* 2008, **73**, 9251– 9258.
 32. R. Bader, *Atoms in Molecules: A Quantum Theory*, Oxford University Press, Oxford, 1994.
 33. A. Ranganathan, G. U. Kulkarni, C. N. R. Rao, *J. Phys. Chem. A* 2003, **107**, 6073– 6081.
 34. X. Zhang, S. L. Sun, H. L. Xu, Z. M. Su, *RSC Adv.* 2015, **5**, 65991.
 35. (a) E. Bernhardt, V. Bernhardt-Pitchougina, H. Willner, N. Ignatiev, *Angew. Chem. Int. Ed.* 2011, **50**, 12085– 12088; *Angew. Chem.* 2011, **123**, 12291– 12294; (b) J. Landmann, J. A. P. Sprenger, R. Bertermann, N. Ignat'ev, V. Bernhardt-Pitchougina, E. Bernhardt, H. Willner, M. Finze, *Chem. Commun.* 2015, **51**, 4989– 4992.
 36. (a) S. N. Eustis, D. Radisic, K. H. Bowen, R. A. Bachorz, M. Haranczyk, G. Schenter, M.

- Gutowski, *Science* 2008, **319**, 936– 939; (b) R. Li, C. Liu, Y. Gao, H. Jiang, H. Xu, W. Zheng, *J. Am. Chem. Soc.* 2013, **135**, 5190– 5199; (c) G. Hou, C. Liu, R. Li, H. Xu, Y. Gao, W. Zheng, *J. Phys. Chem. Lett.* 2017, **8**, 13– 20.
37. A. Chi, S. Pan, L. Meng, M. Luo, L. Zhao, M. Zhou, G. Frenking, *Angew. Chem. Int. Ed.* 2019, **58**, 1732– 1738;
38. (a) K. A. Lundell, X. Zhang, A. I. Boldyrev, K. H. Bowen, *Angew. Chem. Int. Ed.* 2017, **56**, 16593– 16596; *Angew. Chem.* 2017, **129**, 16820– 16823; (b) X. Zhang, I. A. Popov, K. A. Lundell, H. Wang, C. Mu, W. Wang, H. Schnöckel, A. I. Boldyrev, K. H. Bowen, *Angew. Chem. Int. Ed.* 2018, **57**, 14060– 14064; *Angew. Chem.* 2018, **130**, 14256– 14260.

IV. Molecular Activation

Since reactions are essentially the change of electronic structures, and the breakage and formation of chemical bonds, the competence of negative ion photoelectron spectroscopy (NIPS) in probing both of them makes it the ideal tool to study molecular activation in the gas phase. While gas phase studies never account for the many features which may prevail at a surface or in solution, nevertheless when complemented by adequate computational studies, these studies have offered insight to molecular activation processes via providing a conceptual framework for addressing questions as for example: the identity of the atoms which constitute the active part of a single-site catalyst, the identification of which constitutes one of the intellectual cornerstones in contemporary catalysis. Or, how do factors such as stoichiometry, cluster size, charge and spin states, oxidation number, degree of coordinative saturation, etc. affect the outcome of a chemical transformation without being obscured by ill-defined “environmental effects”.

IV.1 CO₂ Activation and Hydrogenation by PtH_n⁻ Cluster Anions

Xinxing Zhang, *Gaoxiang Liu*, Karl-Heinz Meiwes-Broer, Gerd Ganteför, Kit Bowen
*Department of Chemistry, Johns Hopkins University, 3400 N. Charles Street,
Baltimore, MD 21218 (USA)*

*Institut für Physik, Universität Rostock, Albert-Einstein-Str. 24, 18059, Rostock
(Germany)*

Fachbereich Physik, Universität Konstanz (Germany)

Abstract

Gas phase reactions between PtH_n⁻ cluster anions and CO₂ were investigated by mass spectrometry, anion photoelectron spectroscopy, and computations. Two major products, PtCO₂H⁻ and PtCO₂H₃⁻, were observed. The atomic connectivity in PtCO₂H⁻ can be depicted as HPtCO₂⁻, where the platinum atom is bonded to a bent CO₂ moiety on one side and a hydrogen atom on the other. The atomic connectivity of PtCO₂H₃⁻ can be described as H₂Pt(HCO₂)⁻, where the platinum atom is bound to a formate moiety on one side and two hydrogen atoms on the other. Computational studies of the reaction pathway revealed that the hydrogenation of CO₂ by PtH₃⁻ is highly energetically favorable.

The transformation of carbon dioxide into reduced, higher value molecules, such as

methanol and formic acid, is of great interest for both environmental and economic reasons. In solution, ligand-protected transition metal hydride complexes, L_nMH , often play important roles in these processes.¹⁻¹⁹ The critical reduction step involves the insertion of the C=O group of carbon dioxide into the M–H bond to produce a formate–metal adduct, $L_nM-OC(O)H$, from which the formate product can be generated. There are, on the other hand, fewer reports of CO₂ reduction by ligandless metal hydrides. Those studies that have been conducted include the methanation of CO₂ on Mg₂NiH₄ surfaces²⁰ and similar reactions on hydrogen-loaded LaNi₅ and LaNi₄Cr surfaces, where their hydrides play critical roles.²¹ Gas phase work is even rarer. While naked (ligandless) transition metal hydrides have been generated in the gas phase as both positive and negative ions (for example, FeD⁺, CoD⁺, NiD⁺, CrH⁻, NiH⁻, CoH⁻, CuH⁻, and FeH₂⁻)²²⁻²⁵ we are not aware of them being utilized in CO₂ reactivity studies. However, a recent report details the gas phase, ligand-protected, activation of CO₂ by a Cp₂TiH⁺ metal hydride cation.¹⁹

The present work focuses on the hydrogenation of CO₂ via reactions with platinum hydride cluster anions, PtH_{*n*}⁻. Platinum hydride cluster anions were chosen because platinum is an excellent hydrogenation catalyst, their hydrides are good sources of hydrogen, and their excess negative charges promote the activation of CO₂. The two products of these reactions, PtCO₂H⁻ and PtCO₂H₃⁻, were identified by mass

spectrometry and characterized by anion photoelectron spectroscopy. Ab initio computational studies of the mechanistic pathway revealed that the hydrogenation of CO₂ by PtH₃⁻ is strongly favorable energetically.

The details of experimental and computational methods are provided in the Supporting Information. The mass spectra with or without CO₂ pulsed into the reaction cell are shown in Figure 1. With no CO₂ in the cell, only PtH_{*n*}⁻ cluster anions were observed in the mass spectrum (Figure 1 A; Supporting Information, Figure S1). Individual PtH_{*n*}⁻ species were identified by recording anion photoelectron spectra at every mass peak in the series. These spectra are shown in Figure S1 (Supporting Information), beginning at 194 amu and continuing in single amu steps up to 203 amu. (Mass 202 is missing in the mass spectrum, indicating that PtH₄⁻ is not present.) The photoelectron spectrum at mass 194 was identified as the well-known photoelectron spectrum of Pt⁻. As well as Pt⁻ peaks from another Pt⁻ isotope, new peaks in the photoelectron spectrum at mass 195 are due to PtH⁻. New peaks on top of those in the photoelectron spectrum at mass 196 are due to PtH₂⁻, and so on, up to PtH₅⁻. No PtH₄⁻ was present.

When CO₂ was added to the cell, the ion intensity of the PtH_{*n*}⁻ series decreased, and a new series of PtCO₂H_{*m*}⁻ cluster anions appeared (Figure 1 B). No other products

were observed in the entire mass spectrum. The lowest mass peak at 239 amu is due

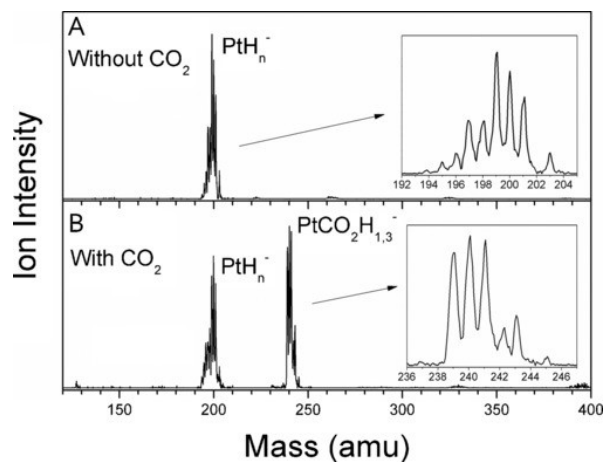


Figure IV.1.1 The mass spectra of PtH_n^- cluster anions A) without and B) with CO_2 injection into the cell.

to PtCO_2H^- , while the highest mass peak at 245 amu is due to $\text{PtCO}_2\text{H}_3^-$; hence, PtCO_2H^- and $\text{PtCO}_2\text{H}_3^-$ coexist in the ion beam. Since there is essentially no mass peak at 244 amu, we are confident that $\text{PtCO}_2\text{H}_2^-$ is not present in the beam. The intensity of $\text{PtCO}_2\text{H}_3^-$ is calculated to be 29% of that of PtCO_2H^- (Supporting Information, Figure S2). More detailed mass spectral and photoelectron spectral analysis of the PtCO_2H^- and $\text{PtCO}_2\text{H}_3^-$ cluster anions are presented in Figure S2 and S3 (Supporting Information). Note that both PtCO_2H^- and $\text{PtCO}_2\text{H}_3^-$ have closed-shell electron configurations.

The photoelectron spectrum of $\text{PtCO}_2\text{H}_3^-$ is presented in Figure 2, and was measured with the third harmonic output of a Nd:YAG laser (3.496 eV). It was recorded at mass

245 amu to ensure that the resulting photoelectron signal was primarily due to $\text{PtCO}_2\text{H}_3^-$. This spectrum is dominated by a band that ranges from electron binding energy (EBE)=3.0 to 3.5 eV, with a maximal spectral intensity at EBE=3.24 eV. Thus, 3.24 eV is the vertical detachment energy (VDE) value for $\text{PtCO}_2\text{H}_3^-$, that is, the transition energy at which the Franck-Condon overlap is at its maximum between the anion's wave function and that of its neutral counterpart. The electron affinity (EA) is the energy difference between the relaxed ground state of the anion, and the relaxed ground state of its neutral counterpart. The EA value for PtCO_2H_3 is estimated to be 3.1 eV by extrapolating the lower EBE side of the band to zero photoelectron intensity. The small peak at EBE=3.08 eV and other very weak features at the low EBE side of the main band are due to the much less abundant isotopomer of PtCO_2H^- at mass=245 (Supporting Information, Figure S2).

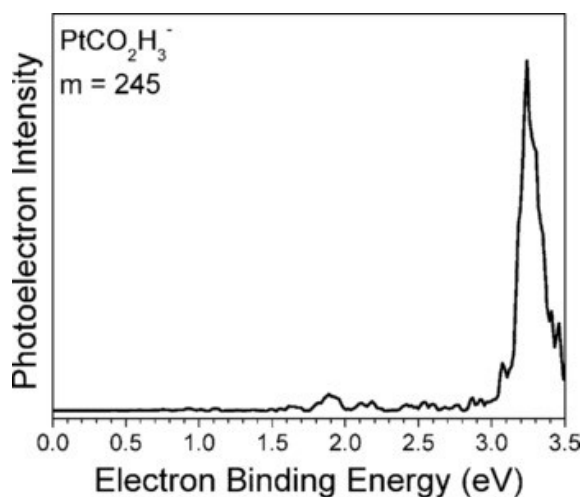


Figure IV.1.2 Photoelectron spectrum of $\text{PtCO}_2\text{H}_3^-$ taken at mass 245 with 355 nm (3.496 eV) photons.

The photoelectron spectrum of PtCO_2H^- is shown in Figure 3 C. With five spectral bands in evidence, it is more complicated than that of $\text{PtCO}_2\text{H}_3^-$. Its features are due, not only to the photodetachment of PtCO_2H^- , but also to the photodissociation of PtCO_2H^- into PtH^- and CO_2 , followed by photodetachment of the resultant anion, PtH^- . The latter is a two-photon process, where one photon is absorbed, inducing fragmentation, while another photon photodetaches the anionic product of dissociation. This can be seen by comparing the photoelectron spectrum of PtCO_2H^- with that of PtH^- . Unfortunately, we did not observe the photoelectron spectrum of PtH^- by itself in these experiments. This was because every isotopic mass peak of PtH^- overlaps with at least one of the following anions: Pt^- , PtH_2^- , or PtH_3^- . Nevertheless, we were still able to identify the photoelectron spectral transitions in PtH^- by comparing the photoelectron spectra at mass=194 (Pt^- ; Figures 3 A) with that at mass=195 (a combination of Pt^- and PtH^- ; 3 B). In the photoelectron spectrum for mass 195 (Figure 3 B), Pt^- peaks at EBE=2.1, 2.2, 2.9, and 3.4 eV (green dots) share the spectrum with three additional peaks at EBE=1.60, 1.85, and 3.08 eV (red dots); these are due to PtH^- . Significantly, the latter peaks reappear in the photoelectron spectrum of PtCO_2H^- in Figure 3 C, not only at the same EBE positions, but also with nearly identical relative intensities. It is clear that the peaks denoted by red dots in the photoelectron spectrum of PtCO_2H^- are due to PtH^- . PtCO_2H^- has undergone both photodetachment and photodissociation.

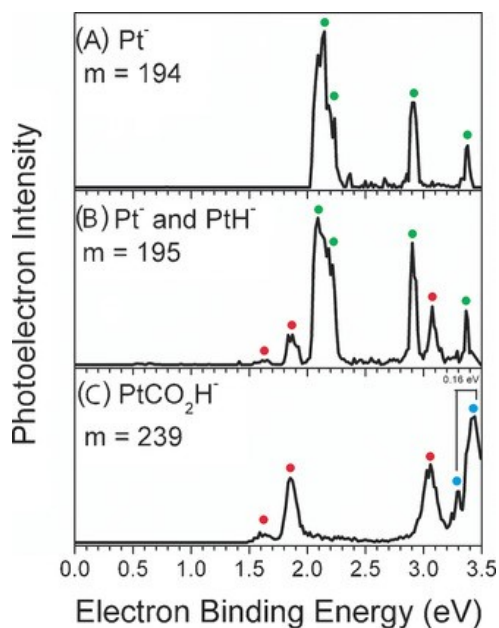


Figure IV.1.3 Photoelectron spectra of A) Pt⁻ (•) taken at mass=194; B) Pt⁻ (•) and PtH⁻ (•) taken at mass=195; C) PtCO₂H⁻ (•) taken at mass=239.

As an aside, the embedded photoelectron spectrum of PtH⁻ has allowed us to determine, for the first time, that the VDE value of PtH⁻ is 1.60 eV and the EA value of PtH is 1.5 eV. While the photoelectron study of PtH_n⁻ was not an explicit goal of this work, it does add to the mosaic of accumulated data on transition metal hydrides.

The photoelectron spectrum of PtCO₂H⁻ resides on the high EBE side of Figure 3 C as two peaks (blue dots), a small peak at EBE=3.30 eV and a broader band that reaches its maximum photoelectron intensity at EBE=3.46 eV. Thus, 3.46 eV is the VDE value for PtCO₂H⁻. We further assign its EA value as 3.30 eV. The spacing between these two peaks is 0.16 eV, which is very close to the 1280 cm⁻¹ C–O stretching frequency

that we calculated for PtCO₂H. This value is consistent with a weakening of the C–O bond caused by the activation of the CO₂ moiety. Based on photodissociation products of PtCO₂H[−] (PtH[−] and CO₂ inferred), we speculate that the structure of PtCO₂H[−] consists of a CO₂ moiety and a PtH[−] moiety. As seen below, our computations bear that expectation out.

Figure 4 presents the optimized structures of PtCO₂H[−] and PtCO₂H₃[−]. The calculated 3D coordinates of these two products are provided in the Supporting Information. For PtCO₂H₃[−], the global minimum is found to have C_{2v} symmetry. It can be viewed as a formate anion/PtH₂ adduct, namely H₂Pt(HCO₂)[−], where the platinum atom is planar tetra-coordinated (PTC) by two hydrogen atoms and the two oxygen atoms of the formate anion moiety. A PTC structure is stable and commonly seen in platinum-containing molecules. Natural Population Analysis (NPA) shows that, along with CO₂ insertion and hydrogen atom migration, charge is also transferred from the platinum hydride anion to CO₂, making the formate anion moiety negatively charged by $-0.77 e$.

In the optimized structure of PtCO₂H[−], the only hydrogen atom is bonded to platinum. The platinum atom also bonds to the carbon atom of the CO₂ moiety, which is bent from its original linear structure, indicating that CO₂ has been activated by PtH[−]. This

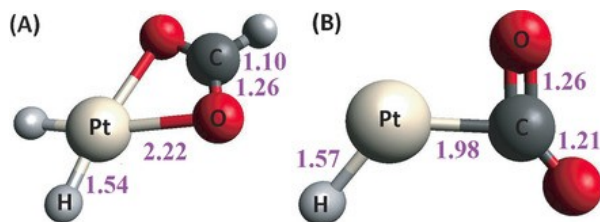


Figure IV.1.4 A) Optimized structures of PtCO₂H₃⁻ and B) PtCO₂H⁻. Bond lengths (Å).

structure is consistent with photodissociation evidence observed in the photoelectron spectrum. NPA shows that the negative charge is also partially transferred from PtH⁻ to CO₂, resulting in a total charge of $-0.66 e$ on the CO₂ moiety. The O-C-O bond angle is determined to be 139.5°, close to the 134° bond angle of the free CO₂⁻ anion at its global minimum.²⁶⁻²⁸ This indicates that, even though hydrogenation of the CO₂ moiety does not occur, CO₂ nevertheless becomes activated by its interaction with PtH⁻. The behavior of PtH⁻ is analogous to that of Au⁻, its isoelectronic analogue, which is known to activate CO₂ by charge transfer.^{29, 30}

Table 1 presents the EA and VDE values of PtCO₂H/PtCO₂H⁻ and PtCO₂H₃/PtCO₂H₃⁻ calculated at different theory levels. Agreement among different levels of theory is very good, and is also excellent between the calculated and experimental values.

DFT calculations were carried out to investigate the mechanism of CO₂ activation and hydrogenation. The reaction pathways were calculated for the reactions of PtH⁻ and

PtH₃⁻ with CO₂, respectively. The pathway of CO₂ hydrogenation by PtH₃⁻ is presented in Figure 5. Before reaction, PtH₃⁻ exhibits C_{2v} symmetry. The first step in

Table 1. Experimental and calculated VDE/EA values for PtCO₂H/PtCO₂H⁻ and PtCO₂H₃/PtCO₂H₃⁻.

VDE/EA values [eV]	PtCO ₂ H ₃ /PtCO ₂ H ₃ ⁻	PtCO ₂ H/PtCO ₂ H ⁻
Experimental	3.24/3.10	3.46/3.30
UPBE0	3.37/3.21	3.55/3.23
CCSD	3.10/2.94	3.38/3.28
CCSD(T)	3.19/2.94	3.46/3.44

the reaction is CO₂ activation by charge transfer from PtH₃⁻. As soon as CO₂ approaches the platinum atom, it bends, and the energy drops by 0.61 eV (structure 1 a). The highest occupied molecular orbital (HOMO) of structure 1 a (Figure 5) indicates that the excess electron density is delocalized over the entire cluster. Furthermore, according to NPA, the net charge on the CO₂ moiety is -0.39 e, showing that it has been significantly activated. After activation, the CO₂ moiety is ready to accept a hydrogen atom from PtH₃⁻. The insertion of CO₂ into the Pt-H bond passes through the first transition state (structure TS1), with an energy barrier of 0.42 eV. Once the hydrogen atom has transferred to CO₂, hydrogenation is complete, yielding structure 1 b (a local minima). Structure 1 b must overcome a small rotational barrier (0.09 eV, TS2) so that PtCO₂H₃⁻ may reach the global minimum structure

shown in Figure 4 A (that is, structure 1 c in Figure 5). This permits the other oxygen atom to coordinate with the platinum atom, further stabilizing the entire cluster.

The potential energy pathway for the reaction between CO_2 and PtH^- is presented in Figure 6. As in the first step in the reaction between CO_2 and PtH_3^- , CO_2 is also activated in this case by charge transfer with the platinum atom, forming a bond between the platinum and carbon atoms (structure 2 a). The HOMO of this structure also shows substantial delocalization. The activation of CO_2 provides 1.70 eV of stabilization energy to structure 2 a of PtCO_2H^- . (Interestingly, this is much larger than the analogous stabilization energy for CO_2 activation in $\text{PtCO}_2\text{H}_3^-$, which is 0.61 eV.) Nevertheless, even though CO_2 activation has been achieved at this point in the CO_2 and PtH^- pathway (via structure 2 a), the reaction cannot proceed further to CO_2 hydrogenation. The reason that the reaction stops at this juncture is because of 2.84 eV energy barrier, against which hydrogen atom transfer from structure 2 a to TS3 would have to occur. (Again, this energy is much higher than the analogous 0.42 eV barrier in the CO_2 and PtH_3^- reaction.) The reaction cannot proceed to structure 2 b. Our photoelectron spectrum of PtCO_2H^- and accompanying calculations imply that we have made and photodetached structure 2 a, rather than structure 2 b. Figure 6 also shows the energy needed to photodissociate structure 2 a into $\text{PtH}^- + \text{CO}_2$ (that is, 1.70 eV + 1.68 eV = 3.38 eV). We irradiated PtCO_2H^- with 3.496 eV photons when

measuring the photoelectron spectrum, which is only slightly more energy than what is required to dissociate PtCO_2H^- . Everything that we deduced from Figure 3 C is consistent with the energetics presented in Figure 6, in terms of the photodetachment and the photodissociation of PtCO_2H^- .

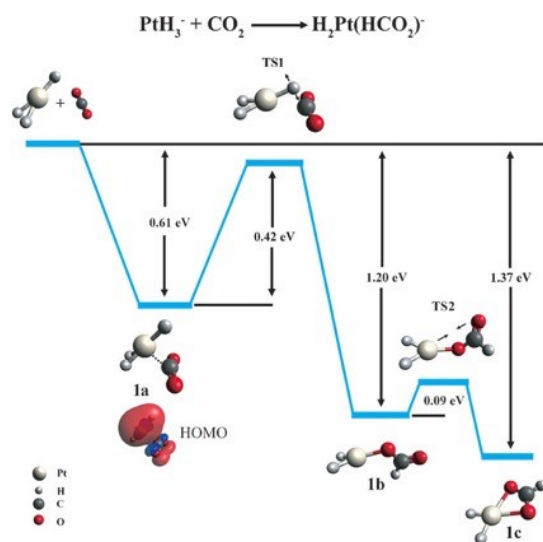


Figure IV.1.5 Calculated reaction pathway for CO_2 hydrogenation by PtH_3^- .

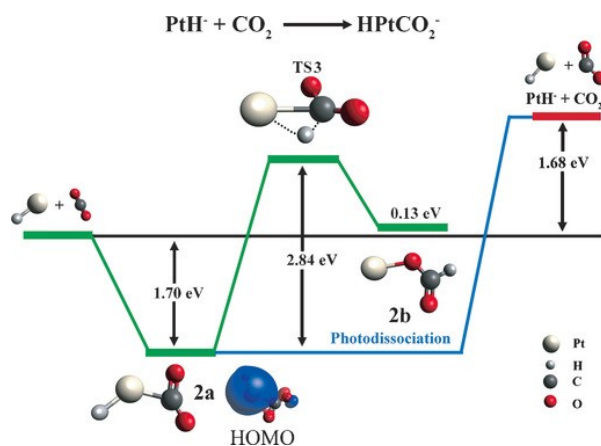


Figure IV.1.6 Calculated reaction pathway for CO_2 activation and thwarted hydrogenation by PtH^- . The photodissociation process of PtCO_2H^- is also presented.

Lastly, while there is some evidence that PtH_5^- existed in the ion beam (Supporting Information, Figure S1), there is no evidence that it reacted with CO_2 ; no $\text{PtCO}_2\text{H}_5^-$ was observed in the mass spectrum. The reasons for the inertness of PtH_5^- toward CO_2 may be both structural and electronic. PtH_5^- exhibits D_{5h} symmetry. Thus, since the platinum atom is surrounded by hydrogen atoms, it is difficult for CO_2 to gain access to the platinum atom. Furthermore, PtH_5^- is a very stable species because of σ -aromatic bonding. Both geometric and electronic features of PtH_5^- are highlighted in Figure S4 (Supporting Information). Our calculations also show that PtH_5^- and CO_2 do not react.

References

1. P. G. Jessop, T. Ikariya, R. Noyori, *Chem. Rev.* 1995, **95**, 259–272.
2. M. S. Jeletic, M. L. Helm, E. B. Hulley, M. T. Mock, A. M. Appel, J. C. Linehan, *ACS Catal.* 2014, **4**, 3755–3762.
3. M. A. Rankin, C. C. Cummins, *J. Am. Chem. Soc.* 2010, **132**, 10021–10023.
4. A. J. M. Miller, J. A. Labinger, J. E. Bercaw, *Organometallics* 2011, **30**, 4308–4314.
5. B. P. Sullivan, T. J. Meyer, *J. Chem. Soc. Chem. Commun.* 1984, **1984**, 1244–1245.
6. M. K. Whittlesey, R. N. Perutz, M. H. Moore, *Organometallics* 1996, **15**, 5166–5169.
7. P. Kang, C. Cheng, Z. Chen, C. K. Schauer, T. J. Meyer, M. Brookhart, *J. Am. Chem. Soc.* 2012, **134**, 5500–5503.
8. D. J. Darensbourg, A. Rokicki, M. Y. Darensbourg, *J. Am. Chem. Soc.* 1981, **103**, 3223–3224.
9. D. L. DuBois, D. E. Berning, *Appl. Organomet. Chem.* 2000, **14**, 860–862.
10. J. R. Pugh, M. R. M. Bruce, B. P. Sullivan, T. J. Meyer, *Inorg. Chem.* 1991, **30**, 86–91.
11. S. E. Clapham, A. Hadzovic, R. H. Morris, *Coord. Chem. Rev.* 2004, **248**, 2201–2237.
12. W. Leitner, *Angew. Chem. Int. Ed. Engl.* 1995, **34**, 2207–2221; *Angew. Chem.* 1995, **107**, 2391–2405.
13. S. Saeidi, N. A. S. Amin, M. R. Rahimpour, *J. CO2 Utilization* 2014, **5**, 66–81.
14. H. Arakawa et al., *Chem. Rev.* 2001, **101**, 953–996.
15. M. Aresta, A. Dibenedetto, *Dalton Trans.* 2007, **28**, 2975–2992.

16. G. Fachinetti, C. Floriani, A. Roselli, S. Pucci, *J. Chem. Soc. Chem. Commun.* 1978, **6**, 269–270.
17. S. Gambarotta, S. Strologo, C. Floriani, A. Chiesi-Villa, C. Guastini, *J. Am. Chem. Soc.* 1985, **107**, 6278–6282.
18. A. Cutler, M. Raja, A. Todaro, *Inorg. Chem.* 1987, **26**, 2877–2881.
19. S. Tang, N. J. Rijs, J. Li, M. Schlangen, H. Schwarz, *Chem. Eur. J.* 2015, **21**, 8483–8490.
20. S. Kato, A. Borgschulte, D. Ferri, M. Biemann, J. C. Crivello, D. Wiedenmann, M. Parlinska-Wojtan, P. Rossbach, Y. Lu, A. Remhof, A. Züttel, *Phys. Chem. Chem. Phys.* 2012, **14**, 5518–5526.
21. K. Soga, K. Otsuka, M. Sato, T. Sano, S. Ikeda, *J. Less-Common Met.* 1980, **71**, 259–263.
22. T. J. Carlin, L. Sallans, C. J. Cassidy, D. B. Jacobson, B. S. Freiser, *J. Am. Chem. Soc.* 1983, **105**, 6320–6321.
23. A. E. S. Miller, C. S. Feigerle, W. C. Lineberger, *J. Chem. Phys.* 1986, **84**, 4127–4131.
24. A. E. S. Miller, C. S. Feigerle, W. C. Lineberger, *J. Chem. Phys.* 1987, **87**, 1549–1556.
25. R. M. D. Calvin, D. H. Andrews, W. C. Lineberger, *Chem. Phys. Lett.* 2007, **442**, 12–16.
26. R. N. Compton, P. W. Reinhardt, C. D. Cooper, *J. Chem. Phys.* 1975, **63**, 3821.
27. M. Knapp, O. Echt, D. Kreisler, T. D. Mark, E. Recknagel, *Chem. Phys. Lett.* 1986, **126**, 225–231.
28. S. T. Arnold, J. V. Coe, J. G. Eaton, C. B. Freidhoff, L. H. Kidder, G. H. Lee, M. R. Manaa, K. M. McHugh, D. Patel-Misra, H. W. Sarkas, J. T. Snodgrass, K. H. Bowen, in *Proceedings of the Enrico Fermi International School of Physics, CVII Course, Varenna*, (Eds.:) North-Holland, Amsterdam, 1989, pp. 467–490.
29. X. Zhang, E. Lim, S. K. Kim, K. H. Bowen, *J. Chem. Phys.* 2015, **143**, 174305.
30. A. D. Boese, H. Schneider, A. N. Gloess, J. M. Weber, *J. Chem. Phys.* 2005, **122**, 154301.

IV.2 Communication: Water Activation and Splitting by Single Metal-Atom Anions

*Gaoxiang Liu*¹, Evangelos Miliordos^{2,a)}, Sandra M. Ciborowski¹, Martin Tschurl³, Ulrich Boesl³, Ulrich Heiz³, Xinxing Zhang^{4,b)}, Sotiris S. Xantheas^{2,5,b)}, and Kit Bowen^{1,b)}

¹*Department of Chemistry, Johns Hopkins University, Baltimore, Maryland 21218, USA*

²*Advanced Computing, Mathematics and Data Division, Pacific Northwest National Laboratory, Richland, Washington 99354, USA*

³*Institute for Physical Chemistry, Technical University of Munich, 85748 Garching, Germany*

⁴*Key Laboratory of Advanced Energy Materials Chemistry (Ministry of Education), College of Chemistry, Nankai University, Tianjin 30071, China*

⁵*Department of Chemistry, University of Washington, Seattle, Washington 98195, USA*

^{a)}*Present address: Department of Chemistry and Biochemistry, Auburn University, Auburn, AL 36830, USA.*

Abstract

We report experimental and computational results pertaining to the activation and splitting of single water molecules by single atomic platinum anions. The anion photoelectron spectra of $[\text{Pt}(\text{H}_2\text{O})]^-$, formed under different conditions, exhibit spectral features that are due to the anion-molecule complex, $\text{Pt}^-(\text{H}_2\text{O})$, and to the

reaction intermediates, HPtOH^- and H_2PtO^- , in which one and two O–H bonds have been broken, respectively. Additionally, the observations of PtO^- and H_2^+ in mass spectra strongly imply that water splitting via the reaction $\text{Pt}^- + \text{H}_2\text{O} \rightarrow \text{PtO}^- + \text{H}_2$ has occurred. Extending these studies to nickel and palladium shows that they too are able to activate single water molecules, as evidenced by the formation of the reaction intermediates, HNiOH^- and HPdOH^- . Computations at the coupled cluster singles and doubles with perturbatively connected triples level of theory provide structures and vertical detachment energies (VDEs) for both HMOH^- and H_2MO^- intermediates. The calculated and measured VDE values are in good agreement and thus support their identification.

Introduction

Water splitting holds great promise as a source of clean, abundant fuel.^{1–5} While electrolysis is effective, its cost is exceedingly high. Likewise, the direct cleavage of water's O–H bond is energetically prohibitive (497.1 kJ/mol).⁶ The solution to this problem is generally thought to lie in catalytic water splitting, a process which depends critically on the activation of water molecules. A variety of molecular and cluster catalysts are known to be effective in aqueous media,^{7,8} on surfaces,^{9,10} and in gas phase environments.^{11,12} Single-atom catalysts provide yet another approach. While single-atom catalysts have been found to facilitate water splitting on

surfaces,^{13–16} water activation and splitting by single atoms in the gas phase have gone virtually unexplored. Here, we investigate this topic, addressing both water activation and water splitting by single metal atomic anions.

We had originally been inspired by experiments in which sub-nano-size platinum clusters deposited onto semiconductor nano-rods and submerged in water were found to be effective water splitting photocatalysts.^{17–19} There, the overall catalytic process was $\text{H}_2\text{O} + \text{Pt}_n^- = \frac{1}{2} \text{H}_2 + \text{Pt}_n + \text{OH}^-$. Rather than studying water activation by platinum *cluster* anions, however, we chose to focus on the simplest set of relevant reactants, i.e., a *single* water molecule, a *single* metal atom (M), and a *single* excess electron (e^-), all interacting together within the sub-nano crucible of gas phase $[\text{M}(\text{H}_2\text{O})]^-$ cluster anions. By extending these studies beyond platinum to include nickel and palladium, as well as several other transition metal atoms, we explored the activation and splitting of single water molecules by single atomic metal anions. Our joint experimental and theoretical effort has resulted in strong evidence for both water activation and water splitting by single atomic platinum anions and for water activation (but without splitting) by single nickel and palladium anions.

Results and Discussions

Experimental studies of $[\text{Pt}(\text{H}_2\text{O})]^-$ were conducted using a laser vaporization ion

source, time-of-flight (TOF) mass spectrometry, and anion photoelectron spectroscopy.²⁰ Source details are presented in the supplementary material. The left panels in Fig. 1 present the mass spectra of the $[\text{Pt}(\text{H}_2\text{O})]^-$ mass region along with the expected isotopic mass distribution pattern of $[\text{Pt}(\text{H}_2\text{O})]^-$ in its top panel. Mass spectra **A**, **B**, and **C** show the effect of increasing the vaporization laser power in three steps (6, 8, and 11 mJ). Note that mass peaks due to PtO^- appeared and became stronger with increasing power. Control experiments without water, but under the same vaporization laser power conditions, did not result in the formation of PtO^- (Fig. S1), suggesting that PtO^- had formed as a result of the reaction between Pt^- and H_2O . The identities of the two putative PtO^- mass peaks ($m = 210$ and 211) were confirmed by measuring their anion photoelectron spectra (see Fig. S2) and comparing them to a previous report.²¹ The fact that the anion photoelectron spectra at these two masses were identical also indicates that no PtOH^- was present in the beam, since it would have appeared at $m = 211$.

The top panel on the right-hand side of Fig. 1 presents the photoelectron spectrum of the platinum atomic anion, Pt^- . This spectrum is presented for reference and agrees with previous reports.²² The lower three panels on the right-hand side of Fig. 1 exhibit anion photoelectron spectra of $[\text{Pt}(\text{H}_2\text{O})]^-$, i.e., **a**, **b**, and **c**, where in each case the subject $[\text{Pt}(\text{H}_2\text{O})]^-$ species had been generated under the same laser vaporization

(source) power conditions that had been used to measure their corresponding mass spectra **A**, **B**, and **C**, respectively. All $[\text{Pt}(\text{H}_2\text{O})]^-$ spectra were taken at mass = 216 to ensure that the photoelectron signals were solely from $[\text{Pt}(\text{H}_2\text{O})]^-$. These three photoelectron spectra of $[\text{Pt}(\text{H}_2\text{O})]^-$ clearly differ substantially from one another, strongly suggesting the presence of $[\text{Pt}(\text{H}_2\text{O})]^-$ isomers, whose generation depended on laser vaporization (source) power. As will be explained below, the anion photoelectron spectra **a**, **b**, and **c** have been labeled with the identities of their $[\text{Pt}(\text{H}_2\text{O})]^-$ isomers.

The top panel on the right-hand side of Fig. 1 presents the photoelectron spectrum of the platinum atomic anion, Pt^- . This spectrum is presented for reference and agrees with previous reports.²² The lower three panels on the right-hand side of Fig. 1 exhibit anion photoelectron spectra of $[\text{Pt}(\text{H}_2\text{O})]^-$, i.e., **a**, **b**, and **c**, where in each case the subject $[\text{Pt}(\text{H}_2\text{O})]^-$ species had been generated under the same laser vaporization (source) power conditions that had been used to measure their corresponding mass spectra **A**, **B**, and **C**, respectively. All $[\text{Pt}(\text{H}_2\text{O})]^-$ spectra were taken at mass = 216 to ensure that the photoelectron signals were solely from $[\text{Pt}(\text{H}_2\text{O})]^-$. These three photoelectron spectra of $[\text{Pt}(\text{H}_2\text{O})]^-$ clearly differ substantially from one another, strongly suggesting the presence of $[\text{Pt}(\text{H}_2\text{O})]^-$ isomers, whose generation depended on laser vaporization (source) power. As will be explained below, the anion

photoelectron spectra **a**, **b**, and **c** have been labeled with the identities of their $[\text{Pt}(\text{H}_2\text{O})]^-$ isomers.

Potentially, the anionic metal-water complex, $[\text{M}(\text{H}_2\text{O})]^-$, could exist in three different structures: (i) one in which M^- is “solvated” by a physisorbed water molecule, resulting in $\text{M}^-(\text{H}_2\text{O})$, (ii) a structure where one of the O–H bonds in H_2O has been broken, resulting in HMOH^- , and (iii) a structure in which both O–H bonds in H_2O have been broken, resulting in H_2MO^- . As we will show, all three of these structural isomers were found to exist in the ion beam. The anionic complexes that result from one or both O–H bonds having been broken and the detached atom(s) having been reattached are water activation products. These activated species are *intermediates* along the reaction pathway that leads to H_2 formation, i.e., water splitting.

We utilized anion photoelectron spectroscopy to distinguish between these isomers.²³ Typically, when weak physisorption (“solvation”) interactions occur between an anion and a water molecule, i.e., in anion-molecule complexes, the photoelectron spectral pattern of the resulting hydrated anion closely resembles that of the anion alone, except for it having been shifted to slightly higher electron binding energy (EBE) values and its features broadened. This is because M^- remains the

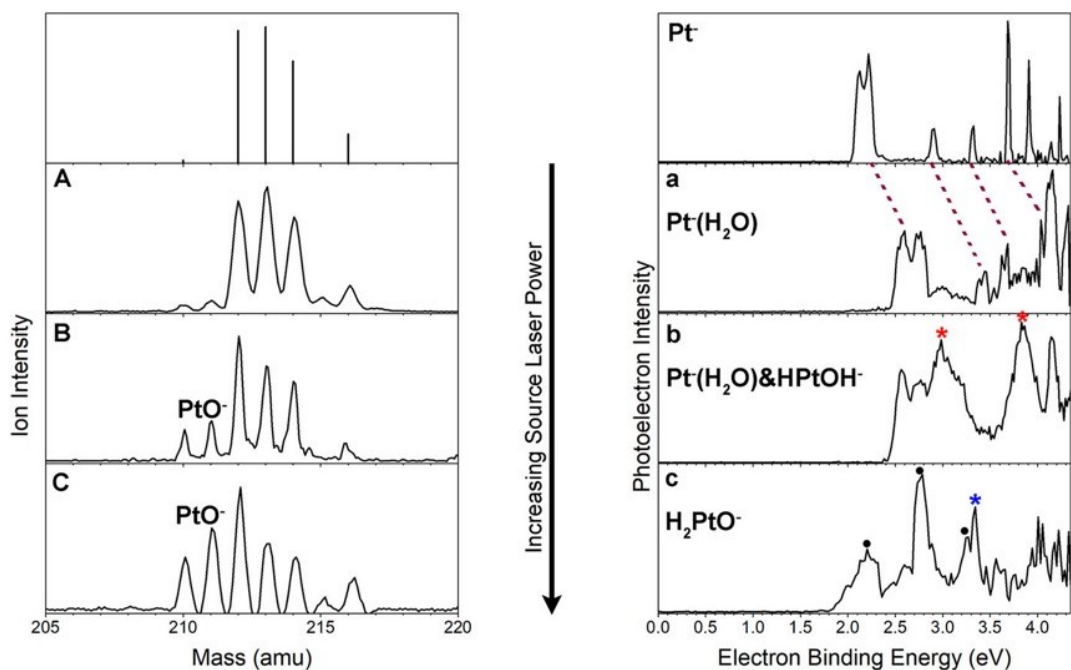


Figure IV.2.1 The top left panel presents a stick mass spectrum showing the simulated isotopic mass distribution of $[\text{Pt}(\text{H}_2\text{O})]^-$. The panels below it show the mass spectra of $[\text{Pt}(\text{H}_2\text{O})]^-$ species formed under three different laser vaporization power source conditions; mass spectrum **A** was recorded under low vaporization laser power, **B** under moderate vaporization laser power, and **C** under high vaporization laser power. In all cases, laser vaporization was carried out using the second harmonic (2.33 eV/photon) of a Nd:YAG laser. The top right panel presents the anion photoelectron spectrum of the Pt^- atomic anion. The panels below it show the anion photoelectron spectra of $[\text{Pt}(\text{H}_2\text{O})]^-$ species **a**, **b**, and **c**, where in each case the $[\text{Pt}(\text{H}_2\text{O})]^-$ anions had been generated under the same laser vaporization power conditions used to record their corresponding mass spectra **A**, **B**, and **C**, respectively. In all cases, the anion photoelectron spectra were measured using the fourth harmonic (4.66 eV/photon) of a Nd:YAG laser.

chromophore for photodetachment; no truly chemical interactions have occurred. Photoelectron spectrum **a** on the right-hand side of Fig. 1 is an example of such an interaction. Its spectrum displays the same spectral pattern as the photoelectron spectrum of Pt^- , which sits above it in Fig. 1, except for its peaks being slightly blue-shifted and broadened. The $[\text{Pt}(\text{H}_2\text{O})]^-$ isomer in photoelectron spectrum **a** is thus seen to be the platinum atomic anion-water “solvation” complex, $\text{Pt}^-(\text{H}_2\text{O})$.

At higher laser vaporization (source) power, PtO^- begins to appear in mass spectrum **B** of Fig. 1. Photoelectron spectrum **b** exhibits both the hydrated anion spectral peaks of spectrum **a** and new features, the most prominent of which are marked with red stars at EBE values of 2.98 eV and 3.83 eV. This new feature is due to another (a second) isomer.

At still higher laser vaporization (source) power, mass peaks due to PtO^- in mass spectrum **C** have become even stronger. In its corresponding anion photoelectron spectrum, i.e., **c**, the peaks due to the solvated anion, $\text{Pt}^-(\text{H}_2\text{O})$, have completely disappeared and four new peaks have appeared. One of them, marked with a blue star at $\text{EBE} = 3.34$ eV, is due to yet another, i.e., a third, isomer of $[\text{Pt}(\text{H}_2\text{O})]^-$, while the other three peaks, marked with black dots, exhibit EBE values that are identical to those in the photoelectron spectrum of PtO^- [see Fig. S2 and Ref. 21]. There are two

possible explanations for the appearance of the PtO^- photoelectron spectrum within photoelectron spectrum **c**: (1) These peaks may have arisen due to two-photon processes, in which the first photon dissociated the newly formed, third $[\text{Pt}(\text{H}_2\text{O})]^-$ isomer, producing PtO^- , while a second photon photodetached an electron from PtO^- . (2) Due to the relatively high source-laser power being used in this case, another possibility is that metastable $[\text{Pt}(\text{H}_2\text{O})]^-$ was formed in the source and that it dissociated along the time-of-flight drift path, resulting in PtO^- , which continued to travel at the velocity of the TOF-extracted $[\text{Pt}(\text{H}_2\text{O})]^-$ anions into the photodetachment region.²⁴ Since photoelectron spectrum **c** was taken at the unambiguous mass of $[\text{Pt}(\text{H}_2\text{O})]^-$, this evidence alone implies that the newly formed (third) isomer in photoelectron spectrum **c** must have been H_2PtO^- and that the other fragment must have been H_2 . Together, anion photoelectron spectra **a**, **b**, and **c** thus revealed the presence of three structural isomers of $[\text{Pt}(\text{H}_2\text{O})]^-$, the hydrated Pt^- anion complex and two others, both of which involved O–H bond breaking.

Normally, the neutral products of a gas-phase reaction can only be indirectly deduced by counting the atom difference between reactants and charged products. Here, however, to search for the presence of H_2 , which had been implied by our observations, we utilized an electron bombardment ionizer located along the beam path between the source and the TOF ion extractor. There, we changed appropriate voltages and

polarities in order to record positive ion mass spectra so that neutral H_2 could be ionized to H_2^+ and observed by our mass spectrometer. Nevertheless, when the laser vaporization (source) power was low, no H_2^+ was seen. The only cations that we observed were He^+ , O^+ , OH^+ , and H_2O^+ as seen in Fig. 2(a), all of which had formed due to ionization of $\text{H}_2\text{O}/\text{He}$ backing gases from the source. However, when the laser power was increased to the level used to record mass spectrum C, H_2^+ was detected as shown in Fig. 2(b). This observation provided direct evidence that a single platinum atomic anion reacting with a single water molecule had produced H_2 .

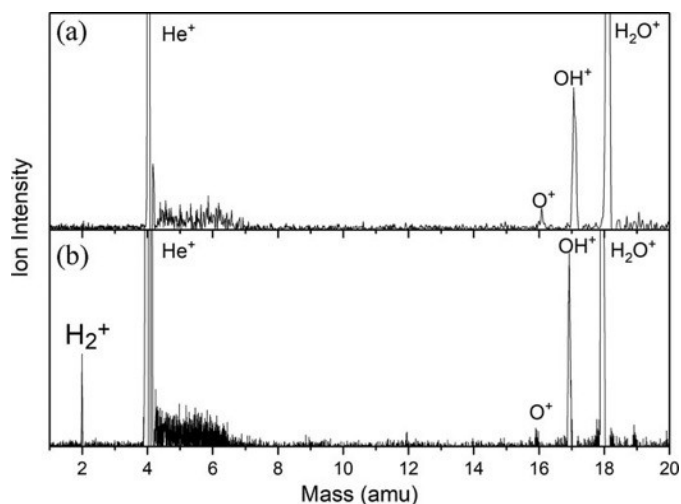


Figure IV.2.2 Positive ion, electron bombardment ionization mass spectra of the species made under low vaporization laser power (a) and high vaporization laser power (b).

The photoelectron spectra of $[\text{Pt}(\text{H}_2\text{O})_2]^-$ and $[\text{Pt}(\text{H}_2\text{O})_3]^-$ are presented in Fig. S3. The absence of new features in these spectra suggests that when Pt^- reacts with either a water dimer or trimer, it only interacts with a single water molecule, while the other

water molecules just solvate the $[\text{Pt}(\text{H}_2\text{O})]^-$.

Parallel experimental studies were also conducted on $[\text{Ni}(\text{H}_2\text{O})]^-$ and $[\text{Pd}(\text{H}_2\text{O})]^-$. Their experimental mass spectra are presented in Fig. S4, along with their expected isotopic mass distributions. Unlike in the case of $[\text{Pt}(\text{H}_2\text{O})]^-$, neither NiO^- nor PdO^- was observed even at elevated source laser powers. Additionally, no H_2^+ was observed in either of these cases, indicating that H_2 was not formed. Figure 3 presents the anion photoelectron spectra of $[\text{Ni}(\text{H}_2\text{O})]^-$ and $[\text{Pd}(\text{H}_2\text{O})]^-$, along with those of their corresponding atomic anions, Ni^- and Pd^- . As in anion photoelectron spectrum **b**, in the case of $[\text{Pt}(\text{H}_2\text{O})]^-$, the photoelectron spectra of $[\text{Ni}(\text{H}_2\text{O})]^-$ and $[\text{Pd}(\text{H}_2\text{O})]^-$ exhibit spectral features that are due to both the solvated anion complexes, $\text{Ni}^-(\text{H}_2\text{O})$ and $\text{Pd}^-(\text{H}_2\text{O})$, and additional structural isomers, these being marked by red dots in Fig. 3. As will be explained below, the anion photoelectron spectra of $[\text{Ni}(\text{H}_2\text{O})]^-$ and $[\text{Pd}(\text{H}_2\text{O})]^-$ have been labeled with the identities of their isomers.

In addition to measuring the anion photoelectron spectra of $[\text{M}(\text{H}_2\text{O})]^-$, where $\text{M} = \text{Pt}, \text{Ni},$ and Pd , we also measured the photoelectron spectra of $[\text{M}(\text{H}_2\text{O})]^-$, where $\text{M} = \text{Cu}, \text{Ag}, \text{Au}, \text{Fe}, \text{Co},$ and V . These latter $[\text{M}(\text{H}_2\text{O})]^-$ species were formed utilizing the same source laser power protocol used to make $[\text{Ni}(\text{H}_2\text{O})]^-$ and $[\text{Pd}(\text{H}_2\text{O})]^-$ and photoelectron spectrum **b** in the case of $[\text{Pt}(\text{H}_2\text{O})]^-$. The anion photoelectron spectra

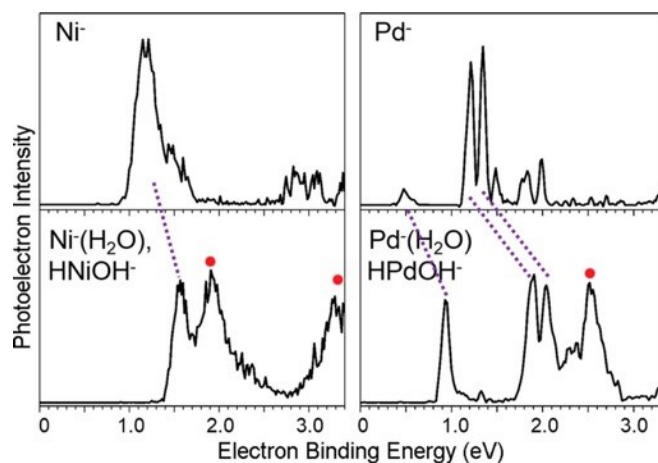


Figure IV.2.3 Photoelectron spectra of the atomic metal anions, M^- , (in the upper panels) and their corresponding $[M(H_2O)]^-$ anions (in the lower panels), where $M = Ni$ and Pd . All of these anion photoelectron spectra were measured using the third harmonic (3.49 eV/photon) of a Nd:YAG laser. Dotted tie-lines link M^- peaks to the corresponding blue-shifted peaks in their $M^-(H_2O)$ anion-molecule complexes. Additional structural isomers are marked by red dots.

of $[M(H_2O)]^-$, where $M = Cu, Ag, Au, Fe, Co,$ and V , are displayed along with their atomic anion photoelectron spectra in Fig. S5. All of them are simple anion-molecule (physisorbed) complexes, i.e., $M^-(H_2O)$. It is important to note that none of them showed any photoelectron spectral features beyond those expected for an anion-molecule complex.

The details of our computational methods are presented in the supplementary material. Briefly, to assess the potential multi-reference nature of $[M(H_2O)]^-$ and its neutral counterparts, we initially relied on the internally contracted Multi-Reference

Configuration Interaction (icMRCI) level of theory. The resultant mainly single reference character implied by those icMRCI calculations allowed us to employ the size-extensive, coupled cluster singles and doubles with perturbatively connected triples [CCSD(T)] approach to calculate vertical detachment energies (VDEs), where VDE is the vertical energy difference between an anion's ground state and its neutral counterpart at the structure of the anion.

The EBE values of the peak maxima in the photoelectron spectra are their VDE values. We have calculated VDE values for both HMOH^- and H_2MO^- isomers ($\text{M} = \text{Pt}, \text{Ni}, \text{Pd}$) and compared them with the measured VDE values of the new spectral features. These are presented in Table I. For the HMOH^- isomer, good agreement was obtained between experimental and calculated VDE values, indicating that the water-activated isomers, HPtOH^- , HNiOH^- , and HPdOH^- , were all present in their respective ion beams.

As for the H_2MO^- isomer, there is strong evidence for the presence of H_2PtO^- in photoelectron spectra of $[\text{Pt}(\text{H}_2\text{O})]^-$. The peak at $\text{EBE} = 3.34 \text{ eV}$ in anion photoelectron spectrum **c** is in good agreement with the theoretically calculated EBE values of 3.40 eV and 3.45 eV. The high intensity of PtO^- in its corresponding mass spectrum, i.e., **C**, the appearance of the photoelectron spectrum of PtO^- within the

TABLE 1. Experimentally determined VDE values for $[\text{Pt}(\text{H}_2\text{O})]^-$, $[\text{Ni}(\text{H}_2\text{O})]^-$, and $[\text{Pd}(\text{H}_2\text{O})]^-$ compared with the computed CCSD(T)/aug-cc-pVTZ VDE values. In the case of $[\text{Pt}(\text{H}_2\text{O})]^-$, experimentally measured VDE values for the isomer features found in photoelectron spectrum **b** are labeled separately from that of the isomer feature found in photoelectron spectrum **c**. Experimentally determined VDE values for the hydrated-anion complexes (isomers), $\text{Pt}^-(\text{H}_2\text{O})$, $\text{Ni}^-(\text{H}_2\text{O})$, and $\text{Pd}^-(\text{H}_2\text{O})$, are not included in this table.

		Theoretical VDE (eV)		Expt. VDE (eV)	
HPtOH ⁻	² A → ³ A	3.02	H ₂ PtO ⁻ ² B ₁ → ³ B ₁	3.45	2.98 b
	² A → ¹ A	3.01	² B ₁ → ¹ A ₁	3.40	3.34 c
	² A → ² ³ A	3.70			3.83 b
HNiOH ⁻	² A → ³ A	1.81	H ₂ NiO ⁻ ² B ₁ → ³ B ₁	2.75	1.91
	² A → ¹ A	3.04	² B ₁ → ¹ A ₁	2.43	3.24
HPdOH ⁻	² A → ³ A	2.64	H ₂ PdO ⁻ ² B ₁ → ³ B ₁	2.49	2.50
	² A → ¹ A	2.37	² B ₁ → ¹ A ₁	3.20	

mass-selected photoelectron spectrum of $[\text{Pt}(\text{H}_2\text{O})]^-$, and the observation of H_2^+ , all under relatively high source laser powers, are consistent with the presence of H_2PtO^- and with its decay into PtO^- and H_2 . However, the case for the presence of H_2PtO^- at moderate source laser powers is less clear. While mass spectrum **B** exhibits PtO^- , although at relatively lower intensities than does mass spectrum **C** and while traces of H_2^+ are detected under moderate source laser power conditions, the theoretically predicted telltale H_2PtO^- peak at EBE ~ 3.4 eV, easily seen in

photoelectron spectrum **c**, was not evident in photoelectron spectrum **b**. Instead, the EBE ~ 3.4 eV region in photoelectron spectrum **b** is an intensity valley, although its floor does exhibit considerable intensity. Also, the PtO^- peaks seen in photoelectron spectrum **c** are absent in photoelectron spectrum **b**. We conclude that if H_2PtO^- is formed under moderate source laser power conditions, there must be much less of it made than under higher laser power conditions. Additionally, Table I and Fig. 3 provide no significant evidence for the presence of H_2NiO^- and H_2PdO^- isomers in the beam. Also, since neither NiO^- , PdO^- nor H_2^+ were observed in $[\text{Ni}(\text{H}_2\text{O})]^-$ and $[\text{Pd}(\text{H}_2\text{O})]^-$ experiments, even at high source laser powers, the implication is that they were not formed.

High level electronic structure calculations provide insight into the reaction mechanisms and detailed rationalizations of the similarities and differences between the different metal anions. Figure 4 shows the calculated potential energy pathways and key structures involved in the reactions of Ni^- , Pd^- , and Pt^- atomic anions with a single water molecule. The coordinates and energies of these structures are provided in the supplementary material. For example, Fig. 4 provides a possible explanation for why only H_2PtO^- was formed among the three group 10 systems we studied. Figure 4 shows that only H_2PtO^- is definitively exothermic relative to $\text{M}^- + \text{H}_2\text{O}$.

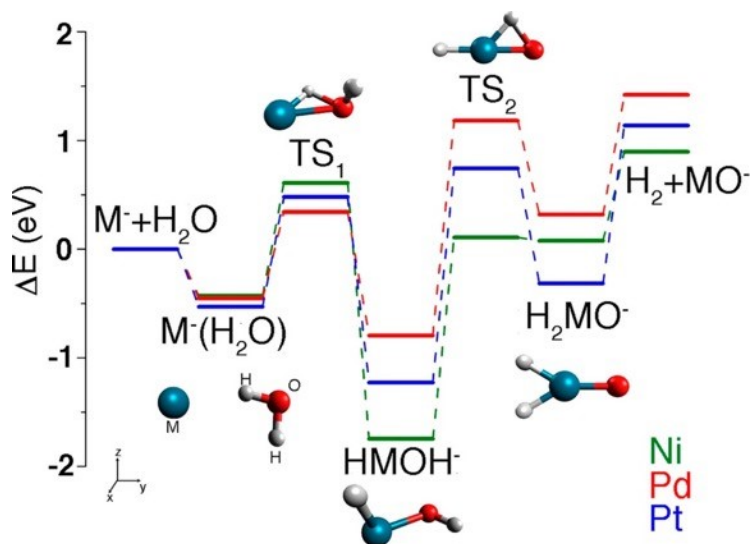


Figure IV.2.4 The calculated potential energy pathways and stationary points involved in the reactions of Ni^- , Pd^- , and Pt^- with a single water molecule, H_2O . Zero-point vibrational and spin-orbit corrections are also included.

Unlike the conversion of $\text{M}^+(\text{H}_2\text{O})$ cationic complexes to HMOH^+ ($\text{M} = \text{Pd}, \text{Pt}$), which according to theory is endothermic,²⁵ the transformation from $\text{M}^-(\text{H}_2\text{O})$ anionic complexes to HMOH^- is exothermic in all three ($\text{M} = \text{Ni}, \text{Pd}, \text{Pt}$) cases shown in Fig. 4. The transition state, TS_1 , however, is higher in energy than the energies of both $\text{M}^- + \text{H}_2\text{O}$ and $\text{M}^-(\text{H}_2\text{O})$ in all three cases. The barrier to be overcome is ~ 0.5 eV, i.e., the energy of TS_1 minus the energy of the reactants, $\text{M}^- + \text{H}_2\text{O}$ or ~ 1.0 eV, the energy of TS_1 minus the energy of $\text{M}^-(\text{H}_2\text{O})$. These computed barriers include zero-point vibrational and spin-orbit corrections. Many reactions are known to proceed with barrier heights that are similar to these values.²⁶⁻²⁹

Let us further consider our results when the highest source-laser power was utilized, i.e., see panels **C** and **c** in Fig. 1. Under those circumstances, excess energy was available to the system, and in the case of H_2PtO^- , the excess energy was used to both make it and drive the reaction to the final products, PtO^- and H_2 . The excess energy is also likely responsible for the formation of metastable H_2PtO^- complexes, these having been discussed above. While the origin of the excess energy that became available under these high source-laser power conditions is not fully resolved, the options are thermal excitation, electronic excitation, or both.

Conclusion

To summarize, we have investigated water activation and splitting by various single atomic anions, which were not previously explored in the gas phase. We demonstrated that platinum is special among all investigated metals and that a single platinum atomic anion can both activate and split a single water molecule, while single palladium and nickel atomic anions only activate water molecules.

In the electrolysis of water, H_2 gas forms at the cathode, which is typically platinum, while O_2 forms at the anode. It is interesting to contemplate the relationship between the microscopic interaction between a single platinum atom, a single electron, and a single water molecule and the more complicated, macroscopic interaction between a

platinum cathode and liquid water during electrolysis. Respectively, both processes involve surmountable energy barriers and low over-potentials, which are characteristically exceptional properties of platinum.

References

1. D. G. Nocera, "The artificial leaf," *Acc. Chem. Res.* **45**, 767–776 (2012).
2. K. Liu, Y. Liu, N. Liu, Y. Han, S. Lee, X. Zhang, J. Zhong, H. Huang, and Z. Kang, "Metal-free efficient photocatalyst for stable visible water splitting via a two-electron pathway," *Science* **347**, 970–974 (2015).
3. B. Rausch, M. D. Symes, G. Chisholm, and L. Cronin, "Decoupled catalytic hydrogen evolution from a molecular metal oxide redox mediator in water splitting," *Science* **345**, 1326–1330 (2014).
4. R. J. Roach, W. H. Woodward, A. W. Castleman, Jr., A. C. Reber, and S. N. Khanna, "Complementary active sites cause size-selective reactivity of aluminum cluster anions with water," *Science* **323**, 492–495 (2009).
5. M. D. Kärkäs, O. Verho, E. V. Johnston, and B. Åkermark, "Artificial photosynthesis: Molecular systems for catalytic water oxidation," *Chem. Rev.* **114**, 11863–12001 (2014).
6. J. A. Kerr, "Activation of water, ammonia, and other small molecules by PC_{carbene}P nickel pincer complexes," *Chem. Rev.* **66**, 465–500 (1966).
7. D. V. Gutsulyak, W. E. Piers, J. Borau-Garcia, and M. Parvez, "Activation of water, ammonia, and other small molecules by PC_{carbene}P nickel pincer complexes," *J. Am. Chem. Soc.* **135**, 11776–11779 (2013).
8. J. Li and K. Yoshizawa, "Computational evidence for hydrogen generation by reductive cleavage of water and α -H abstraction on a molybdenum complex," *Angew. Chem., Int. Ed.* **50**, 11972–11975 (2011).
9. R. Subbaraman, D. Tripkovic, D. Strmcnik, K. C. Chang, M. Uchimura, A. P. Paulikas, V. Stamenkovic, and N. M. Markovic, "Enhancing hydrogen evolution activity in water splitting by tailoring Li⁺-Ni(OH)₂-Pt interfaces," *Science* **334**, 1256–1260 (2011).
10. F. Jiao and H. Frei, "Nanostructured cobalt oxide clusters in mesoporous silica as efficient oxygen-evolving catalysts," *Angew. Chem., Int. Ed.* **48**, 1841–1844 (2009).
11. J. Li, X. Wu, S. Zhou, S. Tang, M. Schlagen, and H. Schwarz, "Distinct mechanistic differences in the hydrogen-atom transfer from methane and water by the heteronuclear oxide cluster [Ga₂MgO₄]⁺," *Angew. Chem., Int. Ed.* **54**, 12298–12302 (2015).
12. S. M. Lang, T. M. Bernhardt, M. Krstic, and V. M. Koutecky, "Water activation by small free ruthenium oxide clusters," *Phys. Chem. Chem. Phys.* **16**, 26578–26583 (2014).
13. X. Yang, A. Wang, B. Qiao, J. Li, J. Liu, and T. Zhang, "Single-atom catalysts: A new

- frontier in heterogeneous catalysis,” *Acc. Chem. Res.* **46**, 1740–1748 (2013).
14. N. Cheng, S. Stambula, D. Wang, M. N. Banis, J. Liu, A. Riese, B. Xiao, R. Li, T. K. Shm, L. M. Liu *et al.*, “Platinum single-atom and cluster catalysis of the hydrogen evolution reaction,” *Nat. Commun.* **7**, 13638 (2016).
 15. C. Ling, L. Shi, Y. Ouyang, X. C. Zeng, and J. Wang, “Nanosheet supported single-metal atom bifunctional catalyst for overall water splitting,” *Nano Lett.* **17**, 5133–5139 (2017).
 16. J. Deng, H. Li, J. Xiao, Y. Tu, D. Deng, H. Yang, H. Tian, J. Li, P. Ren, and X. Bao, “Triggering the electrocatalytic hydrogen evolution activity of the inert two-dimensional MoS₂ surface via single-atom metal doping,” *Energy Environ. Sci.* **8**, 1594–1601 (2015).
 17. M. J. Berr, F. F. Schweinberger, M. Döblinger, K. E. Sanwald, C. Wolff, J. Breimeier, A. S. Crampton, C. J. Ridge, M. Tschurl, U. Heiz *et al.*, “Size-selected subnanometer cluster catalysts on semiconductor nanocrystal films for atomic scale insight into photocatalysis,” *Nano Lett.* **12**, 5903–5906 (2012).
 18. K. Wu, H. Zhu, Z. Liu, W. Rodríguez-Córdoba, and T. Lian, “Ultrafast charge separation and long-lived charge separated state in photocatalytic CdS–Pt nanorod heterostructures,” *J. Am. Chem. Soc.* **134**, 10337–10340 (2012).
 19. L. Amirav and A. P. Alivisatos, “Photocatalytic hydrogen production with tunable nanorod heterostructures,” *J. Phys. Chem. Lett.* **1**, 1051–1054 (2010).
 20. X. Zhang, G. Liu, G. Gantefoär, K. H. Bowen, and A. N. Alexandrova, “PtZnH₅⁻, a σ -aromatic cluster,” *J. Phys. Chem. Lett.* **5**, 1596–1601 (2014).
 21. T. M. Ramond, G. E. Davico, F. Hellberg, F. Svedberg, P. Salén, P. Söderqvist, and W. C. Lineberger, “Photoelectron spectroscopy of nickel, palladium, and platinum oxide anions,” *J. Mol. Spectrosc.* **216**, 1–14 (2002).
 22. J. Thogersen, L. D. Steele, M. Scheer, C. A. Brodie, R. C. Bilodean, and K. Haugen, “Electron affinities of Si, Ge, Sn and Pt by tunable laser photodetachment studies,” *J. Phys. B: At., Mol. Opt. Phys.* **29**, 1323–1330 (1996).
 23. S. E. Eustis, D. Radisic, K. H. Bowen, R. A. Bachorz, M. Haranczyk, G. K. Schenter, and M. Gutowski, “Electron-driven acid-base chemistry proton transfer from hydrogen chloride to ammonia,” *Science* **319**, 936–939 (2008).
 24. The fact that our mass spectra showed both PtO⁻ and H₂⁺ as having been formed between the source and the TOF ion extractor under high source-laser power conditions also implies the formation of metastable H₂PtO⁻ species in the source region.
 25. O. Lakuntza, J. M. Matxain, F. Ruipérez, J. N. Ugalde, and P. B. Armentrout, “Quantum chemical study of the reactions between Pd⁺/Pt⁺ and H₂O/H₂S,” *Chem. - Eur. J.* **19**, 8832–8838 (2013).
 26. A. Sanchez, S. Abbet, U. Heiz, W. D. Schneider, H. Hakkinen, R. N. Barnett, and U. Landman, “When gold is not noble: Nanoscale gold catalysts,” *J. Phys. Chem. A* **103**, 9573–9578 (1999).
 27. H. Schwarz, “Doping effects in cluster-mediated bond activation,” *Angew. Chem., Int. Ed.* **54**, 10090–10100 (2015).
 28. S. M. Lang, T. Bernhardt, V. Chernyy, J. M. Hakker, R. N. Barnett, and U. Landman,

- “Selective C–H bond cleavage in methane by small gold clusters,” *Angew. Chem., Int. Ed.* **56**, 13406–13410 (2017).
29. X. Zhang, G. Liu, K. H. Meiwes-Broer, G. Gantefoer, and K. H. Bowen, “CO₂ activation and hydrogenation by PtH_n[−] cluster anions,” *Angew. Chem., Int. Ed.* **55**, 9644–9647 (2016).

IV.3 Activation of Hydroxylamine by Single Gold Atomic Anions

Gaoxiang Liu, Sandra M. Ciborowski, Zhaoguo Zhu, Kit H. Bowen

*Department of Chemistry, Johns Hopkins University, 3400 N. Charles Street,
Baltimore, MD 21218, USA*

Abstract

Hydroxylamine (HA) is a potential component in next-generation monopropellants. In this work, we present a combined anion photoelectron spectroscopic and density functional theory study of the reaction between a single HA molecule and a single gold atomic anion, Au^- . This study shows that an Au^- anion can activate a HA molecule by inserting into its N–O bond. Our calculations show this reaction to be facilitated by the presence of two minimum energy crossing points (MECP's), i.e., spin flips, along the reaction pathway.

Introduction

Replacing hydrazine with less toxic ionic liquids as monopropellants in spacecraft thrusters is appealing from both a safety and an environmental perspective. Hydroxylammonium nitrate (HAN) is one such ionic liquid being considered. In fact, HAN is a component in the monopropellant used in NASA's Green Propellant Infusion Mission [1,2]. Studies of both the thermal and catalytic

decomposition mechanisms of HAN have informed the further development of HAN-based monopropellants and thus of thrusters [[3]-[18]]. Hydroxylamine (H_2NOH , HA) is a major thermal decomposition product of HAN. As such, HA can further decompose on heated iridium catalysts, creating ignition conditions in HAN-based propellants [17,19].

Single metal atoms are sometimes seen as models for mimicking active sites in heterogeneous catalysts [[20], [21], [22], [23], [24], [25]]. Studying molecular activation and catalysis using gas-phase, metal atomic ions can help to better understand bond activation, dissociation, and new bond formation at the molecular level and thus to aid the design of new catalysts [[26], [27], [28], [29]]. In the present work, we focused on studying the activation of HA by single gold atomic anions. Molecular activation by gold ions has received considerable attention in gas-phase studies. While the gold atomic cation has been found to activate various molecules [[30], [31], [32], [33], [34]], the gold atomic anion tends to be inert in activating small molecules [[35], [36], [37], [38], [39], [40], [41], [42]]. An exception, however, is the activation of CO_2 by Au^- , a process that involves only charge transfer and not bond breaking [43,44]. Here, we utilize a combination of anion photoelectron spectroscopy and density functional theory (DFT) to provide strong evidence that Au- can break the N–O bond in HA, thus activating it. As shown below, Au- spin states

play critical roles in activating HA.

Experimental and Computational Methods

Anion photoelectron spectroscopy is conducted by crossing a beam of mass-selected negative ions with a fixed-frequency photon beam and energy-analyzing the resultant photodetached electrons. The photodetachment process is governed by the energy-conserving relationship: $h\nu = EBE + EKE$, where $h\nu$ is the photon energy, EBE is the electron binding energy, and EKE is the electron kinetic energy. Our apparatus consists of a laser vaporization cluster anion source with an attached ligation cell, a time-of-flight mass spectrometer, a Nd:YAG photodetachment laser (operating at 355 nm), and a magnetic bottle electron energy analyzer with a resolution is ~ 35 meV at 1 eV EKE [45]. Photoelectron spectra were calibrated against the well-known atomic transitions of atomic Cu^- [46].

The interaction between Au^- and HA was studied using a laser vaporization-reaction cell arrangement [47]. Atomic gold anions were generated by laser vaporization of a pure gold foil wrapped around an aluminum rod. The resultant plasma was cooled with helium gas delivered by a pulsed valve, having a backing pressure of 100 psig. The resulting gold anions then traveled through a ligation cell (4-mm diameter), where it encountered HA/H₂O mixed vapor. The HA/H₂O mixed vapor was introduced into

the ligation cell by a second pulsed valve, within which resided a drop of hydroxylamine water solution (Since HA in its pure form is hazardous, it is sold dissolved in water, 50 wt%). The resulting $[\text{Au}(\text{HA})]^-$ anionic clusters were then mass-analyzed and mass-selected by the time-of-flight mass spectrometer and their photoelectron spectra measured.

Density functional theory calculations were performed with the ORCA computational chemistry software package [48]. All calculations were carried out with the PBE0 functional [49,50] with the D3 dispersion correction [51] and the RIJCOSX approximation [52]. The Ahlrichs Def2 basis sets, Def2-TZVP were used throughout our calculations [53]. The Stuttgart effective core potential, SDD [54] and the ECP basis set, Def2-TZVP|Def2-TZVP/J were used for the gold atoms. Vertical detachment energies (VDE) were computed from the energetic difference between the relaxed anionic complex and its corresponding neutral species at the geometry of the relaxed anion. Frequency calculations were performed to verify that no imaginary frequencies existed and all optimized structures were minima. The minimum-energy crossing points (MECPs) for the intersection of the electronic states of different spin multiplicities were searched for and located by using the method developed by Harvey et al. [55].

Results and Discussions

The mass spectra with or without the addition of the HA/H₂O mixed vapor into the reaction cell are shown in Fig. 1. With no HA/H₂O mixed vapor, only Au⁻ was observed in the mass spectrum. After adding HA/H₂O vapor to the reaction cell, peaks due to both [Au(H₂O)]⁻ and [Au(HA)]⁻ complexes appeared in the mass spectrum, these resulting from the interaction of Au⁻ with HA or H₂O, respectively. [Au(H₂O)]⁻ has been studied in our previous work and is not the focus of the current study [41]. [Au(HA)]⁻, on the other hand, could exist either as Au⁻(HA), where HA is physisorbed onto Au⁻ or as a [Au(HA)]⁻ complex, where one or more bonds in HA (N-H, O-H or N-O bond) have been broken. This latter case would correspond to the activation of HA.

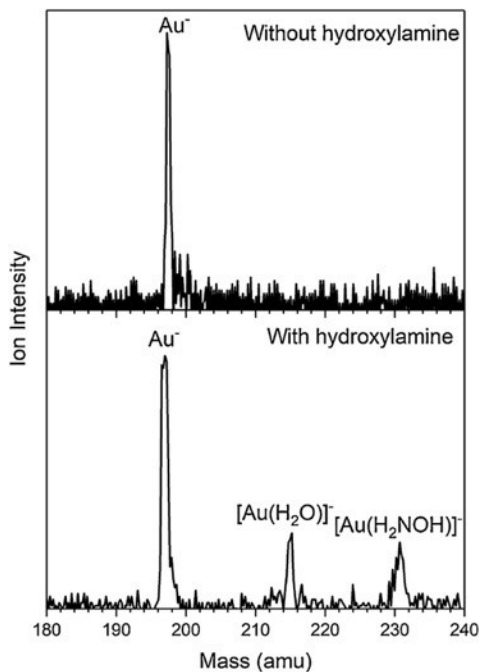


Figure IV.3.1 The mass spectra of Au^- anions without and with the addition of HA/ H_2O mixed vapor.

To distinguish between these isomers, the anion photoelectron spectrum of $[\text{Au}(\text{HA})]^-$ was measured. Typically, when an atomic metal anion is physisorbed by another molecule, the photoelectron spectrum of the resulting weakly-attached cluster anion closely resembles that of the atomic anion alone, since that anion acts as the chromophore. Thus, except for being shifted to higher electron binding energy (EBE) and its features slightly broadened, the resulting photoelectron spectrum looks like that of the atomic anion. Fig. 2 presents the anion photoelectron spectrum of $[\text{Au}(\text{HA})]^-$. The evident feature in this spectrum reaches its maximal intensity at $\text{EBE} = 3.00 \text{ eV}$. Thus, 3.00 eV is determined as the vertical detachment energy (VDE) value, i.e., the transition energy at which the Franck-Condon overlap between the anion's wavefunction and that of its neutral counterpart is at its maximum. Vibrational progressions spaced by 0.1 eV are also observed. The EBE of Au^- alone would have been at 2.3 eV , i.e., its electron affinity. Since the observed difference between the VDE values of Au^- and $[\text{Au}(\text{HA})]^-$ is, at $\sim 0.7 \text{ eV}$, relatively large for an ion-molecule interaction energy, and since there is evident vibrational excitation in the spectrum, it is clear that this is not the spectrum of the anion-molecule physisorbed complex, $\text{Au}^-(\text{HA})$. The observed spectrum implies that a strong chemical interaction has occurred between Au^- and HA, indicating hydroxylamine has been

activated by its interaction with Au⁻.

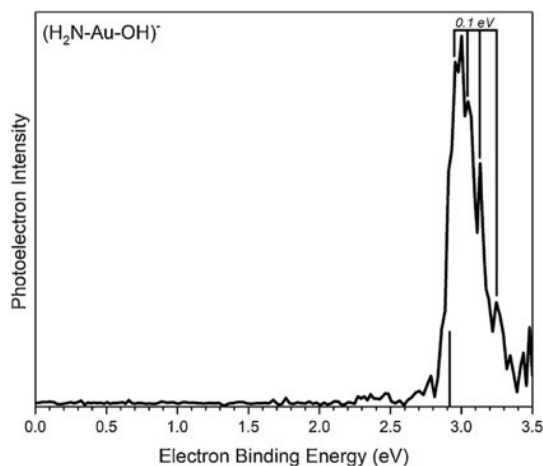


Figure IV.3.2 The photoelectron spectrum of $[\text{Au}(\text{HA})]^-$ taken by 3rd harmonic output of a Nd:YAG laser (3.496 eV). The stick spectrum represents the calculated VDE value.

Fig. 3 presents the DFT optimized structures of different $[\text{Au}(\text{HA})]^-$ isomers. The global minimum of $[\text{Au}(\text{HA})]^-$ has structure in which the Au^- inserts into the N–O bond of HA, that is, $\text{H}_2\text{N-Au-OH}^-$. The other isomers, $\text{H}_2\text{NO-Au-H}^-$, H-Au-NHOH^- and $\text{Au}^-(\text{H}_2\text{NOH})$ are essentially iso-energetic, although all of them are $\sim 1.8\text{--}1.9$ eV higher than the global minimum. The VDE of the global minimum $\text{H}_2\text{N-Au-OH}^-$ is calculated to be 2.91 eV, which agrees well with the experimental VDE of 3.00 eV. Because $\text{H}_2\text{N-Au-OH}^-$ is the most stable calculated isomer and since its calculated VDE agrees with the experimental value, we are confident that Au^- has inserted into the N–O bond of HA. The vibrational progression spaced at 0.1 eV is due to the bending modes of both N–H and O–H bonds.

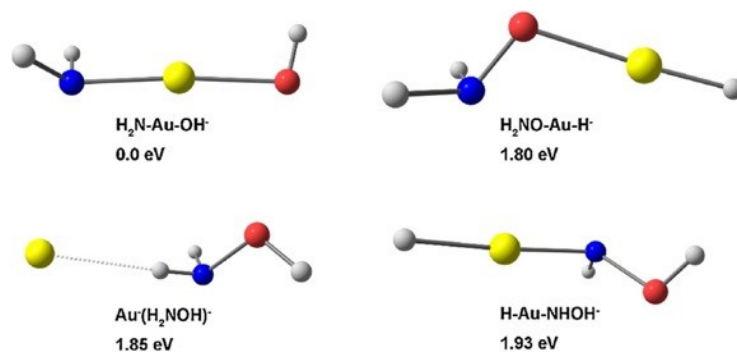


Figure IV.3.3 Optimized structures for $[\text{Au}(\text{HA})]^-$ and their relative energies.

The mechanism of HA activation by Au^- was investigated by DFT calculations. The resulting reaction pathway is presented in Fig. 4. The most salient feature of this pathway is the role of spin states. There, the singlet reactant, Au^- is converted to a triplet transition state before being converted back to the singlet product. Initially, Au^- and HA are both in their singlet ground states. After having formed the singlet adduct, $\text{Au}^-(\text{HA})$, in which HA is physisorbed to Au^- , the insertion of Au^- into the N–O bond begins to take place. Because of the rather high activation barrier (1.95 eV), however, the continuation of the reaction coordinate along the singlet surface is significantly hampered. Instead, the reaction can proceed more easily along the triplet transition state, which is only 0.73 eV above the entrance channel and much lower than the singlet transition state. The first minimal energy crossing point (MECP) is located between the physisorbed adduct and the transition states, where a crossover from the singlet to triplet surfaces occurs. This MECP is 0.95 eV higher than the entrance channel and 0.22 eV higher than the triplet transition state. Therefore, the

highest barrier the reactants need to overcome is the first MECP rather than the triplet transition state. Once the first spin flip has occurred, the insertion of Au⁻ into the NO bond is essentially barrier-free. After passing through the triplet transition state, where the NO bond is significantly lengthened, the activation complex encounters a second MECP, which converts it back to singlet state and to the final H₂N-Au-OH⁻ product.

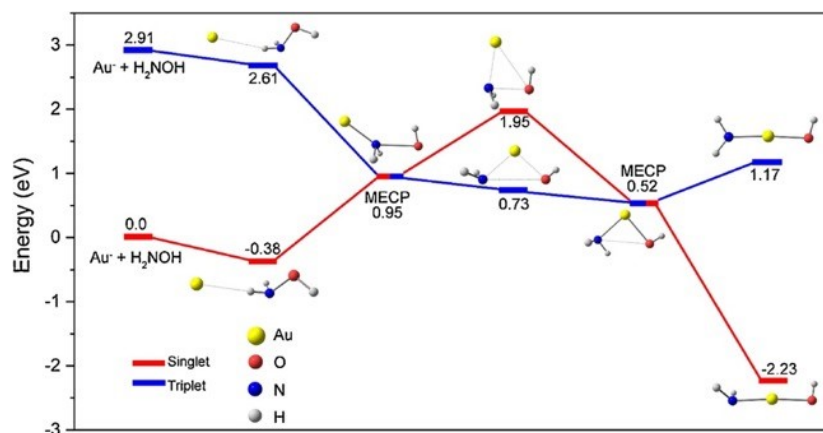


Figure IV.3.4 Calculated reaction pathway for HA activation by Au⁻. The numbers denote the relative energies of different structures.

Usually gold anions are inert to the activation of molecules. Such inertness can be explained by its d¹⁰s² ground state electron configuration: when a σ -bond is to be activated, the activating agent needs to have unpaired electrons, so that it can accept electrons from the bond to be activated. However, due to the lack of unpaired electrons in ground state Au⁻, such electron transfer from the σ -bond to Au⁻ is prohibited. An atomic orbital hybridization, which usually includes electron promotion to the 6p orbital, is thus required. According to our TDDFT calculations, the energy needed for

such promotion is around 2.9 eV, which is too high to surmount. In the present case, however, the interaction of Au⁻ with HA can reduce this promotion energy from 2.9 eV to 0.95 eV. As shown in Fig. 4, at the first MECF the [Au(HA)]⁻ complex converts from its singlet state to its triplet state, suggesting the creation of two unpaired electrons and empty orbitals on Au moiety which can then accept the two σ electrons of the N-O bond.

In summary, we have demonstrated that a single gold atomic anion can activate a hydroxylamine molecule by breaking its N-O bond, inserting there, and forming the H₂N-Au-OH⁻ complex. DFT calculations show that the spin crossover between singlet and triplet surfaces is critical for this activation to occur, as it creates the unpaired electrons and empty orbitals needed to accept the σ electron pair from the N-O bond.

References

1. R. Amrousse, T. Katsumi, N. Azuma, K. Hori, *Combust. Flame*, 176 (2017), pp. 334-348.
2. NASA GPIM. https://www.nasa.gov/mission_pages/tdm/green/overview.html (accessed January 12, 2017).
3. J.T. Cronin, T.B. Brill, *J. Phys. Chem.*, 90 (1986), pp. 178-181.
4. T.B. Brill, T.P. Russell, *Proc. SPIE* (1988), pp. 40-43.
5. J.T. Cronin, T.B. Brill, *Combust. Flame*, 74 (1988), pp. 81-89.
6. T.B. n, P.D. Spohn, J.T. Cronin, *J. Energy Mech. Mater. Manuf. Eng.*, 8 (1990), pp. 75-84.
7. J.W. Schoppelrei, T.B. Brill, *J. Phys. Chem. A*, 101 (1997), pp. 8593-8596.
8. Y.J. Lee, T.A. Litzinger, *Combust. Sci. Technol.*, 141 (1999), pp. 19-36.
9. H. Lee, T.A. Litzinger, *Combust. Flame*, 127 (2001), pp. 2205-2222.
10. H. Lee, T.A. Litzinger, *Combust. Flame*, 135 (2003), pp. 151-169.

11. C. Kappenstein, L. Courtheoux, R. Eloirdi, S. Rossignol, D. Duprez, N. Pillot, 38th AIAA/ASME/SAE/ASEE Joint Propulsion Conference & Exhibit, Joint Propulsion Conferences (2002).
12. L. Courtheoux, D. Amariei, S. Rossignol, C. Kappenstein, *Appl. Catal. B*, 62 (62) (2006), pp. 217-225.
13. D. Amariei, L. Courtheoux, S. Rossignol, C. Kappenstein, *Chem. Eng. Process.*, 46 (2007), pp. 165-174.
14. S. Banerjee, S.A. Shetty, M.N. Gowrav, C. Oommen, A. Bhattacharya, *Surf. Sci.*, 653 (2016), pp. 1-10.
15. C. Oommen, S. Rajaraman, R.A. Chandru, R. Rajeev, *IPCBEE*, 10 (2011), pp. 205-209.
16. R. Amrousse, K. Hori, W. Fetimi, K. Farhat, *Appl. Catal. B*, 127 (2012), pp. 121-128.
17. R. Amrousse, T. Katsumi, N. Itouyama, N. Azuma, H. Kagawa, K. Hatai, H. Ikeda, K. Hori, *Combust. Flame*, 162 (2015), pp. 2686-2692.
18. R. Amrousse, T. Katsumi, Y. Niboshi, N. Azuma, A. Bachar, K. Hori, *Appl. Catal. A Gen.*, 452 (2013), pp. 64-68.
19. S.D. Chambreau, D.M. Popolan-Vaida, G.L. Vaghjiani, S.R. Leone, *J. Phys. Chem. Lett.*, 8 (2017), pp. 2126-2130.
20. H. Schwarz, P. Gonzalez-Navarrete, J. Li, M. Schlangen, X. Sun, T. Weiske, S. Zhou, *Organometallics*, 36 (2017), pp. 8-17.
21. S.M. Lang, T.M. Bernhardt, V. Chernyy, J.M. Bakker, R.N. Barnett, U. Landman, *Angew. Chem. Int. Ed.*, 56 (2017), pp. 13406-13410
22. X.L. Ding, X.N. Wu, Y.X. Zhao, S.G. He, *Acc. Chem. Res.*, 45 (2012), pp. 382-390
23. H. Schwarz, *Isr. J. Chem.*, 54 (2014), pp. 1413-1431.
24. Z. Luo, A.W. Castleman Jr., S.N. Khanna, *Chem. Rev.*, 116 (116) (2016), pp. 14456-14492
25. D.K. Bohme, H. Schwarz, *Angew. Chem. Int. Ed.*, 44 (2005), pp. 2336-2354.
26. H. Schwarz, S. Shaik, J. Li, *J. Am. Chem. Soc.*, 139 (2017), pp. 17201-17212.
27. X.N. Li, X.P. Zou, S.G. He, *Chinese J. Catal.*, 38 (2017), pp. 1515-1527.
28. S. Zhou, J. Li, M. Schlangen, H. Schwarz, *Acc. Chem. Res.*, 49 (2016), pp. 494-502.
29. J. Roithova, D. Schröder, *Chem. Rev.*, 110 (2010), pp. 1170-1211.
30. T.M. Bernhardt, *Int. J. Mass Spec.*, 243 (2005), pp. 1-29.
31. J.M. Weber, *PATAI'S Chemistry of Functional Groups* (2014).
32. S. Zhou, J. Li, X.N. Wu, M. Schlangen, H. Schwarz, *Angew. Chem. Int. Ed.*, 55 (2016), pp. 441-444
33. C. Geng, J. Li, T. Weiske, M. Schlangen, S. Shaik, H. Schwarz, *J. Am. Chem. Soc.*, 139 (2017), pp. 1684-1689.
34. J. Li, S. Zhou, M. Schlangen, T. Weiske, H. Schwarz, *Chem. Select*, 3 (2016), pp. 444-447.
35. A.P. Woodham, G. Meijer, A. Fielick, *Angew. Chem. Int. Ed.*, 51 (2012), pp. 4444-4447.
36. R. Pal, L.M. Wang, Y. Pei, L.S. Wang, X.C. Zeng, *J. Am. Chem. Soc.*, 134 (2012), pp. 9438-9445.

37. R.F. Hockendorf, Y. Cao, M.K. Beyer, *Organometallics*, 29 (2010), pp. 3001-3006.
38. W. Huang, H.J. Zhai, L.S. Wang, *J. Am. Chem. Soc.*, 132 (2010), pp. 4344-4351.
39. Y. Gao, W. Huang, J. Woodford, L.S. Wang, X.C. Zeng, *J. Am. Chem. Soc.*, 131 (2009), pp. 9484-9485.
40. H.J. Zhai, C. Burgel, V. Bonacic-Koutecky, L.S. Wang, *J. Am. Chem. Soc.*, 130 (2008), pp. 9156-9167.
41. W. Zheng, X. Li, S. Eustis, A. Grubisic, O. Thomas, H. de Clercq, K. Bowen, *Chem. Phys. Lett.*, 444 (2007), pp. 232-236.
42. Y. Gao, X.C. Zeng, *ACS Catal.*, 2 (2012), pp. 2614-2621.
43. X. Zhang, E. Lim, S.K. Kim, K.H. Bowen, *J. Chem. Phys.*, 143 (2015), Article 174305.
44. B.J. Knurr, J.M. Weber, *J. Am. Chem. Soc.*, 134 (2012), pp. 18804-18808.
45. X. Zhang, G. Liu, G. Ganteför, K.H. Bowen, A.N. Alexandrova, *J. Phys. Chem. Lett.*, 5 (2014), pp. 1596-1601.
46. J. Ho, K.M. Ervin, W.C. Lineberger, *J. Chem. Phys.*, 93 (1990), pp. 6987-7002.
47. G. Liu, S. Ciborowski, K. Bowen, *J. Phys. Chem. A*, 121 (2017), pp. 5817-5822.
48. F. Neese, *WIREs Comput. Mol. Sci.*, 2 (2012), pp. 73-78.
49. J.P. Perdew, M. Ernzerhof, K. Burke, *J. Chem. Phys.*, 105 (1996), pp. 9982-9985.
50. J.P. Perdew, K. Burke, M. Ernzerhof, *Phys. Rev. Lett.*, 77 (1996), pp. 3865-3868.
51. S. Grimme, J. Antony, S. Ehrlich, H. Krieg, *J. Chem. Phys.*, 132 (2010), 10.1063/1.3382344.
52. F. Neese, F. Wennmohs, A. Hansen, U. Becker, *Chem. Phys.*, 356 (2008), pp. 98-109.
53. F. Weigend, R. Ahlrichs, *Phys. Chem. Chem. Phys.*, 7 (2005), pp. 3297-3305.
54. D. Andrae, U. Häußermann, M. Dolg, H. Stoll, H. Preuß, *Theor. Chim. Acta*, 77 (1990), pp. 123-141
55. J.N. Harvey, M. Aschi, H. Schwarz, W. Koch, *Theo. Chem. Acc.*, 99 (1998), pp. 95-99.

IV.4 The Metallo-Formate Anions, $M(\text{CO}_2)^-$, $M = \text{Ni, Pd, Pt}$, Formed by Electron-Induced CO_2 Activation

Gaoxiang Liu^a, Sandra M. Ciborowski^a, Zhaoguo Zhu^a, Yinlin Chen^a, Xinxing Zhang^b, and Kit H. Bowen^{*a}

^a*Department of Chemistry, Johns Hopkins University, Baltimore, Maryland 21218, USA.*

^b*Key Laboratory of Advanced Energy Materials Chemistry (Ministry of Education), College of Chemistry, Nankai University, Tianjin 300071, China*

Abstract

The metallo-formate anions, $M(\text{CO}_2)^-$, $M = \text{Ni, Pd, and Pt}$, were formed by electron-induced CO_2 activation. They were generated by laser vaporization and characterized by a combination of mass spectrometry, anion photoelectron spectroscopy, and theoretical calculations. While neutral transition metal atoms are normally unable to activate CO_2 , the addition of an excess electron to these systems led to the formation of chemisorbed anionic complexes. These are covalently bound, formate-like anions, in which their CO_2 moieties are significantly reduced. In addition, we also found evidence for an unexpectedly attractive interaction between neutral Pd atoms and CO_2 .

Introduction

The activation of carbon dioxide underpins its chemistry. Since the carbon atom in CO₂ is in its highest oxidation state, the activation of CO₂ inevitably involves reducing it, and that implies CO₂ accepting some degree of negative charge. Accomplishing this, however, requires at least a partial bending of CO₂. The CO₂⁻ anion that results from CO₂ having accepted a full negative charge is metastable; the electron affinity of CO₂ is -0.6 eV. While some studies have dealt with free carbon dioxide anions, most have focused on anionic complexes consisting of CO₂ and various other atoms and molecules.¹⁻⁴³ Anion photoelectron studies of N-heterocycle-CO₂ heterogeneous anionic dimers by Kim *et al.* showed significant covalent character in their intermolecular bond.^{6,7} Subsequent work by Johnson *et al.*⁸ and by ourselves⁹ added additional dimensions to this topic. In all cases, however, the CO₂ moieties were found to be partially negatively-charged and bent. Infrared photodissociation studies of transition metal-CO₂ anionic complexes by Weber *et al.* further explored this topic.¹⁰⁻²³ Both electrostatically-bound, metal atom-multiple CO₂ anionic complexes (physisorption) and covalently-bound, metal atom-multiple CO₂ anionic complexes (chemisorption) were found. In the latter cases, the CO₂ moieties were partially bent and had accepted some significant portion of the negative charge, while in the former cases, the CO₂ were only very slightly bent, suggesting insignificant CO₂ activation. Calculations implied that the metal atoms were far away from the CO₂ moieties in the neutral complexes, and that their

CO₂ moieties were structurally identical to isolated CO₂ molecules. Subsequent work in our laboratory measured the anion photoelectron spectra of copper-, silver-, and gold-CO₂ anionic dimers, finding only physisorption in the case of silver, *i.e.*, Ag⁻(CO₂), only chemisorption in the case of copper, *i.e.*, Cu(CO₂)⁻, and both physisorbed and chemisorbed isomers for gold, *i.e.*, Au⁻(CO₂) and Au(CO₂)⁻, respectively.²⁴

Here, we present our study of the Group 10 transition metal-CO₂ anionic complexes: [Ni(CO₂)]⁻, [Pd(CO₂)]⁻, and [Pt(CO₂)]⁻, using anion photoelectron spectroscopy and theoretical calculations. In contrast to our previous work with the Group 11 coinage (s¹) metals, the Group 10 metals adopt richer outer electron shell configurations (d⁸s² for Ni, d¹⁰ for Pd, and d⁹s¹ for Pt) with significantly greater prospects for complex chemical bonding. Indeed, strong evidence for chemisorption was found in all three of the Group 10 metal-CO₂ anionic complexes studied here, implying that Ni⁻, Pd⁻ and Pt⁻ all activated CO₂ to form Ni(CO₂)⁻, Pd(CO₂)⁻, and Pt(CO₂)⁻, respectively. Thus, all three of these Group 10 metal anions were seen to be able to both reduce and activate CO₂.

Methods

Experimental

Anion photoelectron spectroscopy is conducted by crossing a beam of mass-selected negative ions with a fixed-frequency photon beam and energy-analyzing the resultant photodetached electrons. The photodetachment process is governed by the energy-conserving relationship: $h\nu = EBE + EKE$, where $h\nu$ is the photon energy, EBE is the electron binding (photodetachment transition) energy, and EKE is the electron kinetic energy. Our apparatus consists of a laser vaporization cluster anion source, a time-of-flight mass spectrometer, a Nd:YAG photodetachment laser, and a magnetic bottle electron energy analyzer.⁴⁴ The photoelectron spectrometer resolution is ~ 35 meV at $EKE = 1$ eV. The third harmonic output of a Nd:YAG laser (355 nm) was used to photodetach electrons from mass-selected M^- and $[M(CO_2)]^-$ anions, where $M = Ni, Pd, Pt$. Photoelectron spectra were calibrated against the well-known atomic transitions of atomic Cu^- .⁴⁵ The $[M(CO_2)]^-$ ($M = Ni, Pd, Pt$) anion complexes were generated in a laser vaporization ion source. It consisted of rotating, translating nickel, palladium, or platinum rods, which were ablated with second harmonic (532 nm) photon pulses from a Nd:YAG laser, while 10%/90% He/ CO_2 gas mixtures at 60 psi were expanded from a pulsed valve over the rods.

Theoretical

Density functional theory calculations were performed with the ORCA computational chemistry software package.⁴⁶ All calculations were carried out with the B3LYP

functional⁴⁷ with the D3 dispersion correction⁴⁸ and the RIJCOSX approximation.⁴⁹ The Ahlrichs Def2 basis sets were used throughout our calculations.⁵⁰ For geometry optimization, Def2-TZVP and auxiliary Def2-TZVP/J basis sets⁵¹ were chosen for carbon, oxygen and nickel atoms; the Stuttgart effective core potential SDD⁵² and ECP basis set Def2-TZVP|Def2-TZVP/J were used for palladium and platinum atoms. The potential energy surfaces of neutral Ni, Pt–CO₂ along the M–C coordinate were computed by scanning the M–C bond length with a step width of 0.1 Å, while relaxing the rest of the cluster. Single-point calculations were then improved with Def2-QZVPP|Def2-QZVPP/J basis sets and all-electron relativistic calculations (ZORA). The structure of neutral PdCO₂ was also checked using the PBE0 and M06-L functionals.⁵³ The vertical detachment energy (VDE) is the energy difference between the ground state anion and its corresponding neutral at the geometry of the anion, *i.e.*, these are vertical photodetachment transitions. The adiabatic detachment energy (ADE) is the energy difference between the lowest energy, relaxed geometry of the anion and the relaxed geometry of a structurally similar isomer (nearest minimum) of its neutral counterpart. The adiabatic electron affinity (EA) is the energy difference between the lowest energy, relaxed geometry of the anion and the relaxed geometry of the lowest energy isomer (the global minimum) of its neutral counterpart. When the nearest local minimum and the global minimum are one and the same, ADE = EA. In this work, we calculated ADE values. In the

systems studied here, there is only one credible minimum for the neutral species, and it is therefore the global minimum. For that reason, we report ADE values as EA values here. Also, note that since the Franck–Condon principle governs which spectral features are seen within its anion-to-neutral wavefunction overlap window, there is often a correspondence between the lowest EBE transition observed experimentally and the properly calculated ADE value. Franck–Condon simulation was performed for the PdCO_2^- spectrum. This simulation, however, was not practical for NiCO_2^- and PtCO_2^- due to the large structural changes between anions and neutrals. Frequency calculations were performed to verify that no imaginary frequencies existed for any of the optimized structures.

Results and Discussion

The photoelectron spectra of $[\text{M}(\text{CO}_2)]^-$ ($\text{M} = \text{Ni}, \text{Pd}, \text{Pt}$) are presented in Fig. 1. For comparison, the atomic anion photoelectron spectra of Ni^- , Pd^- , and Pt^- are also presented above each $[\text{M}(\text{CO}_2)]^-$ spectrum there. In the anionic complexes, $[\text{M}(\text{CO}_2)]^-$, the CO_2 moiety can be either physisorbed or chemisorbed to M^- . For physisorbed complexes, the interaction between M^- and CO_2 is weak; they can be considered to be M^- anions “solvated” by CO_2 molecules, *i.e.*, $\text{M}^-(\text{CO}_2)$. In physisorbed anion-molecule complexes such as these, their M^- anion moieties act as chromophores for photodetachment, with the resulting photoelectron spectra closely

resembling the photoelectron spectral patterns of M^- , just shifted to higher electron binding energies (EBE) with their spectral features slightly broadened.^{54,55} These shifts are typically a few tenths of an eV, corresponding approximately to ion-solvation stabilization energies. This spectral behavior provides a distinctive spectroscopic signature for physisorbed (solvated) anion complexes. The photoelectron spectra of $[\text{Ni}(\text{CO}_2)]^-$, $[\text{Pd}(\text{CO}_2)]^-$, and $[\text{Pt}(\text{CO}_2)]^-$, however, do not exhibit this behavior in relation to their atomic anion photoelectron spectra, *i.e.*, Ni^- , Pd^- , and Pt^- . They are not physisorbed species. Moreover, their spectral shifts are far too large to be due to weak, solvation-like interactions. The spectral shifts between the lowest EBE features of the atomic anions and those of their corresponding anionic complexes are about an electron volt. The anionic complexes studied here, *i.e.*, $[\text{Ni}(\text{CO}_2)]^-$, $[\text{Pd}(\text{CO}_2)]^-$, and $[\text{Pt}(\text{CO}_2)]^-$, are chemisorbed complexes, *i.e.*, NiCO_2^- , PdCO_2^- , and PtCO_2^- . Significant chemical interactions have occurred, resulting in bonds between the metal atoms and their CO_2 moieties.

Energetic parameters can also be determined from the spectra. When there is sufficient Franck–Condon overlap between the ground state of the anion and the ground state of the neutral, and when vibrational hot bands are absent, the threshold EBE (E_T) is the value of the electron affinity (EA). The E_T in PdCO_2^- spectrum can be determined definitively. For NiCO_2^- and PdCO_2^- , however, the relatively weak, shelf-like

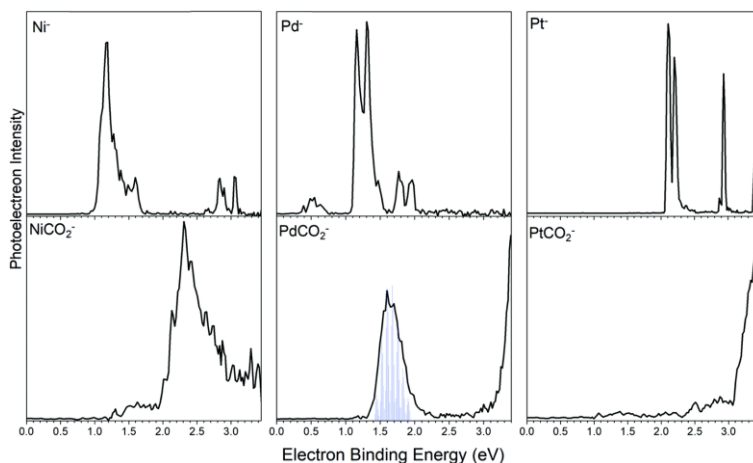


Figure IV.4.1 Anion photoelectron spectra of Ni^- and NiCO_2^- , Pd^- and PdCO_2^- , and Pt^- and PtCO_2^- . The vertical lines in the PdCO_2^- spectrum represent Franck–Condon simulated vibrational progression.

features on the low EBE side of the major peaks are likely hot bands. Thus, the E_T values for those two systems were determined by extrapolating the low EBE sides of their major peaks to baseline. In all three anionic complexes, the EBE values of the intensity maxima in their major peaks are their vertical detachment energy (VDE) values, corresponding to the transitions that have maximum Franck–Condon overlap between the ground electronic states of the anionic complexes and their neutral counterparts. The onset of the higher EBE feature in PdCO_2^- spectrum is due to the vertical photodetachment transition from the ground state anion to its neutral counterpart in its first excited electronic state. The EA and VDE values of $\text{NiCO}_2^{0/-}$, $\text{PdCO}_2^{0/-}$, and $\text{PtCO}_2^{0/-}$ are listed in Table 1.

Table 1 Experimental and theoretical EA and VDE values for MCO_2 and MCO_2^- , M = Ni, Pd, Pt, respectively. All values are in eV

	EA (expt/theo.)	VDE (expt/theo.)
$\text{NiCO}_2^{0/-}$	1.9/1.86	2.33/2.31
$\text{PdCO}_2^{0/-}$	1.3/1.10	1.60/1.57
$\text{PtCO}_2^{0/-}$	3.0/2.81	3.43/3.37

A synergy between theoretical calculations and anion photoelectron spectroscopy can provide insights into the structures, energetics and the nature of chemical bond of the investigated clusters.⁵⁵⁻⁶¹ The calculated structures of the anionic complexes and their corresponding neutrals are presented in Fig. 2. The first row shows the geometries of the anionic complexes along with their respective HOMOs, while the second row provides the geometries of their neutral counterparts. The M–C bond length (Å), the C–O bond length (Å), and the O–C–O bond angle (in degrees) are shown for each case. For the chemisorption species, NiCO_2^- , PdCO_2^- , and PtCO_2^- , the M–C bond lengths are 2.01 Å, 2.03 Å, and 2.02 Å, respectively, suggesting the formation of single bonds between M and C in all cases. The CO_2 moiety is significantly bent in all three anionic complexes, with an O–C–O bond angle of 138.26° for NiCO_2^- , 140.62° for PdCO_2^- and 136.34° for PtCO_2^- , respectively. A natural population analysis shows that the CO_2 moieties in NiCO_2^- , PdCO_2^- , and PtCO_2^- have negative charges of $-0.75 e$, $-0.59 e$, and $-0.67 e$, respectively. Thus, the CO_2 moiety has been

significantly reduced in all of these anionic complexes. The O–C–O bond angles in all three systems are similar one another, as are the negative charges on their CO₂ moieties. The fact that they are not completely synchronized is likely due to the natural population analysis (NPA) being less reliable than the structural calculations. For the three anionic complexes, the C–O bond lengths are all between 1.22–1.23 Å, which is longer than the 1.16 Å C–O bond length in isolated CO₂ (1.16 Å). This implies that when negative charge is transferred to the CO₂ moiety, the C–O bond is elongated and weakened. Thus, NiCO₂[−], PdCO₂[−], and PtCO₂[−] all share a metalloformate geometry. Furthermore, they are structurally quite similar in terms of M–C bond length, C–O bond length and O–C–O bond angle. Note that based on the calculated structures and charge distributions, Pd[−] seems to have the weakest interaction with CO₂ of all three metal anions, although Pd has the lowest electron affinity which is expected to facilitate the charge transfer to the CO₂ moiety. One possible reason for Pd[−] being the outlier is its electron configuration, d₁₀s, which is different to that of Ni[−] and Pt[−], d₉s₂. The calculated EA and VDE values are listed in Table 1 along with their corresponding experimental values. Excellent agreement between experimental and theoretical values, is seen for all three anionic complexes, validating the geometry optimizations shown in Fig. 2.

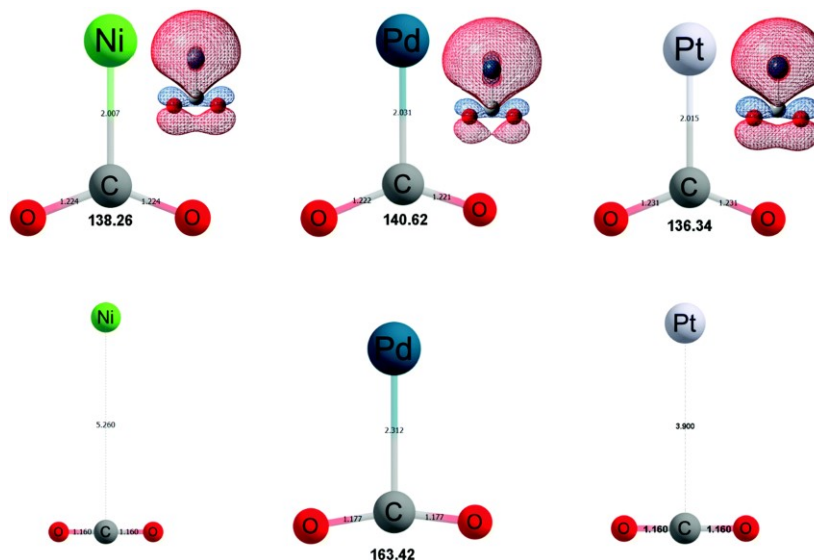


Figure IV.4.2 Calculated structures of NiCO₂⁻, PdCO₂⁻, PtCO₂⁻ (first row) and NiCO₂, PdCO₂, PtCO₂ (second row). The HOMOs of the anionic complexes are also presented.

In neutral NiCO₂ and PtCO₂, the metal atom is far away from CO₂. Also, their CO₂ moieties are structurally identical to an isolated CO₂ molecule. The potential energy surfaces of neutral NiCO₂ and PtCO₂ seem to show a shallow energy well at a M-C bond length of around 2.0 Å, but the energies of these local minima are higher than when CO₂ is far away (Fig. 3). The repulsive part of the neutral surfaces occurs at a M-C bond length less than 1.9 Å. Since NiCO₂⁻ and PtCO₂⁻ have a M-C bond length of 2.01 and 2.02 Å, respectively, the repulsive part of each neutral surface is not accessed during the vertical photodetachment process. The structural parameters show that there is little interaction between the neutral atoms of Ni and Pt and CO₂, which is as expected based on our previous research.²⁴ Surprisingly, however, the

optimized neutral PdCO₂ structure shows incipient chemisorption character, that while much weaker than in its PdCO₂⁻ anionic counterpart, is significantly stronger than the physisorption interactions seen in neutral NiCO₂ and PtCO₂. In neutral PdCO₂, the Pd–C bond length is 2.31 Å, which is characteristic of a metal–carbon bond. The CO₂ moiety is noticeably bent, with the O–C–O bond angle being 163.42°. The NPA analysis shows the CO₂ moiety as possessing a negative charge of -0.16 e, indicating a degree of charge transfer between neutral Pd and CO₂. The neutral PdCO₂ structure was also verified using the PBE0 and M06-L functionals. Both functionals yielded the same PdCO₂ structure as the B3LYP one. In addition, the Franck–Condon simulated spectrum of PdCO₂⁻ reproduces the experimental one (Fig. 1), offering a further validation of the neutral PdCO₂ structure. Taken together, these features suggest that CO₂ can be activated by a single neutral Pd atom.

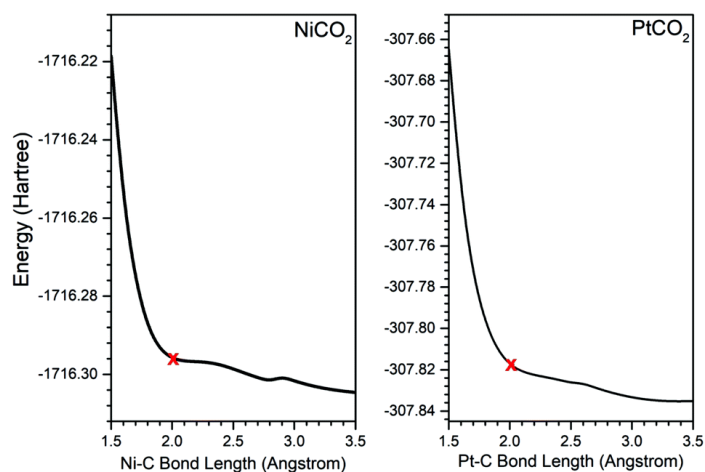


Figure IV.4.3 The potential energy surfaces of neutral NiCO₂ and PtCO₂ with respect to the M–C bond length. The red crosses represent the M–C bond length of optimized anionic NiCO₂[−] and PtCO₂[−].

In order to provide further insight into the nature of the bonding in neutral PdCO₂, we analyzed its molecular orbitals. In most cases, the molecular orbitals of neutral M(CO₂) species are composed of atomic orbitals of M and molecular orbitals of CO₂, which are essentially independent of one another. The molecular orbitals of neutral PtCO₂ (HOMO to HOMO−8) are presented on the left side of [Fig. 4](#), and they provide typical examples of the molecular orbitals in neutral MCO₂ species. The absence of wavefunction overlap between the M and CO₂ moieties is consistent with a lack of interaction between neutral M atoms and CO₂ moieties. In the case of neutral PdCO₂, most of its molecular orbitals can also be viewed as independent atomic orbitals of Pd and molecular orbitals of CO₂. However, this is not the case for all orbital interactions between Pd and CO₂. The HOMO−4 and HOMO−6 orbitals, seen on the right side of [Fig. 3](#), clearly result from the combination of Pd atomic orbitals and CO₂ molecular orbitals. There, one observes significant interaction, *i.e.*, overlap, between some of the orbitals of Pd and CO₂. For HOMO−4, the interaction is mainly between the Pd d_{z²} orbital and the B₁ orbital of bent CO₂. For HOMO−6, the interaction is through the overlap between Pd d_{xy} orbital and the B₂ orbital of bent CO₂. The wavefunction overlap between these Pd atomic and CO₂ molecular orbitals is likely the reason for

the weak binding interaction and the partial charge transfer between neutral Pd atom and CO₂. Although we are unaware of corroborating experimental evidence for their weak binding, our calculations imply a neutral PdCO₂ bond dissociation energy of 0.85 eV. For comparison, the bond dissociation energy of the PdCO₂⁻ anionic complex is predicted to be 1.78 eV.

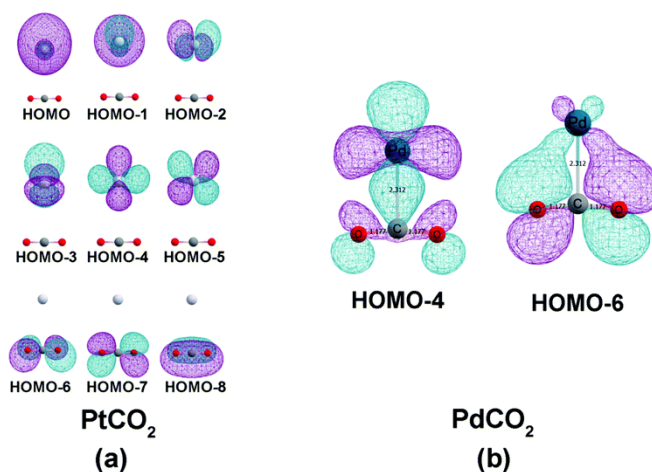


Figure IV.4.4 Selected molecular orbitals of neutral (a) PtCO₂ and (b) PdCO₂. The overlap between the metal atomic orbitals and the CO₂ molecular orbitals is barely present in neutral PtCO₂, but is significant in neutral PdCO₂.

Conclusion

This combined anion photoelectron spectroscopic and computational study characterized the metallo-formate anions, M(CO₂)⁻, where M = Ni, Pd, and Pt, and demonstrated that the addition of an excess electron led to significant CO₂ reduction in these systems. While neutral transition metals are normally incapable of reducing CO₂, we found evidence of an unusual attractive interaction between neutral Pd and

CO₂.

References

1. N. Compton, P. W. Reinhardt and C. D. Cooper, *J. Chem. Phys.*, 1975, **63**, 3821.
2. M. Knapp, O. Echt, D. Kreisle, T. D. Mark and E. Recknagel, *Chem. Phys. Lett.*, 1986, **126**, 225.
3. S. T. Arnold, J. V. Coe, J. G. Eaton, C. B. Freidhoff, L. H. Kidder, G. H. Lee, M. R. Manaa, K. M. McHugh, D. Patel-Misra, H. W. Sarkas, J. T. Snodgrass and K. H. Bowen, in *Proceedings of the Enrico Fermi International School of Physics, CVII Course, Varenna*, ed. G. Scoles, North-Holland, Amsterdam, 1989, pp. 467–490.
4. C. E. Klots, *J. Chem. Phys.*, 1979, **71**, 4172.
5. T. Tsukuda and T. Nagata, *J. Phys. Chem. A*, 2003, **107**, 8476.
6. S. Y. Han, I. Chu, J. H. Kim, J. K. Song and S. K. Kim, *J. Chem. Phys.*, 2000, **113**, 596.
7. S. H. Lee, N. Kim, D. G. Ha and S. K. Kim, *J. Am. Chem. Soc.*, 2008, **130**, 16241.
8. M. Z. Kamrath, R. A. Relph and M. A. Johnson, *J. Am. Chem. Soc.*, 2010, **132**, 15508.
9. J. D. Graham, A. M. Buytendyk, Y. Wang, S. K. Kim and K. H. Bowen, *J. Chem. Phys.*, 2015, **142**, 234307.
10. J. M. Weber, *Int. Rev. Phys. Chem.*, 2014, **33**, 489.
11. H. Schneider, A. D. Boese and J. M. Weber, *J. Chem. Phys.*, 2005, **123**, 074316.
12. A. D. Boese, H. Schneider, A. N. Glöß and J. M. Weber, *J. Chem. Phys.*, 2005, **122**, 154301.
13. B. J. Knurr and J. M. Weber, *J. Am. Chem. Soc.*, 2012, **134**, 18804.
14. B. J. Knurr and J. M. Weber, *J. Phys. Chem. A*, 2013, **117**, 10764.
15. B. J. Knurr and J. M. Weber, *J. Phys. Chem. A*, 2014, **118**, 4056.
16. B. J. Knurr and J. M. Weber, *J. Phys. Chem. A*, 2014, **118**, 10246.
17. B. J. Knurr and J. M. Weber, *J. Phys. Chem. A*, 2014, **118**, 8753.
18. M. C. Thompson, J. Ramsay and J. M. Weber, *J. Phys. Chem. A*, 2017, **121**, 7537.
19. M. C. Thompson, Leah G. Dodson and J. M. Weber, *J. Phys. Chem. A*, 2017, **121**, 4132.
20. M. C. Thompson, J. Ramsay and J. M. Weber, *Angew. Chem., Int. Ed.*, 2016, **55**, 15171.
21. L. G. Dodson, M. C. Thompson and J. M. Weber, *J. Phys. Chem. A*, 2018, **122**, 2983.
22. M. C. Thompson and J. M. Weber, *J. Phys. Chem. A*, 2018, **122**, 3772.
23. L. G. Dodson, M. C. Thompson and J. M. Weber, *Annu. Rev. Phys. Chem.*, 2018, **69**, 231.
24. X. Zhang, E. Lim, S. K. Kim and K. H. Bowen, *J. Chem. Phys.*, 2015, **143**, 174305.
25. N. Kim, *Bull. Korean Chem. Soc.*, 2015, **34**, 2247.
26. M. J. DeLuca, B. Niu and M. A. Johnson, *J. Chem. Phys.*, 1988, **88**, 5857.
27. S. H. Fleischman and K. D. Jordan, *J. Phys. Chem.*, 1987, **91**, 1300.
28. T. Tsukuda, M. A. Johnson and T. Nagata, *Chem. Phys. Lett.*, 1977, **268**, 429.
29. J. W. Shin, N. I. Hammer, M. A. Johnson, H. Schneider, A. Glöß and J. M. Weber, *J. Phys. Chem. A*, 2015, **109**, 3146.

30. D. W. Arnold, S. E. Bradforth, E. H. Kim and D. M. Neumark, *J. Chem. Phys.*, 1995, **102**, 3493.
31. G. Markovich, R. Giniger, M. Levin and O. Cheshnovsky, *Z. Phys. D: At., Mol. Clusters*, 1991, **20**, 69.
32. D. W. Arnold, S. E. Bradforth, E. H. Kim and D. M. Neumark, *J. Chem. Phys.*, 1992, **97**, 9468.
33. D. W. Arnold, S. E. Bradforth, E. H. Kim and D. M. Neumark, *J. Chem. Phys.*, 1995, **102**, 3510.
34. A. Muraoka, Y. Inokuchi, N. I. Hammer, J. W. Shin, M. A. Johnson and T. Nagata, *J. Phys. Chem. A*, 2009, **113**, 8942.
35. K. Hiraoka and S. Yamabe, *J. Chem. Phys.*, 1992, **97**, 643.
36. K. Sudoh, Y. Matsuyama, A. Muraoka, R. Nakanishi and T. Nagata, *Chem. Phys. Lett.*, 2006, **433**, 10.
37. T. Sanford, S. Y. Han, M. A. Thompson, R. Parson and W. C. Lineberger, *J. Chem. Phys.*, 2005, **122**, 054307.
38. R. F. Höckendorf, K. Fischmann, Q. Hao, C. v. d. Linde, O. P. Balaj, C. K. Siu and M. K. Beyer, *Int. J. Mass Spectrom.*, 2013, **354**, 175.
39. A. Akhgarnusch, R. F. Hoeckebdorf, Q. Hao, K. P. Jaeger, C. K. Siu and M. K. Beyer, *Angew. Chem., Int. Ed.*, 2013, **53**, 9327.
40. A. Akhgarnusch and M. K. Beyer, *Int. J. Mass Spectrom.*, 2014, **365**, 295.
41. R. Oh, E. Lim, X. Zhang, J. Heo, K. H. Bowen and S. K. Kim, *J. Chem. Phys.*, 2017, **146**, 134304.
42. X. Zhang, G. Liu, K. Meiwes-Broer, G. Ganteför and K. Bowen, *Angew. Chem., Int. Ed.*, 2016, **55**, 9644.
43. J. D. Graham, A. M. Buytendyk, X. Zhang, S. K. Kim and K. H. Bowen, *J. Chem. Phys.*, 2015, **143**, 184315.
44. G. Liu, S. M. Ciborowski and K. H. Bowen, *J. Phys. Chem. A*, 2017, **121**, 5817.
45. J. Ho, K. M. Ervin and W. C. Lineberger, *J. Chem. Phys.*, 1990, **93**, 6987.
46. F. Neese, *WIREs Comput. Mol. Sci.*, 2012, **2**, 73.
47. (a) A. D. Becke, *Phys. Rev. A: At., Mol., Opt. Phys.*, 1988, **38**, 3098; (b) A. D. Becke, *J. Chem. Phys.*, 1993, **98**, 5648.
48. (a) C. Lee, W. Yang and R. G. Parr, *Phys. Rev. B: Condens. Matter Mater. Phys.*, 1988, **37**, 785; (b) R. Krishnan, J. S. Binkley, R. Seeger and J. A. Pople, *J. Chem. Phys.*, 1980, **72**, 65.
49. S. Grimme, J. Antony, S. Ehrlich and H. A. Krieg, *J. Chem. Phys.*, 2010, **132**, 154104.
50. F. Neese, F. Wennmohs, A. Hansen and U. Becker, *Chem. Phys.*, 2008, **356**, 98.
51. (a) F. Weigend and R. Ahlrichs, *Phys. Chem. Chem. Phys.*, 2005, **7**, 3297; (b) F. Weigend, *Phys. Chem. Chem. Phys.*, 2006, **8**, 1057.
52. D. Andrae, U. Häußermann, M. Dolg, H. Stoll and H. Preuß, *Theor. Chim. Acta*, 1990, **77**, 123.
53. (a) C. Adamo and V. Barone, *J. Chem. Phys.*, 1994, **110**, 6158–6170; (b) J. P. Perdew, K.

- Burke and M. Ernzerhof, *Phys. Rev. Lett.*, 1997, **77**, 3865; (c) Y. Zhao and D. G. Truhlar, *J. Phys. Chem. A*, 2006, **110**, 13126–13130; (d) Y. Zhao and D. G. Truhlar, *Theor. Chem. Acc.*, 2007, **120**, 215–241.
54. G. Liu, E. Miliordos, S. M. Ciborowski, M. Tschurl, U. Boesl, U. Heiz, X. Zhang, S. S. Xantheas and K. H. Bowen, *J. Chem. Phys.*, 2018, **149**, 221101.
55. G. Liu, Z. Zhu, S. M. Ciborowski, I. R. Ariyaratna, E. Miliordos and K. H. Bowen, *Angew. Chem., Int. Ed.*, 2019, **131** DOI.
56. X. Zhang, G. Liu, S. Ciborowski and K. Bowen, *Angew. Chem., Int. Ed.*, 2017, **56**, 9897.
57. K. A. Lundell, X. Zhang, A. I. Boldyrev and K. H. Bowen, *Angew. Chem., Int. Ed.*, 2017, **56**, 16593.
58. P. J. Robinson, G. Liu, S. Ciborowski, C. Martinez-Martinez, J. R. Chamorro, X. Zhang, T. M. McQueen, K. H. Bowen and A. N. Alexandrova, *Chem. Mater.*, 2017, **29**, 9892.
59. X. Zhang, G. Liu, S. Ciborowski and K. H. Bowen, *Angew. Chem., Int. Ed.*, 2017, **56**, 9897.
60. E. F. Belogolova, G. Liu, E. P. Doronina, S. Ciborowski, V. F. Sidorkin and K. H. Bowen, *J. Phys. Chem. Lett.*, 2018, **9**, 1284.
61. X. Zhang, I. A. Popov, K. A. Lundell, H. Wang, C. Mu, W. Wang, H. Schnöckel, A. I. Boldyrev and K. H. Bowen, *Angew. Chem., Int. Ed.*, 2018, **130**, 14256.

IV.5 Selective Activation of the C–H Bond in Methane by Single Platinum Atomic Anions

Gaoxiang Liu, Zhaoguo Zhu, Sandra M. Ciborowski, Isuru R. Ariyaratna, Evangelos Miliordos, Kit H. Bowen

Department of Chemistry, Johns Hopkins University Baltimore, MD 21218(USA).

Department of Chemistry and Biochemistry, Auburn University Auburn, AL 36849(USA).

Abstract

Mass spectrometric analysis of the anionic products of interaction between platinum atomic anions, Pt^- , and methane, CH_4 and CD_4 , in a collision cell shows the preferred generation of $[\text{PtCH}_4]^-$ and $[\text{PtCD}_4]^-$ complexes and a low tendency toward dehydrogenation. $[\text{PtCH}_4]^-$ is shown to be H-Pt-CH_3^- by a synergy between anion photoelectron spectroscopy and quantum chemical calculations, implying the rupture of a single C–H bond. The calculated reaction pathway accounts for the observed selective activation of methane by Pt^- . This study presents the first example of methane activation by a single atomic anion.

Converting methane into high value chemicals requires it first to be chemically activated. However, because the dissociation energy of the C–H bond is high, i.e., 440

kJ mol^{-1} ,¹ activation is challenging. Typically, either elevated reaction temperatures or high activity catalysts are required,^{2,3} but these inevitably compromise selectivity.⁴ Industrially, the end product of methane conversion is usually the generation of syngas, but this process consumes large amounts of energy. Clearly, it would be advantageous to functionalize methane through the selective and energy-efficient activation of the thermodynamically strong C–H bond. This goal is therefore among the greatest challenges in catalysis.

Gas-phase studies of methane activation by metal atoms and clusters have provided insight into methane functionalization at the molecular level.⁵⁻⁴² In the case of platinum the reactivities of its cationic, neutral, and anionic atoms and clusters with methane have been widely investigated.³⁶⁻⁴⁹ For its atoms, in particular, both cationic and neutral platinum atoms have been shown to activate methane, yielding both dehydrogenation and C–H insertion products, whereas anionic platinum atoms were found in FT-ICR mass spectrometric experiments to exhibit only negligible reactivity toward methane.³⁶

Here, we show that under our experimental conditions, platinum atomic anions, Pt^- , activate methane, and that due to their preference for activating only one C–H bond, they do so with significant selectivity. This study represents the first observation of

methane activation by single atomic anions.

Our experimental apparatus has been described previously.⁵⁰⁻⁵² Briefly, Pt^- was prepared in a laser vaporization source and interacted with methane introduced into a reaction cell downstream. The resultant anionic products were identified by time-of-flight mass spectrometry. Anions of interest were mass-selected and then characterized by anion photoelectron spectroscopy, which involves crossing a mass-selected beam of anions with a fixed-frequency photon beam and energy-analyzing the resultant photodetached electrons. The photodetachment process is governed by the energy-conserving relationship, $h\nu = \text{EKE} + \text{EBE}$, where EKE is the electron kinetic energy and EBE is the electron binding (transition) energy.

Figure 1 presents mass spectra with or without the addition of methane. With no methane in the reaction cell, only Pt^- and weak intensities of PtC^- and PtO^- were observed (Figure 1 A). The formation of PtC^- and PtO^- was likely due to trace amounts of carbon and oxygen present on the platinum metal surface. When methane or deuterated methane was added to the reaction cell, prominent mass series of $[\text{PtCH}_4]^-$ and $[\text{PtCD}_4]^-$ anionic complexes appeared (Figure 1 B,C). The presence of strong $[\text{PtCH}_4]^-$ and $[\text{PtCD}_4]^-$ ion intensities shows that Pt^- interacts efficiently with methane under our experimental conditions. The much weaker intensity peaks on the

low mass side of the $[\text{PtCH}_4]^-$ or $[\text{PtCD}_4]^-$ peaks are due to PtC^- , $[\text{PtCH}_2]^-$ or $[\text{PtCD}_2]^-$. The presence of reaction products, $[\text{PtCH}_2]^-$ and $[\text{PtCD}_2]^-$, is indicative of relatively weak dehydrogenation of methane by Pt^- . By contrast, dehydrogenation and the formation of platinum-carbene complexes were the dominant outcomes of reactions between neutral and cationic platinum atoms and methane.⁴³⁻⁴⁶

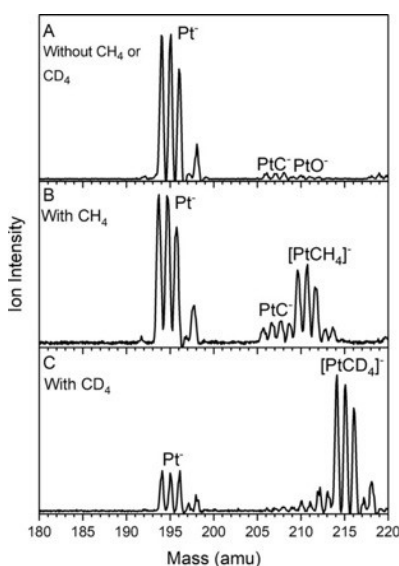


Figure IV.5.1 The mass spectra of Pt^- without methane (A), with methane (B), and with deuterated methane (C).

Figure 2 presents the anion photoelectron spectra of Pt^- , $[\text{PtCH}_4]^-$, and $[\text{PtCD}_4]^-$, all measured with 3.496 eV photons. The photoelectron spectrum of Pt^- shows no transitions originating from excited-state Pt^- (Figure 2 A), confirming that the reaction occurs between ground-state Pt^- and methane. The anion photoelectron spectra of $[\text{PtCH}_4]^-$ and $[\text{PtCD}_4]^-$ are presented in Figures 2 B and 3 C, respectively.

Potentially, these spectra could be due to physisorbed complexes, activation species, or both. In the physisorbed case, Pt^- and methane would be weakly bound together to form $\text{Pt}^-(\text{CH}_4)$ and $\text{Pt}^-(\text{CD}_4)$. Typically, when an anion is solvated by another molecule, the anion photoelectron spectrum of the resulting physisorbed anionic complex closely resembles that of the anion alone, except for its spectral pattern having been shifted to higher electron binding energies (EBE) and its features slightly broadened.⁵³ In the activation case, one or more C–H/C–D bonds would be broken, leading to the formation of $\text{H}_n\text{-Pt-CH}_{4-n}^-$ and $\text{D}_n\text{-Pt-CD}_{4-n}^-$. The anion photoelectron spectrum of such activation species would be drastically different to that of the anion due to changes in the electronic structure. The photoelectron spectra of $[\text{PtCH}_4]^-$ and $[\text{PtCD}_4]^-$ bear no resemblance to the spectrum of Pt^- , and in fact their lowest EBE peaks lie below the EBE of the lowest EBE peak in the Pt^- spectrum. Therefore the spectroscopic evidence strongly supports that $[\text{PtCH}_4]^-$ and $[\text{PtCD}_4]^-$ are activation species rather than physisorbed complexes. Thus, within each of these entities, methane activation has occurred; chemistry has taken place. The fact that Figures 2 B and 2 C have essentially identical features confirms that the activation species, $[\text{PtCH}_4]^-$ and $[\text{PtCD}_4]^-$, have the same geometries and electronic structures.

The lowest EBE feature in the photoelectron spectra of both $[\text{PtCH}_4]^-$ and $[\text{PtCD}_4]^-$ has its maximum spectral intensity centered at $\text{EBE}=1.93$ eV. Thus, 1.93 eV

is their common vertical detachment energy (VDE). The VDE is defined as the photodetachment transition energy at which the Franck-Condon overlap is at its maximum between the anion's vibrational wave function and that of its neutral

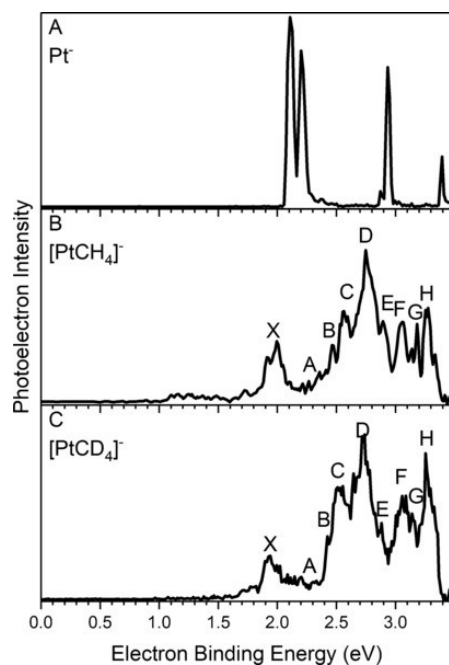


Figure IV.5.2 Photoelectron spectra of Pt^- (A), $[\text{PtCH}_4]^-$ (B), and $[\text{PtCD}_4]^-$ (C), all measured with 355 nm (3.496 eV) photons.

counterpart with both in their ground electronic states. The other peaks in the spectra are due to vertical photodetachment transitions from the ground state anion to its neutral counterpart in its various excited electronic states. All of the experimental vertical photodetachment transition energies values are tabulated in Table 1.

Density functional theory (DFT) calculations were performed to find the most thermodynamically stable isomer of $[\text{PtCH}_4]^-$, which was expected to be the main

contributor of the photoelectron spectrum. The energetics of the low-energy isomers were then refined at the CCSD(T) level of theory. The computational details are given in the Supporting Information (SI). Figure 3 presents the structures of different

Table IV.5.2 Experimental and calculated vertical photodetachment transition energy values for the GM structure, H–Pt–CH₃[−].

Peak	Final neutral state	Vertical photodetachment transition energy	
		Expt.	Theory ^[a]
X	¹ A'	1.98	1.95
A	³ A'	2.27	2.34
B	³ A''	2.46	2.52
C	¹ A'	2.56	2.64
D	³ A'	2.75	2.73
E	³ A''	2.88	2.78
F	¹ A''	3.07	2.99
G	¹ A'	3.18	3.15
H	¹ A''	3.28	3.49

[a] CCSD(T) calculated VDE plus MRCI+Q calculated excitation energies; see the Supporting Information.

[PtCH₄][−] isomers along with their relative energies. All energies are zero-point energy corrected. The global minimum (GM) of [PtCH₄][−] features C_s symmetry and one activated C–H bond, i.e., H–Pt–CH₃[−]. The physisorbed complex, Pt[−](CH₄), is 0.62 eV above the GM. Two isomers corresponding to the breakage of two C–H bonds, the hydrogen-Pt-carbene complex (H₂)–Pt–CH₂[−] and the dihydrido-Pt-carbene complexes H₂–Pt–CH₂[−], are, respectively 0.63 and 0.69 eV higher than the GM. Note

that the H–H bond length (0.99 Å) in $(\text{H}_2)\text{-Pt-CH}_2^-$ is significantly longer than that in the free H_2 molecule (0.74 Å). Such elongation suggests H_2 activation due to back-donation from the Pt-CH_2^- moiety to the H_2 σ^* antibonding orbital (Figure S2). This back-donation strengthens the interaction between H_2 and Pt-CH_2^- moieties and can lead to a high dehydrogenation energy.⁵⁴ The two structures that resulted from activating three and four C–H bonds have relative energies of 1.57 and 2.69 eV, respectively, making them unlikely to form under our experimental conditions. The isomers of $[\text{PtCD}_4]^-$ have the same structures as $[\text{PtCH}_4]^-$; their relative energies are provided in Figure 3 in parenthesis. To verify that the calculated GM of $[\text{PtCH}_4]^-$ describes the experimental spectrum, its vertical photodetachment transition energies values were computed at the multi-reference configuration interaction (MRCI+Q) level of theory and compared with the observed experimental values (Table 1). The calculated values accurately reproduce all the transitions observed in the photoelectron spectrum of $[\text{PtCH}_4]^-$, thus providing unambiguous validation of the GM structure, H-Pt-CH_3^- , as the major reaction product. Therefore, the combined results from mass spectroscopy, anion photoelectron spectroscopy, and ab initio quantum calculations have confirmed that atomic Pt^- readily activates methane, and that such activation process leads to H-Pt-CH_3^- with high selectivity.

To provide mechanistic insight into the highly selective C–H bond cleavage and low

dehydrogenation tendency observed when Pt^- activates methane, the reaction pathway was investigated with quantum calculations. The reaction pathway energy diagram is presented in Figure 4. The reaction occurs entirely on a doublet potential energy surface. Initially, CH_4 physisorbs onto Pt^- and forms the van der Waals complex **1**, $\text{Pt}^-(\text{CH}_4)$, with a binding energy of 0.08 eV. This solvation complex then

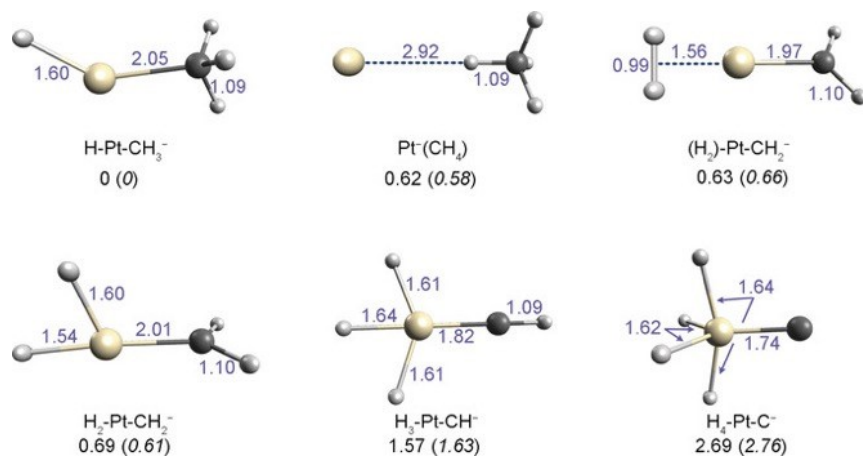


Figure IV.5.1 Optimized structures for $[\text{PtCH}_4]^-$ and their relative energies compared to its GM. The relative energies of $[\text{PtCD}_4]^-$ are shown in parenthesis. Energies are given in eV. Bond lengths are given in Å.

Passes over a transition state **TS1/2** in which one C–H bond is weakened and elongated. The activation barrier is 0.42 eV above local minima **1**. Such a moderate barrier can be overcome under the multi-collision conditions in the reaction cell, where translational energy is provided by collisions with the supersonically-expanded He carrier gas.¹² After overcoming **TS1/2**, Pt^- is inserted into the C–H bond and methane is activated, yielding the GM structure **2**, H-Pt-CH_3^- , the major activation

product observed in the current experiments. The activation complex would next need to overcome **TS2/3** with a barrier of 0.80 eV, in order for a second H atom to migrate from the methyl group to Pt to form **3**, $\text{H}_2\text{-Pt-CH}_2^-$. The subsequent H transfer over **TS3/5** to form $\text{H}_3\text{-Pt-CH}^-$ (structure **5**) is not favored, since it is quite endothermic with a large barrier of 0.89 eV above the entrance channel. Instead, $\text{H}_2\text{-Pt-CH}_2^-$ (structure **3**) can pass over the negligible barrier of **TS3/4** to form $(\text{H}_2)\text{-Pt-CH}_2^-$ (structure **4**), where the two H atoms have combined to form a H_2 -like molecule attached to the Pt-carbene moiety. Its subsequent dissociation into H_2 and PtCH_2^- is quite endothermic by 0.93 eV, which is consistent with the previous analysis of a strong binding between H_2 and Pt-CH_2^- . The overall reaction of $\text{Pt}^- + \text{CH}_4 \rightarrow \text{PtCH}_2^- + \text{H}_2$ is thus endothermic by 0.86 eV. Note that this is significantly different from the cases of methane reacting with Pt^+ or Pt^0 , where dehydrogenation is exothermic or only slightly endothermic.^{43, 44} Our computed reaction pathway thus gives a quantitative rationale for the highly selective C–H bond cleavage and the low dehydrogenation tendency that occurs when Pt^- activates methane. It also explains the lack of an efficient hydrogen dissociation channel, and especially the fact that the H-Pt-CH_3^- is trapped in the minimum on the potential energy surface, resulting in its highly selective formation

The ground state of Pt^- , $^2\text{D}(6s^25d^9)$, has one unpaired electron, allowing the formation

of only one σ -bond. In order for Pt^- to form the GM H-Pt-CH_3^- structure, one electron is promoted from the 5d to the 6p orbital to generate the $^4\text{G}(6s^25d^86p^1)$ excited state with three available unpaired electrons. Two of them can couple with the unpaired electrons of the $\text{H}(^2\text{S})$ and $\text{CH}_3(^2\text{A}_2'')$ fragments to form the two Pt-H and Pt-C σ -bonds. The formations of these two σ -bonds stabilizes the $\text{H}(^2\text{S})/\text{Pt}^-(^4\text{G})/\text{CH}_3(^2\text{A}_2'')$ interaction, resulting in the formation of the GM. The remaining one electron occupies a 5d-6p hybrid orbital that couples with the CH_4 anti-bonding orbital during the activation process (Figure 5), fulfilling the accepted donor-acceptor model for σ -bond activation.⁴³

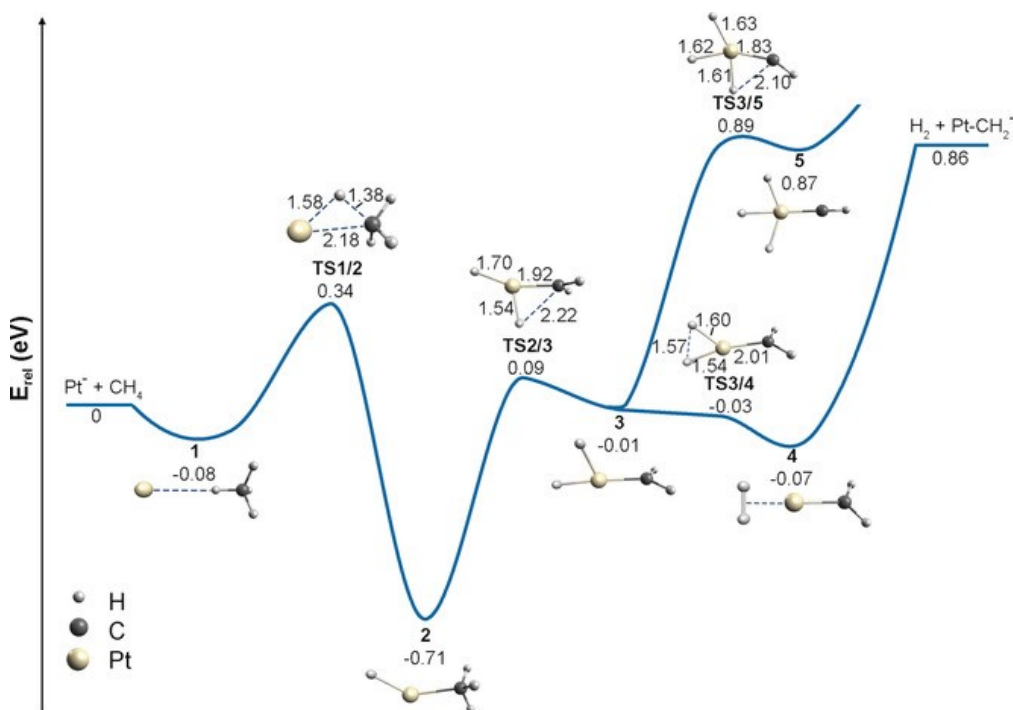


Figure IV.5.2 Calculated reaction pathway for methane activation by Pt^- . Zero-point energy corrected energies are given in eV. Bond lengths of the transition states are given in Å.

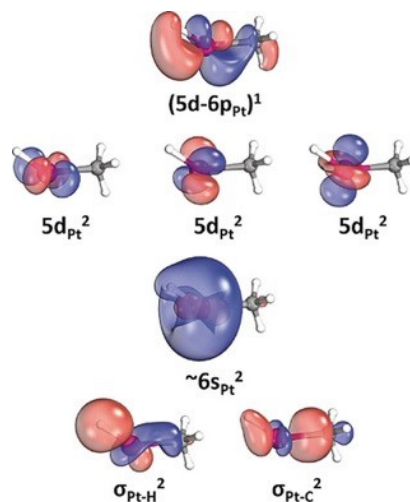


Figure IV.5.3 Selected molecular orbitals of the GM H-Pt-CH_3^- depicting the Pt-C and Pt-H bonds and the nearly intact valence Pt orbitals.

To summarize, we have demonstrated that Pt^- is able to selectively activate only one C-H bond in methane, representing the first example of methane activation by atomic anions. Mass spectrometric analysis of the reaction products between Pt^- and CH_4 shows the preferred generation of $[\text{PtCH}_4]^-$ and a low tendency toward dehydrogenation. $[\text{PtCH}_4]^-$ is confirmed as H-Pt-CH_3^- by anion photoelectron spectroscopy and quantum chemical calculation, suggesting a selective rupture of just one C-H bond. The single unpaired electrons in ground-state Pt^- necessitates electron promotion to the 6p orbital in order to facilitate the reaction over a moderate barrier. The demonstration of methane activation by atomic anions has opened a new route

for designing novel catalysts for C–H bond functionalization.

References

1. S. J. Blanksby, G. B. Ellison, *Acc. Chem. Res.* 2003, **36**, 255–263.
2. Q. Zhu, S. L. Wegener, C. Xie, O. Uche, M. Neurock, T. J. Marks, *Nat. Chem.* 2013, **5**, 104–109.
3. J. J. Spivey, G. Hutchings, *Chem. Soc. Rev.* 2014, **43**, 792–803.
4. H. Schwarz, *Angew. Chem. Int. Ed.* 2011, **50**, 10096–10115.
5. D. K. Böhme, H. Schwarz, *Angew. Chem. Int. Ed.* 2005, **44**, 2336–2354.
6. D. Schröder, H. Schwarz, *Proc. Natl. Acad. Sci. USA* 2008, **105**, 18114–18119.
7. J. Roithová, D. Schröder, *Chem. Rev.* 2010, **110**, 1170–1211.
8. H. Schwarz, *Isr. J. Chem.* 2014, **54**, 1413–1431.
9. X. L. Ding, X. N. Wu, Y. X. Zhao, S. G. He, *Acc. Chem. Res.* 2012, **45**, 382–390.
10. Z. Luo, A. W. Castleman, Jr., S. N. Khanna, *Chem. Rev.* 2016, **116**, 14456–14492.
11. S. Zhou, J. Li, M. Schlangen, H. Schwarz, *Acc. Chem. Res.* 2016, **49**, 494–502.
12. S. M. Lang, T. M. Bernhardt, V. Chernyy, J. M. Bakker, R. N. Barnett, U. Landman, *Angew. Chem. Int. Ed.* 2017, **56**, 13406–13410.
13. H. Schwarz, S. Shaik, J. Li, *J. Am. Chem. Soc.* 2017, **139**, 17201–17212.
14. Y. Zhao, Z. Li, Y. Yang, S. G. He, *Acc. Chem. Res.* 2018, **51**, 2603–2610.
15. L. Yue, S. Zhou, X. Sun, M. Schlangen, H. Schwarz, *Angew. Chem. Int. Ed.* 2018, **57**, 3251–3255.
16. X. Sun, S. Zhou, L. Yue, M. Schlangen, H. Schwarz, *Angew. Chem. Int. Ed.* 2018, **57**, 5934–5937.
17. L. F. Halle, P. B. Armentrout, J. L. Beauchamp, *J. Am. Chem. Soc.* 1981, **103**, 962–963.
18. K. K. Irikura, J. L. Beauchamp, *J. Am. Chem. Soc.* 1989, **111**, 75–85.
19. M. M. Armentrout, F. Li, P. B. Armentrout, *J. Phys. Chem. A* 2004, **108**, 9660–9672.
20. P. B. Armentrout, *J. Phys. Chem. A* 2006, **110**, 8327–8338.
21. P. B. Armentrout, L. Parke, C. Hinton, M. Citir, *Chem. Plus. Chem.* 2013, **78**, 1157–1173.
22. M. Citir, F. Liu, P. B. Armentrout, *J. Chem. Phys.* 2009, **130**, 054309.
23. S. Zhou, J. Li, M. Schlangen, H. Schwarz, *Angew. Chem. Int. Ed.* 2017, **56**, 413–416.
24. S. M. Lang, T. M. Bernhardt, R. N. Barnett, U. Landman, *Angew. Chem. Int. Ed.* 2010, **49**, 980–983.
25. S. Feyel, J. Döbler, D. Schröder, J. Sauer, H. Schwarz, *Angew. Chem. Int. Ed.* 2006, **45**, 4681–4685.
26. X. N. Wu, X. N. Li, X. L. Ding, S. G. He, *Angew. Chem. Int. Ed.* 2013, **52**, 2444–2448.
27. G. E. Johnson, R. Mitrić, M. Nössler, E. C. Tyo, V. Bonačić-Koutecký, A. W. Castleman, Jr., *J. Am. Chem. Soc.* 2009, **131**, 5460–5470.
28. Y. X. Zhao, Z. Y. Li, Z. Yuan, X. Li, S. G. He, *Angew. Chem. Int.*

- Ed.* 2014, **53**, 9482– 9486.
29. H. F. Li, Z. Y. Li, Q. Y. Liu, X. N. Li, Y. X. Zhao, S. G. He, *J. Phys. Chem. Lett.* 2015, **6**, 2287– 2291.
30. J. H. Meng, X. J. Deng, Z. Y. Li, S. G. He, W. J. Zheng, *Chem. Eur. J.* 2014, **20**, 5580– 5583.
31. Q. Y. Liu, J. B. Ma, Z. Y. Li, C. Zhao, C. G. Ning, H. Chen, S. G. He, *Angew. Chem. Int. Ed.* 2016, **55**, 5760– 5764.
32. Y. X. Zhao, X. N. Li, Z. Yuan, Q. Y. Liu, Q. Shi, S. G. He, *Chem. Sci.* 2016, **7**, 4730– 4735.
33. J. Jian, W. Li, X. Wu, M. F. Zhou, *Chem. Sci.* 2017, **8**, 4443– 4449.
34. J. Jian, H. Lin, M. Luo, M. Chen, M. F. Zhou, *Angew. Chem. Int. Ed.* 2016, **55**, 8371– 8374.
35. C. Chi, H. Qu, L. Meng, F. Kong, M. Luo, M. F. Zhou, *Angew. Chem. Int. Ed.* 2017, **56**, 14096– 14101.
36. U. Achatz, C. Berg, S. Joos, B. S. Fox, M. K. Beyer, G. Niedner-Schatteburg, V. E. Bondybey, *Chem. Phys. Lett.* 2000, **320**, 53– 58.
37. C. Adlhart, E. Uggerud, *Chem. Commun.* 2006, 2581– 2582.
38. G. Kummerlöwe, I. Balteanu, Z. Sun, O. P. Balaj, V. E. Bondybey, M. K. Beyer, *Int. J. Mass Spectrom.* 2006, **254**, 183– 188.
39. C. Adlhart, E. Uggerud, *Chem. Eur. J.* 2007, **13**, 6883– 6890.
40. D. J. Harding, C. Kerpál, G. Meijer, A. Fielicke, *Angew. Chem. Int. Ed.* 2012, **51**, 817– 819.
41. G. Albert, C. Berg, M. Beyer, U. Achatz, S. Joos, G. Niedner-Schatteburg, V. E. Bondybey, *Chem. Phys. Lett.* 1997, **268**, 235– 241.
42. D. J. Trevor, D. M. Cox, A. Kaldor, *J. Am. Chem. Soc.* 1990, **112**, 3742– 3749.
43. X. Zhang, R. Liyanage, P. B. Armentrout, *J. Am. Chem. Soc.* 2001, **123**, 5563– 5575.
44. M. Perera, R. B. Metz, O. Kostko, M. Ahmed, *Angew. Chem. Int. Ed.* 2013, **52**, 888– 891.
45. C. Heinemann, R. Wesendrup, H. Schwarz, *Chem. Phys. Lett.* 1995, **239**, 75– 83.
46. J. J. Carroll, J. C. Weisshaar, P. E. M. Siegbahn, C. A. M. Wittborn, M. R. A. Blomberg, *J. Phys. Chem.* 1995, **99**, 14388– 14396.
47. M. L. Campbell, *J. Chem. Soc. Faraday Trans.* 1998, **94**, 353– 358.
48. K. Koszinowski, D. Schröder, H. Schwarz, *J. Phys. Chem. A* 2003, **107**, 4999– 5006.
49. H. G. Cho, L. Andrews, *J. Phys. Chem. A* 2008, **112**, 12293– 12295.
50. X. Zhang, G. Liu, K. H. Meiwes-Broer, G. Ganteför, K. H. Bowen, *Angew. Chem. Int. Ed.* 2016, **55**, 9644– 9647.
51. G. Liu, S. Ciborowski, K. Bowen, *J. Phys. Chem. A* 2017, **121**, 5817– 5822.
52. G. Liu, S. M. Ciborowski, Z. Zhu, K. H. Bowen, *Int. J. Mass Spectrom.* 2019, **435**, 114– 117.
53. G. Liu, E. Miliordos, S. M. Ciborowski, M. Tschurl, U. Boesl, U. Heiz, X. Zhang, S. S. Xantheas, K. H. Bowen, *J. Chem. Phys.* 2018, **149**, 221101.

V. Electron-Molecule Interactions

Negative ions are formed by the interactions between electrons and neutral molecules or clusters. Therefore, negative ion photoelectron spectroscopy (NIPS) is a natural tool to study such interactions. Understanding electron-molecule interactions is of fundamental importance to physical chemistry. The two types of electron-molecule interactions I have primarily investigated are electron-induced proton transfer (EIPT) and bounded electrons due to weak attractions.

EIPT is a fundamental chemistry process. It is particularly relevant to electrochemistry, radiation chemistry, and biology. For inter-molecular EIPT, electrons are first attached to an aggregation of at least two molecules, inducing the transfer of a proton from the acidic site of one molecule to the basic site of another nearby molecule.

Negative ions can be formed due to electron capture by long-range, weak attractive interactions, in which the excess electrons reside in diffuse non-valence orbitals. Weak attractions between electrons and neutral molecules lead to the formation of diffuse excess electron states, these including correlation-bound, quadrupole-bound, polarizability-bound, and dipole-bound electrons.

V.1 Dipole-Bound Anions of Intramolecular Complexes

Elena F. Belogolova[§], *Gaoxiang Liu*[§], Evgeniya P. Doronina, Sandra M. Ciborowski,
Valery F. Sidorkin*, Kit H. Bowen*

*A. E. Favorsky Irkutsk Institute of Chemistry, Siberian Branch of the Russian Academy
of Sciences, Favorsky, 1, Irkutsk 664033, Russian Federation*

*Department of Chemistry, Johns Hopkins University, Baltimore, Maryland 21218,
United States*

§ These authors contribute equally to this work

Abstract

Dipole-bound molecular anions are often envisioned as unperturbed neutral, polar molecules with single excess electrons. We report the observation of intramolecular structural distortions within silatrane molecules due to the formation of their dipole-bound anions. The combination of Rydberg electron transfer–anion photoelectron spectroscopy (RET-PES) and ab initio computational methodologies (CCSD and MP2) was used to study 1-hydro- (**HS**) and 1-fluoro- (**FS**) silatranes and their dipole bound anions, **HS**[−] and **FS**[−]. The vertical detachment energies (VDEs) of **HS**[−] and **FS**[−] were measured to be 48 and 93 meV, respectively. Ab initio calculations accurately reproduced these VDE values as well as their photoelectron spectral profiles. This work revealed significant shortening (by ~0.1 Å) of dative Si ← N bond lengths

when **HS** and **FS** formed dipole-bound anions, **HS⁻** and **FS⁻**. Detailed computational (Franck–Condon) analyses explained the absence of vibrational features in the photoelectron spectra of **HS⁻** and **FS⁻**.

Dipole-bound anions can be formed by the interaction of electrons with highly polar neutral molecules or small clusters.(1–6) The formation of dipole-bound states is thought to be the initial step in the attachment of electrons to many polar molecules. Thus dipole-bound anions that play this role are sometimes referred to as “doorway” or “stepping stone” states.(7–16) A combination of experimental findings and theoretical predictions implies that molecules with dipole moments greater than 2.5 D can form dipole-bound anions.(17,18)

The excess electron in a dipole-bound molecular anion can be envisioned as a highly delocalized cloud, tethered at the positive end of the molecular dipole and extending over a relatively large volume. Because it interacts only weakly with the larger molecule, the excess electron’s binding energy is very small, and there is little distortion of the molecule’s nuclear framework. For these reasons, dipole-bound anions exhibit a distinctive anion photoelectron spectroscopic signature, consisting of a single narrow peak at very low electron binding energy (EBE).(19,20) The narrow peak derives from the fact that the structures of dipole-bonded molecular anions are

essentially the same as their corresponding neutral molecules, which, in turn, leads to near-perfect Franck–Condon overlap and thus to a single narrow peak. In cases where significant structural distortion does occur, however, additional peaks can appear in the anion photoelectron spectra. These are often seen in the dipole-bound anions of hydrogen bond, dimers, and trimers, such as $(\text{HF})_2$ (21,22) and indole $(\text{H}_2\text{O})_{1,2}$ (16) where intermolecular structural changes have occurred. Such peaks are due to combination bands of molecular and intermolecular (weak) vibrations. The dipole-bound anions of lone molecules do not show clear evidence of structural distortion; that is, they tend to exhibit single narrow peaks in their anion photoelectron spectra without evidence of additional Franck–Condon combination bands.

Silatrane, $\text{XSi}(\text{OCH}_2\text{CH}_2)_3\text{N}$ (see Figure 1), are highly polar ($\sim 6\text{--}9$ D) molecular cages with labile, internal $\text{Si} \leftarrow \text{N}$ dative bonds. These bonds are strongly sensitive to the nature of their axial substituents, X, and to external factors.(23–27) An attractive interaction $\text{Si} \leftarrow \text{N}$ in silatrane predetermines the peculiarity of their structure, unusual spectral characteristics, and reactivity as well as a wide spectrum of biological activity.(23,24)

Here we present results from our combined experimental–theoretical study of 1-hydro-silatrane (**HS**) and 1-fluoro-silatrane (**FS**) and their anions. These two were

initially selected because they do not have low-lying vacant orbitals (primarily of π -type)(25–28) and therefore are candidates for forming dipole-bound anions, **HS**⁻ and **FS**⁻. It is also important to note that **HS** and **FS** differ in their Si ← N bond strengths(23,25) and that their geometries are known from electron diffraction studies.(29,30)

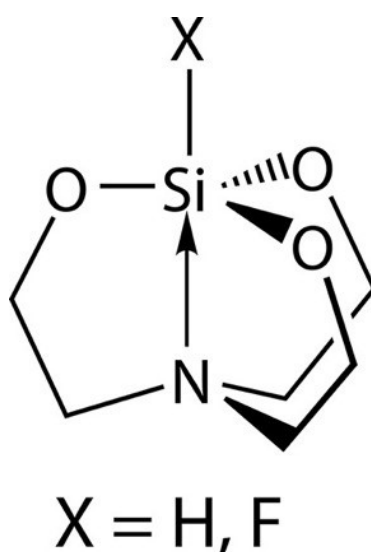


Figure 1. Structure of 1-hydro- (**HS**) and 1-fluoro- (**FS**) silatrane.

The formation of the anions **HS**⁻ and **FS**⁻ benefited from our use of specialized experimental methods. Rydberg electron transfer (RET) is the ideal technique for forming dipole-bound anions. Schermann, Compton, Hammer, and ourselves have used RET extensively to prepare dipole-bound anions and analyze their EBEs using a semiempirical formula.(17,18,31–33) The recently developed combination of RET and anion photoelectron spectroscopy (PES), however, provides a somewhat more

comprehensive picture of dipole-bound anion energetics and structural aspects. In this work, we used our one-of-a-kind RET-PES apparatus and state-of-the-art ab initio computational methods to study the dipole-bound anions of 1-hydro- (**HS**) and 1-fluoro- (**FS**) silatrane, that is, **HS⁻** and **FS⁻**.

Silatrane anions, **HS⁻** and **FS⁻**, were generated by a RET source. Neutral silatrane molecules, **HS** and **FS**, were vaporized in a heated pulsed valve and expanded with 10 psig of helium gas. Their anions, **HS⁻** and **FS⁻**, were formed when the neutral **HS** and **FS** molecules collided with a thermally expanded beam of potassium atoms, which had been excited to nd Rydberg states, where n is the principal quantum number, in two steps using two dye lasers. The anion signals were found to optimize at the 14d Rydberg state for **HS⁻** and 13d Rydberg state for **FS⁻**. The anions were then extracted into a time-of-flight mass spectrometer and mass-selected, after which their excess electrons were photodetached with another laser and energy-analyzed using velocity-map imaging spectroscopy. Details of the experiments are presented in the Supporting Information.

Figure 2 presents the anion photoelectron spectra of **HS⁻** and **FS⁻**. The comb-like spikes along the baseline are due to noise and are of no consequence. Each spectrum consists of a major, sharp peak at rather low EBE, strongly implying

that **HS**⁻ and **FS**⁻ are dipole-bound anions. For **HS**⁻, the EBE peak is centered at 48 meV with a full width at half-maximum (fwhm) of ~35 meV (Figure 2A). The EBE peak of **FS**⁻ is centered at 93 meV also with an fwhm of ~35 meV (Figure 2B), 35 meV being only slightly greater than the experimental resolution. We assign these two peaks as the origins of the transitions between the dipole-bound anions and their corresponding neutral molecules. Therefore, the vertical detachment energy (VDE) values for **HS**⁻ and **FS**⁻ anions are 48 and 93 meV, respectively. Note that the EBE value of **FS**⁻ is higher than that of **HS**⁻, which is to be expected due to the higher dipole moment of **FS** as compared with **HS** (Table S1). In photoelectron spectra such as these, which are dominated by single sharp peaks due to the close similarity between the structures of the anion and its neutral counterpart, the anion's VDE value is only slightly greater than the value of its corresponding neutral's electron affinity (EA).

The computed C_3 symmetry structures of **HS**, **FS**, and their dipole-bound anions, **HS**⁻ and **FS**⁻, optimized at MP2/B2(s) and CCSD/6-31++G(d,p) levels of theory are presented in Figure 3. Both the ²A₁ dipole-bound anions and their corresponding neutral molecules were all found to exhibit single minima on their potential energy surfaces. For neutral molecules, the CCSD/6-31++G(d,p) method accurately reproduces the Si ← N bond lengths, $d_{\text{Si} \leftarrow \text{N}}$, as determined from electron

diffraction data(29,30) to within ~ 0.03 Å, while with the MP2/B2(s) method, the discrepancy is ~ 0.05 Å. More importantly, regardless of the method used for geometry optimization, a significant deformation of the coordination center around the silicon atom, XSiO_3N , is observed upon the addition of an excess electron. This is also accompanied by an increase in η_e , that is, the pentacoordinate character or trigonal bipyramidal structure of the silicon atom (Figure 3, Table S2). Such structural deformation is mainly manifested by a decrease in $d_{\text{Si}\leftarrow\text{N}}$ in the anion compared with that of its corresponding neutral. So, as a measure of the silatrane geometry response to the extra electron addition, we have chosen the $\Delta d_{\text{Si}\leftarrow\text{N}}$ value, which is defined as the difference between the experimental Si \leftarrow N bond lengths for neutral molecules and the calculated bond lengths for their dipole-bound anions. For HS^- , $\Delta d_{\text{Si}\leftarrow\text{N}}$ is predicted to be 0.106 Å when calculated by the MP2/B2(s) method and 0.224 Å when computed by the CCSD/6-31++G(d,p) method. For FS^- , $\Delta d_{\text{Si}\leftarrow\text{N}}$ is computed to be 0.101 Å by MP2/B2(s) and 0.189 Å by CCSD/6-31++G(d,p) (see Figure S1, its legend and corresponding comments).

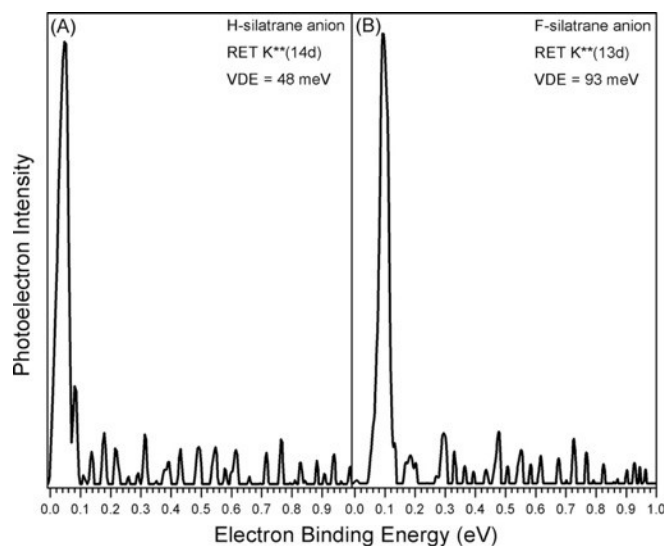


Figure 2. Anion photoelectron spectra of the dipole-bound anions of (A) 1-hydro- and (B) 1-fluoro-silatrane measured with the first harmonic of a Nd:YAG laser (1064 nm, 1.165 eV).

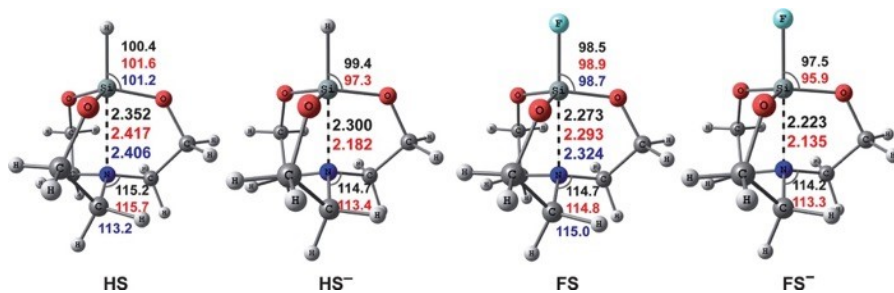


Figure 3. MP2/B2(s) (in black) and CCSD/6-31++G(d,p) (in red) optimized geometries of silatranes, **HS** and **FS**, and their dipole-bound anions, **HS⁻** and **FS⁻**. Electron diffraction structural parameters for **HS** and **FS** are shown in blue. The bond lengths are in angstroms and the bond angles are in degrees. B2(s) is the 6-311++G(d,p) triple- ζ basis set augmented with an additional diffuse s function on each H atom and a set of diffuse s and p functions on the other atoms (see further description in the Supporting Information).

It is pertinent to note that upon the formation of valence-bound silatrane anions, calculations show their dative Si \leftarrow N bonds elongating rather than shortening.(34)

Figure 4 shows that the spin density in **HS⁻** and **FS⁻** is localized outside the nuclear frame on the positive dipole end, confirming them as dipole-bound anions (see also the Figure S2). Therewith, in accordance with the dipole moment values in **HS** and **FS**, the electron cloud density for **FS⁻** is higher than that for **HS⁻** (see, for example, ref (35)).

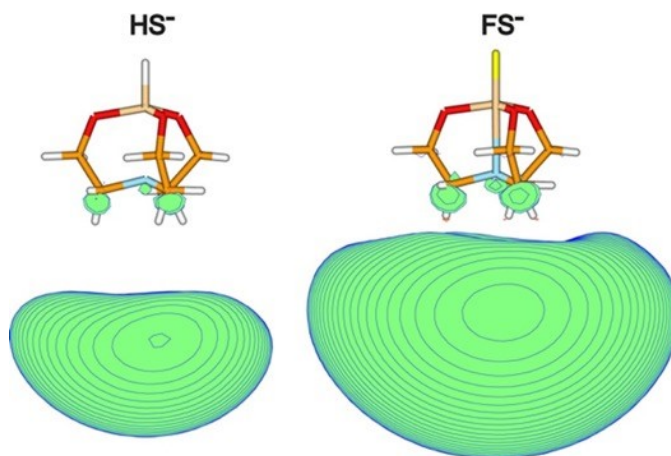


Figure 4. Spin density distributions of **HS⁻** and **FS⁻** obtained at the MP2/B2(s) level (plotted with 0.00003 e·bohr⁻³ contour spacing).

The experimental and calculated VDE values for the dipole-bound anions, **HS⁻** and **FS⁻**, are presented in Table1. The MP2/aug-cc-pVDZ+5s5p4d(N) and MP2/aug-cc-pVDZ+5s5p(H₃) methods predict negative VDE values, incorrectly

estimating the stability of the dipole-bound anions. Only methods that invoke basis sets with a large number of diffuse functions or account for more electron correlation give qualitatively correct predictions on electron attachment to these molecules. Exceptional agreement with experimental VDE values is observed when using the CCSD/6-31++G(d,p) geometries with MP2/aug-cc-pVDZ+5s5p4d(H₃N) and MP2/B2(s) methods. On the contrary, for MP2/B2(s) geometries, the best quality VDE calculations are demonstrated by using CCSD and CCSD(T) methods with the B2(s) and B2 basis sets. Noticeably, the EAs of **HS** and **FS** are calculated at the CCSD(T)/B2 level to be 39 and 90 meV, respectively, these being slightly lower than their VDE values, as expected. Because the VDE and EA values virtually coincide when there is near-perfect Franck–Condon overlap, as is the case for dipole-bound anions, the EA values of **HS** and **FS** were not separately determinable by the experiment.

Table 1. Experimental and Calculated Values of the Vertical Detachment Energies (VDEs, in eV) for the Dipole-Bound Anions, HS⁻ and FS^{-b}

Geometry	CCSD/6-31++G(d,p)		MP2/B2(s)	
Energy	HS ⁻	FS ⁻	HS ⁻	FS ⁻
Exp.	0.048	0.093	0.048	0.093
MP2/aug-cc-pVDZ+5s5p4d(N)	-0.003	0.001	-0.005	-0.001
MP2/aug-cc-pVDZ+5s5p(H ₃)	-0.004	-0.004	-0.005	-0.004
MP2/aug-cc-pVDZ+5s5p4d(H ₃ N)	0.050	0.094	0.031	0.072 ^[a]
MP2/B2(s)	0.047	0.089	0.031	0.068
MP2/B2	0.052	0.099	0.033	0.075
CCSD/B2(s)	0.063	0.111	0.042	0.086
CCSD(T)/B2(s)	0.066	0.115	0.045	0.089
CCSD/B2	0.068	0.120	0.045	0.094
CCSD(T)/B2	0.071	0.123	0.048	0.097

^a The same VDE value was obtained using the MP2/aug-cc-pVDZ+7s7p8d(N) method.

^b Red boxes encapsulate the combinations of theoretical methods for geometry and energies that best match experiment.

The $\Delta d_{\text{Si}\leftarrow\text{N}}$ values predicted by CCSD/6-31++G(d,p) are considerably larger than those predicted by MP2/B2(s), specifically by 0.108 Å for HS⁻ and 0.088 Å for FS⁻ (see Figure 3). Because excellent agreement between the experimental and calculated VDE values is found for both MP2 and CCSD optimized geometries, it is difficult to determine which geometry is more accurate based only on the quality of the VDE calculations.

The choice between the geometry optimization methods for silatranes and their anions can also be done using the Franck–Condon simulation of the photoelectron spectra

of **HS⁻** and **FS⁻** (Figure 5). An excellent match between experimental and theoretical photoelectron spectra is achieved when using the MP2 optimized geometries for **HS⁻** and **FS⁻** (Figure 5A,B). The estimated fwhm values for the dominant peak in the theoretical photoelectron spectra of **HS⁻** and **FS⁻** (0.036 and 0.035 eV, respectively) agree with the experimental widths. The simulated photoelectron spectra of **HS⁻** and **FS⁻** using the CCSD geometries have complex vibrational profiles, which are fundamentally different from the observed experimental photoelectron spectra (Figure 5C,D). As a result, we conclude that the CCSD/6-31++G(d,p) method overestimates the change of the Si ← N bond length and also other structural parameters when an excess electron is attached to **HS** or **FS**. The MP2/B2(s) level of theory predicts more accurate anionic geometries and reasonable $\Delta d_{\text{Si} \leftarrow \text{N}}$ values of 0.106 Å for **HS⁻** and 0.101 Å for **FS⁻**. Such a large deformation of bond contacts is unprecedented for dipole-bound molecular anions.

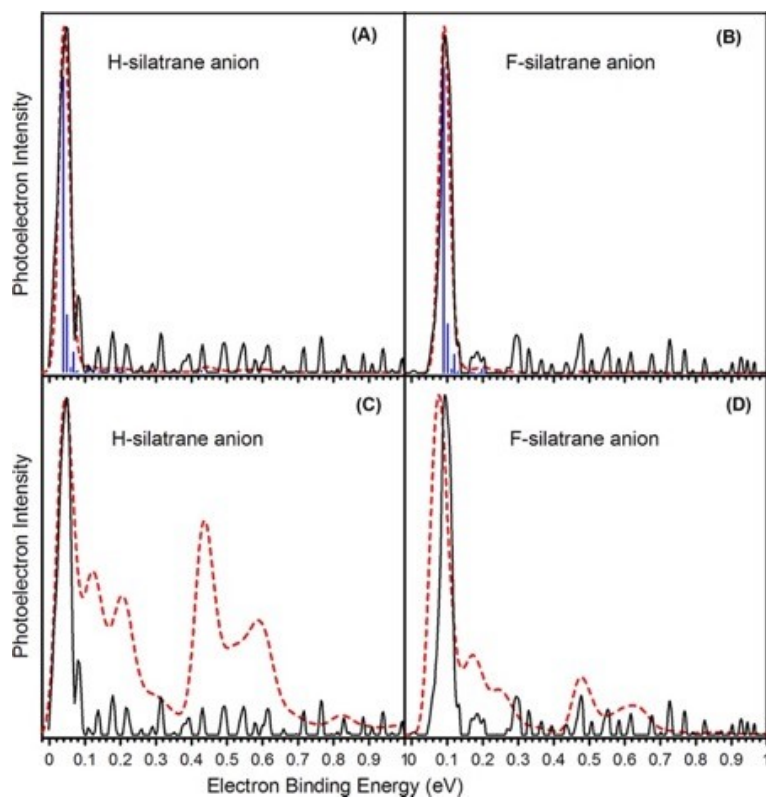


Figure 5. Overlaid experimental (black solid line) and Franck–Condon (red dashed line) photoelectron spectra of HS^- and FS^- . Vibrational progressions are given by a blue line spectrum. (A,B) MP2/B2(s) geometry optimizations and normal vibrational modes. In determining the position of the 0–0 transition, we used the CCSD(T)/B2 adiabatic electron affinity (AEA) value (0.039 eV) for HS^- and the CCSD/B2 AEA value (0.090 eV) for FS^- . (C,D) CCSD/6-31++G(d,p) optimized geometries and MP2/B2(s) normal vibrational modes.

Franck–Condon factors are listed in Table S3. We show that the main peaks in the simulated photoelectron spectra of HS^- and FS^- are formed by the superposition of the 0_0^0 , 1_0^1 , 4_0^1 and 0_0^0 , 1_0^1 , 6_0^1 transitions, respectively. These transitions are spaced

apart from one another by <0.03 eV, which is comparable to the instrumental resolution. This situation can explain the observed asymmetry and broadening at the bottom of the **HS**⁻ and **FS**⁻ peaks on their high EBE sides. The geometric relaxation upon the attachment of an electron occurs mainly along the first and fourth normal vibrational modes in **HS** and along the first and sixth modes in **FS**. They correspond to the Si ← N dative bond stretching and torsional motion of the SiO₃ and N(CH₂)₃ fragments around the C₃ symmetry axis in the silatrane molecule. The corresponding harmonic vibrations have very low frequencies (ω): for **HS**, $\omega_1 = 85$ cm⁻¹ and $\omega_4 = 235$ cm⁻¹ with increases of 2 and 10 cm⁻¹, respectively, upon transition to the anionic state; for **FS**, $\omega_1 = 91$ cm⁻¹ and $\omega_6 = 237$ cm⁻¹ with increases of 0 and 14 cm⁻¹, respectively, in the anionic state. The reason for this is the high lability of the Si ← N dative bond in **HS**, **FS**, and their dipole-bound anions, where <0.017 eV of energy is needed to change the Si ← N distance by 0.1 Å (see Figure S1 and refs (36–38)). Consequently, the vibrational transitions ($0_0^0, 1_0^1, 4_0^1$) and ($0_0^0, 1_0^1, 6_0^1$), which are associated with the donor–acceptor moiety XSiO₃ ← N(CH₂)₃, are very energetically close and form a separate, narrow main peak (typical of dipole bound anions) in the photoelectron spectra of **HS**⁻ and **FS**⁻.

In addition to the above, the vibrational transitions 13_0^1 at 0.11 eV and 33_0^1 at 0.19 eV for **HS**⁻ and 22_0^1 at ~ 0.20 eV for **FS**⁻ were observed in their theoretical spectra (Table

S3). However, despite the significant structural changes in the coordination center XSiO_3N of **HS** and **FS** upon the extra electron attachment, the intensity of these additional peaks in the photoelectron spectra of **HS**⁻ and **FS**⁻ does not exceed the noise level in the experimental spectrum. Indeed, judging from the Franck–Condon factors values (Table S3), the relatively rigid modes 13 (HSiO bending) and 33 (CO bond stretching) in **HS** and mode 22 (SiF bond stretching) in **FS** are practically not populated upon the electron photodetachment from **HS**⁻ and **FS**⁻.

To summarize, we report the observation of an unusual structural change when a lone molecule (intramolecular complex) forms dipole-bound anions. This provides new insight into our current understanding about dipole-bound anions, where excess electrons are weakly bound to the neutral molecular framework. The novel combination of RET and PES is promising for investigating anions that were not easily attained previously.

References

1. Jordan, K. D. Studies of the Temporary Anion States of Unsaturated Hydrocarbons by Electron Transmission Spectroscopy. *Acc. Chem. Res.* 1979, *12*, 36–42.
2. Simons, J.; Jordan, K. D. Ab Initio Electronic Structure of Anions. *Chem. Rev.* 1987, *87*, 535–555.
3. Gutowski, G.; Skurski, P.; Boldyrev, A. I.; Simons, J.; Jordan, K. D. Contribution of Electron Correlation to the Stability of Dipole-Bound Anionic States. *Phys. Rev. A: At., Mol., Opt. Phys.* 1996, *54*, 1906–1909.
4. Simons, J. Molecular Anions. *J. Phys. Chem. A* 2008, *112*, 6401–6511.
5. Liu, H. T.; Ning, C. G.; Huang, D. L.; Dau, P. D.; Wang, L. S. Observation of Mode-

- Specific Vibrational Autodetachment from Dipole-Bound States of Cold Anions. *Angew. Chem., Int. Ed.* 2013, 52, 8976– 8979.
- Huang, D.; Liu, H.; Ning, C.; Zhu, G.; Wang, L. Probing the Vibrational Spectroscopy of the Deprotonated Thymine Radical by Photodetachment and State-Selective Autodetachment Photoelectron Spectroscopy via Dipole-Bound States. *Chem. Sci.* 2015, 6, 3129– 3138.
 - Dabkowska, I.; Rak, J.; Gutowski, M.; Nilles, J. M.; Stokes, S. T.; Radisic, D.; Bowen, K. H., Jr. Barrier-Free Proton Transfer in Anionic Complex of Thymine with Glycine. *Phys. Chem. Chem. Phys.* 2004, 6, 4351– 4357.
 - Chomicz, L.; Zdrowowicz, M.; Kasprzykowski, F.; Rak, J.; Buonaugurio, A.; Wang, Y.; Bowen, K. H. How to Find Out Whether a 5-Substituted Uracil Could Be a Potential DNA Radiosensitizer. *J. Phys. Chem. Lett.* 2013, 4, 2853– 2857.
 - Bachorz, R. A.; Kloppe, W.; Gutowski, M.; Li, X.; Bowen, K. H. Photoelectron Spectrum of Valence Anions of Uracil and First-Principles Calculations of Excess Electron Binding Energies. *J. Chem. Phys.* 2008, 129, 054309.
 - Xu, S. J.; Nilles, J. M.; Bowen, K. H. Zwitterion Formation in Hydrated Amino Acid, Dipole Bound Anions: How Many Water Molecules Are Required. *J. Chem. Phys.* 2003, 119, 10696– 10701.
 - Sommerfeld, T. Intramolecular Electron Transfer from Dipole-Bound to Valence Orbitals: Uracil and 5-Chlorouracil. *J. Phys. Chem. A* 2004, 108, 9150– 9154.
 - Eustis, S. N.; Radisic, D.; Bowen, K. H.; Bachorz, R. A.; Haranczyk, M.; Schenter, G.; Gutowski, M. Electron-Driven Acid Base Chemistry: Proton Transfer from Hydrogen Chloride to Ammonia. *Science* 2008, 319, 936– 939.
 - Sommerfeld, T. Doorway Mechanism for Dissociative Electron Attachment to Fructose. *J. Chem. Phys.* 2007, 126, 124301– 124305.
 - Desfrancois, C.; Baillon, B.; Schermann, J. P.; Arnold, S. T.; Hendricks, J. H.; Bowen, K. H. Prediction and Observation of a New, Ground State, Dipole-Bound Dimer Anion: The Mixed Water/Ammonia System. *Phys. Rev. Lett.* 1994, 72, 48– 51.
 - Kelly, J.; Xu, S.; Graham, J.; Nilles, M.; Radisic, D.; Buonaugurio, A.; Bowen, K.; Hammer, N.; Tschumper, G. Photoelectron Spectroscopic and Computational Study of Hydrated Pyrimidine Anions. *J. Phys. Chem. A* 2014, 118, 11901– 11907.
 - Buytendyk, A. M.; Buonaugurio, A. M.; Xu, S. J.; Nilles, J. M.; Bowen, K. H.; Kirnosov, N.; Adamowicz, L. Computational and Photoelectron Spectroscopic Study of the Dipole-Bound Anions, Indole(H₂O)_{1,2}⁻. *J. Chem. Phys.* 2016, 145, 024301.
 - Compton, R. N.; Hammer, N. I. *Adv. Gas Phase Ion Chem.*; JAI Press: Stamford, CT, 2001.
 - Desfrancois, C.; Khelifa, N.; Lisfi, A.; Schermann, J. P.; Eaton, J. G.; Bowen, K. H. Electron Transfer Collisions Between Small Water Clusters and Laser-Excited Rydberg Atoms. *J. Chem. Phys.* 1991, 95, 7760– 7762.
 - Jordan, K. D.; Luken, W. Theoretical Study of the Binding of an Electron to a Molecular Dipole: LiCl⁻. *J. Chem. Phys.* 1976, 64, 2760– 2766.

20. Castleman, A. W.; Bowen, K. H. Clusters: Structure, Energetics, and Dynamics of Intermediate States of Matter. *J. Phys. Chem.* 1996, *100*, 12911– 12944.
21. Hendricks, J. H.; de Clercq, H. L.; Lyapustina, S. A.; Bowen, K. H. Negative Ion Photoelectron Spectroscopy of the Ground State, Dipole-Bound Dimeric Anion, $(\text{HF})_2^-$. *J. Chem. Phys.* 1997, *107*, 2962– 2967.
22. Gutowski, M.; Skurski, P. Theoretical Study of the Dipole-Bound Anion $(\text{HF})_2^-$. *J. Chem. Phys.* 1997, *107*, 2968– 2973, DOI: 10.1063/1.474654.
23. Pestunovich, V.; Kirpichenko, S.; Voronkov, M. *The Chemistry of Organic Silicon Compounds*; Wiley: Chichester, U.K., 1998.
24. Puri, J. K.; Singh, R.; Chahal, V. K. Silatranes: A Review on Their Synthesis, Structure, Reactivity and Applications. *Chem. Soc. Rev.* 2011, *40*, 1791– 1840.
25. Belogolova, E. F.; Sidorkin, V. F. Correlation Among the Gas-Phase, Solution, and Solid-Phase Geometrical and NMR Parameters of Dative Bonds in the Pentacoordinate Silicon Compounds. 1-Substituted Silatranes. *J. Phys. Chem. A* 2013, *117*, 5365– 5376.
26. Sidorkin, V. F.; Belogolova, E. F.; Doronina, E. P. Assignment of Photoelectron Spectra of Silatranes: First Ionization Energies and the Nature of the Dative Si←N Contact. *Phys. Chem. Chem. Phys.* 2015, *17*, 26225– 26237.
27. Sidorkin, V. F.; Belogolova, E. F.; Wang, Y.; Jouikov, V.; Doronina, E. P. Electrochemical Oxidation and Radical Cations of Structurally Non-Rigid Hypervalent Silatranes: Theoretical and Experimental Studies. *Chem. - Eur. J.* 2017, *23*, 1910– 1919.
28. Trofimov, A. B.; Zakrzewski, V. G.; Dolgounitcheva, O.; Ortiz, J. V.; Sidorkin, V. F.; Belogolova, E. F.; Belogolov, M.; Pestunovich, V. A. Silicon-Nitrogen Bonding in Silatranes: Assignment of Photoelectron Spectra. *J. Am. Chem. Soc.* 2005, *127*, 986– 995.
29. Shishkov, I. F.; Khristenko, L. V.; Rudakov, F. M.; Golubinskii, A. V.; Vilkov, L. V.; Karlov, S. S.; Zaitseva, G. S.; Samdal, S. Molecular Structure of Silatrane Determined by Gas Electron Diffraction and Quantum-Mechanical Calculations. *Struct. Chem.* 2004, *15*, 11– 16.
30. Forgács, G.; Kolonits, M.; Hargittai, I. The Gas-Phase Molecular Structure of 1-Fluorosilatrane from Electron Diffraction. *Struct. Chem.* 1990, *1*, 245– 250.
31. Hammer, N.; Diri, K.; Jordan, K.; Desfrancois, C.; Compton, R. Dipole-Bound Anions of Carbonyl, Nitrile, and Sulfoxide Containing Molecules. *J. Chem. Phys.* 2003, *119*, 3650– 3660.
32. Hammer, N.; Compton, R. N.; Adamowicz, L.; Stepanian, S. Isotope Effects in Dipole-Bound Anions of Acetone. *Phys. Rev. Lett.* 2005, *94*, 153004.
33. Hammer, N.; Hinde, R.; Compton, R.; Diri, K.; Jordan, K.; Radisic, D.; Stokes, S. T.; Bowen, K. Dipole-Bound Anions of Highly Polar Molecules: Ethylene Carbonate and Vinylene Carbonate. *J. Chem. Phys.* 2004, *120*, 685– 690.
34. Belogolova, E. F.; Vakul'skaya, T. I.; Sidorkin, V. F. Radical Anions of Hypervalent Silicon Compounds: 1-Substituted Silatranes. *Phys. Chem. Chem. Phys.* 2015, *17*, 12735– 12746.
35. Smith, D. M. A.; Jalbout, A. F.; Smets, L.; Adamowicz, L. Cytosine Anions: Ab Initio

- Study. *Chem. Phys.* 2000, 260, 45– 51.
36. Sidorkin, V. F.; Doronina, E. P. Cage Silaphosphanes with a P-Si Dative Bond. *Organometallics* 2009, 28, 5305– 5315.
 37. Csonka, G. I.; Hencsei, P. Ab Initio Molecular Orbital Study of 1-Fluorosilatrane. *J. Comput. Chem.* 1994, 15, 385– 394.
 38. Schmidt, M. W.; Windus, T. L.; Gordon, M. S. Structural Trends in Silicon Atranes. *J. Am. Chem. Soc.* 1995, 117, 7480– 7486.

V.2 Dipole-Bound Anions: Formed by Rydberg Electron Transfer (RET) and Studied by Velocity Map Imaging–Anion Photoelectron Spectroscopy (VMI–aPES)

Sandra M. Ciborowski, *Gaoxiang Liu*, Jacob D. Graham, Allyson M. Buytendyk, Kit H. Bowen

Department of Chemistry, Johns Hopkins University, Baltimore, USA

Abstract

Here, we demonstrate the capabilities of the unique combination of Rydberg Electron Transfer (RET) and Velocity Map Imaging–Anion Photoelectron Spectroscopy (VMI–aPES) to form dipole bound anions and to measure their photoelectron spectra. For these purposes, we have chosen the dipole bound anions of acetonitrile, ammonia–water dimer, water dimer, dimethyl sulfoxide and thymine as examples. All of these had been previously formed and/or studied but by other methodologies.

Introduction

The interactions between electrons and atoms, molecules, or clusters govern many processes in chemistry and physics. When stable negative ions are formed as a result of these interactions, they may exist either as valence anions or as diffuse electron states [1-39]. As negative ions, they can be mass-analyzed in mass spectrometers

and, once mass-selected, their anion photoelectron spectra can be measured. While we can utilize a variety of ion sources to create negative ions, we focus here on the Rydberg electron transfer (RET) anion source as a means of forming them and on velocity map imaging as a technique for measuring their anion photoelectron spectra.

Rydberg electron transfer (RET) is a gentle process that transfers an electron from a highly-excited atom to a neutral molecule, forming a negative ion. In RET, a pulsed, helium-seeded beam of neutral molecules is crossed with a continuous, thermal beam of potassium atoms, which have been excited to one of their Rydberg levels by two dye laser pulses: one set at a fixed frequency to pump the potassium atoms to their $^2P_{3/2}$ state and the other tuned to the appropriate nd Rydberg level. Upon collision of the neutral molecule and the highly excited Rydberg atom, charge transfer occurs, forming an ion pair. Once it separates into ions, the anions produced by RET are pulsed through a time-of-flight mass spectrometer, mass-selected, photodetached by another laser pulse, and their resultant electrons energy-analyzed by anion photoelectron spectroscopy (aPES). Negative ion photoelectron spectroscopy (aPES) is a powerful tool for probing electronic structure information about neutral molecules and/or clusters. Anion PES is governed by the energy-conserving relationship, $h\nu = EBE + EKE$, where $h\nu$ is the energy of the photon beam, EBE is the binding energy of the electron, and EKE is the kinetic energy of the electron. Our time-of-flight mass

spectrometric and photoelectron spectroscopic apparatus has previously been described [11,40]. The apparatus includes both a magnetic bottle energy analyzer, which has a resolution of about 35 meV at EKE of 1 eV, as well as a velocity-map imaging (VMI) energy analyzer, with $\Delta E/E \sim 0.03$. The most common information provided by anion photoelectron spectra is the vertical detachment energy (VDE) of the anion being studied. The VDE is the photodetachment transition energy from the anion's ground state to its neutral counterpart at the structure of the anion. (Photodetachment is an ultra-fast and therefore vertical process.) The adiabatic electron affinity (EA) is the energy difference between the ground states of the anion and its neutral counterpart. Its appearance in a photoelectron spectrum is dependent on the structural similarity between the anion and its neutral, i.e., on Franck-Condon overlap. In most of the anions presented here, the structures of the anion and its neutral are almost identical, making the VDE and the EA values essentially the same values. The VDE value in a given photoelectron spectrum is the electron binding energy (EBE) corresponding to the intensity maximum of the lowest EBE peak in the spectrum. When the VDE value is small, the electron binding energy for that anion is also small and in all likelihood the geometries of the anion and its corresponding neutral molecule are quite similar. The RET technique allows us to create unusually fragile anions. Here, we demonstrate some of the capabilities of this one-of-a-kind combination of a Rydberg electron transfer anion source and velocity map imaging-

anion photoelectron spectroscopy. Velocity map imaging is the electron energy analysis technique of choice for measuring the anion photoelectron spectra of low VDE anions.

Results

Below in Figure 1, we present mass spectra of eight anions made with our RET ion source, whereas in Figure 2-7, we present the corresponding anion photoelectron spectra of six of those same systems. Five of the six anions presented in Figure 2 are dipole bound anions. For molecules (or small clusters) that do not form valence anions, they can often form dipole bound anions when their dipole moments are large enough to capture an excess electron. The critical dipole moment required is equal or greater than ~ 2.5 Debye. The RET and VMI-aPES combination is especially well-suited for studying dipole bound anion states.

Figures 2-7 present anion photoelectron spectra of the species we formed by RET. Since RET is a resonant process, the K^{**} Rydberg level used to make a given anion is indicated on the spectrum by nd , where n is the principle quantum number. For the five dipole bound anions discussed here, Table 1 compares VDE values from previous experiments, from the present RET-aPES experiments, and from theory, along with listing the dipole moments of their neutral counterparts.

Acetonitrile was found to form a dipole bound anion in both stand-alone RET experiments [14-16], in conventional anion photoelectron experiments using a non-

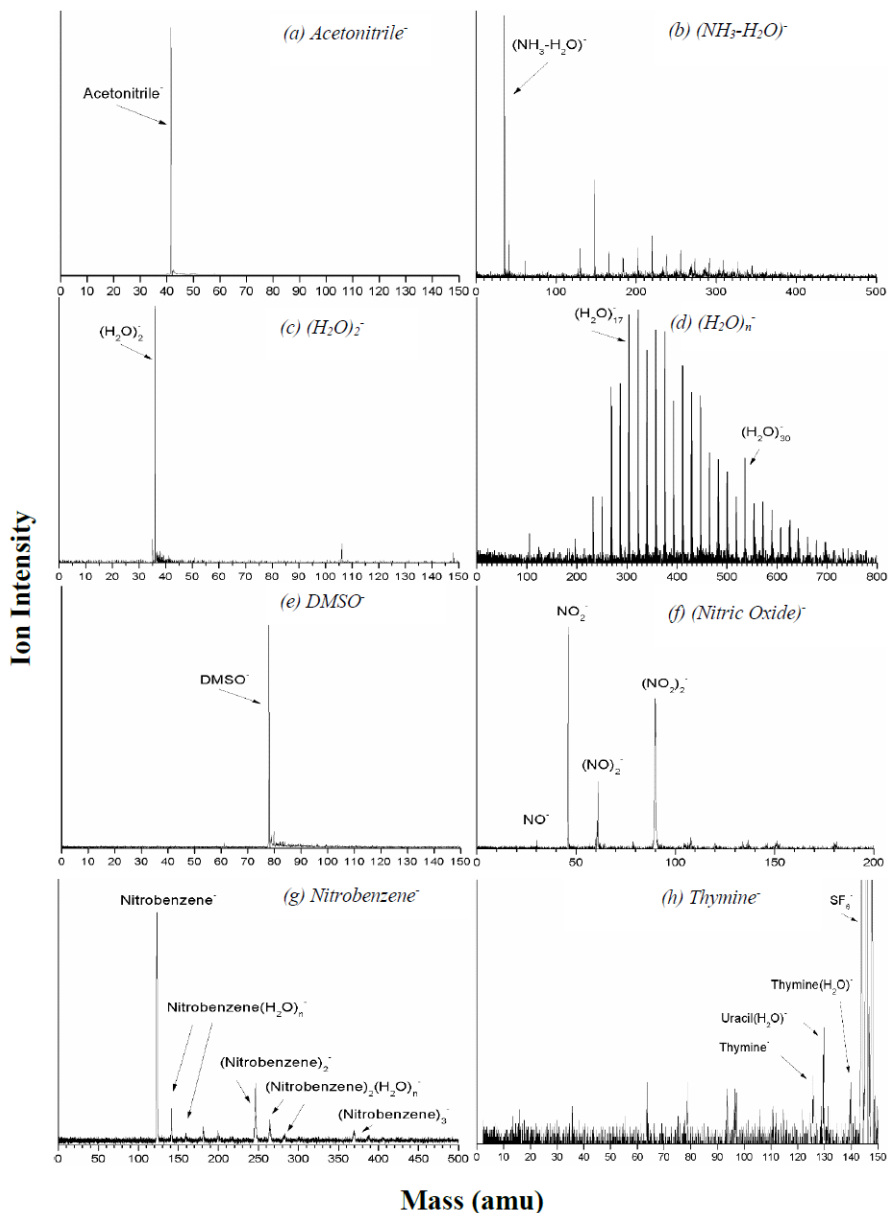


Figure 1. Mass spectra of the anions: (a) acetonitrile anion, (b) ammonia-water dimer anion, (NH₃-H₂O)⁻, (c) water dimer anion, (H₂O)₂⁻, (d) water cluster anions, (H₂O)_n⁻,

(e) dimethyl sulfoxide anion, DMSO^- , (f) nitric oxide anions, NO^- , (g) nitrobenzene anions, and (h) thymine anions, made with the Rydberg electron transfer (RET) source and analyzed by our TOF mass spectrometer.

RET anion source [17,20,30,36], and through theoretical calculations [19,30]. Our photoelectron spectrum of the acetonitrile anion, generated and measured by the combined RET-VMI-aPES technique, is shown in Figure 2. The single, narrow peak at very low electron binding energy (EBE) is characteristic of diffuse electron states, such as dipole bound anions. The peak's narrowness is due to the structures of the anion and the neutral being nearly identical. The low EBE value of its peak center (low VDE) is due to its excess electron being weakly bound. While there is some variation in the acetonitrile anion's VDE values listed in Table 1, they are also broadly consistent.

While ammonia alone has a relatively low dipole moment of ~ 1.4 D, its hetero-dimer with water, i.e., $(\text{NH}_3\text{-H}_2\text{O})$, has a dipole moment of 2.9 D. This led us to predict that it would form a dipole bound dimer anion. Stand-alone RET experiments and calculations showed that it does [21,22]. Our anion photoelectron spectrum of $(\text{NH}_3\text{-H}_2\text{O})^-$, generated and measured by the combined RET-VMI-aPES technique, is shown in Figure 3. VDE comparisons in Table 1 are again broadly consistent with one another.

While the water molecule also has a modest dipole moment of ~ 1.85 D, its dimer, i.e., $(\text{H}_2\text{O})_2$, has a dipole moment of ~ 2.6 D [21,23] and, since it is greater than 2.5 D, it forms a dipole bound anion. The water dimer anion, $(\text{H}_2\text{O})_2^-$, was the first dipole bound anion to be seen by anion photoelectron spectroscopy [13,21,23,24,33]. Our anion photoelectron spectrum of $(\text{H}_2\text{O})_2^-$, generated and measured by the combined RET-VMI-aPES technique, is shown in Figure 4. VDE comparisons in Table 1 are consistent with one another.

Dimethyl sulfoxide ($(\text{CH}_3)_2\text{SO}$) has a dipole moment of 3.96 D and was shown by through stand-alone RET experiments to form a dipole bound anion [16,26]. Our anion photoelectron spectrum of DMSO^- , generated and measured by the combined RET-VMI-aPES technique, is shown in Figure 5, again in broad agreement with other measurements.

Thymine has a dipole moment of 4.13 D and, thus, is also able to bind an excess electron via its dipolar field. A combination of experimental and theoretical assessments agrees [27,28,30,38]. Our anion photoelectron spectrum of the thymine dipole bound anion, generated and measured by the combined RET-VMI-aPES technique, is shown in Figure 6, and is again in broad agreement with other

measurements.

The last spectrum to be presented is that of $(\text{H}_2\text{O})_{17}^-$. While not a dipole bound anion, it is nevertheless a diffuse electron state and is usually considered to be an embryonic hydrated electron state. It was originally measured by both stand-alone RET and conventional anion photoelectron spectroscopy [24,33]. Our anion photoelectron spectrum of $(\text{H}_2\text{O})_{17}^-$, generated and measured by the combined RET-VMI-aPES technique, is shown in Figure 7 and matches previous anion photoelectron spectra of it quite well.

Table 1. Comparison of the vertical detachment energy (VDE) values from this work, previous experiments, and theoretical calculations for the studied anionic species.

Anionic Species	Dipole Moment (μ , D)	VDE (meV)		
		Current Exp.	Previous Exp.	Theory
Acetonitrile	3.92 ^{a,b}	22	3, ^c 11, ^d 12, ^e 18.0, ^f 18.2 ^g	13.4, ^h 15.5 ^g
(NH ₃ -H ₂ O)	2.9 ⁱ	7	9 ⁱ	13.5 ^j
(H ₂ O) ₂	2.6 ^{i,k}	35	42 ^{i,l} 45, ^{k,m} 48 ⁿ	41.9 ^o
DMSO	3.96 ^{a,b}	5	7.4, ^a 13.9 ^b	13.9 ^b

Thymine	4.13 ^p	71	69 ^q	51 ^r , 69 ^g
---------	-------------------	----	-----------------	--------------------------------------

^aSee ref. 16; ^bSee ref. 26; ^cSee ref. 20; ^dSee ref. 15,16,36; ^eSee ref. 14; ^fSee ref. 17; ^gSee ref. 30;
^hSee ref. 19; ⁱSee ref. 21; ^jSee ref. 22; ^kSee ref. 23; ^lSee ref. 33; ^mSee ref. 13; ⁿSee ref. 24; ^oSee ref.
25; ^pSee ref. 28; ^qSee ref. 27; ^rSee ref. 38.

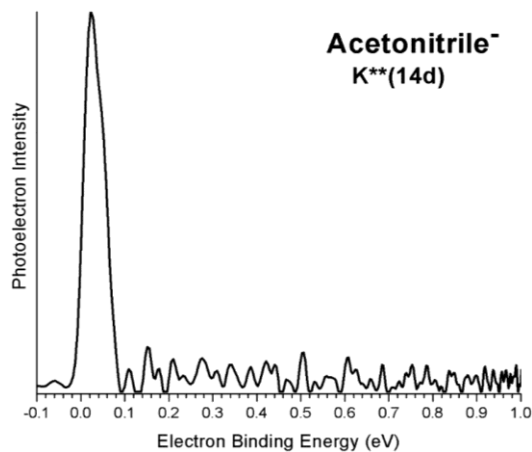


Figure 2. Photoelectron spectrum of the acetonitrile anion taken with the first harmonic (1064 nm) of a Nd:YAG laser.

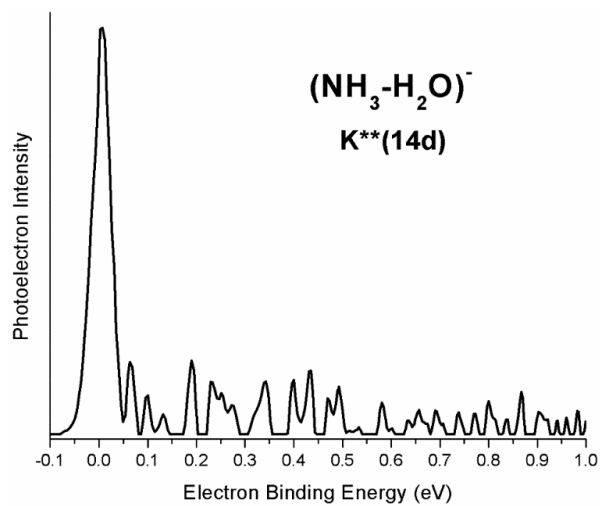


Figure 3. Photoelectron spectrum of the ammonia-water dimer anion taken with the first harmonic (1064 nm) of a Nd:YAG laser.

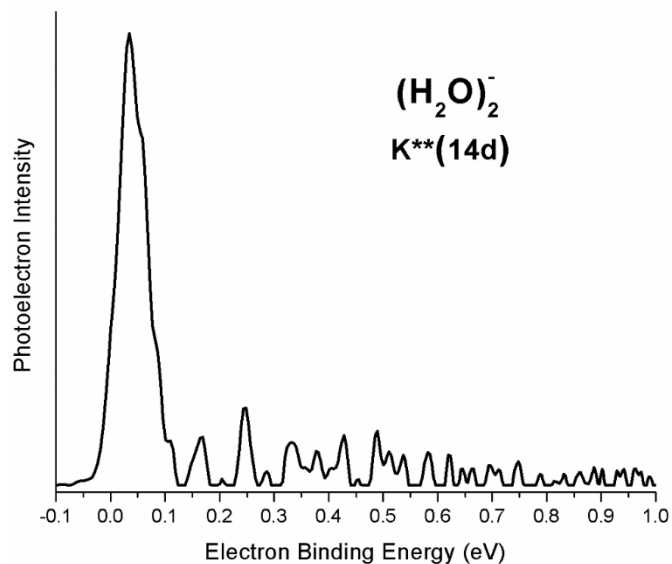


Figure 4. Photoelectron spectrum of the water dimer anion taken with the first harmonic (1064 nm) of a Nd:YAG laser.

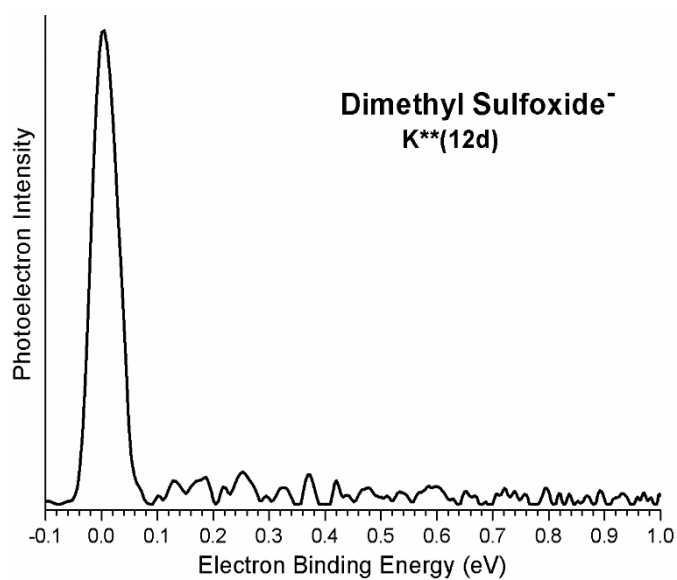


Figure 5. Photoelectron spectrum of the dimethyl sulfoxide anion, DMSO^- , taken with

the first harmonic (1064 nm) of a Nd:YAG laser.

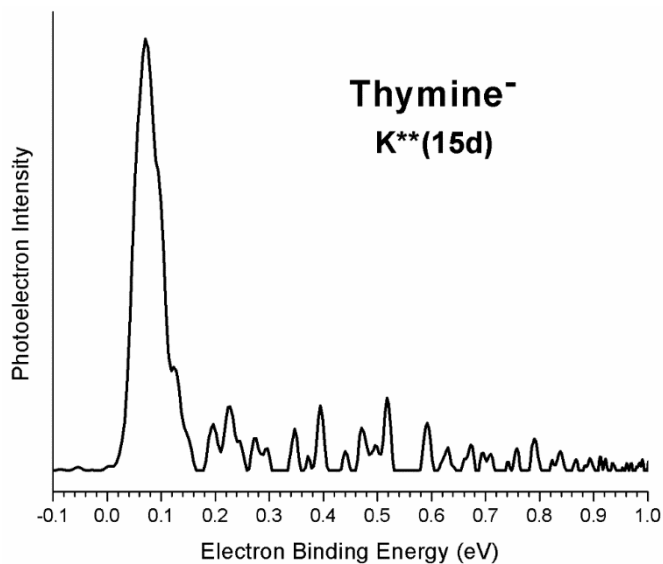


Figure 6. Photoelectron spectrum of the thymine anion taken with the first harmonic (1064 nm) of a Nd:YAG laser.

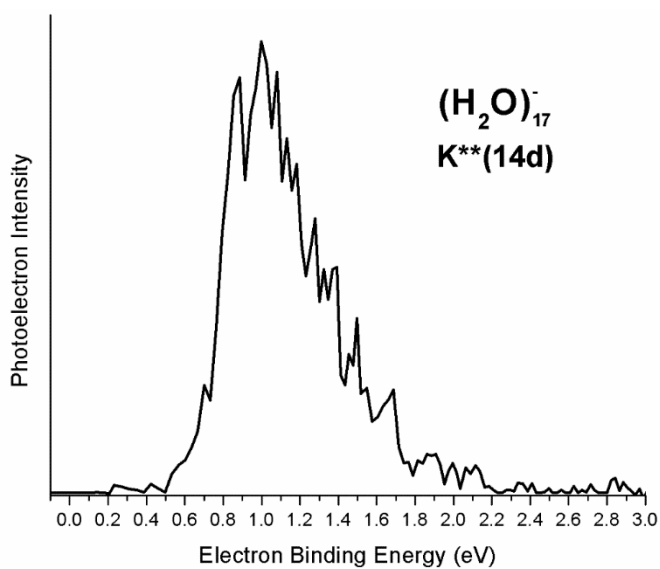


Figure 7. Photoelectron spectrum of the water cluster anion, (H₂O)₁₇⁻, taken with the

third harmonic (355 nm) of a Nd:YAG laser.

Summary

Here, we have presented a collection of mostly dipole-bound, anion photoelectron spectra, generated and measured by our combined RET-VMI-aPES technique, for the purpose of demonstrating the capabilities of this unique methodology.

References

1. G. H. Lee, S. T. Arnold, J. G. Eaton, H. W. Sarkas, K. H. Bowen, C. Ludewigt, and H. Haberland, *Z. Phys. D* **20**, 9 (1991).
2. J. G. Eaton, S. T. Arnold, and K. H. Bowen, *Int. J. Mass Spec. Ion Proc.* **102**, 303 (1990).
3. J. V. Coe, J. T. Snodgrass, C. B. Freidhoff, K. M. McHugh, and K. H. Bowen, *J. Chem. Phys.* **87**, 4302 (1987).
4. J. V. Coe, J. T. Snodgrass, C. B. Freidhoff, K. M. McHugh, and K. H. Bowen, *Chem. Phys. Lett.* **124**, 274 (1986).
5. P. Storoniak, H. Wang, Y. J. Ko, X. Li, S. T. Stokes, S. Eustis, K. H. Bowen, and J. Rak, in *Practical Aspects of Computational Chemistry III*, edited by J. Leszczynski and M. K. Shukla (Springer, Boston, MA, 2014).
6. M. Haranczyk, M. Gutowski, X. Li, and K. H. Bowen, *Proc. Natl. Acad. Sci.* **104**, 4804 (2007).
7. K. Mazurkiewicz, M. Haranczyk, M. Gutowski, J. Rak, D. Radisic, S. N. Eustis, D. Wang, and K. H. Bowen, *J. Am. Chem. Soc.* **129**, 1216 (2007).
8. D. Svozil, P. Jungwirth, and Z. Havlas, *Collect. Czech. Chem. Commun.* **69**, 1395 (2004).
9. M. R. Nimlos and G. B. Ellison, *J. Phys. Chem.* **90**, 2574 (1986).
10. O. Dolgounitcheva, V. G. Zakrzewski, and J. V. Ortiz, *Chem. Phys. Lett.* **307**, 220 (1999).
11. E. F. Belogolova, G. Liu, E. P. Doronina, S. M. Ciborowski, V. F. Sidorkin, and K. H. Bowen, *J. Phys. Chem. Lett.* **9**, 1284 (2018).
12. T. Sommerfeld, *J. Chem. Phys.* **121**, 4097 (2004).
13. J. H. Hendricks, H. L. de Clercq, S. A. Lyapustina, C. A. Fancher, T. P. Lippa, J. M. Collins, S. T. Arnold, G. H. Lee, and K. H. Bowen, in *Structures and Dynamics of Clusters, Proceedings of Yamada Conference XLIII, Shimoda, Japan, 1995*, edited by T. Kondow, K. Kaya, and A. Terasaki (Universal Academy Press, Tokyo, 1996), p. 321.
14. C. Desfrancois, H. Abdoul-Carime, C. Adjouri, N. Khelifa, and J. P. Schermann, *Europhys.*

- Lett.* **26**, 25 (1994).
15. R. A. Popple, C. D. Finch, and F. B. Dunning, *Chem. Phys. Lett.* **234**, 172 (1995).
 16. L. Suess, Y. Liu, R. Parthasarathy, and F. B. Dunning, *J. Chem. Phys.* **119**, 12890 (2003).
 17. C. Desfrancois, *Phys. Rev. A* **51**, 3667 (1995).
 18. K. D. Jordan, F. Wang, *Annu. Rev. Phys. Chem.* **54**, 367 (2003).
 19. M. Gutowski, P. Skurski, K. D. Jordan, and J. Simons, *Int. J. Quantum Chem.* **64**, 183 (1997).
 20. C. G. Bailey, C. E. H. Dessent, M. A. Johnson, and K. H. Bowen, *J. Chem. Phys.* **104**, 6976 (1996).
 21. C. Desfrancois, B. Baillon, J. P. Schermann, S. T. Arnold, J. H. Hendricks, and K. H. Bowen, *Phys. Rev. Lett.* **72**, 48 (1994).
 22. P. Skurski and M. Gutowski, *J. Chem. Phys.* **108**, 6303 (1998).
 23. G. H. Lee, S. T. Arnold, J. G. Eaton, and K. H. Bowen, *Chem. Phys. Lett.* **321**, 333 (2000).
 24. C. Desfrancois, N. Khelifa, A. Lisfi, J. P. Schermann, J. G. Eaton, and K. H. Bowen, *J. Chem. Phys.* **95**, 7760 (1991).
 25. Y. Bouteiller, C. Desfrancois, J. P. Schermann, Z. Latajka, and B. Silvi, *J. Chem. Phys.* **108**, 7967 (1998).
 26. N. I. Hammer, K. Diri, K. D. Jordan, C. Desfrancois, and R. N. Compton, *J. Chem. Phys.* **119**, 3650 (2003).
 27. J. H. Hendricks, S. A. Lyapustina, H. L. de Clercq, J. T. Snodgrass, and K. H. Bowen, *J. Chem. Phys.* **104**, 7788 (1996).
 28. I. Kulakowska, M. Geller, B. Lesyng, and K. L. Wierzchowski, *Biochim. Biophys. Acta* **361**, 119 (1974).
 29. C. Desfrancois, Y. Bouteiller, J. P. Schermann, D. Radisic, S. T. Stokes, K. H. Bowen, N. I. Hammer, and R. N. Compton, *Phys. Rev. Lett.* **92**, 083003 (2004).
 30. H. Abdoul-Carime and C. Desfrancois, *Eur. Phys. J. D* **2**, 149 (1998).
 31. M. V. N. A. Prasad, R. F. Wallis, and R. Herman, *Phys. Rev. B* **40**, 5924 (1989).
 32. G. L. Gutsev, P. Jena, and R. J. Bartlett, *J. Chem. Phys.* **111**, 504 (1999).
 33. J. V. Coe, G. H. Lee, J. G. Eaton, S. T. Arnold, H. W. Sarkas, and K. H. Bowen, *J. Chem. Phys.* **92**, 3980 (1990).
 34. R. N. Compton, H. S. Carman, C. Desfrancois, H. Abdoul-Carime, J. P. Schermann, J. H. Hendricks, S. A. Lyapustina, and K. H. Bowen, *J. Chem. Phys.* **105**, 3472 (1996).
 35. T. Sommerfeld, *Phys. Chem. Chem. Phys.* **4**, 2511 (2002).
 36. C. Desfrancois, H. Abdoul-Carime, N. Khelifa, and J. P. Schermann, *Phys. Rev. Lett.* **73**, 2436 (1994).
 37. D. J. Goebbert, K. Pichugin, and A. Sanov, *J. Chem. Phys.* **131**, 164308 (2009).
 38. D. Svozil, T. Frigato, Z. Havlas, and P. Jungwirth, *Phys. Chem. Chem. Phys.* **7**, 840 (2005).
 39. C. Desfrancois, V. Periquet, Y. Bouteiller, and J. P. Schermann, *J. Phys. Chem. A* **102**, 1274 (1998).
 40. A. M. Buytendyk, J. D. Graham, K. D. Collins, K. H. Bowen, C.-H. Wu, and J. I. Wu, *Phys. Chem. Chem. Phys.* **17**, 25109 (2015).

V.3 The Ground State, Quadrupole-Bound Anion of Succinonitrile Revisited

Gaoxiang Liu, Sandra M. Ciborowski, Jacob D. Graham, Allyson M. Buytendyk, Kit H.

Bowen

Department of Chemistry, Johns Hopkins University, 3400 N. Charles Street, Baltimore, MD 21218, USA

Abstract

Using a combination of Rydberg electron transfer and negative ion photoelectron spectroscopy, we revisited an earlier study which, based on several separate pieces of evidence, had concluded that *trans*- and *gauche*-succinonitrile can form quadrupole bound anions (QBA) and dipole bound anions (DBA), respectively. In the present work, succinonitrile anions were formed by Rydberg electron transfer and interrogated by negative ion photoelectron spectroscopy. The resulting anion photoelectron spectra exhibited distinctive spectral features for *both* QBA and DBA species in the *same* spectrum, thereby providing direct spectroscopic confirmation of previous indirect conclusions. Just as importantly, this work also introduces the integrated combination of Rydberg electron transfer and anion photoelectron spectroscopy as a powerful, tandem technique for studying diffuse excess electron states.

Introduction

Negative ions can be formed not only through attachment of electrons to conventional, valence orbitals but also due to electron capture by long-range, electrostatic forces and/or dispersion effects. Negative ions formed by the latter route possess excess electrons that are very weakly bound and spatially diffuse. The component electrostatic potentials associated with these forces can be expressed through the multipole expansion for a given charge distribution as monopole, dipole, quadrupole, octupole... moments, although this representation is strictly valid only at a distance. Nevertheless, in cases where there is no valence binding of the excess electron, and where all but one of the electrostatic moments are null, it is customary to credit that non-zero moment as the primary interaction responsible for any excess electron binding that is observed. The best studied case among these are dipole-bound anions, i.e., anions whose excess electrons are weakly bound due to the dipolar fields of the anions' neutral counterparts. The formation of dipole bound anions have been postulated as the first step in electron attachment to polar molecules, and for that reason they are sometimes referred to as "doorway" states.¹⁻¹⁶

The next higher term in the multipole expansion is the quadrupole moment. Unlike dipole-bound anions, evidence for quadrupole-bound anions, where electrons are bound by long-range charge-quadrupole attraction, has been scarce. Quadrupole-bound anions

were first predicted theoretically in 1979.¹⁷ Early experimental searches for quadrupole-bound anions examined the negative ions of carbon disulfide,^{18,19} formamide,²⁰ para-dinitrobenzene,²¹ and small clusters of magnesium oxide.^{12,22} However, due either to a lack of theoretical confirmation and/or to strong indications that they were instead valence-bound, the excess electrons in none of these exhibited the weakly bound and/or spatially diffuse properties expected of quadrupole bound anions.

The first convincing evidence for the existence of quadrupole bound anions was presented by Schermann, Desfrancois, Bowen, and Compton in 2004.²³ Their conclusion, that the *trans*-succinonitrile anion is a quadrupole bound anion, was based on two different types of experimental measurements and on their theoretical calculations. **1.** Rydberg electron transfer (RET) experiments were performed by crossing a beam of succinonitrile molecules with a beam of laser-excited Rydberg atoms and monitoring the formation of parent succinonitrile anions mass spectrometrically as a function of Rydberg principle quantum number, *n*. The succinonitrile beam contained both *trans*- and *gauche*-conformers, with the former possessing a large quadrupole moment but a null dipole moment and with the latter exhibiting a large dipole moment.²⁴ These experiments were conducted at both the University of Paris Nord using xenon Rydberg atoms and at the University of Tennessee using rubidium Rydberg atoms. Both RET experiments gave fully consistent results, with each exhibiting a sharply-peaked, anion

intensity versus n feature at and around $n = 12$. Application of the semi-empirical formula, $EA = 23 \text{ eV}/n^{2.8}$, implied an electron affinity (EA) of 22 meV for the molecules that formed anions at $n = 12$.²⁵ This was interpreted as the EA value of neutral *trans*-succinonitrile and as evidence for it having formed a ground state, quadrupole bound anion. Surprisingly, however, neither of the Rydberg electron transfer experiments showed discernible evidence for a sharply-peaked feature, corresponding to the expected dipole bound anion of *gauche*-succinonitrile, even though such peaks are characteristic of dipole bound anions formed in RET experiments.

2. The other type of experimental measurement performed on succinonitrile anions utilized negative ion photoelectron spectroscopy and was conducted at Johns Hopkins University. There, a beam of succinonitrile anions was formed by a nozzle-ion source, mass-selected, and photodetached, after which its photoelectrons were energy analyzed.²⁶ The resulting anion photoelectron spectrum exhibited a sharp peak at an electron binding energy (EBE) of 108 meV and with two weaker molecular vibrational features at higher electron binding energies. Its spectral profile was typical of dipole bound anion photoelectron spectra.³ Because of this distinctive signature and the EBE value of its principle peak, it was interpreted as being due to the dipole bound, *gauche*-succinonitrile anion with an EA value of 108 meV for neutral *gauche*-succinonitrile. Interestingly, however, there was no evidence for a photoelectron peak with an EBE value in the vicinity of 22 meV and thus no indication of a quadrupole bound anion. On

the other hand, such weakly-bound excess electrons could have easily been field-detached by the gauntlet of electric fields from multiple lenses along the ion path in that particular apparatus, if in fact quadrupole bound anions had been formed by the nozzle-ion source.

Thus, while the Rydberg electron transfer experiment gave evidence for a quadrupole bound, *trans*-succinonitrile anion but not for a dipole bound, *gauche*-succinonitrile anion, the anion photoelectron spectroscopic experiment gave evidence for a dipole bound, *gauche*-succinonitrile anion but not for a quadrupole bound, *trans*-succinonitrile anion. Nevertheless, DFT/B3LYP calculations conducted as part of that work found the anions of *trans*- and *gauche*-succinonitrile to be quadrupole bound and dipole bound, respectively. Thus, the conclusion that the *trans*-succinonitrile anion is a ground state, quadrupole bound anion was based on several separate pieces of evidence.

Subsequent high-level calculations on succinonitrile anions by Sommerfeld concluded that while the dipole moment of *gauche*-succinonitrile is sufficient to explain excess electron binding in its anion, excess electron binding in the *trans*-succinonitrile anion is more complex and is due both to the quadrupole moment of *trans*-succinonitrile and to electron correlation effects, with the latter playing the larger role.²⁴ Dispersion is an electron correlation effect. In diffuse excess electron states, such as dipole bound and

quadrupole bound anions, London dispersion forces, acting between the diffuse excess electron cloud and its home (neutral) molecule, can have attractive interactions that are comparable to or even exceed those of electron-multipole interactions.^{10,27} Dispersion appears to have made an important contribution to excess electron binding in the *trans*-succinonitrile anion and possibly in the *gauche*-succinonitrile anion as well. In anion photoelectron spectra, sharp peaks at low electron binding energies are characteristic of all types of *diffuse-electron anion states*, e.g., correlation-bound,^{9,28,29} polarizability-bound, dipole-bound,²⁻⁴ quadrupole-bound,²³ and double Rydberg anions.³⁰ This is because the weak interaction between the excess electron and its home molecule leads not only to low excess electron binding energies for the resulting anion, but it also leaves the anion and its corresponding neutral in nearly identical structures, leading to high Franck-Condon overlap and narrow peaks.

In the years since 2004, interest in quadrupole bound anions has continued to grow with the development of several new computational models,³¹⁻³⁴ the theoretical prediction of specific quadrupole-bound anions,^{24,35} and the observation of excited, quadrupole-bound states in a valence-bound, ground state anion.³⁶

In the present work, we revisit succinonitrile anions, using the unique combination of Rydberg electron transfer to efficiently prepare their ground state, diffuse-electron anion

states and negative ion photoelectron spectroscopy to directly and spectroscopically measure their electron binding energies. This approach allows us to comprehensively tackle unfinished business from the earlier work and to present a more complete story.

Experimental Method

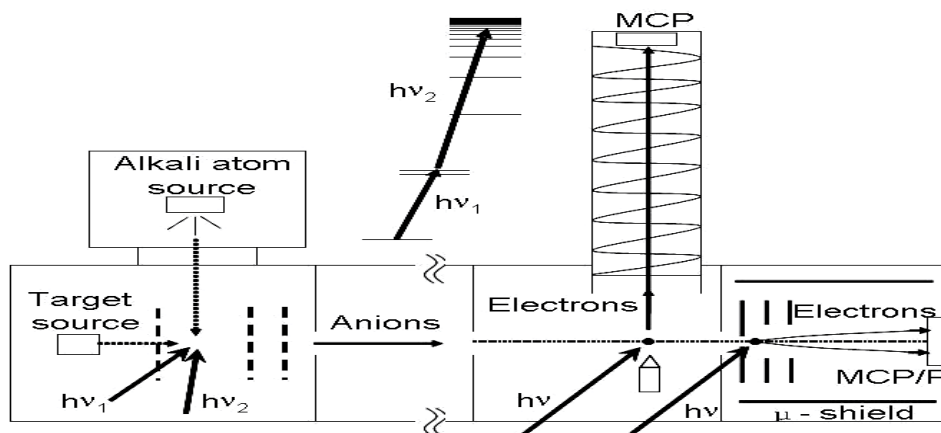


Figure 1. Schematic of our combined Rydberg electron transfer anion source and its associated negative ion photoelectron spectrometer.

Figure 1 presents a schematic of our combined Rydberg electron transfer - anion photoelectron (photodetachment) spectroscopic apparatus. The RET region, where target molecules and optically-prepared Rydberg atoms collide to form anions, is on the left, while the photoelectron region, where the resultant mass-selected anions are photodetached and their electrons energy-analyzed, is on the right. A beam of neutral succinonitrile molecules was generated by expanding succinonitrile vapor in helium (10 psig) through the nozzle of a pulsed valve into vacuum. This beam was then crossed with

an effusive beam of potassium atoms, which had been excited to nd Rydberg states in two steps using two dye lasers. One dye laser pumped the potassium atoms to the $^2P_{3/2}$ state using 766.7 nm photons, while the other was tuned to reach specific Rydberg levels. Upon collisions between Rydberg excited potassium atoms and succinonitrile molecules inside the ion extraction region of the apparatus, charge transfer occurred, producing potassium cations and parent succinonitrile anions, which momentarily formed ion pairs before dissociating into their component ions. The nascent anions were then pulsed into the negative ion photoelectron spectrometer portion of the apparatus, where they were mass-selected using time-of-flight mass spectrometry before their electrons were photodetached using 1064 nm linearly-polarized light from a Nd:YAG laser. The kinetic energies of these photoelectrons were then measured using a velocity-map imaging (VMI) spectrometer. (An available “magnetic bottle” type electron energy analyzer on this apparatus was not used in this work.) VMI analysis was achieved by accelerating the electrons along the axis of the ion beam toward a position-sensitive detector coupled to a CCD camera. The resulting two-dimensional image was then reconstructed via the BASEX method,³⁷ yielding the corresponding anion photoelectron spectrum. Since the photoelectron technique is governed by the energy-conserving relationship, $h\nu = EKE + EBE$, where $h\nu$, EKE, and EBE are the photon energy, the electron kinetic energy, and the electron binding (transition) energy, respectively, knowing $h\nu$ and measuring EKE values, provides corresponding EBE values. Photoelectron spectra in this work were

calibrated against the well-known spectrum of NO^- .²⁶

Results and Discussions

The study in 2004 was interpreted in terms of the *trans*-succinonitrile anion being a quadrupole bound anion, whose neutral counterpart had an electron affinity of 22 meV, and in terms of the *gauche*-succinonitrile anion being a dipole-bound anion state, whose corresponding neutral had an electron affinity of 108 meV. That work provides a reference point for the present combination RET - photoelectron study of succinonitrile anions.

Figure 2 presents the photoelectron spectra of succinonitrile anions made by charge transfer with Rydberg potassium atoms, $\text{K}^{**}(11d)$, presented alongside its corresponding velocity mapping image. In the anion photoelectron spectrum at the left, two sharp peaks at low electron binding energies are in evidence. For the reasons described above, both of these peaks are symptomatic of photoelectron spectroscopic signatures of diffuse excess electron states. The lower EBE peak is centered at 18 meV with a full width at half-maximum (fwhm) ~ 40 meV, while the higher EBE peak is centered at 135 meV with a fwhm of ~ 33 meV, where the peak widths are a consequence of the resolution of the instrument. These peak centers are vertical detachment energies (VDE), i.e., the transition energy from the anion to its corresponding neutral at the geometry of the anion. Since the structures of diffuse excess electron states (anions) and their corresponding

neutrals are essentially identical, their measured VDE values are also the adiabatic electron affinity (EA) values of their corresponding neutrals. Thus, the EA value of 22 meV estimated through RET in the earlier work and the EBE value of 11 meV calculated at about the same time²⁴ both compare reasonably well with the EA = VDE value of 18 meV determined in the present photoelectron work. Furthermore, the EA = VDE value of 108 meV determined by photoelectron spectroscopy in the earlier work compares well with the EA = VDE value of 135 meV in the present combined RET-photoelectron work. It is clear that the VDE and EA values determined in the present work are in satisfactory accord with corresponding EA and VDE values measured in the earlier work, albeit under different experimental circumstances. As a result, we interpret the lower EBE peak in Figure 2 as arising from the ground state, quadrupole bound anion (QBA) of *trans*-succinonitrile and the slightly higher EBE peak there as arising from the ground state, dipole-bound anion (DBA) of *gauche*-succinonitrile. Figure 2 thus presents strong evidence for *both* QBA and DBA species in the *same* spectrum, i.e., measured by the same technique. Our sightings of both QBA and DBA species over our RET n-region of n = 11d - 15d also raises the question of whether the sharp feature centered at n = 12 over the relatively narrow RET n-region of n = 10 - 15 in the earlier (2004) experiments might have also included both QBA and DBA species.

In addition to the foregoing, affirmation that the two peaks in Figure 2 originate from

different types of succinonitrile anions is also supported by the fact that we see slight, yet definitive variations in their intensity ratios as a function of nearby n principal quantum numbers. This is because electron attachment to diffuse electron anion states in RET is a resonant process, and maximal electron transfer efficiency can occur at different Rydberg n numbers, when electrons are attached via different multipole interactions.

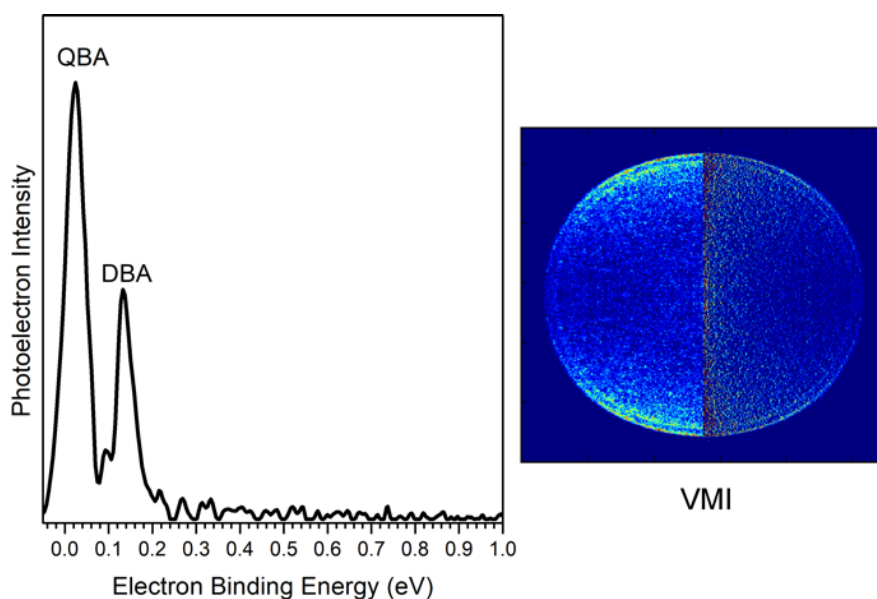


Figure 2. At left: Anion photoelectron spectrum showing both quadrupole- and dipole-bound succinonitrile anions made by collisions of succinonitrile molecules with Rydberg potassium atoms, $K^{**}(11d)$. At right: The corresponding velocity mapping image (VMI), taken with linearly-polarized light that was aligned perpendicular to the direction of the anion beam. The left side shows its raw image, while the right side shows its processed image. Note the two rings at the outer edge of the image.

The photoelectron VMI image in Figure 2 reveals significant anisotropy in both the dipole- and quadrupole-bound states of the succinonitrile anion. The anisotropy parameters, β , for the photodetached quadrupole- and dipole- bound electrons were each calculated to be between 1.8-2.0, which is close to the theoretical upper limit. A large β value is consistent with an outgoing p wave, which means that photodetachment occurred from an s -orbital with nearly zero angular momentum.³⁸ Since both dipole- and quadrupole-bound succinonitrile anions are spatially diffuse excess electron states, their excess electrons can be viewed as possessing s -orbital character, consistent with the observed anisotropy.

References

1. R.A. Bachorz, W. Klopper, M. Gutowski, X. Li, K.H. Bowen, Photoelectron Spectrum of Valence Anions of Uracil and First Principles Calculations of Excess Electron Binding Energies, *J. Chem. Phys.* 129 (2008) 054309.
2. A.M. Buytendyk, A.M. Buonaugurio, S.J. Xu, J.M. Nilles, K.H. Bowen, N. Kirnosov, L. Adamowicz, Computational and Photoelectron Spectroscopic Study of the Dipole-Bound Anions, Indole(H₂O)_{1,2}⁻, *J. Chem. Phys.* 145 (2016) 024301.
3. E. F. Belogolova, G. Liu, E. P. Doronina, S. Ciborowski, V. F. Sidorkin, K. H. Bowen, Dipole-Bound Anions of Intramolecular Complexes, *J. Phys. Chem. Lett.* 9 (2018) 1284–1289.
4. S. M. Ciborowski, G. Liu, J. D. Graham, A. M. Buytendyk, K. H. Bowen, Dipole-Bound Anions: Formed by Rydberg Electron Transfer (RET) and Studied by Velocity Map Imaging-Anion Photoelectron Spectroscopy (VMI-aPES), *Eur. Phys. J. D* 72 (2018) 139.
5. J. V. Coe, G. H. Lee, J. G. Eaton, S. T. Arnold, H. W. Sarkas, C. Ludewigt, H. Haberland, D. R. Worsnop, K. H. Bowen, Photoelectron Spectroscopy of Hydrated Electron Cluster Anions, (H₂O)⁻ n=2-69, *J. Chem. Phys.* 92 (1990) 3980-3982.
6. C. Desfrancois, B. Baillon, J.P. Schermann, S.T. Arnold, J.H. Hendricks, K.H. Bowen, Prediction and Observation of a New, Ground State, Dipole-Bound Dimer Anion: The Mixed Water/ Ammonia System, *Phys. Rev. Lett.* 72 (1994) 48–51.
7. R. N. Compton, H.S. Carman, Jr., C. Desfrancois, H. Abdoul-Carime, J.P. Schermann, J.H. Hendricks, S.A. Lyapustina, K.H. Bowen, On the Binding of Electrons to

- Nitromethane: Dipole and Valence Bound Anions, *J. Chem. Phys.* 105 (1996) 3472-3478.
8. N. I. Hammer, R. J. Hinde, R. N. Compton, K. Diri, K. D. Jordan, D. Radisic, S. T. Stokes, K. H. Bowen, Dipole-Bound Anions of Highly Polar Molecules: Ethylene Carbonate and Vinylene Carbonate, *J. Chem. Phys.* 120 (2004) 685-690.
 9. S. M. Ciborowski, R. H. Harris, G. Liu, C. J. Martinez-Martinez, P. Skurski, K. H. Bowen, The Correlation-Bound Anion of p-Chloroaniline, *J. Chem. Phys.* 150 (2019) 161103-1-4.
 10. G. Gutowski, P. Skurski, A.I. Boldyrev, J. Simons, K.D. Jordan, Contribution of Electron Correlation to the Stability of Dipole Bound Anionic States, *Phys. Rev. A: At., Mol., Opt. Phys.* 54 (1996) 1906-1909.
 11. J. Simons, K.D. Jordan, Ab Initio Electronic Structure of Anions, *Chem. Rev.* 87 (1987) 535-555.
 12. J. Simons, Molecular Anions, *J. Phys. Chem. A* 112 (2008) 6401-6511.
 13. D. L. Huang, C. G. Ning, H. T. Liu, L. S. Wang, Conformation-Selective Resonant Photoelectron Spectroscopy via Dipole-Bound States of Cold Anions, *J. Phys. Chem. Lett.* 6 (2015) 2153-2157.
 14. V.K. Voora, K.D. Jordan, Nonvalence Correlation-Bound Anion State of C₆F₆: Doorway to Low-Energy Electron Capture, *J. Phys. Chem. A* 118 (2014) 7201-7205.
 15. T. Sommerfeld, Intramolecular Electron Transfer from Dipole Bound to Valence Orbitals: Uracil and 5-Chlorouracil, *J. Phys. Chem. A* 108 (2004) 9150-9154.
 16. T. Sommerfeld, Doorway Mechanism for Dissociative Electron Attachment to Fructose, *J. Chem. Phys.* 126 (2007) 124301-124305.
 17. K.D. Jordan, J.F. Liebman, Binding of an Electron to a Molecular Quadrupole: (BeO)₂⁻, *Chem. Phys. Lett.* 62 (1979) 143.
 18. C. Desfrancois, N. Khelifa, J.P. Schermann, T. Kraft, M.W. Ruf, H. Hotop, Energy exchanges following very low energy electron attachment to neat CS₂ and CS₂-containing clusters, *Z. Phys. D* 27 (1993) 365.
 19. R.N. Compton, F.B. Dunning, P. Nordlander, On the binding of electrons to CS₂: Possible role of quadrupole-bound states, *Chem. Phys. Lett.* 253 (1996) 8-12.
 20. C. Desfrancois, V. Periquet, S. Carles, J.P. Schermann, L. Adamowicz, Neutral and negatively-charged formamide, N-methylformamide and dimethylformamide clusters, *Chem. Phys.* 239 (1998) 475-483.
 21. C. Desfrancois, V. Periquet, S.A. Lyapustina, T.P. Lippa, D.W. Robinson, K.H. Bowen, H. Nonaka, R.N. Compton, Electron binding to valence and multipole states of molecules: Nitrobenzene, para- and meta-dinitrobenzenes, *J. Chem. Phys.* 111 (1999) 4569.
 22. M. Gutowski, P. Skurski, X. Li, L.S. Wang, (MgO)_n⁻ (n=1-5) Clusters: Multipole-Bound Anions and Photodetachment Spectroscopy, *Phys. Rev. Lett.* 85 (2000) 3145-3148.
 23. C. Desfrancois, Y. Bouteiller, J.P. Schermann, D. Radisic, S.T. Stokes, K.H. Bowen, N.I. Hammer, R.N. Compton, Long-Range Electron Binding to Quadrupolar Molecules, *Phys. Rev. Lett.* 92 (2004) 083003.

24. T. Sommerfeld, *J. Chem. Phys.* 121 (2004) 4097-4104.
25. C. Desfrancois, *Phys. Rev. A* 51 (1995) 3667.
26. J. Hendricks, H. de Clercq, C. B. Freidhoff, S. T. Arnold, J. G. Eaton, C. Fancher, S. A. Lyapustina, J. T. Snodgrass, K. H. Bowen, Anion Solvation at the Microscopic Level: Photoelectron Spectroscopy of the Solvated Anion Clusters, $\text{NO}^-(\text{Y})_n$, where $\text{Y} = \text{Ar}, \text{Kr}, \text{Xe}, \text{N}_2\text{O}, \text{H}_2\text{S}, \text{NH}_3, \text{H}_2\text{O}$, and $\text{C}_2\text{H}_4(\text{OH})_2$, *J. Chem. Phys.* 116 (2002) 7926-7938.
27. R.A. Bachorz, W. Klopper, M. Gutowski, X. Li, K.H. Bowen, Photoelectron Spectrum of Valence Anions of Uracil and First Principles Calculations of Excess Electron Binding Energies, *J. Chem. Phys.* 129 (2008) 054309.
28. J.N. Bull, J.R.R. Verlet, Observation and ultrafast dynamics of a nonvalence correlation-bound state of an anion, *Sci. Adv.* 3 (2017) e1603106.
29. J.P. Rogers, C.S. Anstöter, J.R.R. Verlet, Ultrafast dynamics of low-energy electron attachment via a non-valence correlation-bound state, *Nat. Chem* 10 (2018) 341-346.
30. S. J. Xu, J. M. Nilles, J. H. Hendricks, S. A. Lyapustina, K. H. Bowen, Double Rydberg Anions: Photoelectron Spectroscopy of NH_4^- , N_2H_7^- , $\text{N}_3\text{H}_{10}^-$, $\text{N}_4\text{H}_{13}^-$, and $\text{N}_4\text{H}_{16}^-$, *J. Chem. Phys.* 117 (2002) 5742-5747.
31. W.R. Garrett, Quadrupole-bound anions: Efficacy of positive versus negative quadrupole moments, *J. Chem. Phys.* 136 (2012) 054116.
32. T. Sommerfeld, Method for Visualizing and Quantifying the Nonvalence Character of Excess Electrons, *J. Chem. Theory Comput.* 9 (2013) 4866-4873.
33. K. Fosse, X. Mao, W. Nazarewicz, N. Michel, W. R. Garrett, M. Płoszajczak, Resonant spectra of quadrupolar anions, *Phys. Rev. A* 94 (2016) 032511.
34. X. Mao, K. Fosse, W. Nazarewicz, Resonant spectra of multipole-bound anions, *Phys. Rev. A* 98 (2018) 062515.
35. T. Sommerfeld, K.M. Dreux, R. Joshi, Excess Electrons Bound to Molecular Systems with a Vanishing Dipole but Large Molecular Quadrupole, *J. Phys. Chem. A* 118 (2014) 7320-7329.
36. G.Z. Zhu, Y. Liu, L.S. Wang, Observation of Excited Quadrupole-Bound States in Cold Anions, *Phys. Rev. Lett.* 119 (2017) 023002.
37. V. Dribinski, A. Ossadtchi, V. A. Mandelshtam, H. Reisler, Reconstruction of Abel-transformable images: The Gaussian basis-set expansion Abel transform method, *Rev. Sci. Instrum.* 73 (2002) 2634-2642.
38. C.L. Adams, H. Schneider, K.M. Ervin, J.M. Weber, Low-energy photoelectron imaging spectroscopy of nitromethane anions: Electron affinity, vibrational features, anisotropies, and the dipole-bound state, *J. Chem. Phys.* 130 (2009) 074307.

V.4 The Correlation-Bound Anion of *p*-Chloroaniline

Sandra M. Ciborowski, Rachel M. Harris, *Gaoxiang Liu*, Chalynette J. Martinez-Martinez, Piotr Skurski, *and* Kit H. Bowen Jr.

Abstract

The *p*-chloroaniline anion was generated by Rydberg electron transfer and studied via velocity-map imaging anion photoelectron spectroscopy. The vertical detachment energy (VDE) of the *p*-chloroaniline anion was measured to be 6.6 meV. This value is in accord with the VDE of 10 meV calculated by Skurski and co-workers. They found the binding of the excess electron in the *p*-chloroaniline anion to be due almost entirely to electron correlation effects, with only a small contribution from the long-range dipole potential. As such, the *p*-chloroaniline anion is the first essentially correlation-bound anion to be observed experimentally.

Introduction

Very weak attractions between electrons and neutral molecules exert subtle influences on many phenomena in chemistry. When these attractions result in the formation of bound anions, their weakly bound excess electrons occupy extremely diffuse orbitals. In principle, there exist several types of diffuse excess electron anion states, their binding deriving from electron-correlation, electron-polarizability, electron-dipole, or

electron-quadrupole interactions, or, as often is the case, from some combination thereof. Anions formed by these particular interactions may be expected to possess excess electron binding strengths that increase roughly in the following order: correlation-bound, quadrupole-bound, polarizability-bound, and dipole-bound anions. In order to study these anion categories separately, it is desirable to select examples whose excess electron binding interactions, other than the one of interest, are either absent or negligible.

Contributions to excess electron binding and anion stability due to the aforementioned excess electron binding interactions have been examined in several theoretical studies.¹⁻¹⁰ Among these interactions, electron correlation effects are perhaps the most elusive, in part because they contribute to excess electron binding to some degree in most weakly bound anions. Excess electron binding due to correlation has been the focus of several landmark computational investigations.⁵⁻¹⁰

Calculations by Skurski and co-workers¹⁰ found the excess electron in the *p*-chloroaniline anion to be highly spatially diffuse and its binding to be overwhelmingly due to electron correlation effects. While *p*-chloroaniline has a significant dipole moment (3.28 D), leading to competition between dipole-binding and correlation, it is electron correlation that was found to dominate excess electron binding in the *p*-

chloroaniline anion. Even so, it is the anion's residual dipole-bound character that is likely responsible for the excess electron density preferring to reside toward the positive end of the molecular dipole. Upon finding the structures of the anion and its neutral counterpart to be essentially identical, Skurski *et al.* chose to calculate the excess electron binding energy (EBE) at the equilibrium geometry of the *p*-chloroaniline anion. Their calculated value of 10 meV is therefore the vertical detachment energy (VDE) of the *p*-chloroaniline anion. Because of the close structural similarity between the *p*-chloroaniline anion and its neutral counterpart, this anion's VDE value can be assumed to be only incrementally greater than neutral *p*-chloroaniline's electron affinity (EA) value.

We have examined excess electron binding to *p*-chloroaniline by measuring the photoelectron spectrum of its parent anion. Neutral *p*-chloroaniline is an aromatic amine, also known as 4-chloroaniline. It has many agricultural, pharmaceutical, and industrial uses and has been characterized by a wide variety of physical and chemical means.¹¹⁻⁴² In addition to studies of neutral *p*-chloroaniline, its positive ion has also been characterized by both mass spectrometric and spectroscopic methods. While theory predicted its parent anion to be stable, the *p*-chloroaniline anion had not been observed experimentally prior to the current study.

In this work, we present the negative ion mass spectrum of the *p*-chloroaniline anion, which was made by Rydberg electron transfer (RET), along with its anion photoelectron spectrum, which was measured via velocity-map imaging (VMI) anion photoelectron spectroscopy. Using the latter, we determine the VDE value of the *p*-chloroaniline anion and compare it to its theoretically predicted value.

Experimental Methods

Rydberg electron transfer (RET) provides a fragile-anion-friendly environment in which to form previously inaccessible diffuse and otherwise weakly bound electron states. In RET, an electronically excited Rydberg atom transfers its outer electron to a target neutral molecule during their collision, resulting in an ion pair which separates into atomic cation and molecular anion products.^{43,44} RET is a slow electron attachment process in which the receding positive ion plays a uniquely stabilizing role. As a result, Rydberg electron transfer provides an unusually gentle, highly quantum state-specific, laser-tunable, anion formation environment. In a typical RET experiment, atoms are optically pumped to specific Rydberg states (n^*) at the point where they collide with a beam of neutral target molecules. In the present case, the target is a beam of *p*-chloroaniline molecules, these having been vaporized in a heated pulsed valve and expanded with 10 psig of helium gas. To generate high intensities of product anions, we use alkali (K) atoms and two pulsed dye lasers. One laser optically

pumps to the $^2P_{3/2}$ level of the potassium atoms, while the second laser selectively excites that population to the ns and nd Rydberg levels of interest. Beams of Rydberg-excited K atoms and neutral target molecules cross between the ion extraction grids of our time-of flight mass analyzer/selector. There, parent anions of *p*-chloroaniline are formed by RET and accelerated (after a short delay) into a flight tube, along which they are mass-selected, prior to being photodetached. See Fig. 1 for a schematic of our apparatus.

Anion photoelectron (photodetachment) spectroscopy is conducted by crossing a beam of negative ions with a fixed-frequency photon beam and energy-analyzing the resultant photodetached electrons. This technique is governed by the energy-conserving relationship: $h\nu = EBE + EKE$, where $h\nu$ is the photon energy, EBE is the electron binding (photodetachment transition) energy, and EKE is the electron kinetic energy. The electron energies of the photodetached electrons are measured using a velocity-map imaging (VMI) anion photoelectron spectrometer, which has been described previously.⁴⁴ There, mass-selected anions are crossed with 1064 nm linearly polarized photons from a Nd:YAG laser. The resultant photodetached electrons are then accelerated along the axis of the ion beam toward a position-sensitive detector, which is coupled to a CCD camera. The basis set expansion (BASEX) Abel transform method is used to reconstruct the two-dimensional image, formed by the sum of these

electrons, into a portion of the three-dimensional distribution. Our resulting anion photoelectron spectrum is calibrated relative to the well-known photoelectron spectrum of NO^- .⁴⁵

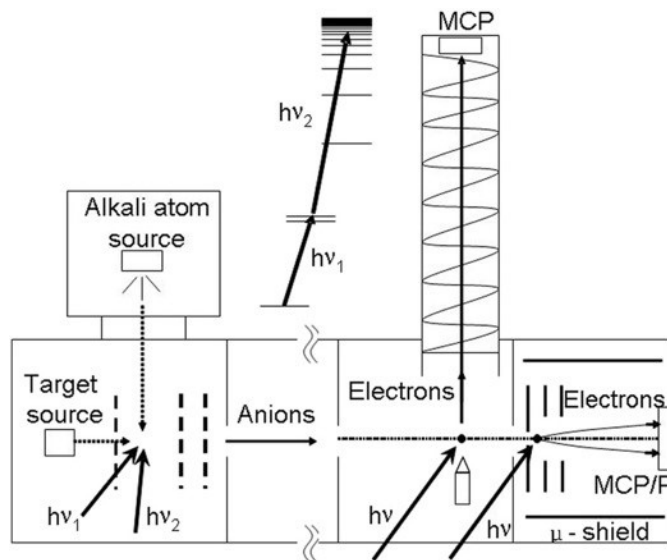


Fig. 1. Schematic of our combined Rydberg electron transfer (RET)—velocity-map imaging (VMI) anion photoelectron spectrometer.

Results and Discussion

The mass spectrum of *p*-chloroaniline anions is presented in [Fig. 2](#). All four nested mass peaks are due to the natural abundance isotope pattern of the *p*-chloroaniline parent anion. Since RET is a resonant process, we surveyed several Rydberg levels, i.e., $n^* = 12d-15d$, to find the most intense ion signal. It occurred at the $n^* = 14d$ Rydberg level. The photoelectron spectrum for the *p*-chloroaniline anion is presented in [Fig. 3](#). It consists of a single broad, symmetric peak located near an EBE of zero.

The width of this peak is entirely due to instrumental resolution limitations. To precisely locate the EBE value of the peak's maximum, we applied a Gaussian fit, finding it to be 6.6 meV. This is the VDE value of the *p*-chloroaniline anion, and as mentioned above, this value is only slightly greater than the EA value of neutral *p*-chloroaniline. Thus, our measured VDE value is in good agreement with the predicted VDE value of 81 cm⁻¹ or 10 meV, calculated by Skurski and co-workers, using *ab initio* coupled-cluster single double (triple) [CCSD(T)]/aug-cc-pVDZ+5s4p3d methodology.¹⁰ The agreement between our measurement and their computations supports Skurski and co-workers' finding that the *p*-chloroaniline anion is primarily a correlation-bound anion with minor excess electron binding contributions from dipole binding. Thus, the *p*-chloroaniline anion, whose excess electron is incredibly weakly bound, sits near the base of a hierarchy of increasing excess electron binding interaction strengths. In addition, the *p*-chloroaniline anion is the first essentially correlation-bound anion to be observed experimentally.

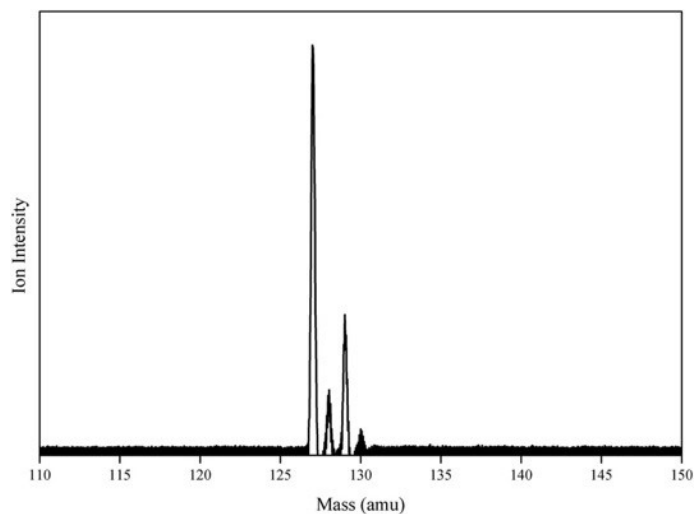


Fig. 2. Mass spectrum of *p*-chloroaniline anions made by Rydberg electron transfer ($n^* = 14d$).

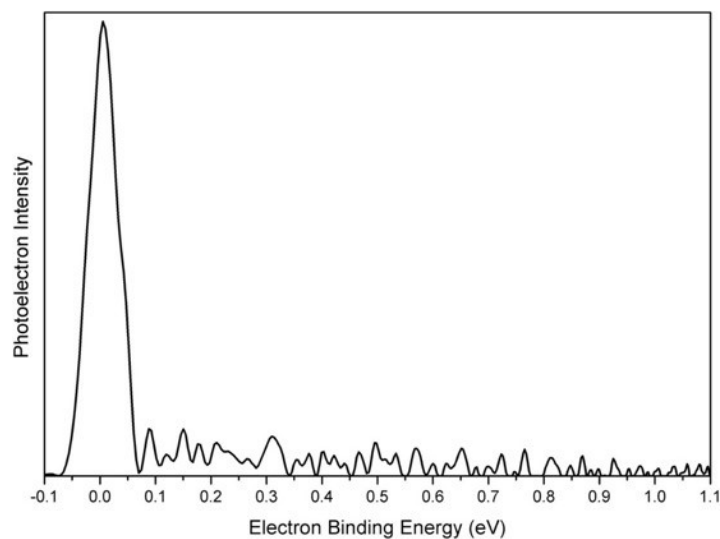


Fig. 3. Anion photoelectron spectrum of *p*-chloroaniline anions measured by velocity-map imaging (VMI) photoelectron spectroscopy using 1.165 eV (1064 nm) photons.

References

- ¹ United States Environ. Prot. Agency TSCA Chem. Subst. Invent. (2018).

- ² A. Boehncke, J. Kielhorn, G. Konnecker, C. Pohlenz-Michel, and I. Mangelsdorf, *4-Chloroaniline* (Geneva, 2003).
- ³ A. Moreale and R. Van Bladel, *J. Soil Sci.* **27**, 48 (1976).
- ⁴ P. Ekici, G. Leupold, and H. Parlar, *Chemosphere* **44**, 721 (2001).
- ⁵ R. Kühn, M. Pattard, K.D. Pernak, and A. Winter, *Water Res.* **23**, 495 (1989).
- ⁶ A. Di Corcia and R. Samperi, *Anal. Chem.* **62**, 1490 (1990).
- ⁷ M. Del Nogal Sánchez, C. Pérez Sappó, J.L. Pérez Pavón, and B.M. Cordero, *Anal. Bioanal. Chem.* **404**, 2007 (2012).
- ⁸ W.K. Gavlick, *J. Chromatogr. A* **623**, 375 (1992).
- ⁹ M.C. Hennion, P. Subra, V. Coquart, and R. Rosset, *Fresenius. J. Anal. Chem.* **339**, 488 (1991).
- ¹⁰ W.J. Ehlhardt and J.J. Howbert, *Drug Metab. Dispos.* **19**, 366 (1993).
- ¹¹ H.G. Bray, S.P. James, and W. V Thorpe, *Biochem. J.* **64**, 38 (1956).
- ¹² A.F. Pizon, A.R. Schwartz, L.M. Shum, J.C. Rittenberger, D.R. Lower, S. Giannoutsos, M.A. Virji, and M.D. Krasowski, *Clin. Toxicol.* **47**, 132 (2009).
- ¹³ M. Kiese and G. Renner, *Naunyn-Schmiedeberg's Arch. Für Exp. Pathol. Und Pharmakologie* **246**, 163 (1963).
- ¹⁴ J. Trotter, S.H. Whitlow, and T. Zobel, *J. Chem. Soc. A Inorganic, Phys. Theor.* **19**, 353 (1966).
- ¹⁵ J.H. Palm, *Acta Crystallogr.* **21**, 473 (1966).
- ¹⁶ G. Ploug-Sørensen and E.K. Andersen, *Acta Crystallogr. Sect. C Cryst. Struct. Commun.* **41**, 613 (1985).
- ¹⁷ A.P. Marchetti, *J. Chem. Phys.* **56**, 5101 (1972).
- ¹⁸ A.P. Marchetti, *J. Chem. Phys.* **57**, 5475 (1972).
- ¹⁹ N. Nishi and M. Kinoshita, *Bull. Chem. Soc. Jpn.* **49**, 1221 (1976).
- ²⁰ R. Ambrosetti, A. Colligiani, P. Grigolini, and F. Salvetti, *J. Chem. Phys.* **60**, 459 (1974).
- ²¹ H.C. Meal, *J. Chem. Phys.* **24**, 1011 (1956).
- ²² J. Huang, J.L. Lin, and W.B. Tzeng, *Chem. Phys. Lett.* **422**, 271 (2006).
- ²³ A.P. Marchetti, *Chem. Phys. Lett.* **23**, 213 (1973).
- ²⁴ G.N.R. Tripathi and J.E. Katon, *J. Chem. Phys.* **70**, 1383 (1979).
- ²⁵ J.L.D. Sky and E.I. Von Nagy-Felsobuki, *J. Mol. Struct.* **475**, 241 (1999).
- ²⁶ V.B. Singh, R.N. Singh, and I.S. Singh, *Spectrochim. Acta* **22**, 927 (1966).
- ²⁷ K. Othmen, P. Boule, B. Szczepanik, K. Rotkiewicz, and G. Grabner, 9525 (2000).
- ²⁸ P.F. COX, R.L. EVERY, and O.L. RIGGS, *CORROSION* **20**, 299t (1964).
- ²⁹ M.A.V. Ribeiro Da Silva, J.R.B. Gomes, and A.I.M.C.L. Ferreira, *J. Phys. Chem. B* **109**, 13356 (2005).
- ³⁰ M. Straka, K. Růžicka, and V. Růžicka, *J. Chem. Eng. Data* **52**, 1375 (2007).
- ³¹ V. Piacente, P. Scardala, D. Ferro, and R. Gigli, *J. Chem. Eng. Data* **30**, 372 (1985).
- ³² J. Padmanabhan, R. Parthasarathi, V. Subramanian, and P.K. Chattaraj, *J. Phys. Chem. A* **110**, 9900 (2006).
- ³³ S. Smuczyńska, I. Gwarda, I. Anusiewicz, and P. Skurski, *J. Chem. Phys.* **130**, (2009).

- ³⁴ M. Gutowski, P. Skurski, A.I. Boldyrev, J. Simons, and K.D. Jordan, *Phys. Rev. A - At. Mol. Opt. Phys.* **54**, 1906 (1996).
- ³⁵ M. Gutowski and K.D. Jordan, **5639**, 2624 (1998).
- ³⁶ P. Skurski, M. Gutowski, and J. Simons, *J. Chem. Phys.* **110**, 274 (1999).
- ³⁷ J. Simons, *Annu. Rev. Phys. Chem.* **62**, 107 (2011).
- ³⁸ J. Simons and P. Skurski, in *Theor. Prospect Negat. Ions*, edited by J. Kalcher (Research Signpost, Trivandrum, 2002), pp. 99–120.
- ³⁹ M. Gutowski and P. Skurski, *Recent Res. Dev. Phys. Chem.* **3**, 245 (1999).
- ⁴⁰ E.F. Belogolova, G. Liu, E.P. Doronina, S.M. Ciborowski, V.F. Sidorkin, and K.H. Bowen, *J. Phys. Chem. Lett.* **9**, (2018).
- ⁴¹ J.H. Hendricks, H.L. De Clercq, C.B. Freidhoff, S.T. Arnold, J.G. Eaton, C. Fancher, S.A. Lyapustina, J.T. Snodgrass, and K.H. Bowen, *J. Chem. Phys.* **116**, 7926 (2002).

V.5 Observation of the Dipole- and Quadrupole-Bound Anions of 1,4-Dicyanocyclohexane

Gaoxiang Liu, Sandra M. Ciborowski, Cody Ross Pitts, Jacob D. Graham, Allyson M.

Buytendyk, Thomas Lectka, and Kit H. Bowen*

Department of Chemistry, Johns Hopkins University, 3400 N. Charles Street, Baltimore, MD 21218, USA

Abstract

Quadrupole-bound anions are negative ions in which their excess electrons are loosely bound by long-range electron-quadrupole attractions. Experimental evidence for quadrupole-bound anions has been scarce; until now, only *trans*-succinonitrile had been experimentally confirmed to form a quadrupole-bound anion. In this study, we present experimental evidence for a new quadrupole-bound anion. Our combined Rydberg electron transfer/anion photoelectron spectroscopy study demonstrates that the *ee* conformer of 1,4-dicyanocyclohexane (DCCH) supports a quadrupole-bound anion state, and that the *cis*-DCCH conformer forms a dipole-bound anion state. The electron binding energies of the quadrupole- and dipole-bound anions are measured as 18 and 115 meV, respectively, both of which are in excellent agreement with theoretical calculations by Sommerfeld.

Introduction

Negative ions can be formed due to electron capture by long-range, electrostatic forces, in which the excess electrons reside in diffuse non-valence orbitals. The component potentials associated with these electrostatic forces can be expressed through the multipole expansion for a given charge distribution, e.g., dipole, quadrupole, and octupole moments. Whereas this representation is strictly valid only at a distance, in cases where there is no valence electron binding, and where all but one of the electrostatic moments are null, it is customary to attribute that non-zero moment as the primary attractive interaction responsible for the binding of the excess electron. The formation of such weakly-bound states is thought to be the initial step in certain electron attachment processes, thus these are also referred as “doorway” states.¹⁻¹¹ The best studied category of weakly-bound anions are dipole-bound anions, i.e., anions whose excess electrons are weakly tethered by the dipolar fields of the anions’ neutral counterparts.¹²⁻²⁴

The next higher term in the multipole expansion is the quadrupole moment. Unlike dipole-bound anions, the evidence for quadrupole-bound anions, where their excess electrons are bound by the long-range charge-quadrupole attraction, has been scarce. Quadrupole-bound anions were first predicted theoretically in 1979.²⁵ Early experimental studies on quadrupole-bound anions were conflicting: the anions of

carbon disulfide, formamide, and para-dinitrobenzene were investigated by Rydberg electron transfer and suggested to be quadrupole-bound anions, but the lack of theoretical support rendered them less convincing;²⁶⁻²⁹ the small cluster anions of magnesium oxide were investigated by photoelectron spectroscopy and interpreted as quadrupole-bound anions, but their high electron binding energies and rather localized orbitals made them more characteristic of conventional valence-bound anions.³⁰ It was not until 2004 that Schermann, Bowen, and Compton presented the first convincing evidence of quadrupole-bound anions by combining results from two different, but complimentary experimental techniques: the dipole-bound anion state of the *gauche*-succinonitrile conformer was revealed by anion photoelectron spectroscopy, and the quadrupole-bound anion state of the *trans*-succinonitrile conformer was revealed by Rydberg electron transfer.³¹ While each of these techniques revealed one type of a multipole-bound anion, they were each unable to discern the other type. This led us to revisit this earlier study using the unique combination of Rydberg electron transfer and negative ion photoelectron spectroscopy. In that study, the anion photoelectron spectra of succinonitrile anions, which were formed via Rydberg electron transfer, exhibited distinctive features for both dipole- and quadrupole-bound anions in the same photoelectron spectrum, providing direct spectroscopic confirmation for the presence of both multipole-bound states in the same molecule and in a single experiment.³²

Additional progress in the study of quadrupole-bound anions has included the development of computational models,³³⁻³⁶ theoretical prediction of several stable quadrupole-bound anions,³⁷ and the discovery of excited-state, quadrupole-bound states in a valence-bound anion.³⁸ Despite these advances, however, the *trans*-succinonitrile anion remained the only experimentally-confirmed example of a ground-state, quadrupole-bound anion. The search for quadrupole-bound anions is intrinsically challenging because (i) their weakly-bound nature requires specialized experimental techniques for making and analyzing them; (ii) unlike dipole-bound anions, whose electron binding energies are proportionally correlated to the magnitude of the neutrals' dipole moments, there is no clear correlation between the magnitude of the molecular quadrupole moment and the electron binding energy of the quadrupole-bound anion;³⁷ thus, the prediction of stable quadrupole-bound anions relies heavily on high-level *ab initio* calculations; (iii) if the molecule can sustain both quadrupole-bound and valence-bound states, the nascent quadrupole-bound state may quickly decay into the more stable valence-bound state, hiding the incipient quadrupole-bound anion state from view.³⁸

Recently, several neutral molecules have been theoretically predicted by Sommerfeld to form quadrupole-bound anions.³⁷ Among these, the 1,4-dicyanocyclohexane

(DCCH) molecule was seen as a promising candidate for the experimental interrogation for two reasons. While its conformers were predicted to support both dipole- and quadrupole-bound anionic states, it was not predicted to form a valence state. In addition, its laboratory synthesis was deemed to be more tractable than other candidates. In the present work, the parent anions of DCCH were formed by Rydberg electron transfer and interrogated by velocity mapping imaging, anion photoelectron spectroscopy. The resulting anion photoelectron spectra exhibited distinctive spectral features for both dipole- and quadrupole-bound anions, whose electron binding energies were measured as 115 meV and 18 meV, respectively. These values are in excellent agreement with theoretical calculations. Thermodynamic analysis rationalized the relative quantity of the two types of anions.

Experimental Methods

Synthesis of 1,4-Dicyanocyclohexane This compound can be prepared according to a known literature procedure.^{39,40} It was obtained as a mixture of *cis*- and *trans*- conformations, which appeared as an off-white solid; m.p. 54-55 °C. Characterization data: ¹H NMR (400 MHz, CDCl₃) δ 2.77-2.72 (2H, m), 2.10-1.97 (4H, m), 1.89-1.75 (4H, m); ¹³C NMR (400 MHz, CDCl₃) δ 120.9, 120.8, 26.3, 26.2, 26.1, 26.0; $\nu_{\max}/\text{cm}^{-1}$ 2238 (CN, strong).

Anion Photoelectron Spectroscopy Our Rydberg electron transfer/anion photoelectron spectroscopy apparatus has been described previously.^{23,24,32,41} Anion photoelectron spectroscopy is conducted by crossing a mass-selected beam of negative ions with a fixed-frequency photon beam and energy-analyzing the resultant photodetached electrons. This technique is governed by the energy-conserving relationship, $h\nu = \text{EKE} + \text{EBE}$, where $h\nu$, EKE, and EBE are the photon energy, the electron kinetic energy, and the electron binding (transition) energy, respectively. Electron kinetic energies were measured using a velocity-map imaging (VMI) spectrometer. Mass-selected anions were crossed with 1064 nm, linearly polarized photons in an electric field. The resultant photodetached electrons were accelerated along the axis of the ion beam toward a position-sensitive detector coupled to a CCD camera. The two-dimensional image formed from the sum of the electrons was reconstructed into a portion of the three-dimensional distribution via the BASEX method.⁴² Photoelectron spectra are calibrated against the well-known spectrum of NO^- .⁴³

DCCH anions were generated by our Rydberg electron transfer (RET) source. Neutral DCCH molecules were vaporized in a pulsed valve, which was heated to 140 °C, and then supersonically expanded with 10 psi of helium gas. DCCH anions, DCCH^- , were formed when neutral DCCH molecules collided with a thermally-expanded beam of

potassium atoms, which had been excited to specific Rydberg states in two steps using two dye lasers. One dye laser pumped the potassium atoms to the $^2P_{3/2}$ state with 766.7 nm light, while the other was tuned to reach specific nd Rydberg levels, where n is the principal quantum number. In this study, Rydberg levels from $n = 13d$ to $18d$ were selected. Upon electron transfer and subsequent ion-pair separation, the resulting anions, $DCCH^-$, were extracted into a time-of-flight mass spectrometer. There, they were mass-selected before having their excess electrons photodetached and energy-analyzed by velocity-map imaging spectroscopy.

Calculations The electron affinities of $DCCH$ had been accurately calculated by Sommerfeld in an earlier contribution.³⁷ The calculations conducted during the present work serve to explain the relative amounts of dipole- versus quadrupole-bound $DCCH$ anions that were formed. The second-order Møller-Plesset perturbation theory calculations were performed with the ORCA computational chemistry software package.⁴⁴ All calculations were carried out with the resolution of identity (RI) and the RIJCOSX approximation.⁴⁵ The cc-pVTZ basis set⁴⁶ was used throughout our calculations in conjugation with the auxiliary basis sets def2/J⁴⁷ and cc-pVTZ/C⁴⁸. Frequency calculations were performed to verify the optimized structures and transition states.

Results and Discussions

Figure 1a shows the structures of the three DCCH conformers. In *cis*-DCCH, one CN group is at the equatorial(*e*) site, and the other one is at the axial(*a*) position. The *trans*-DCCH can have two conformers, which are labeled as *aa*-DCCH and *ee*-DCCH, depending on the positions of the CN groups. Since the sample was synthesized as a mixture of *trans*- and *cis*-conformations, all three conformers were present. Also provided in Figure 1a are calculated dipole and quadrupole moments of these conformers as well as their vertical electron affinity (VEA) values.³⁷ Calculations show that the *aa*-DCCH molecule is unable to form a weakly-bound anion; the *ee*-DCCH, which has a vanishing dipole moment but a significant quadrupole moment, can form a quadrupole-bound anion with a VEA of 19 meV; the *cis*-DCCH, which has a large dipole moment, can form a dipole-bound anion with a VEA of 108 meV.

Figure 1b presents a representative mass spectrum of molecular and cluster anions of DCCH made via Rydberg electron transfer (RET). Cluster anions of the dimer and trimer of DCCH are observed, demonstrating the capability of RET to make not only molecular, but also cluster anions. A mass peak corresponding to CN^- physisorbed (solvated) by three DCCH molecules is also observed. The CN^- anion results from the dissociative electron attachment to DCCH clusters. While it would be interesting to investigate the nature of electron binding to DCCH clusters, i.e., quadrupole-binding,

dipole-binding or a synergy of quadrupole- and dipole-binding, the focus of the present study is on identifying the weakly-bound states of the DCCH parent molecular anion, DCCH^- .

Figure 2 presents the anion photoelectron spectra of DCCH anions made at different Rydberg n levels. Spectra collected at $n = 13d, 14d,$ and $18d$ Rydberg levels are dominated by a single sharp peak at a low electron binding energy (EBE). For spectra obtained at $n = 15d, 16d$ and $17d$, an additional sharp, yet weaker peak appears on the

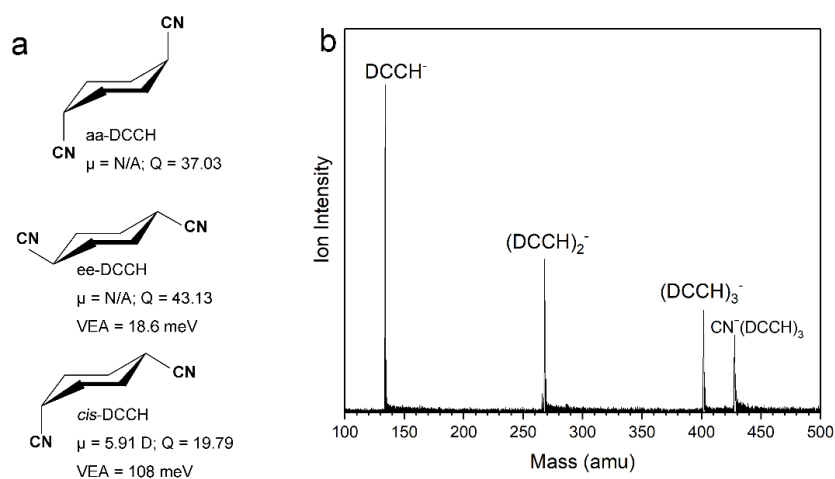


Figure 1. (a) Structures of the *trans*- and *cis*- isomers of 1,4-dicyanocyclohexane (DCCH), along with their electronic properties. The unit of the quadrupole moment, Q , is the atomic unit ea_0^2 . (b) Mass spectrum of molecular and cluster anions of DCCH made by Rydberg electron transfer.

lower EBE side of the principal peak. These sharp peaks at low EBE in photoelectron

spectra are the signature of weakly-bound anions. In RET, the electron attachment to diffuse electron states occurs via resonance charge transfer, and thus maximal electron transfer efficiency occurs at different Rydberg levels, when electrons are attached to different multipole environments. Therefore, the appearance of the lower EBE feature at only $n = 15d-17d$ suggests that it is associated with a different multipole field environment than is the higher EBE feature. The lower EBE peak is centered at 18 meV, with a full width at half-maximum (fwhm) of ~ 37 meV. The higher EBE peak is centered at 115 meV, with a fwhm of ~ 35 meV. These peaks are due to the photodetachment transitions between the anions and their corresponding neutral molecules. Therefore, the vertical detachment energy (VDE) values of these two peaks are 18 and 115 meV, respectively. When anion photoelectron spectra are dominated by single sharp peaks, it strongly suggests a close similarity between the structures of the anion and its neutral counterpart. In such cases of structural similarity, the anion's VDE value will be almost identical to that of its corresponding neutral's adiabatic electron affinity (EA) and to its VEA value. By comparing our experimentally-determined VDE values with VEA values from previous calculations³⁷, we assigned the feature at 18 meV to be the signature of the quadrupole-bound anion of *ee*-DCCH, and the feature at 115 meV to be the signature of the dipole-bound anion of *cis*-DCCH.

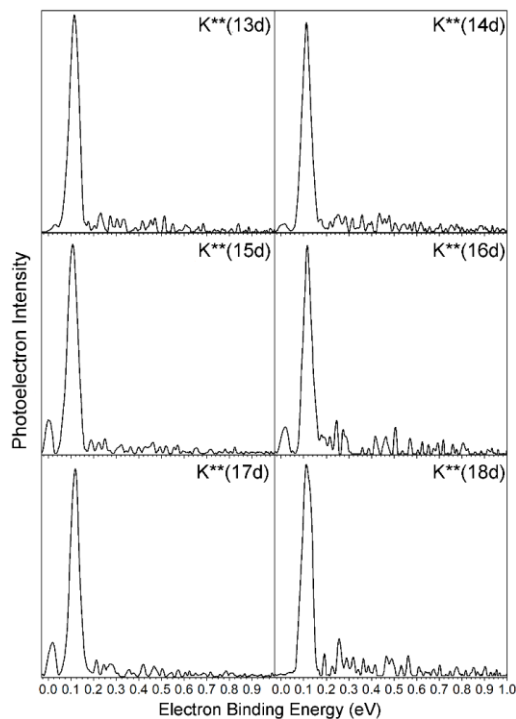


Figure 2. Anion photoelectron spectra of dipole- and quadrupole-bound DCCH anions, DCCH^- , made at different Rydberg levels ($n = 13d-18d$).

Figure 3 presents a representative photoelectron image of dipole- and quadrupole-bound DCCH anions, which were formed at the $n = 17d$ Rydberg level. The inner brighter ring corresponds to the dipole-bound anion state, while the outer weaker intensity ring corresponds to the quadrupole-bound anion state. Both dipole- and quadrupole-bound anion states show significant anisotropy. The anisotropy parameters, β , of the photodetached dipole-bound electrons are calculated to be between 1.8-2.0. For the photodetached quadrupole-bound electrons their β values are calculated to be 1.4-1.6. Since both the dipole- and quadrupole-bound states can be viewed as spatially diffuse s -character orbitals, the matter wave of photodetached

electrons should have p character and a sizeable β value close to 2.⁴⁹ The experimental β value associated with the photodetached dipole-bound electrons is consistent with this number. While the β value associated with the photodetached quadrupole-bound electrons is less than expected, it may only be because the intensity of photodetached quadrupole-bound electrons was too low to yield an accurate evaluation of β .

The feature from quadrupole-bound anions is only weakly seen in the photoelectron spectrum and the velocity map image of DCCH anions (Figure 3), suggesting that only a small portion of the DCCH anions are quadrupole-bound. We explain this with a quantum mechanical and thermodynamic analysis, the results of which are summarized in Table 1 and Figure 4. Calculations at the RI-MP2/cc-pvtz level of theory reveal that the *aa*-DCCH, which is unable to bind an excess electron, is the

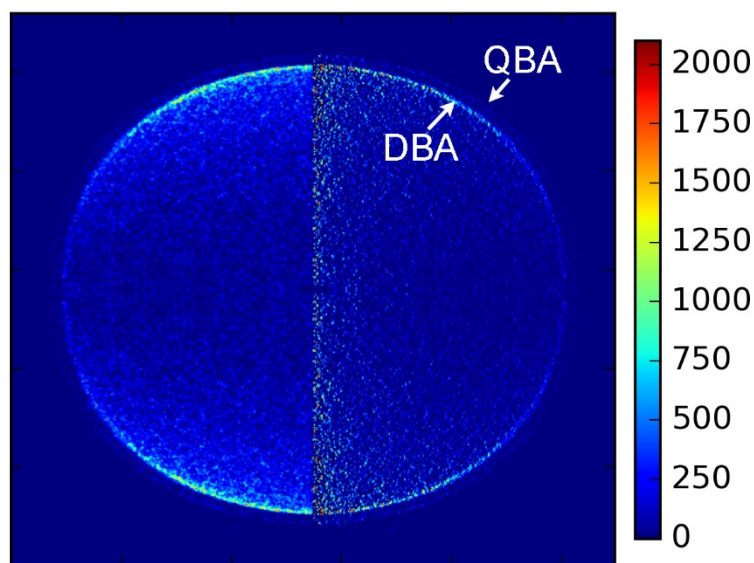


Figure 3. Photoelectron image of DCCH anions collected at the $n = 17d$ Rydberg level.

most stable conformer. The *cis*-DCCH, which forms dipole-bound anions, is 5.1 kJ/mol higher in energy, while *ee*-DCCH, which forms quadrupole-bound anions, is the least stable conformer, at 9.3 kJ/mol above *aa*-DCCH. As shown in Figure 4, quantum calculations show barriers of 0.56 and 0.63 eV for the interconversion from *ee* to *aa* and from *aa* to *ee*, respectively. Such interconversions constantly occur at room temperature when DCCH is in the solid state. In the molecular beam, however, due to the low temperature achieved by supersonic expansion and the lack of external energy input, these barriers are high enough to quench interconversion. Therefore, we estimate the composition of DCCH conformers in the molecular beam to be similar to that in the DCCH vapor before expansion, i.e., in the heated pulse valve. A thermodynamic analysis shows that at an elevated pulse valve temperature (140°C), nearly 80% of the DCCH exists as the *aa* conformer. Therefore, most of the DCCH in the molecular beam will not form anions. The neutral candidate for the dipole-bound anion, *cis*-DCCH, makes up 17.3% of the DCCH in the beam, while the neutral candidate for the quadrupole-bound anion, *ee*-DCCH, makes up only 5.1%. Therefore, only a small portion of DCCH neutral molecules in the beam can form quadrupole-bound anions. This is the main reason for the weak intensity of the quadrupole-bound feature compared to the dipole-bound feature in the photoelectron spectra. While increasing the pulse valve temperature favors the conversion to *ee*-DCCH,

temperatures higher than 140°C were found to cause the sample to decompose.

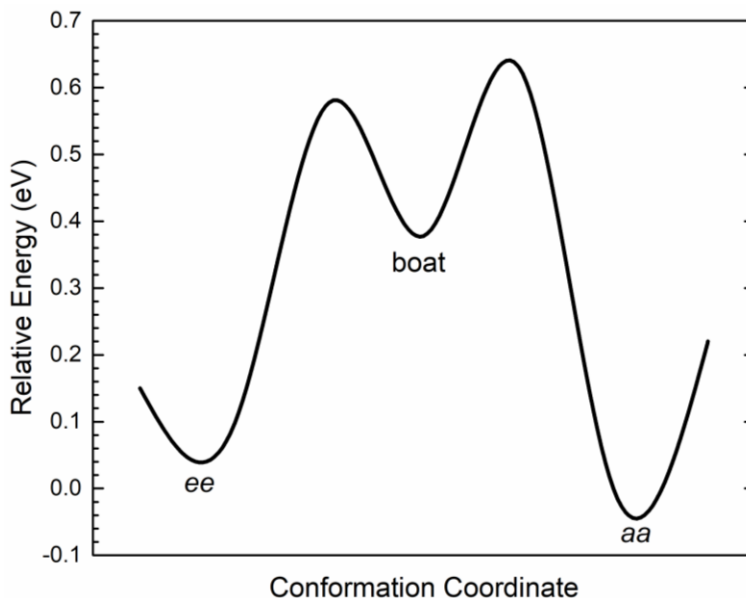


Figure 4. Potential energy surface for neutral *trans*-DCCH along the conformation coordinate connecting the *ee*- and the *aa*-conformers.

Table 1. Relative energies, E_{rel} , of the three DCCH conformers and their relative percentages, P , at room and experimental temperatures.

	E_{rel} (kJ/mol)	$P_{25^{\circ}\text{C}}$ (%)	$P_{140^{\circ}\text{C}}$ (%)	Anion Type
<i>aa</i> -DCCH	0	85.1	77.6	Electron not bound
<i>cis</i> -DCCH	5.1	10.9	17.3	Dipole-bound
<i>ee</i> -DCCH	9.3	2.0	5.1	Quadrupole-bound

Summary

In this contribution, we present experimental evidence for a new, ground state, quadrupole-bound anion obtained in a combined Rydberg electron transfer-anion photoelectron spectroscopic study. The sharp peaks in the photoelectron spectra and the highly anisotropic rings in photoelectron imaging reveal the dipole- and quadrupole-bound anion states of DCCH^- . The quadrupole- and dipole-bound electron affinities are measured as 18 and 115 meV, respectively, these being in excellent agreement with previous theoretical calculations.³⁷ The discovery of this new quadrupole-bound anion extends the knowledge base about quadrupole-bound anions and provides an experimental benchmark for additional theoretical modelling.

References

1. Dabkowska, J. Rak, M. Gutowski, J.M. Nilles, S.T. Stokes, D. Radisic and K.H. Bowen, *Phys. Chem. Chem. Phys.*, 2004, **6**, 4351–4357.
2. L. Chomicz, M. Zdrowowicz, F. Kasprzykowski, J. Rak, A. Buonaugurio, Y. Wang and K.H. Bowen, *J. Phys. Chem. Lett.*, 2013, **4**, 2853–2857.
3. R.A. Bachorz, W. Klopper, M. Gutowski, X. Li and K.H. Bowen, *J. Chem. Phys.* 2008, **129**, 054309.
4. S.J. Xu, J.M. Nilles and K.H. Bowen, *J. Chem. Phys.*, 2003, **119**, 10696–10701.
5. T. Sommerfeld, *J. Phys. Chem. A*, 2004, **108**, 9150–9154.
6. S.N. Eustis, D. Radisic, K.H. Bowen, R.A. Bachorz, M. Haranczyk, G. Schenter and M. Gutowski, *Science*, 2008, **319**, 936–939.
7. T. Sommerfeld, *J. Chem. Phys.*, 2007, **126**, 124301–124305.
8. J. Kelly, S. Xu, J. Graham, M. Nilles, D. Radisic, A. Buonaugurio, K.H. Bowen, N. Hammer and G. Tschumper, *J. Phys. Chem. A*, 2014, **118**, 11901–11907.
9. J.N. Bull and J.R.R. Verlet, *Sci. Adv.* 2017, **3**, e1603106.
10. J.P. Rogers, C.S. Anstöter and J.R.R. Verlet, *Nat. Chem.*, 2018, **10**, 341–346.
11. V.K. Voora and K.D. Jordan, *J. Phys. Chem. A*. 2014, **118**, 7201–7205.
12. K.D. Jordan, *Acc. Chem. Res.*, 1979, **12**, 36–42.
13. J. Simons and K.D. Jordan, *Chem. Rev.* 1987, **87**, 535–555.
14. G. Gutowski, P. Skurski, A.I. Boldyrev, J. Simons and K.D. Jordan, *Phys. Rev. A: At.*,

- Mol., Opt. Phys.* 1996, **54**,1906–1909.
15. J. Simons, *J. Phys. Chem. A.*, 2008, **112**, 6401–6511.
 16. J. V. Coe, G. H. Lee, J. G. Eaton, S. T. Arnold, H. W. Sarkas, C. Ludewigt, H. Haberland, D. R. Worsnop and K. H. Bowen, *J. Chem. Phys.*, 1990, **92**, 3980-3982.
 17. B. Desfrancois, B. Baillon, J.P. Schermann, S.T. Arnold, J.H. Hendricks and K.H. Bowen, *Phys. Rev. Lett.*, 1994, **72**, 48–51.
 18. J. H. Hendricks, S.A. Lyapustina, H. L. de Clercq, J. T. Snodgrass and K. H. Bowen, *J. Chem. Phys.*, 1996, **104**, 7788-7791.
 19. R. N. Compton, H.S. Carman, Jr., C. Desfrancois, H. Abdoul-Carime, J.P. Schermann, J.H. Hendricks, S.A. Lyapustina and K.H. Bowen, *J. Chem. Phys.*, 1996, **105**, 3472-3478.
 20. N. I. Hammer, R. J. Hinde, R. N. Compton, K. Diri, K. D. Jordan, D. Radisic, S. T. Stokes and K. H. Bowen, *J. Chem. Phys.*, 2004, **120**, 685-690.
 21. B. L. Huang, C. G. Ning, H. T. Liu and L. S. Wang. *Phys. Chem. Lett.*, 2015, **6**, 2153-2157.
 22. A.M. Buytendyk, A.M. Buonaugurio, S.J. Xu, J.M. Nilles, K.H. Bowen, N. Kirnosov and L. Adamowicz, *J. Chem. Phys.*, 2016, **145**, 024301.
 23. E. F. Belogolova, G. Liu, E. P. Doronina, S. Ciborowski, V. F. Sidorkin and K. H. Bowen, *J. Phys. Chem. Lett.*, 2018, **9**, 1284–1289.
 24. S. M. Ciborowski, G. Liu, J. D. Graham, A. M. Buytendyk, and K. H. Bowen, *Eur. Phys. J. D*, 2018, **72**, 139.
 25. K.D. Jordan and J.F. Liebman, *Chem. Phys. Lett.*, 1979, **62**, 143.
 26. C. Desfrancois, N. Khelifa, J.P. Schermann, T. Kraft, M.W. Ruf and H. Hotop, *Z. Phys. D*, 1993, **27**, 365.
 27. R.N. Compton, F.B. Dunning and P. Nordlander, *Chem. Phys. Lett.*, 1996, **253**, 8–12.
 28. C. Desfrancois, V. Periquet, S. Carles, J.P. Schermann and L. Adamowicz, *Chem. Phys.*, 1998, **239**, 475–483.
 29. C. Desfrancois, V. Periquet, S.A. Lyapustina, T.P. Lippa, D.W. Robinson, K.H. Bowen, H. Nonaka and R.N. Compton, *J. Chem. Phys.*, 1999, **111**, 4569.
 30. M. Gutowski, P. Skurski, X. Li and L.S. Wang, *Phys. Rev. Lett.*, 2000, **85**, 3145–3148.
 31. C. Desfrancois, Y. Bouteiller, J.P. Schermann, D. Radisic, S.T. Stokes, K.H. Bowen, N.I. Hammer and R.N. Compton, *Phys. Rev. Lett.*, 2004, **92**, 083003.
 32. G. Liu, S. M. Ciborowski, J. D. Graham, A. M. Buytendyk and K. H. Bowen, *J. Chem. Phys.*, accepted.
 33. W.R. Garrett, *J. Chem. Phys.*, 2012, **136**, 054116.
 34. T. Sommerfeld, *J. Chem. Theory Comput.*, 2013, **9**, 4866–4873
 35. K. Fosse, X. Mao, W. Nazarewicz, N. Michel, W. R. Garrett and M. Płoszajczak, *Phys. Rev. A*, 2016, **94**, 032511.
 36. X. Mao, K. Fosse and W. Nazarewicz, *Phys. Rev. A*, 2018, **98**, 062515.
 37. T. Sommerfeld, K.M. Dreux and R. Joshi, *J. Phys. Chem. A.*, 2014, **118**, 7320–7329.
 38. G.Z. Zhu, Y. Liu and L.S. Wang, *Phys. Rev. Lett.*, 2017, **119**, 023002.

39. R. Malachowski, J. J. Wasowska and S. Józkiewicz, *Chem. Ber.* 1938, **71**, 759-767.
40. C. Bengtsson, S. Blaho, D.B. Saitton, K. Brickmann, J. Broddefalk, Ö. Davidsson, T. Drmota, R. Folmer, K. Hallberg, S. Hallén, R. Hovland, E. Isin, P. Johannesson, B. Kull, L. O. Larsson, L. Löfgren, K. E. Nilsson, T. Noeske, N. Oakes, A.T. Plowright, V. Schneck, P. Ståhlberg, P. Sörme, H. Wan, E. Wellner and L. Öster, *Bioorg. Med. Chem.* 2011, **19**, 3039-3053.
41. S. M. Ciborowski, R. M. Harris, G. Liu, C. J. Martinez-Martinez, P. Skurski and K. H. Bowen, *J. Chem. Phys.*, 2019, **150**, 161103.
42. V. Dribinski, A. Ossadtchi, V. A. Mandelshtam, H. Reisler, *Rev. Sci. Instrum.*, 2002, **73**, 2634-2642.
43. J. Hendricks, H. de Clercq, C. B. Freidhoff, S. T. Arnold, J. G. Eaton, C. Fancher, S. A. Lyapustina, J. T. Snodgrass and K. H. Bowen, *J. Chem. Phys.*, 2002, **116**, 7926-7938.
44. F. Neese, WIREs Comput. Mol. Sci., 2012, **2**, 73–78.
45. F. Neese, A. Wennmohs, U. Hansen and U. Becker, *Chem. Phys.*, 2008, **356**, 98–109.
46. T. H. Dunning, Jr., *J. Chem. Phys.*, 1989, **90**, 1007.
47. Weigend, *Phys. Chem. Chem. Phys.*, 2006, **8**, 1057.
48. F. Weigend, A. Kohn and C. Hattig, *J. Chem. Phys.*, 2012, **116**, 3175.
49. C.L. Adams, H. Schneider, K.M. Ervin, J.M. Weber, *J. Chem. Phys.*, 2009, **130**, 074307.

VI. Appendix

The appendix contains majorly a collection of unpublished data.

VI.1 HMoO and H₂MoO: Molecular Mimics for Rhodium and Platinum

Gaoxiang Liu, Nikita Fedik, Zhaoguo Zhu, Mary Marshall, Xinxing Zhang, Alexander Boldyrev, and Kit H. Bowen

Noble metals are widely used in catalysis. There has been a long-standing interest in finding a less expensive replacement for noble metals. Building molecular clusters that mimic the properties of noble metals is considered as a promising approach. In this study, we discovered that the photoelectron spectra of HMoO⁻ and H₂MoO⁻ are respectively alike to those of Rh⁻ and Pt⁻: the HMoO⁻ spectrum appears to be the Rh⁻ spectrum being shifted to a higher electron binding energy, while the H₂MoO⁻ spectrum seems the Pt⁻ spectrum being shifted to a lower electron binding energy. Because anion photoelectron spectra are the reflection of the neutral electronic structures, this similarity suggests that neutral HMoO and H₂MoO have similar electronic structures as neutral Rh and Pt atoms, respectively. The similarity in electronic structure further indicates that HMoO and H₂MoO may have similar chemical properties as compared to Rh and Pt.

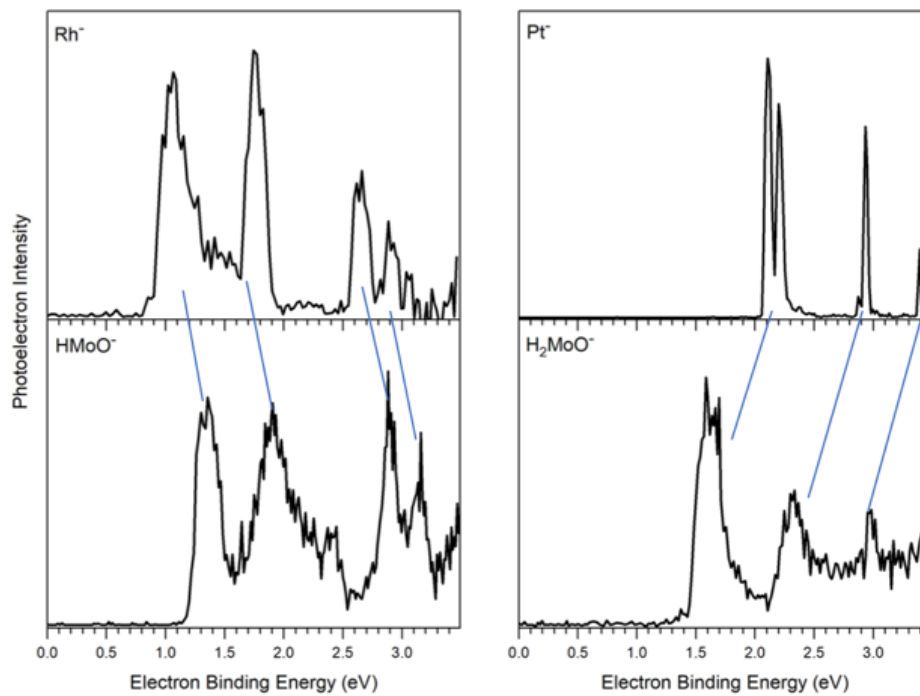


Figure 1. Photoelectron spectra of Rh^- and HMoO^- , and Pt^- and H_2MoO^- .

VI.2 CO₂ Hydrogenation by the Hydride of Platinum Mimic

Gaoxiang Liu, Zhaoguo Zhu, Mary Marshall, Alexander Boldyver, and Kit H. Bowen

We applied H₂MoO⁻ in small molecule activation to further demonstrate that it is the molecular mimic of Pt atom, whose catalytic activity has been demonstrated in our previous studies. In this work, we prepared the hydride of H₂MoO⁻, H₃MoO⁻, and let it react with H₂ and CO₂. We observed the adduct, H₃MoO(H₂)(CO₂)⁻, and characterized it using anion photoelectron spectroscopy.

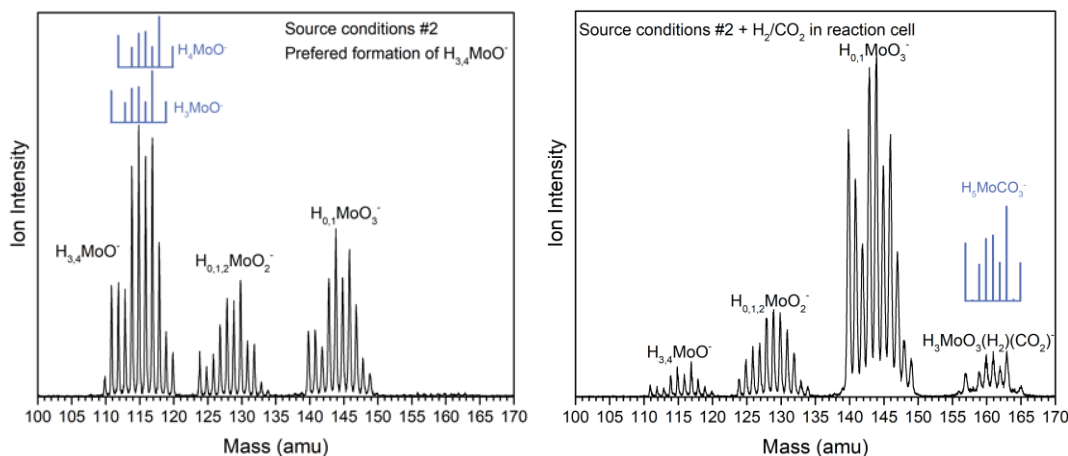


Figure 1. Mass spectra of the hydride of H₂MoO⁻, and the products of its reaction with H₂ and CO₂.

Under source condition #2, the generation of H₃MoO⁻ and H₄MoO⁻ is preferred, note that no H₅MoO⁻ is observed. The absence of H₅MoO⁻ has implications for the following CO₂ hydrogenation step. After adding CO₂ into the reaction cell, a new series of clusters

with a formula of $\text{H}_5\text{MoCO}_3^-$ is observed. This is the only cluster observed as a result of reaction with CO_2 and H_2 . It is unlikely that $\text{H}_5\text{MoCO}_3^-$ comes from the reactions between CO_2 and $\text{H}_x\text{MoO}_{2,3}^-$, because that requires breaking the $\text{C}=\text{O}$ bond and removing one or two O atoms. Therefore, $\text{H}_5\text{MoCO}_3^-$ comes from the reactions between CO_2 and $\text{H}_{3,4}\text{MoO}^-$. The extra H is from H_2 which also exists in the reaction cell. Then, it is very unlikely that $\text{H}_5\text{MoCO}_3^-$ is from the reaction $\text{H}_4\text{MoO}^- + \text{CO}_2 + \text{H}_2$, because the extra H atom has to be removed. Therefore, what happens in the cell is $\text{H}_3\text{MoO}^- + \text{CO}_2 + \text{H}_2 \rightarrow \text{H}_5\text{MoCO}_3^-$, and thus $\text{H}_5\text{MoCO}_3^-$ can be written as $\text{H}_3\text{MoO}(\text{H}_2)(\text{CO}_2)^-$.

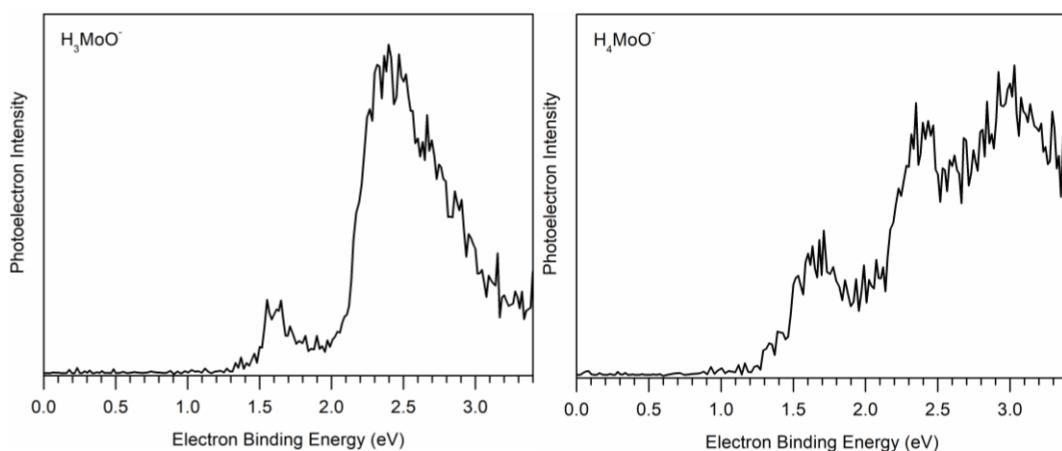


Figure 2. Photoelectron spectra of $\text{H}_{3,4}\text{MoO}^-$.

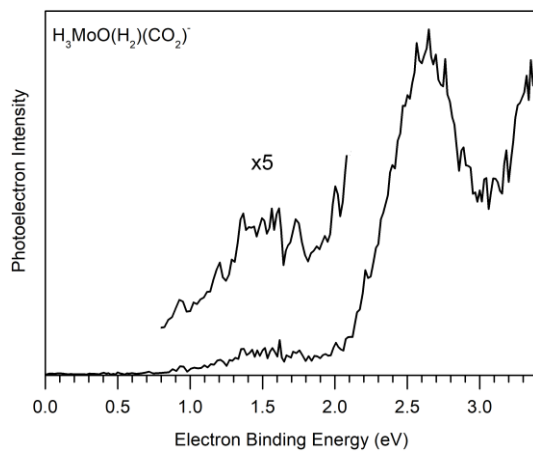


Figure 3. Photoelectron spectrum of the reaction product, $\text{H}_3\text{MoO}(\text{H}_2)(\text{CO}_2)^-$.

Whether H_4MoO^- is a mimic or not is not clear yet. Its features seem to be a widely broadened version of H_2MoO^- , so it is possible that H_4MoO^- has the form $(\text{H}_2)\text{H}_2\text{MoO}^-$. The fact that H_5MoO^- is not observed without the addition of CO_2 suggests that H_3MoO^- does not absorb H_2 . With the presence of CO_2 , $\text{H}_3\text{MoO}(\text{H}_2)(\text{CO}_2)^-$ is observed. It is hinting that H_3MoO^- absorbs(activates) CO_2 first, which somehow facilitates the followed absorption (activation) of H_2 . If CO_2 undergoes hydrogenation by the absorbed/activated H_2 , then $\text{H}_3\text{MoO}(\text{H}_2)(\text{CO}_2)^-$ shall have structures such as $\text{H}_3\text{MoO}(\text{HCOOH})^-$ or $\text{H}_4\text{MoO}(\text{HCOO}^-)$. This mirrors our previous results on CO_2 hydrogenation by PtH_3^- , and is a further demonstration that H_2MoO^- is a mimic of Pt^- .

VI.3 Ligated low oxidation state aluminum cluster anions Al_nL^- ($n = 1-14$, $L = N[Si(Me)_3]_2$)

Gaoxiang Liu,^a Sandra M. Ciborowski,^a Anil K. Kandalam,^{*b} and Kit H. Bowen^{*a}

^a *Department of Chemistry, Johns Hopkins University, Baltimore, Maryland 21218, United States*

^b *Department of Physics, West Chester University of Pennsylvania, West Chester, Pennsylvania 19383, United States*

Introduction

In recent years, aluminum chemistry has flourished as a result of the major progress in the research on aluminum's low oxidation states (OS).¹⁻² These studies started by the advent of low OS aluminum precursors such as AlX ($X = Cl, Br, I, Cp^*$)³⁻⁸ and largely advanced by utilizing various organic ligands to protect the low OS aluminum compounds.⁹⁻³¹ Among these ligands, deprotonated pentamethylcyclopentadiene (Cp^*) and deprotonated hexamethyldisilazane (HMDS) received special attention.^{9-12, 17-31} Cp^* has been reported to protect low OS aluminum compounds of various structures, such as rings and cages,²⁴⁻²⁷ and of various stoichiometries, including either aluminum-poor or aluminum-rich clusters.²⁹⁻³¹ The other ligand, deprotonated HMDS, $N[Si(Me)_3]_2$, which is isovalent to NH_2^- and large in size, has also been widely used to protect the central aluminum cluster cores from outer environments. For example,

cluster-like Al_7 , Al_{12} , Al_{69} , and Al_{77}^{9-12} with different numbers of $N[Si(Me)_3]_2$ as protective ligands were synthesized using various AlX precursors. Studying such clusters can provide insights into the crossover between the molecular species and the bulk metal for main-group elements.¹²

Recently, we extended the study of Cp^* - and deprotonated HMDS-ligated aluminum clusters into the gas phase by exploring the reactions between aluminum hydride cluster anions $Al_xH_y^-$ and Cp^*H or HMDS. The formation of and the anion photoelectron spectra of a number of previously unknown cluster anions, $Cp^*Al_nH^-$ ($n=1-3$)³² and Al_nL^- ($n = 2-4$, $L = N[Si(Me)_3]_2$)³³, were reported. In these studies, the precursors $Al_xH_y^-$ were generated by a pulsed-arc cluster ion source (PACIS)³⁴ and then allowed to drift into a beam-gas reaction cell³⁵ to react with the ligand (Cp^*H or HMDS).

In the present work, we adopted another strategy to generate ligated aluminum clusters in the gas phase: we used a laser vaporization source to make bare aluminum cluster anions Al_n^- , instead of $Al_xH_y^-$, and reacted them with HMDS in a reaction cell. A number of ligated aluminum cluster anions Al_nL^- ($L = N[Si(Me)_3]_2$), where $n = 1-14$, were produced by this approach, many of which were not observed in our previous work.³³ Two new Al_nL^- species, Al_6L^- and Al_7L^- , were selected for anion photoelectron

spectroscopic and density functional theory (DFT) study. Excellent agreement was achieved between the experimental and theoretical vertical detachment energies (VDEs) and adiabatic detachment energies (ADEs), which validated the computed structures.

Methods

Experimental

Anion photoelectron spectroscopy is conducted by crossing a beam of mass-selected negative ions with a fixed-frequency photon beam and energy-analyzing the resultant photodetached electrons. The photodetachment process is governed by the energy-conserving relationship: $h\nu = EBE + EKE$, where $h\nu$ is the photon energy, EBE is the electron binding energy, and EKE is the electron kinetic energy. Our apparatus consists of a laser vaporization cluster anion source with an attached reaction cell, a time-of-flight mass spectrometer, a Nd:YAG photodetachment laser, and a magnetic bottle electron energy analyzer.³⁶ The photoelectron spectrometer resolution is ~ 35 meV at 1 eV EKE. The third (355 nm) harmonic output of a Nd:YAG laser was used to photodetach electrons from mass-selected Al_nL^- clusters. Photoelectron spectra were calibrated against the well-known atomic transitions of atomic Cu^- .³⁷ Aluminum cluster anions Al_n^- were generated by laser vaporization of an aluminum rod. The resultant plasma was cooled with 100 psig of helium gas delivered by a

pulsed valve. The resulting aluminum cluster anions then traveled through a reaction cell (4-mm diameter), where they mixed with HMDS vapor. The HMDS vapor was introduced into the reaction cell by a second pulsed valve, which was backed by 15 psig of helium gas. The resulting Al_nL^- anionic clusters were mass-analyzed by the time-of-flight mass spectrometer and their photoelectron spectra were recorded.

Results and discussion

The mass spectra, with and without HMDS pulsed into the reaction cell, are shown in Figure 1. With no HMDS in the reaction cell, bare aluminum cluster anions, Al_n^- , are observed in the mass spectrum; when HMDS is injected into the cell, a new series of ligated aluminum cluster anions Al_nL^- appears, where L is identified as deprotonated HMDS, i.e., $N[Si(Me)_3]_2$. The size of the aluminum core in Al_nL^- ranges from 1 to 14, of which Al_5L^- to $Al_{14}L^-$ have not been observed prior to the current work. This further demonstrates the capability of this laser vaporization–reaction cell setup in preparing various ligated metal cluster anions in the gas phase.³⁶

Photoelectron spectra were recorded for three selected Al_nL^- species: Al_4L^- , Al_6L^- and Al_7L^- , and these are displayed in Figure 2. In an anion photoelectron spectrum, the electron binding energy (EBE) value at the peak position in the lowest EBE spectral feature is the vertical detachment energy (VDE), which corresponds to the

photodetachment transition at which the Franck-Condon overlap is maximal between the wavefunctions of the anion and its neutral counterpart. The electron affinity (EA) is the energy difference between the respective lowest energy states of the anion and the neutral. When there is sufficient Franck-Condon overlap between these two energy states, and when no vibrational hot bands are present, the EA value can be determined as the EBE value at the threshold of the lowest EBE band. Here, the EA values are assigned by extrapolating the low EBE side of the lowest EBE spectral feature to zero intensity. The adiabatic detachment energy (ADE) is the energy difference between a certain anionic isomer and its neutral counterpart relaxed to the nearest local minimum. The Al_4L^- spectrum was taken to compare with the previous Al_4L^- spectrum³³ as a cross-validation, and no significant difference between them can be observed. This demonstrates that the Al_nL^- species made in the current work should be similar to those made previously, though they are prepared by reacting HMDS with different low OS aluminum precursors, i.e., bare aluminum cluster anions versus aluminum hydride cluster anions. For Al_6L^- , the first EBE feature starts at about 2.2 eV and peaks at 2.98 eV. Thus, the experimental EA is 2.2 eV for neutral Al_6L and the experimental VDE is 2.98 eV for Al_6L^- . In the spectrum of Al_7L^- , we observe that its lowest EBE band starts at approximately 1.9 eV and reaches maximal intensity at 2.34 eV. Therefore, the EA of neutral Al_7L^- and the VDE of Al_7L^- are determined as 1.9 and 2.34 eV, respectively.

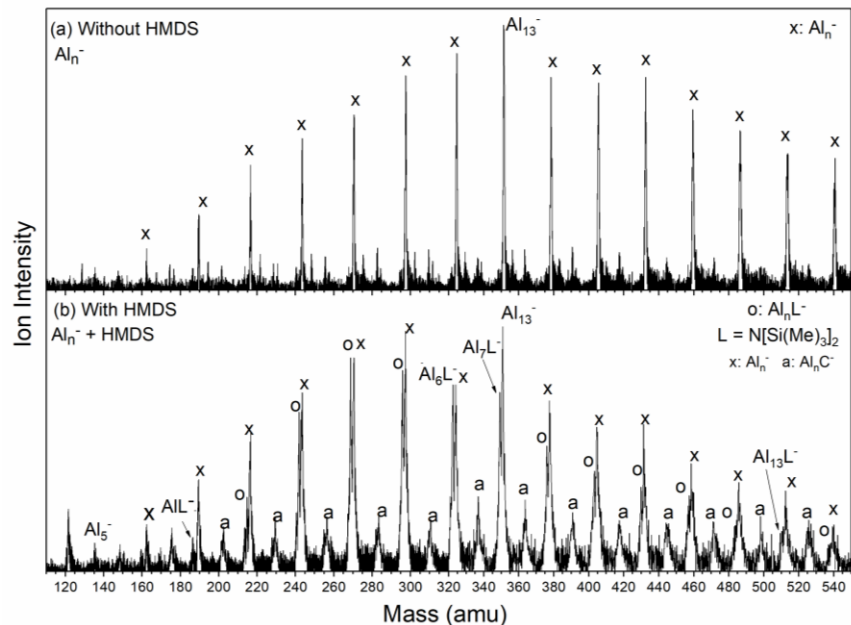


Figure 1. Mass spectra of (a) bare aluminum cluster anions, Al_n^- , and (b) deprotonated HMDS-ligated aluminum cluster anions, Al_nL^- ($L = N[Si(Me)_3]_2$).

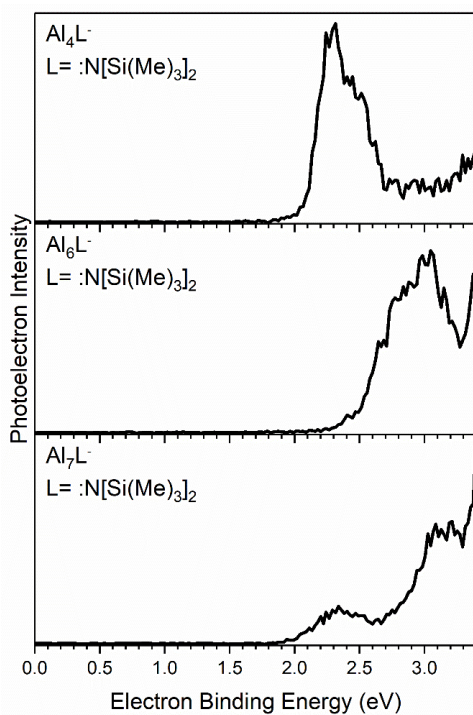


Figure 2. Anion photoelectron spectra of Al_4L^- , Al_6L^- , and Al_7L^- ($L = N[Si(Me)_3]_2$),

taken with the third harmonic (355 nm wavelength) of a Nd:YAG laser.

References

1. W. Roesky and S. S. Kumar, *Chem. Commun.*, 2005, 4027
2. H. W. Roesky, *Inorg. Chem.*, 2004, **43**, 7284.
3. M. Tacke and H. Schnöckel, *Inorg. Chem.*, 1989, **28**, 2896.
4. M. Mocker, C. Rob and H. Schnöckel, *Angew. Chem.*, 1994, **106**, 1860.
5. A. Ecker and H. Schnöckel, *Z. Anorg. Allg. Chem.*, 1996, **622**, 149.
6. C. Dohmeier, C. Roble, M. Tacke and H. Schnöckel, *Angew. Chem.*, 1991, **103**, 594.
7. C. Dohmeier, D. Loos and H. Schnöckel, *Angew. Chem.*, 1996, **108**, 141.
8. J. Gauss, U. Schneider, R. Ahlrichs, C. Dohmeier and H. Schnöckel, *J. Am. Chem. Soc.*, 1993, **115**, 240.
9. A. Purath, R. Köppe and H. Schnöckel, *Angew. Chem.*, 1999, **111**, 31 (*Angew. Chem. Int. Ed.*, 1999, **38**, 2926).
10. A. Purath, R. Köppe and H. Schnöckel, *Chem. Commun.*, 1999, 1933.
11. H. Köhnlein, A. Purath, C. Klemp, E. Baum, I. Krossing, G. Stösser and H. Schnöckel, *Inorg. Chem.*, 2001, **40**, 4830.
12. E. Ecker, E. Weckert and H. Schnöckel, *Nature*, 1997, **387**, 379.
13. C. Dohmeier, M. Mocker, H. Schnöckel, A. Lötze, U. Schneider and R. Ahlrichs, *Angew. Chem.*, 1993, **105**, 1491. (*Angew. Chem. Int. Ed.*, 1993, **32**, 1428).
14. A. Schnepf and H. Schnöckel, *Adv. Organomet. Chem.*, 2001, **47**, 235.
15. C. Üffing, A. Ecker, R. Köppe, K. Merzweiler and H. Schnöckel, *Chem. Eur. J.*, 1998, **4**, 2142.
16. N. Etkin and D. W. Stephan, *Organometallics*, 1998, **17**, 763.
17. S. J. Urwin, D. M. Rogers, G. S. Nichol and M. J. Cowley, *Dalton Trans.*, 2016, **45**, 13695.
18. A. Haaland, K.-G. Martinsen, S. A. Shlykov, H. V. Volden, C. Dohmeier and H. Schnöckel, *Organometallics*, 1995, **14**, 3116.
19. J. D. Gordon, A. Voigt, C. L. B. Macdonald, J. S. Silverman and A. H. Cowley, *J. Am. Chem. Soc.*, 2000, **122**, 950.
20. C. Dohmeier, H. Krautscheid and H. Schnöckel, *Angew. Chem.*, 1994, **106**, 2570.
21. C. Üffing, A. Ecker, R. Köppe and H. Schnöckel, *Organometallics*, 1998, **35**, 2373.
22. Q. Yu, A. Purat, A. Douchev and H. Schnöckel, *J. Organomet. Chem.*, 1999, **584**, 94.
23. J. Weiß, D. Stetzkamp, B. Nuber, R. A. Fischer, C. Boehme and G. Frenking, *Angew. Chem. Int. Ed.*, 1997, **36**, 70.
24. D. Weiß, T. Steinke, M. Winter, R. A. Fischer, N. Fröhlich, J. Uddin and G. Frenking, *Organometallics*, 2000, **19**, 4583.
25. S. Schulz, T. Schoop, H. W. Roesky, L. Häming, A. Steiner and R. Herbst-Irmer, *Angew. Chem. Int. Ed.*, 1995, **34**, 919.
26. C. K. F. von Haenish, C. Üffing, M. A. Junker, A. Ecker, B. O. Kneisel and H. Schnöckel, *Angew. Chem. Int. Ed.*, 1996, **35**, 2875.

27. C. Dohmeier, H. Schnöckel, C. Robl, U. Schneider and R. Ahlrichs, *Angew. Chem. Int. Ed.*, 1994, **33**, 199.
28. C. Ganesamoorthy, S. Loerke, C. Gemel, P. Jerabek, M. Winter, G. Frenking and R. A. Fischer, *Chem. Commun.*, 2013, **49**, 2858.
29. J. Vollet, J. R. Hartig and H. Schnöckel, *Angew. Chem. Int. Ed.*, 2004, **43**, 3186.
30. K. Weiß and H. Schnöckel, *Anal. Bioanal. Chem.*, 2003, **377**, 1098.
31. K. S. Williams and J. P. Hooper, *J. Phys. Chem. A*, 2011, **115**, 14100.
32. X. Zhang, G. Gantefoer, B. Eichhorn, D. Mayo, W. H. Sawyer, A. F. Gill, A. K. Kandalam, H. Schnöckel and K. Bowen, *J. Chem. Phys.*, 2016, **145**, 074305.
33. X. Zhang, L. Wang, G. Montone, A. Gill, G. Gantefoer, B. Eichhorn, A. Kandalam and K. H. Bowen, *Phys. Chem. Chem. Phys.*, 2017, **19**, 15541-15548.
34. X. Zhang, G. Liu, G. Gantefoer, K. H. Bowen and A. N. Alexandrova, *J. Phys. Chem. Lett.*, 2014, **5**, 1596.
35. X. Zhang, G. Liu, K.-H. Meiwes-Broer, G. Ganteför and K. H. Bowen, *Angew. Chem. Int. Ed.*, 2016, **55**, 9644.
36. G. Liu, S. Ciborowski and K. H. Bowen, *J. Phys. Chem. A*, 2017, **121**, 5817.
37. J. Ho, K. M. Ervin and W. C. Lineberger, *J. Chem. Phys.*, 1990, **93**, 6987.

VI.4 Two new double-Rydberg anions: $\text{Li}(\text{OH}_2)_{1,2}^-$

Xinxing Zhang, *Gaoxiang Liu*, Sandy Ciborowski, Mary Marshall and K. H. Bowen*

Department of Chemistry, Johns Hopkins University, Baltimore MD 21218

Héctor H. Corzo, O. Dolgounitcheva, V. G. Zakrzewski and J. V. Ortiz*

Department of Chemistry and Biochemistry, Auburn University, Auburn AL 36849-5312

Zhen Zeng and Weijun Zheng*

Beijing National Laboratory for Molecular Sciences, State Key Laboratory of Molecular Reaction Dynamics, Institute of Chemistry, Chinese Academy of Sciences, Beijing 100190, China

Abstract

For several years, researchers have been seeking the Double-Rydberg anions (DRAs) H_3O^- and H_5O_2^- , but no positive results have been reported other than theoretical predictions. By substituting one H atom in H_3O^- or H_5O_2^- with a Li atom, we have successfully characterized DRAs $\text{Li}(\text{OH}_2)_{1,2}^-$ via anion photoelectron spectroscopy and theoretical calculations. The photoelectron spectrum of LiOH_2^- strikingly showed a red shift compared to that of Li^- , whereas a simple anion solvation process would have resulted in a blue shift. Comparison of our calculations with experimental data confirmed that only the DRA LiOH_2^- is present in the experiments, even though

calculations found two atomic anion-molecule alternatives: Li-(H₂O) and H-(LiOH). For Li(OH₂)₂⁻, the anion detected experimentally has a structure that is similar to that of DRA H₅O₂⁻, with the Li atom residing in the bridging position between the two oxygen atoms, according to the calculations. Four alternative structures that consist of atomic anions or DRA LiOH₂⁻ coordinated to molecules also have been found computationally. Both DRAs have diffuse Dyson orbitals of electron detachment whose largest amplitudes lie nearest to the Li atom.

Introduction

Double-Rydberg Anions (DRAs) are characterized by a pair of electrons delocalized in a diffuse orbital surrounding a stable, closed-shell cationic core, such as H₃O⁺ or NH₄⁺.^{1,2} With an electron pair described by extra-valence orbitals, DRAs exhibit a novel pattern of electronic structure.³ In 1988, the first experimental observation of the DRA NH₄⁻ with a vertical detachment energy (VDE) of 0.472 eV was reported.⁴ The DRA character of NH₄⁻ was further confirmed by *ab initio* calculations.^{5,6} Anion photoelectron spectra and theory suggested that N_nH_{3n+1}⁻ (n = 2-7) species are DRAs.⁷⁻⁹ Other nitrogen-centered DRAs, such as NH₃R⁻ (R = F, OH, CH₃), were predicted by *ab initio* theory.¹⁰ Another intriguing DRA, H₃O⁻, has been predicted by calculations to be stable,^{2,6,10-12} with a VDE of 0.466 or 0.50 eV¹¹ and a pyramidal, C_{3v} structure.^{6,12} H₅O₂⁻, as a counterpart of N₂H₇⁻, was predicted by theory.¹¹ To date,

there is no experimental evidence of the existence of DRA H_3O^- , but its isomer, $\text{H}^-(\text{H}_2\text{O})$, has been detected with a VDE of 1.53 eV.¹³ The $\text{H}^-(\text{H}_2\text{O})$ isomer can be viewed as an H^- anion solvated by one water molecule. Although numerous experimental efforts have been made to produce DRA H_3O^- , no success has been achieved, perhaps because this species is much higher in energy than $\text{H}^-(\text{H}_2\text{O})$.¹¹ On the other hand, the metastable Rydberg radicals, H_3O and D_3O , have been identified with neutralized ion beam spectroscopy experiments by Porter and coworkers.¹⁴⁻¹⁶ However, the production of H_3O via neutralization-reionization spectroscopy still remains uncertain.^{17,18}

As lithium is the closest element to hydrogen in the alkali metal group, it would be interesting to see whether it is possible to generate DRAs by replacing the H atoms in H_3O^- and H_5O_2^- with Li atoms. In this work, we have investigated $\text{Li}(\text{H}_2\text{O})_{1,2}^-$ clusters by anion photoelectron spectroscopy and have studied theoretically the structures and electronic properties of these anions as well as their corresponding neutrals. We have found that the LiH_2O^- formula has three types of low-lying isomers through ab initio calculations: 1) a DRA with a pyramidal oxygen atom, 2) a solvation isomer in the form of $\text{Li}^-(\text{H}_2\text{O})$, 3) another solvation isomer, $\text{H}^-(\text{LiOH})$. By comparing theoretical calculations with experimental data, we have confirmed that the DRA LiOH_2^- is the only isomer detected in our experiment. In the past, the photoelectron spectra of

$\text{Li}(\text{H}_2\text{O})_{1,2}^-$ have been published by Fuke¹⁹ and Zheng,²⁰ but the DRA nature of the anions was not discussed in those papers. In the current study, to compare with our computational results, we have revisited the experiment, and have reproduced published data very well with enhanced spectral resolution. Through calculations, we also have found structures with the $\text{Li}(\text{H}_2\text{O})_2^-$ formula that correspond to: 1) a DRA with two Li-O bonds to water molecules, 2) a complex in which H^- and a water molecule are coordinated to a LiOH molecule, 3) complexes that consist of a water molecule and DRA LiOH_2^- , 4) a complex that consists of Li^- and a water dimer. Only the DRA isomer is represented in the photoelectron spectrum.

Experimental and theoretical methods

Anion photoelectron spectroscopy is conducted by crossing a mass-selected beam of negative ions with a fixed-frequency photon beam and energy-analyzing the resultant photo-detached electrons. It is governed by the energy-conserving relationship, $h\nu = \text{EBE} + \text{EKE}$, where $h\nu$ is the photon energy, EBE is the electron binding (transition) energy, and EKE is the electron kinetic energy. The experiment was conducted on a home-built apparatus consisting of a laser vaporization source, a time-of-flight mass spectrometer, and velocity-map imaging photoelectron spectrometer, which has been described previously.²¹ The Li^- and $(\text{LiOH}_2)^-$ anions were generated in the laser vaporization source by ablating a rotating and translating lithium rod with the second

harmonic (532 nm) light pulses of a nanosecond Nd:YAG laser (Continuum Surelite II-10), while helium carrier gas with 45 psi backing pressure seeded with water vapor was allowed to expand through a pulsed valve for providing H₂O molecules and for cooling. The cluster anions were mass-analyzed by a time-of-flight mass spectrometer. The Li⁻, and Li(H₂O)_{1,2}⁻ anions were each mass-selected before being photo-detached by the fundamental (1064 nm) light pulses of another Nd: YAG laser (Continuum Surelite II-10). Electron kinetic energy was measured using a velocity-map imaging (VMI) 22,23 spectrometer. There, mass-gated anions are crossed with 1064 nm, linearly polarized photons in an electric field, so that resultant photo-detached electrons are accelerated along the axis of the ion beam toward a position sensitive detector (75 mm diameter dual microchannel plate detector with a phosphor screen coupled to a CCD camera). The sum of ~50,000 electrons forms a 2D image which is then reconstructed into a slice of the 3d Distribution via the BASEX²⁴ method. Photoelectron spectra were calibrated against the well-known photoelectron spectrum of NO⁻.

All geometry optimizations, harmonic frequency and energy calculations for the Li(H₂O)_{1,2}⁻ isomers were carried out with the Gaussian Development Version.²⁵ Preliminary geometry optimizations with the full-orbital coupled-cluster-singles-doubles (CCSD)²⁶ method and the 6-311++G(2df,2pd) basis set²⁷⁻²⁹ were

performed to assess stationary structures and to estimate their relative stabilities. Local minima were identified by the absence of imaginary harmonic frequencies. Further refinements were obtained by re-optimization with two sets of *sp* and *d* diffuse functions (Table 1). These augmentations had little effect on the optimized structures but were important for the refinement of energies. Single-point energies at the CCSD plus perturbative triples, or CCSD(T),³⁰ level and CCSD zero-point vibrational energies were computed for the final estimation of anion isomerization energies. The latter calculations confirmed that the optimized anionic structures of Figs. 2 and 3 correspond to minima in potential-energy hypersurfaces. Vertical detachment energies (VDEs) were calculated with the augmented, quadruple- ζ , correlation-consistent (aug-cc-pvqz)³¹ set. The BD-T1 electron propagator method^{32,33} was employed to calculate VDEs, corresponding Dyson orbitals (see Figs. 4-11) and pole strengths (norms of Dyson orbitals) directly. These transition energies also were evaluated with CCSD(T) total-energy differences. Optimized geometries (see Fig. 12) and frequencies of Li(OH₂)_{1,2}⁻ were computed as well with the 6-311++G(2df,2pd) plus extra-diffuse-function (see Table 1) basis mentioned above. Cationic minima were calculated with the same methods.

Experimental results

The photoelectron spectra of Li⁻ and Li(OH₂)_{1,2}⁻ taken with 1064 nm radiation are

presented in Fig. 1. These spectra were reported in our previous publication²⁰ and are also in agreement with those reported by Takasu *et al.*¹⁹ We revisited these experiments with better instrumental resolution. The spectrum of Li^- has a peak centered at 0.62 eV, which perfectly reproduced published Li^- data.³⁴ That of $\text{Li}(\text{OH}_2)^-$ has a peak centered at 0.56 eV. Compared to Li^- , the spectrum of $\text{Li}(\text{OH}_2)^-$ red shifts to the low EBE side by 0.06 eV. This red shift indicates that the interaction between Li^- and H_2O in $\text{Li}(\text{OH}_2)^-$ is different from micro-solvation by the molecule on the anion because the latter effect usually induces a blue shift. Because copious cases possessing this kind of blue shift have been observed,³⁵⁻⁴⁴ the $\text{Li}(\text{OH}_2)^-$ case is unusual. Without further calculations, we could speculate that such a red shift is strong evidence that $\text{Li}(\text{OH}_2)^-$ is a DRA where the oxygen atom in the water molecule attaches to the Li atom. This scenario is similar to the red shift between the spectrum of tetrahedral NH_4^- and that of H^- .⁴

The spectrum of $\text{Li}(\text{OH}_2)_2^-$ presents two peaks. The second small peak was not identified in previous experiments due to lesser resolution.^{19,20} The first peak appears at the same position as that of LiOH_2^- , indicating that the chromophores of these two anions could be similar, i.e. both could be DRAs. Hence, the 0.56 eV peak of $\text{Li}(\text{OH}_2)_2^-$ corresponds to a DRA with a central Li atom bound to the two oxygen atoms in the water molecules: $\text{H}_2\text{OLiOH}_2^-$. This structure is a counterpart of the H_5O_2^-

and N_2H_7^- DRAs.^{7,11} The smaller 0.60 eV peak represents a small blue shift with respect to the principal peak in the $\text{Li}(\text{OH}_2)^-$ spectrum. This feature could be assigned (see below) to a VDE for the latter DRA anion coordinated to a water molecule or to a satellite in which photo-detachment is accompanied by vibrational excitation. This isomer has much lower photoelectron intensity, indicating that it might be higher in energy than $\text{H}_2\text{OLiOH}_2^-$.

Theoretical results

For LiOH_2^- , three minima were found through geometry optimizations (Figure 2). The first may be considered to be a linear complex in which a hydride anion is ionically bound to the metal atom in LiOH . In this $C_{\infty v}$ structure, the H - Li separation of 1.77 Å indicates a dative bonding relationship with charge donation by the hydride to an unoccupied Li hybrid orbital. This $\text{H}^-(\text{LiOH})$ minimum is 1.43 eV more stable than a complex composed of Li^- coordinated to the hydrogen atoms of H_2O in a C_{2v} structure. In the latter, $\text{Li}^-(\text{H}_2\text{O})$ case, the Li-H distance is 3.68 Å and the Li-O distance is 4.21 Å. In the third, C_s minimum, the oxygen nucleus is separated by 1.89 and 0.97 Å from the lithium and hydrogen nuclei, respectively, in a pyramidal arrangement that resembles that of the H_3O^- DRA.¹² Li-O-H and H-O-H bond angles respectively are 112° and 105°. This species is 1.12 eV less stable than the $\text{H}^-(\text{LiOH})$ minimum and is denominated as LiOH_2^- . Optimizations initiated at C_s , $\text{LiO}^- \dots \text{H}_2$ geometries rearrange via proton transfer to the $\text{H}^-(\text{LiOH})$ minimum; when $C_{\infty v}$ symmetry is

imposed, dissociation to $\text{LiOH} + \text{H}^-$ occurs.

VDEs are displayed along with relative energies of anions in Table 2. For the BD-T1, electron-propagator calculations, all pole strengths exceed 0.9 and therefore validate the one-electron picture that accompanies the Dyson orbitals. $\Delta\text{CCSD(T)}$ and BD-T1 values agree closely. Results for the C_s , pyramidal species (i.e. the DRA) are in excellent agreement (within 0.01 eV) with the peak seen in the photoelectron spectrum. The VDE predicted for the most stable isomer, 3.00 eV, is larger than the photon energy employed in the present experiment. (The presence of this isomer in the experimental sample therefore cannot be discounted.) No peak corresponding to the predicted VDE of 0.89 eV for $\text{Li}^-(\text{H}_2\text{O})$ appears in the spectrum.

Dyson orbitals for the three isomers in the order of their stability are shown in Figs. 4-6. The corresponding Dyson orbital for the C_s geometry (Fig. 5) is diffuse, with large amplitudes occurring outside the Li and H nuclei. This function resembles its counterpart for C_{3v} H_3O^- , a DRA, but exhibits greater polarization toward regions near the Li nucleus. The VDEs calculated for the $\text{Li}^-(\text{H}_2\text{O})$ isomers are blue shifted by approximately 0.25 eV with respect to their counterparts for Li^- in Table 2. The corresponding Dyson orbital for C_{2v} $\text{Li}^-(\text{H}_2\text{O})$ (Fig. 6) is localized on the Li atom and has only small amplitudes on the water molecule. In the more stable, hydride-

molecule isomer, $\text{H}^-(\text{LiOH})$, the strong electrostatic potential associated with ionic bonding in LiOH is responsible for the large blue shift in the VDE (2.25 eV) with respect to that of bare H^- , 0.75 eV. The Dyson orbital (Fig. 4) is dominated by diffuse s functions on H^- that are orthogonalized to occupied valence molecular orbitals.

For the $\text{Li}(\text{OH}_2)_2^-$, five minima were found through geometry optimization (Fig. 3). The most stable isomer corresponds to a complex in which H^- is coordinated to the lithium atom of the ionic molecule LiOH ; the latter species has a hydrogen bond between its oxygen atom and a water molecule. This structure has a hydride-Li separation of 1.74 Å that closely resembles its counterpart in the $\text{H}^-(\text{LiOH})$ structure, 1.77 Å; the 0.03 Å shortening is a consequence of increased positive charge on the Li atom induced by the hydrogen bond. It therefore may be represented by the formula $\text{H}^-(\text{LiOH})(\text{H}_2\text{O})$. Comparison of Figs. 4 and 7 reveals that the Dyson orbital for the VDE of $\text{H}^-(\text{LiOH})(\text{H}_2\text{O})$ is similar to that of $\text{H}^-(\text{LiOH})$. Because its VDE of 3.45 eV (see Table 3) is too large to be detected in the experiment, this anion's presence in the experimental source cannot be ruled out.

The next most stable species has two Li-O bonds of length 1.88 Å that are near the 1.89 Å value seen in DRA LiOH_2^- . A bent O-Li-O angle of 115° suggests the presence of negative charge near the Li atom and along the symmetry axis of this C_2

species. Diffuse amplitudes dominate the Dyson orbital of the VDE and are located outside the H and Li nuclei. Polarization of the amplitudes toward the Li atom is similar to that seen for DRA LiOH_2^- . (Compare Figs. 5 and 8.) This isomer therefore may be denominated as DRA $\text{Li}(\text{OH}_2)_2^-$. VDE predictions for this DRA, 0.53 eV for BD-T1 and 0.55 eV for $\Delta\text{CCSD(T)}$, coincide very well with experiment.

Only 0.03 eV separates the energies of the third and fourth most stable structures. Both consist of a DRA LiOH_2^- moiety with a Li-O bond length of 1.89-1.90 Å (versus 1.89 Å in the parent DRA) that is coordinated to a water molecule. In the third case, a hydrogen bond exists between a proton of the DRA and the oxygen atom of H_2O , but in the fourth case, the water molecule's protons are attracted to the DRA's diffuse electrons. These relatively weakly bound species have VDEs that respectively are lower (0.50 eV) and higher (0.70 eV) than that of DRA $\text{Li}(\text{OH}_2)_2^-$. In the former case, the 0.03 eV red shift with respect to the predicted value 0.53 eV for DRA $\text{Li}(\text{OH}_2)_2^-$ cannot account for the minor peak seen at 0.60 eV. No experimental peak corresponds to the predicted VDE of the fourth most stable structure. In both cases, the Dyson orbitals of the VDEs (see Figs. 9 and 10) resemble that of the DRA LiOH_2^- . In the third most stable structure, the VDE is smaller than that of DRA $\text{Li}(\text{OH}_2)_2^-$ for two reasons: 1) the oxygen atom of the coordinating water molecule donates electronic charge to the bridging H atom of the DRA fragment and 2) the oxygen atom's negative

charge destabilizes the diffuse electrons near the Li atom. The opposite trend in VDEs occurs in the fourth most stable isomer, for the H atoms of the coordinating water molecule are oriented toward the diffuse electrons.

In the least stable of the five structures, a second water molecule forms a hydrogen bond with the water molecule that coordinates to Li^- in $\text{Li}^-(\text{H}_2\text{O})$. Whereas the latter anion has a Li-O distance of 4.21 Å, the enhanced dipole moment of the water dimer results in a Li-O separation of 3.94 Å for this isomer. The Dyson orbital of this anion's VDE consists chiefly of diffuse Li s functions, as was the case for $\text{Li}^-(\text{H}_2\text{O})$. (See Figs. 6 and 11.) Because of the enhanced anion-dipole interaction, the VDE of 1.09 eV is larger than that of $\text{Li}^-(\text{H}_2\text{O})$ by 0.20 eV. As in the cases of the third and fourth most stable isomers, the fifth most stable structure does not correspond to any peak seen in the experiment.

After electron detachment from DRA $\text{Li}(\text{OH}_2)_2^-$, the resulting uncharged species relaxes to a geometry with a smaller O-Li-O angle that is shown in Fig. 12. This trend follows from the removal an electron from a diffuse, totally symmetric orbital in the C_2 anion. A normal mode that corresponds to O-Li-O bending has a frequency of 0.04 eV in the uncharged final state. These data suggest that the satellite peak at 0.60 eV in the spectrum may be assigned to electron detachment accompanied by an

elementary vibrational excitation.

Discussion

Complexes of atomic anions and molecules are not detected in the experimental photoelectron spectrum of $\text{Li}^-(\text{H}_2\text{O})^-$. The $\text{Li}^-(\text{H}_2\text{O})^-$ anion may not have been observed because its energy is the highest of the three isomers listed in Table 2. However, with a much lower energy, $\text{H}^-(\text{LiOH})^-$ was not observed either. The results of Table 2 indicate that this species has a VDE which is too large to detect with the present source of photons. It may be present in the experiment's mass-selected beam of anions. One more possibility is that the barrier for breaking one O-H bond in water is too high to allow this isomer's presence in the anion source region.

The C_s LiOH_2^- species detected in the anion photoelectron spectrum of Fig. 1 is isoelectronic with the C_{3v} DRA H_3O^- and has a similar structure in which a hydrogen atom has been replaced by a lithium atom. The isovalent Li_2OH^- and Li_3O^- anions also merit consideration. Li_2OH^- has been calculated to have a C_{2v} structure⁴⁵ (with both of the Li atoms and the H atom being connected to the central O atom) similar to that of DRA H_3O^- . Li_3O^- has been made experimentally⁴⁶ and investigated theoretically.⁴⁷ Previous works emphasized this anion's relationships with superalkalis, but did not consider possible DRA characteristics. The Dyson orbital for the

VDE of LiOH_2^- has important contributions from diffuse (i.e. extra-valence) functions on its hydrogen atoms and therefore more closely resembles its counterpart for DRA OH_3^- than its counterpart for Li_3O^- . Therefore, LiOH_2^- may be classified as a DRA.

Replacement of H_2O by NH_3 leads to related species. LiNH_3^- , being iso-valent to NH_4^- and having an approximately tetrahedral structure, could be a DRA. Anion photoelectron spectroscopy and calculations provide confirmation, even though these works did not focus on similarities with other DRAs.^{48,49} Li_4N^- has been investigated theoretically; its tetrahedral structure resembles that of DRA NH_4^- .⁵⁰ Species such as Li_2NH_2^- and Li_3NH^- with tetrahedral nitrogen atoms are probable DRA candidates.

Complexes of atomic anions with molecules also are absent from the photoelectron spectrum of $\text{Li}(\text{OH}_2)_2^-$. For the most stable structure, where a hydride anion forms an ionic bond to LiOH and the latter fragment's oxygen atom enters into a hydrogen bond with a water molecule, the VDE is too large to be measured in the present experiment. The least stable structure for $\text{Li}(\text{OH}_2)_2^-$ displays a Li^- anion that is attracted to $(\text{H}_2\text{O})_2$. There is no VDE near the predicted value of 1.1 eV, nor was there a peak near 0.9 eV in the spectrum of $\text{Li}(\text{OH}_2)_2^-$. Structures that consist of Li^- anions plus water molecules do not contribute to either spectrum.

The DRA $\text{Li}(\text{OH}_2)_2^-$ has a structure that resembles that of the DRA O_2H_5^- in which the latter anion's bridging hydrogen atom is replaced by a lithium atom. Whereas the bridging atom in O_2H_5^- has unequal O-H separations, the two O-Li distances are identical in $\text{Li}(\text{OH}_2)_2^-$. Sequential replacement of non-bridging hydrogen atoms by lithium atoms may lead to stable $\text{O}_2\text{Li}_{5-n}\text{H}_n^-$ species for $n=0,1,2,3$ with similar structures and Dyson orbitals. The third and fourth structures of Table 3 are related to the other DRA isomer of O_2H_5^- , an anion-molecule complex of DRA OH_3^- with H_2O . In the former case, a water molecule coordinates to DRA LiOH_2^- through a hydrogen bond that destabilizes the anion's diffuse electrons, leading to a reduced VDE. (The latter hydrogen bond's dissociation energy is approximately 0.2 eV.) In the latter case, the water molecule orients its dipole moment toward the diffuse electrons, producing a higher VDE. This structure resembles that of the DRA $\text{OH}_3^-(\text{H}_2\text{O})$ anion; a lithium atom instead of a hydrogen atom bridges between the anion and the molecule. There is no peak at 0.7 eV in the spectrum and therefore the fourth most stable structure may be ruled out. There is no evidence of a satellite at lower electron binding energy with respect to the chief peak at 0.56 eV; the third most stable structure also may be eliminated from further consideration.

Experimental and theoretical evidence for the coexistence of two DRAs of a given formula, one with a hydrogen bridge and the other with a DRA-molecule structure,

exists for N_2H_7^- . In one case, a tetrahedral NH_4^- fragment is coordinated to an ammonia molecule, with the protons of the latter species oriented toward the DRA. In the other DRA structure, an asymmetric N-H-N bridge is accompanied by a Dyson orbital for the VDE which is distributed chiefly outside the three hydrogens of the tetrahedral fragment that are not engaged in the hydrogen bond. A similar structure for LiN_2H_6^- with a lithium atom in the bridging position may be another DRA, along with $\text{Li}_n\text{N}_2\text{H}_{7-n}^-$ species with $n=2-7$.

Unlike the case of NH_4^- in which there is little structural difference between the DRA and its parent cation or radical, there are substantial changes in Li-O distances between DRAs $\text{Li}(\text{OH}_2)_{1,2}^-$ and the related uncharged or cationic species. In addition, O-Li-O bond angles are 180° , 107° and 115° respectively for the D_{2d} cation $\text{Li}(\text{OH}_2)^+$, the corresponding radical and the DRA $\text{Li}(\text{OH}_2)_2^-$.

Conclusions

Close agreement between vertical detachment energies inferred from an anion photoelectron spectrum and *ab initio* electron propagator calculations establishes that the LiOH_2^- species observed experimentally corresponds to a pyramidal structure in which Li and H atoms are bound to a central O atom, in resemblance to the cationic structure. The Dyson orbital for the vertical detachment energy is diffuse, with its

largest amplitudes concentrated outside the Li and H nuclei. Therefore, the observed LiOH_2^- species is a double-Rydberg anion, with a pair of electrons described by extra-valence orbitals on the hydrogen nuclei and by 2s orbitals on the lithium nucleus.

$\text{Li}(\text{OH}_2)_2^-$ also is an anion with two diffuse electrons that cause the O-Li-O angle to be bent, unlike the linear structure seen in the cation. The largest amplitudes of the Dyson orbital also occur in exterior regions, but are close enough to affect O-Li bond lengths and the O-Li-O angle. Excellent agreement between the spectral peak and the calculated vertical detachment energy also occurs in this case. In addition, a vibrational satellite has been assigned.

No evidence of the most energetically stable anion-molecule complexes, $\text{H}(\text{LiOH})(\text{H}_2\text{O})_{0,1}$, has been found in the spectra, but the presence of these species cannot be ruled out. Calculations indicate that photon sources above 3 eV would be needed to determine their electron detachment energies. There also is no experimental evidence for the less stable $\text{Li}^-(\text{H}_2\text{O})_{1,2}$ species or for DRA $\text{LiOH}_2^-(\text{H}_2\text{O})$ complexes that is in agreement with theory.

Table 1. Extra-diffuse-function exponents

Atom	sp	d
Li	0.0025	0.033

		0.00082	0.0011
	O	0.028	0.215
		0.0095	0.071
	H	s	p
		0.012	0.125
		0.004	0.042

Table 2. Relative Energies and Vertical Electron Detachment Energies of $(\text{LiOH}_2)^-$

Isomers

Structure	Description	Relative Energy ^a	VDE: BD-T1 ^b	VDE: $\Delta\text{CCSD(T)}$ ^b
H-(LiOH) $C_{\infty v}$	Anion-Molecule	0	3.00	2.97
$\text{LiOH}_2^- C_s$	Double Rydberg	1.12	0.55	0.54
$\text{Li}^-(\text{H}_2\text{O}) C_{2v}$	Anion-Molecule	1.43	0.89	0.86
Li^-			0.63	0.62

^aeV, CCSD(T)/aug-cc-pvqz single point + CCSD/6-311++(2df,2pd) + extra functions + zero-point corrections

^beV, aug-cc-pvqz basis

Table 3. Relative Energies and Vertical Electron Detachment Energies of $(\text{LiO}_2\text{H}_4)^-$

Isomers

Structure	Description	Relative Energy ^a	VDE: BD-T1b	VDE: $\Delta\text{CCSD(T)}$ ^b
1 H^- $(\text{LiOH})(\text{H}_2\text{O})$	Anion- Molecule	0	3.45	3.41
2 $\text{Li}(\text{OH}_2)_2^-$ C_2	Double Rydberg	1.26	0.53	0.55
3 LiOH_2^- (H_2O)	Anion- Molecule	1.59	0.50	0.52
4 LiOH_2^- (H_2O)	Anion- Molecule	1.62	0.70	0.72
5 $\text{Li}^-(\text{H}_2\text{O})_2$	Anion- Molecule	1.78	1.09	1.08

^a eV, CCSD(T)/aug-cc-pvqz single point + CCSD/6-311++(2df,2pd) + extra functions + zero-point corrections^b eV, aug-cc-pvqz basis

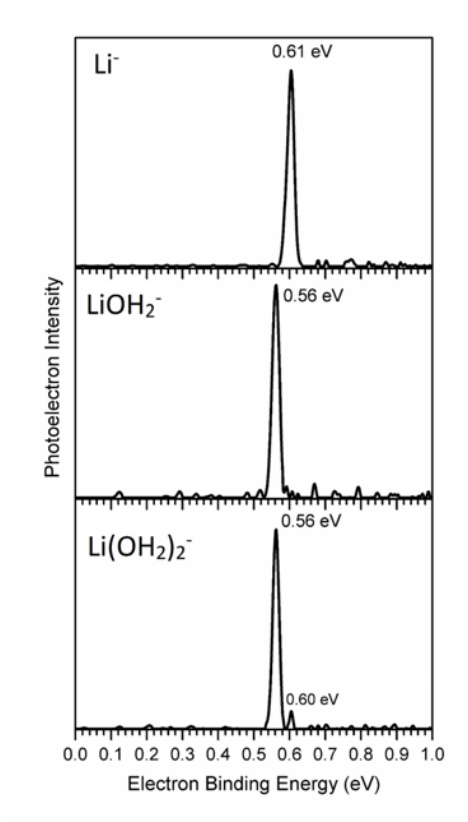


Figure 1. Photoelectron spectra of Li^- and $(\text{LiOH}_2)_{1,2}^-$ taken with 1064 nm photon

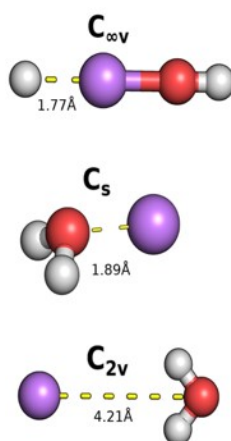


Figure 2. Structures of the three isomers of LiH_2O^- .

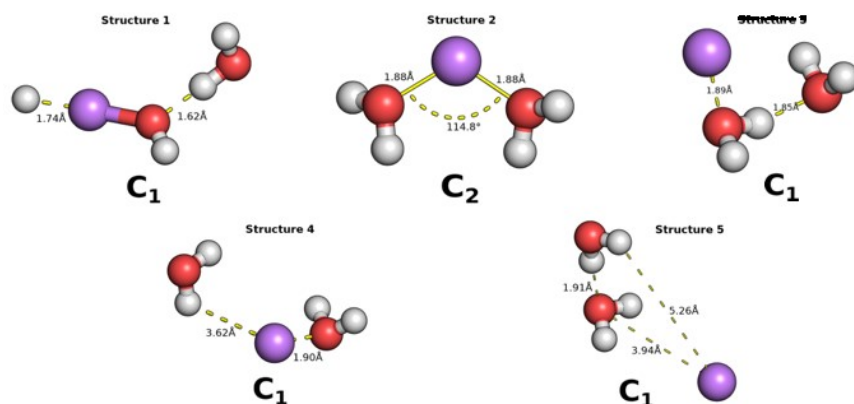


Figure 3. Structures of the five isomers of $\text{Li}(\text{OH}_2)_2^-$.

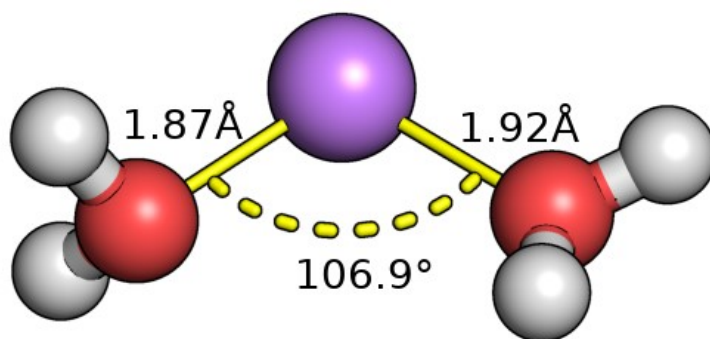


Figure 4. Optimized geometry of LiO_4H_2 after electron detachment from DRA $\text{Li}(\text{OH}_2)_2^-$.

References

1. J. Simons and M. Gutowski, *Chem. Rev.* **91**, 669 (1991).
2. J. V. Ortiz, *J. Phys. Chem.* **94**, 4762 (1990).
3. J. Melin, G. Seabra and J. V. Ortiz, Electronic Structure and Reactivity in Double Rydberg Anions: Characterization of a Novel Kind of Electron Pair, in *Theoretical Aspects of Chemical Reactivity*, Volume 19, 87-100, A. Toro-Labbé, Editor, Elsevier, Amsterdam, 2007.
4. J. T. Snodgrass, J. V. Coe, C. B. Freidhoff, K. M. McHugh, and K. H. Bowen, *Faraday Discuss. Chem. Soc.* **86**, 241 (1988).
5. J. V. Ortiz, *J. Chem. Phys.* **87**, 3557 (1987).
6. M. Gutowski and J. Simons, *J. Chem. Phys.* **93**, 3874 (1990).
7. S. -J. Xu, J. M. Nilles, J. H. Hendricks, S. A. Lyapustina, and K. H. Bowen, *J. Chem. Phys.* **117**, 5742 (2002).
8. D. Radisic, S. T. Stokes, and K. H. Bowen, *J. Chem. Phys.* **123**, 011101 (2005).

9. J. V. Ortiz, *J. Chem. Phys.* **117**, 5748 (2002).
10. H. Hopper, M. Lococo, O. Dolgounitcheva, V. G. Zakrzewski, and J. V. Ortiz, *J. Am. Chem. Soc.* **122**, 12813 (2000).
11. J. Melin and J. V. Ortiz, *J. Chem. Phys.* **127**, 014307 (2007).
12. J. V. Ortiz, *J. Chem. Phys.* **91**, 7024 (1989).
13. E. de Beer, E. H. Kim, D. M. Neumark, R. F. Gunion and W. C. Lineberger *J. Phys. Chem.* **99**, 13627 (1995).
14. B. W. Williams and R. F. Porter, *J. Chem. Phys.* **73**, 5598 (1980).
15. G. I. Gellene and R. F. Porter, *J. Chem. Phys.* **81**, 5570 (1984).
16. D. M. Hudgins and R. F. Porter, *Int. J. Mass. Spec.* **130**, 49 (1994).
17. W. J. Griffiths, F. M. Harris, and J. H. Beynon, *Inter. J. Mass Spec. Ion Proc.* **77**, 233 (1987).
18. R. E. March and A. B. Young, *Inter. J. Mass Spec. Ion Proc.* **85**, 237, (1988).
19. R. Takasu, T. Taguchi, K. Hashimoto, and K. Fuke, *Chem. Phys. Lett.* **290**, 481 (1998).
20. Z. Zeng, C. Liu, G. Hou, G. Feng, H. Xu, Y. Gao, and W. Zheng, *J. Phys. Chem. A* **119**, 2845 (2015).
21. A. Buytendyk, J. Graham, H. Wang, X. Zhang, E. Collins, Y. J. Ko, G. Gantefoer, B. Eichhorn, A. Regmi, K. Boggavarapu, K. H. Bowen, *Int. J. of Mass Spectrom.* **365-366**, 140 (2014).
22. A. T. J. B. Eppink, and D. H. Parker, *Rev. Sci. Instrum.* **68**, 3477 (1997).
23. R. Mabbs, E. Surber, and A. Sanov. *Analyst.* **128**, 765 (2003).
24. V. Dribinski, A. Ossadtchi, V. A. Mandelshtam, and H. Reisler, *Rev. Sci. Instrum.* **73**, 2634, (2002).
25. Gaussian Development Version, Revision I.09, M. J. Frisch, G. W. Trucks, H. B. Schlegel, G. E. Scuseria, M. A. Robb, J. R. Cheeseman, G. Scalmani, V. Barone, G. A. Petersson, H. Nakatsuji, X. Li, M. Caricato, A. Marenich, J. Bloino, B. G. Janesko, R. Gomperts, B. Mennucci, H. P. Hratchian, J. V. Ortiz, A. F. Izmaylov, J. L. Sonnenberg, D. Williams-Young, F. Ding, F. Lipparini, F. Egidi, J. Goings, B. Peng, A. Petrone, T. Henderson, D. Ranasinghe, V. G. Zakrzewski, J. Gao, N. Rega, G. Zheng, W. Liang, M. Hada, M. Ehara, K. Toyota, R. Fukuda, J. Hasegawa, M. Ishida, T. Nakajima, Y. Honda, O. Kitao, H. Nakai, T. Vreven, K. Throssell, J. A. Montgomery, Jr., J. E. Peralta, F. Ogliaro, M. Bearpark, J. J. Heyd, E. Brothers, K. N. Kudin, V. N. Staroverov, T. Keith, R. Kobayashi, J. Normand, K. Raghavachari, A. Rendell, J. C. Burant, S. S. Iyengar, J. Tomasi, M. Cossi, J. M. Millam, M. Klene, C. Adamo, R. Cammi, J. W. Ochterski, R. L. Martin, K. Morokuma, O. Farkas, J. B. Foresman, and D. J. Fox, Gaussian, Inc., Wallingford CT, 2016.
26. G. D. Purvis, and R. J. Bartlett, *J. Chem. Phys.* **76**, 1910 (1982).
27. R. Krishnan, J. S. Binkley, R. Seeger and J. A. Pople, *J. Chem. Phys.* **72**, 650 (1980).
28. T. Clark, J. Chandrasekhar, G. W. Spitznagel and P. v. R. Schleyer, *J. Comput. Chem.* **4**, 294 (1983).
29. M. J. Frisch, J. A. Pople and J. S. Binkley, *J. Chem. Phys.* **80**, 3265 (1984).
30. K. Raghavachari, G. W. Trucks, J. A. Pople, M. Head-Gordon, *Chem. Phys. Lett.* **157**, 479

- (1989).
31. R. A. Kendall, T. H. Dunning and R. J. Harrison, *J. Chem. Phys.* **96**, 6796 (1992).
 32. J. V. Ortiz, *J. Chem. Phys.* **109**, 5741 (1998).
 33. J. V. Ortiz, *Wiley Interdiscip. Rev.: Comput. Mol. Sci.* **3**, 123 (2013).
 34. A. N. Alexandrova, A. I. Boldyrev, X. Li, H. W. Sarkas, J. H. Hendricks, S. T. Arnold, and K. H. Bowen, *J. Chem. Phys.*, **134**, 044322 (2011).
 35. W. Zheng, X. Li, S. Eustis, A. Grubisic, O. Thomas, H. deClercq, and K. Bowen, *Chem. Phys. Lett.*, **444**, 232 (2007).
 36. C. Chi, H. Xie, Y. Li, R. Cong, M. Zhou, and Z. Tang, *J. Phys. Chem. A* **115**, 5380 (2011).
 37. G. J. Rathbone, T. Sanford, D. Andrews and W. Carl Lineberger, *Chem. Phys. Lett.* **401**, 570 (2005).
 38. T. Nagata, H. Yoshida and T. Kondow, *Z. Phys. D: At., Mol. Clusters* **26**, 367 (1993).
 39. G. Markovich, S. Pollack, R. Giniger, and O. Cheshnovsky, *J. Chem. Phys.* **101**, 9344 (1994).
 40. G. Markovitch, R. Giniger, M. Levin, and O. Cheshnovsky, *Z. Phys. D: At., Mol. Clusters* **20**, 69 (1991).
 41. G. Markovich, O. Cheshnovsky, and U. Kaldor, *J. Chem. Phys.* **99**, 6201(1993).
 42. D. W. Arnold, S. E. Bradforth, E. H. Kim, and D. M. Neumark, *J. Chem. Phys.* **102**, 3510 (1995).
 43. D. W. Arnold, S. E. Bradforth, E. H. Kim, and D. M. Neumark, *J. Chem. Phys.* **97**, 9468 (1992).
 44. D. W. Arnold, S. E. Bradforth, E. H. Kim, and D. M. Neumark, *J. Chem. Phys.* **102**, 3493 (1995).
 45. V. G. Solomonik, V. V. Sliznev and T. P. Pogrebnaya, *J. Struct. Chem.* **29**, 675 (1989).
 46. D. Wang, J. D. Graham, A. M. Buytendyk, and K. H. Bowen *J. Chem. Phys.* **135**, 164308 (2011).
 47. S. Zein and J. V. Ortiz, *J. Chem. Phys.* **135**, 164307 (2011).
 48. H. Zhang and Z. Liu, *J. Chem. Phys.* **136**, 124314 (2012).
 49. R. Takasu, F. Misaizu, K. Hashimoto, and K. Fuke, *J. Phys. Chem. A* **101**, 3078 (1997).
 50. N. M. Klimenko, S. S. Kramarenko and O. P. Charkin, *Russ. J. Coord. Chem.* **10**, 325 (1984).

VI.5 On the Existence of Triple Rydberg Anions

Gaoxiang Liu, Evan Collins, Sandra M. Ciborowski, J. Vincent Ortiz, Evangelos Miliordos, and Kit H. Bowen

Similar to the double-Rydberg anion, the triple Rydberg anions are characterized by three electrons delocalized in a diffuse orbital surrounding a stable, closed-shell doubly charged cationic core. With three electrons described by extra-valence orbitals, triple Rydberg anions are expected to exhibit a novel pattern of electronic structure. The concept of triple Rydberg anions is hereby demonstrated by $\text{Mg}(\text{NH}_3)_{4,5,6}^-$ anions. The molecular framework of these anions is the doubly positively charged Mg^{2+} ligated by 4, 5, or 6 NH_3 molecules, that is, $\text{Mg}(\text{NH}_3)_{4,5,6}^{2+}$. Their lowest unoccupied molecular orbitals are atom-like Rydberg orbitals. Therefore, $\text{Mg}(\text{NH}_3)_{4,5,6}^{2+}$ can be viewed as a superatom or united atom. Adding three electrons to the superatomic Rydberg orbitals makes the triple Rydberg anions, $\text{Mg}(\text{NH}_3)_{4,5,6}^-$.

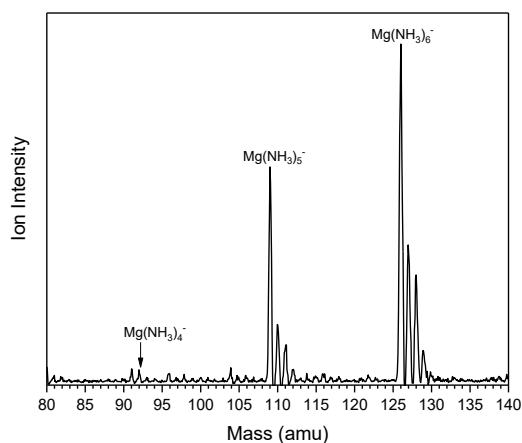


Figure 1. Mass spectrum of $\text{Mg}(\text{NH}_3)_{4,5,6}^-$

Figure 1 presents the mass spectrum of $\text{Mg}(\text{NH}_3)_{4,5,6}^-$ made by laser-vaporization source. High-intensity signals of $\text{Mg}(\text{NH}_3)_5^-$ and $\text{Mg}(\text{NH}_3)_6^-$ were observed. The $\text{Mg}(\text{NH}_3)_4^-$ signal was weaker. The isotopic patterns deviate from the theoretical patterns a little bit. This observation suggests some other anions may exist at 1 amu higher than the $\text{Mg}(\text{NH}_3)_{4,5,6}^-$.

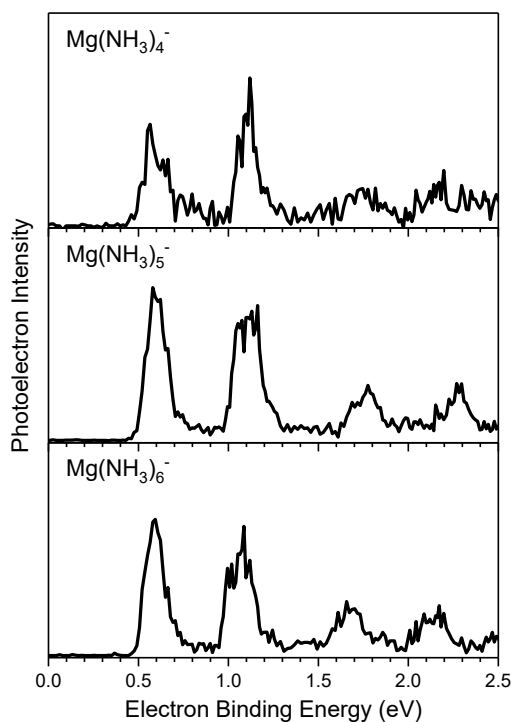


Figure 2. Photoelectron spectra of $\text{Mg}(\text{NH}_3)_{4,5,6}^-$.

Figure 2 presents the photoelectron spectra of $\text{Mg}(\text{NH}_3)_{4,5,6}^-$. The spectra of $\text{Mg}(\text{NH}_3)_{4,5,6}^-$ show characteristic features of a triple Rydberg anion: (1) The first vertical detachment energy is 0.58 eV, which is close to a double Rydberg anion; (2)

The spectral features of $\text{Mg}(\text{NH}_3)_{4,5,6}^-$ are almost irrelevant to the number of NH_3 ligation. Such a phenomenon has been observed in double Rydberg anions.

Table 1. Electron binding energies of $\text{Mg}(\text{NH}_3)_{4,5,6}^-$.

	EBE ₁	EBE ₂	EBE ₃	EBE ₄
$\text{Mg}(\text{NH}_3)_4^-$	0.56	1.12	1.73	2.20
$\text{Mg}(\text{NH}_3)_5^-$	0.58	1.11	1.78	2.26
$\text{Mg}(\text{NH}_3)_6^-$	0.58	1.09	1.70	2.17

Vincent Ortiz and Evangelos Miliordos just notified us (08/2019) that with an updated theoretical approach, they were able to predict a triple Rydberg $\text{Mg}(\text{NH}_3)_4^-$ structure with vertical detachment energies that agree well with experimental results.

VI.6 Superatomic Clusters with Four Diffuse Rydberg Electrons

Gaoxiang Liu, Isuru R. Ariyaratna, Zhaoguo Zhu, Mary Marshall, Sandra M. Ciborowski, Evangelos Miliordos, and Kit H. Bowen

In this study, we went one step further than the triple Rydberg anion. Here we devised and prepared $\text{La}(\text{NH}_3)_{5,6}^-$, which possesses a $[\text{La}(\text{NH}_3)_5]^{3+}$ core and four diffuse Rydberg electrons. This is an extraordinary piece of work because the ability of this superatomic cluster to hold up to four diffuse valence electrons can open doors to designing electronic devices with unique properties.

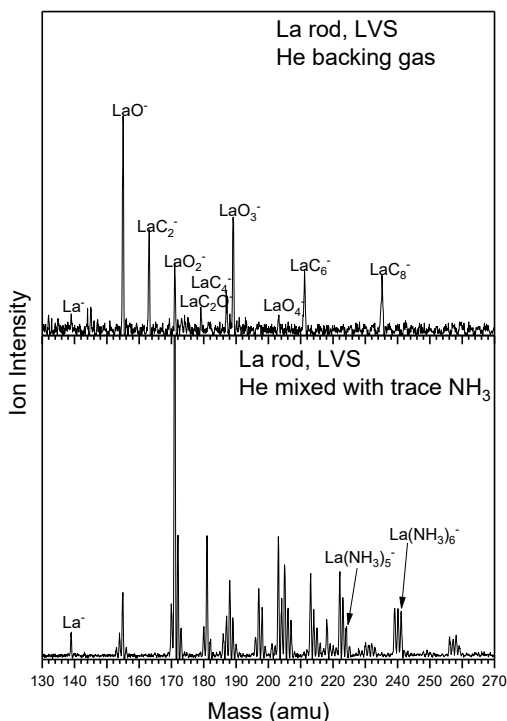


Figure 1. The mass spectra of La products made by laser vaporization source

With only helium as the backing gas, La^- , LaO_x^- , and LaC_x^- were observed. After adding NH_3 , the mass spectrum changed significantly. $\text{La}(\text{NH}_3)_{5,6}^-$ were observed in the mass spectrum. It seems that $\text{La}(\text{NH}_3)_n^-$ always come with dissociation products such as $\text{La}(\text{NH}_2)(\text{NH}_3)_{n-1}^-$ and $\text{La}(\text{NH})(\text{NH}_3)_{n-1}^-$ ($n = 5$ and 6).

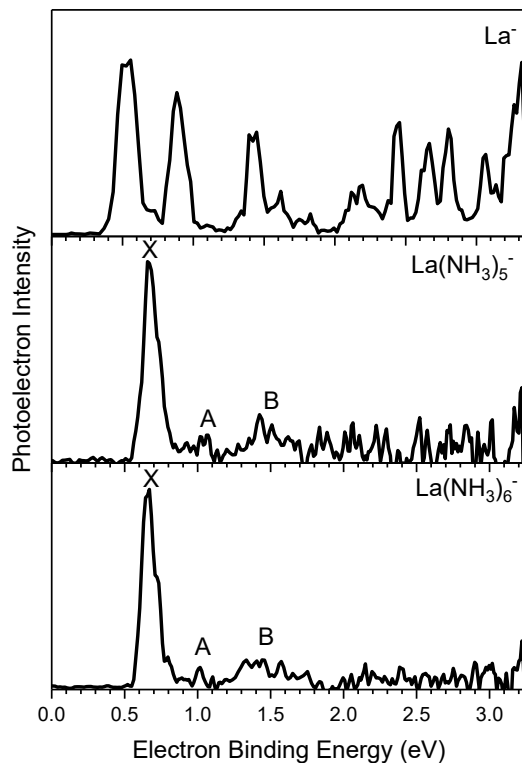


Figure 2. Photoelectron spectra of La^- , $\text{La}(\text{NH}_3)_5^-$, and $\text{La}(\text{NH}_3)_6^-$.

The photoelectron spectra of $\text{La}(\text{NH}_3)_5^-$ and $\text{La}(\text{NH}_3)_6^-$ are fundamentally different from that of La^- , suggesting changes of the electronic structure due to the addition of NH_3 . This confirms that the interaction between La^- and NH_3 is chemical rather than physisorbed. The spectra of $\text{La}(\text{NH}_3)_5^-$ and $\text{La}(\text{NH}_3)_6^-$ are essentially identical to each other. They both show a strong and sharp feature around 0.65 eV, characteristic of

Rydberg anions. The transitions at higher electron binding energy are due to the photodetachment from deeper Rydberg orbitals.

Quantum chemistry calculations confirmed that the global minimum structures for $\text{La}(\text{NH}_3)_5^-$ and $\text{La}(\text{NH}_3)_6^-$ have all their NH_3 ligated to La, forming a superatomic structure. The calculated vertical detachment energies are in good agreement with the experiment. The superatomic electronic configuration of $\text{La}(\text{NH}_3)_5^-$ is $1s^2 1p^1 1p^1$ or $(24a')^2 (25a')^1 (16a'')^1$, which is a triplet. The superatomic electronic configuration of $\text{La}(\text{NH}_3)_6^-$ is $1s^2 1p^1 1p^1$ or $(15a_g)^2 (9a_u)^1 (14b_u)^1$, which is also a triplet.

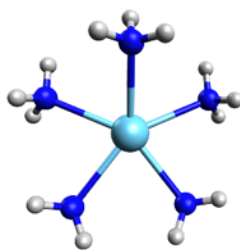


Figure 3. Optimized lowest energy structure of $\text{La}(\text{NH}_3)_5^-$.

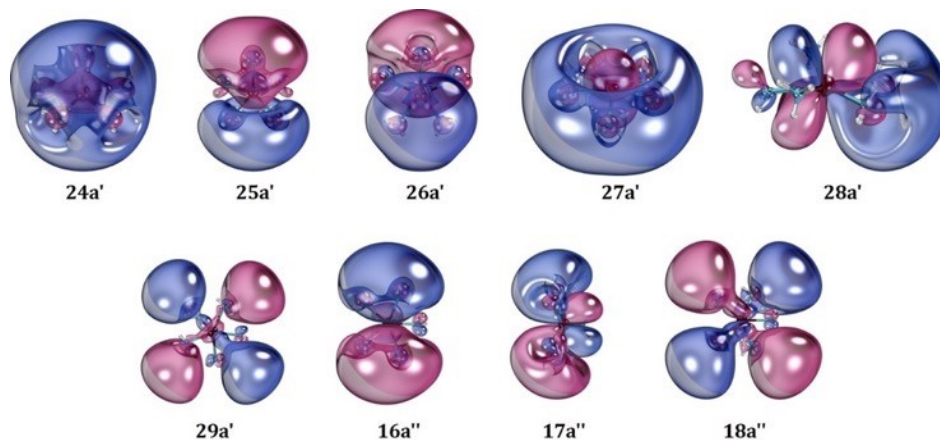


Figure 4. Selected molecular orbitals of $\text{La}(\text{NH}_3)_5^-$

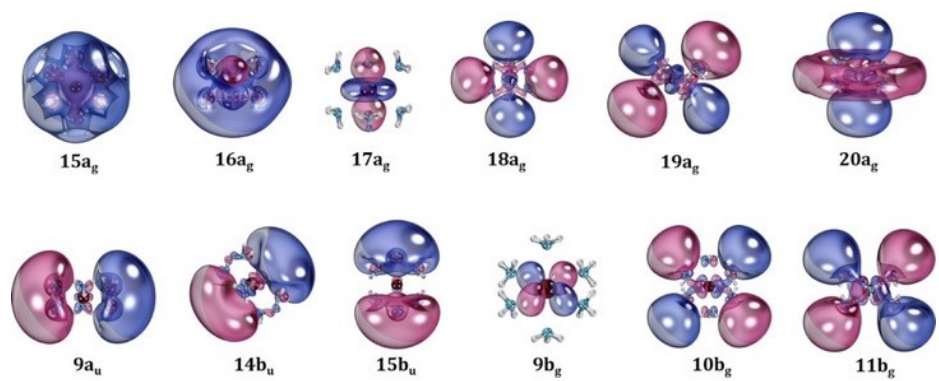


Figure 5. Selected molecular orbitals of the $\text{La}(\text{NH}_3)_6^-$

VI.7 Direct Mapping of the Electronic Structures of Hexavalent Uranium Complex

Gaoxiang Liu, Sandra M. Ciborowski, Lan Cheng, and Kit H. Bowen

Hexavalent uranium, U(VI), is one of the most ubiquitous forms of uranium, manifested by the prevalence of uranyl compounds, UO_2^{2+} . The electronic structure of U(VI) compound has been of considerable research interest. In particular, in U(VI) compounds all six valence electrons of uranium are involved in chemical bonds, making U(VI) compounds closed shell. This offers an ideal playground for theorists to develop and test their theoretical methods on heavy metals without facing the tremendous challenge of dealing unpaired electrons at the same time. Many theoretical studies have been published on the electronic structures of U(VI) complexes, but there is substantial disagreement among different theories. An experimental benchmark, on the other hand, is still absent. Solution and solid phase absorption spectroscopy results are inevitably interfered by environmental effects, which add another dimension of complexity. Gas-phase studies on isolated U(VI) compounds are expected to provide the ideal benchmark for theory. However, gas-phase studies so far have only covered either compounds where uranium is in other oxidation states or ligated U(VI) complexes. The former is not of particular interest, and the photoelectron spectra of the latter mostly reflect the ligand orbitals rather than

the electronic structure of the U(VI) core. A direct mapping of the isolated U(VI) complex is highly demanded to resolve the debate in theory.

In this study, we prepared uranium dinitride anion, UN_2^- , via the reaction between laser vaporized uranium and nitrogen gas and measured its photoelectron spectrum. The spectrum of UN_2^- anion is the direct mapping of the electronic structure of UN_2 neutral at the anion's geometry. Coupled with state-of-the-art electronic structure calculations, we are able to interpret the electronic structure of this U(VI) compound and validate the theoretical approach.

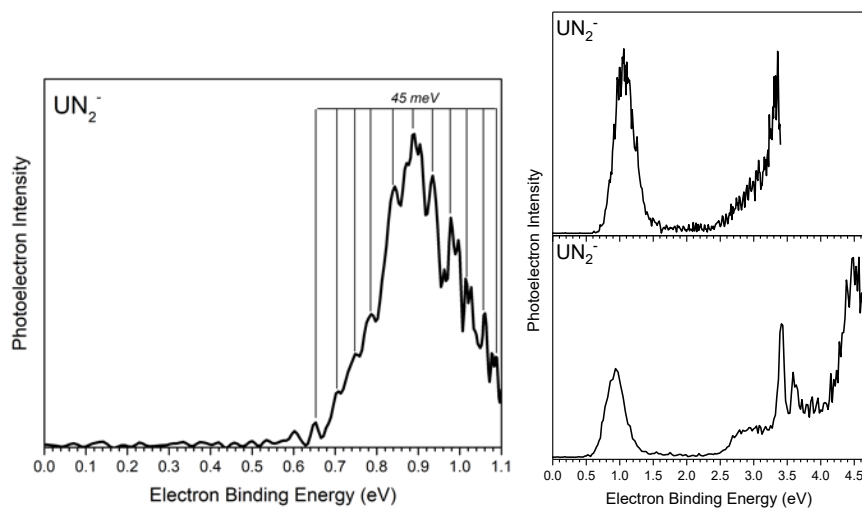


Figure 1. Photoelectron spectra of UN_2^- taken with 1.165, 3.495, and 4.660 eV photons.

Figure 1 presents the photoelectron spectra of UN_2^- taken with lasers of different photon energies. The 1064 nm spectrum shows a vertical detachment energy of 0.89

eV and a vibrational progression with a spacing of 45 meV. The spacing corresponds to a UN₂ vibrational mode. The 4th harmonic spectrum shows a number of features corresponding to photodetachment transitions to excited states of neutral UN₂, that is, a reflection of neutral UN₂ electronic structure. The feature from 2.5 to 3.3 eV is broad and less intense, suggestive of many weak transitions. The features at 3.4 and 3.6 eV are strong and sharp, indicating that these transitions have high cross-sections, and the final electronically-excited states of neutral UN₂ have similar structures to the UN₂ anion.

Prof. Lan Cheng has done very advanced, state-of-the-art electronic structure calculations on this project. So far, an excellent agreement between theory and experiment has been reached. According to Prof. Cheng, the calculations have converged to a level that is less than the experimental resolution, though some improvement in convergence is still needed.

VI.8 CO₂ Hydrogenation to Formate and Formic Acid by Bimetallic Palladium-Copper Hydride Clusters

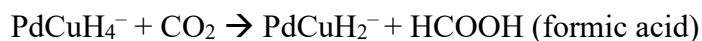
Gaoxiang Liu, Patricia Poths, Zhaoguo Zhu, Mary Marshall, Xinxing Zhang, Anastassia Alexandrova, and Kit H. Bowen

Transforming carbon dioxide into reduced, higher value molecules is of great interest for both environmental and economic reasons. For catalytic CO₂ functionalization, bimetallic catalysts have shown improved activity and selectivity over single-component ones, because lattice engineering is readily utilized to tailor the surface and electronic structures of bimetallic catalysts which regulate their performance. The rational design of high-efficiency bimetallic catalysts demands a mechanistic understanding on how the catalytic CO₂ transformation processes on the active sites. While it is well-established that the formation of metal hydrides and the insertion of CO₂ into the metal-hydride bond are the critical steps in CO₂ hydrogenation, a comprehensive knowledge about them is still limited due to a lack of direct experimental characterization on these key reaction intermediates. In particular, it is less clear how the interplay between different metals can alter catalyst properties such as hydrogen and CO₂ binding sites, electronic structures, charge transfer property, and release of products that determine, which determine the catalytic performance.

Benefited from the synergy between experimental characterization of reaction intermediates and state-of-the-art quantum chemistry calculations, the gas-phase studies of CO₂ reduction and hydrogenation have provided mechanistic insight into CO₂ functionalization at the molecular level. While hydrides of single metal (for example, Cp₂TiH⁺, PtH₃⁻, FeH⁻, and Cu_{1,2}H₂⁻) can convert CO₂ to form formate or formate complexes, we are not aware of utilizing bimetallic hydrides as the model system to study CO₂ hydrogenation on bimetallic catalysts. The present work focuses on the hydrogenation of CO₂ via reaction with the anionic bimetallic palladium-copper tetra-hydride cluster, PdCuH₄⁻. We selected the hydride of palladium-copper because various bimetallic palladium-copper catalysts have been recently reported to show enhanced CO₂ hydrogenation activity when compared to the single-component palladium or copper catalysts, and the reactions between their hydride and CO₂ serve as the ideal model to understand the hydrogenation process. The different hydrogen-binding patterns in PdCuH₄⁻ clusters render their reactions with CO₂ follow distinct mechanisms to produce formate and formic acid, respectively.

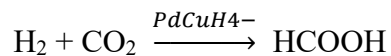
PdCuH₄⁻ was prepared in a pulsed arc cluster ionization source. Briefly, a ~30 us duration, high voltage and current discharge was applied to vaporize Pd and Cu powders. Almost simultaneously, high-pressure hydrogen gas was injected into the discharge region. The resulting mixture of atoms, ions, and electrons reacted to form

PdCuH₄⁻. The hydrogen gas carried the nascent PdCuH₄⁻ downstream to the reaction cell to interact with CO₂. The resultant anionic products were identified by time-of-flight mass spectrometry. Figure 1 presents mass spectra with or without introducing CO₂. With no CO₂ in the reaction cell, we observed the mass series of PdCuH₄⁻, and its match with the simulated isotopic pattern suggests PdCuH₄⁻ the only palladium-copper hydride formed under our experimental conditions. When CO₂ was added to the reaction cell, prominent mass series appeared at masses higher and lower than PdCuH₄⁻. The higher-mass series is the reaction intermediate PdCuCO₂H₄⁻, and the lower-mass peaks are formate- and formic acid-containing anionic clusters. The tagging of neutral formic acid to anionic formate makes its observation possible by mass spectrometry. The strong summed intensities of formate and formic acid products show that PdCuH₄⁻ hydrogenates CO₂ efficiently. Note that the observation of formic acid suggests the reaction



yet PdCuH₂⁻ or other palladium-copper hydrides were absent after PdCuH₄⁻ reacted with CO₂. This implies regeneration of PdCuH₄⁻ via H₂ addition to PdCuH₂⁻.

Therefore, we tentatively concluded that the catalytic reaction



occurred under our experimental conditions.

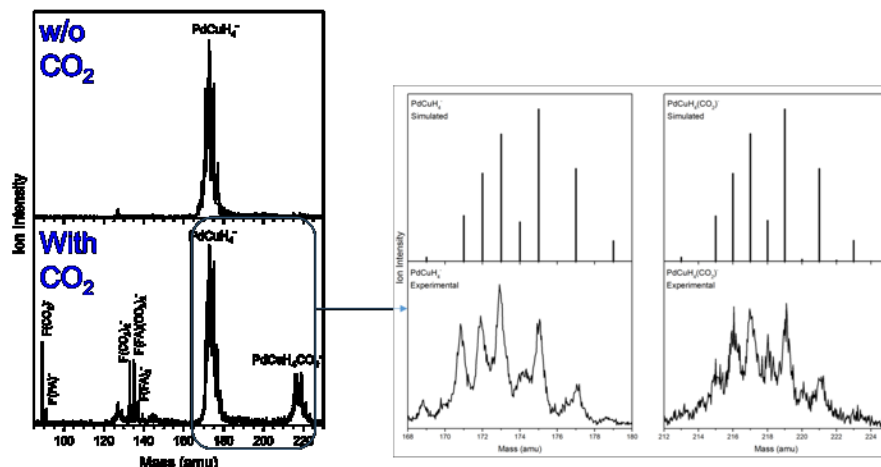


Figure 1. The mass spectra of PdCuH_4^- cluster anions A) without and B) with CO_2 injection into the cell.

We then applied anion photoelectron spectroscopy to characterize PdCuH_4^- and $\text{PdCuCO}_2\text{H}_4^-$. The photoelectron spectra were taken at every isotopic peak for each mass series to make sure that each series contains only PdCuH_4^- or $\text{PdCuCO}_2\text{H}_4^-$ (Figure 1 and S1). For PdCuH_4^- , two electron binding energy (EBE) peaks at 3.35 and 3.83 eV are assigned as the vertical detachment energies (VDE). For $\text{PdCuCO}_2\text{H}_4^-$, its VDE values are 2.50, 4.09, and 4.47 eV.

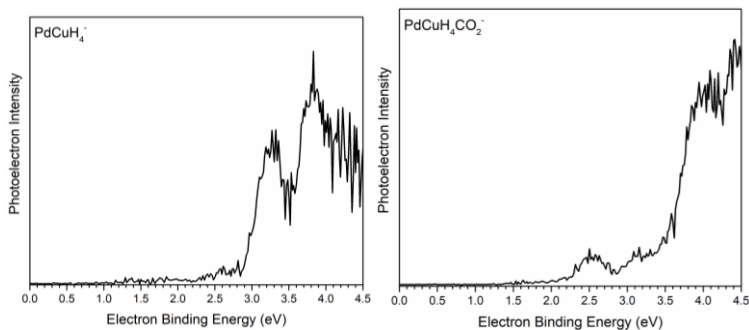


Figure 2. Photoelectron spectra of (A) PdCuH_4^- and (B) $\text{PdCuCO}_2\text{H}_4^-$, both measured

with 266 nm (4.66 eV) photons.

Geometry optimization of the PdCuH_4^- cluster yielded two similar lowest energy structures. The global minimum (GM) structure is shown in Fig. X (a), consisting of one H_2 η^2 coordinated to the Pd atom, one μ_2 bridging H atom, and one H bound to Cu. The second lowest energy isomer, which will be referred to as the local minimum 1, or LM1, seen in Fig. X (b) is 0.51 eV higher in energy than the GM, and is structurally very similar to the GM. The main difference is that one of the η^2 H atoms has migrated to form a second μ_2 H between Pd and Cu. Table 1 lists the calculated VDEs for all structures presented, and their corresponding experimental peaks. The GM has a calculated VDE of 3.98 eV, while LM1 has a calculated VDE of 3.61 eV. These correspond to the 3.8 eV and 3.3 eV peaks in the experimental PES, indicating that a mixture of ions was present.

Next, CO_2 binding to the clusters was investigated. CO_2 was placed in close proximity to the GM and LM structures and structural optimization was performed. Figure X (c) shows the GM structure for the cluster- CO_2 structure, while (d) shows the second lowest energy isomer. Note that these structures do not contain CO_2 bound to PdCuH_4^- , but rather HCOO^- bound to PdCuH_3 . CO_2 is not present in the low energy isomers, as lone H atoms prefer to migrate to carbon from either Pd or Cu in a barrierless process. Figure X (c) shows the result of the addition of CO_2 on Cu to the GM, while (d) shows

the addition on CO₂ on Pd to LM1. The calculated VDE for (c) is 4.63 eV, corresponding to the 4.4 eV peak in the experimental PES, however the VDE for (d) at 5.64 eV is out of range of the experimental data. This structure is included, however, as structures which result from it are present in the PES. The first of these resulting structures is seen in Figure X (e). It is similar to that of (d), however one bridging H atoms has migrated to an oxygen atom, producing PdCuH₂⁻(HCOOH). This structure has a VDE of 3.94 eV, which corresponds to the 4.1 eV peak in the PES. So far this has accounted for all but one of the peaks on the PdCuH₄⁻•CO₂ PES. The final peak at 2.5 eV is accounted for by the structure of PdCuH₂⁻ seen in Figure X (f), with a calculated VDE of 2.51 eV. This is the structure that would form upon the removal of HCOOH from (e).

Two potential energy profiles for PdCuH₄⁻ + CO₂ forming formic acid are shown in Figure Z. Path A links the global minimum PdCuH₄⁻ and PdCuH₄⁻•CO₂ structures, ending with the dissociation of HCOO⁻ from PdCuH₃. This is a plausible pathway, as the reactant and intermediate are both present in their respective PES, and the VDE of HCOO⁻, at 3.82 eV, could be responsible for the 4.1 eV peak. However, the energy difference between the intermediate and the product, at 2.49 eV, is too high for this to be the main path.

Path B is the alternative with a more reasonable energy profile. Despite starting from a 0.51 eV higher energy isomer, it proceeds to the LM1 CO₂-cluster structure, 0.91 eV lower. The step to the second intermediate is 0.52 eV uphill, followed by another 1.00 eV step up to reach PdCuH₂⁻ + HCOOH. While these are generally fairly large steps, the species are in a fast-moving ion beam in a collision chamber with an excess of fast-moving H₂ molecules, so endothermic steps of ~1eV are just within reason. The presence of peaks attributable to PdCuH₂⁻(HCOOH) and PdCuH₂⁻ in the PES further supports this as the pathway of choice, emphasizing the importance of accounting for low-lying isomers for catalytic behavior, a topic of growing importance^[18-21]. PdCuH₄⁻ would then be regenerated in the presence of excess H₂, as PdCuH₄⁻ is 0.43 (LM) or 0.94 (GM) eV lower in energy than PdCuH₂⁻ + H₂.

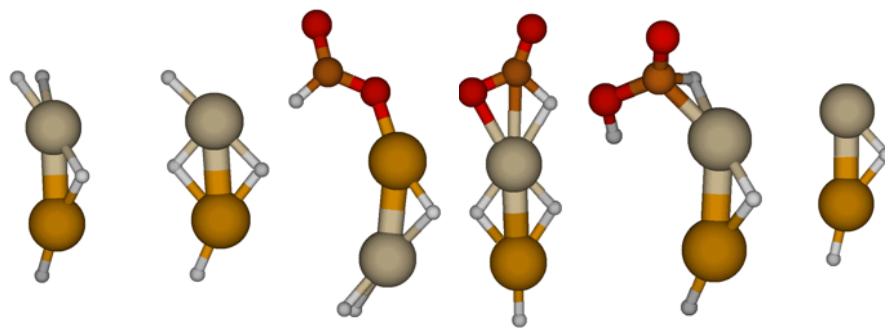


Figure 3. the global minimum (a) and second lowest energy (b) PdCuH₄⁻ clusters calculated. (c) shows the global minimum structure for the cluster-CO₂ structure. (d) is the second lowest CO₂-cluster isomer, which is 0.98 eV higher in energy than the GM. (e) is an HCOOH solvated structure, which is another intermediate in the formic acid formation process. (f) is the PdCuH₂⁻ structure which would form after the

formic acid leaves the cluster.

VI.9 CO₂ Hydrogenation to Formate by Palladium Hydride Clusters

Gaoxiang Liu, Zhaoguo Zhu, Mary Marshall, and Kit H. Bowen

Palladium is a natural hydrogen absorber: each unit volume of palladium can absorb up to 900 unit volume of hydrogen gas. The absorbed hydrogen exists in the form of palladium hydrides, PdH_x. In this work, we studied CO₂ hydrogenation by PdH⁻ in the gas phase. This can shed light on applying this metal hydrogen “sponge” to convert CO₂ into value-added products.

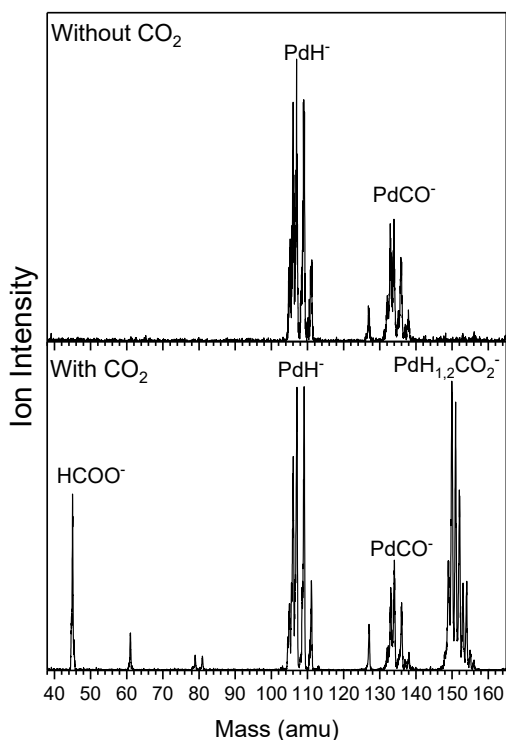


Figure 1. Mass spectra of PdH_x⁻ with or without the addition of CO₂.

Without the addition of CO_2 , PdH^- was made. After adding CO_2 , the adduct $\text{PdH}(\text{CO}_2)^-$ and the reaction product HCOO^- were observed. PdCO^- should be due to carbon and oxygen absorbed on Pd powder.

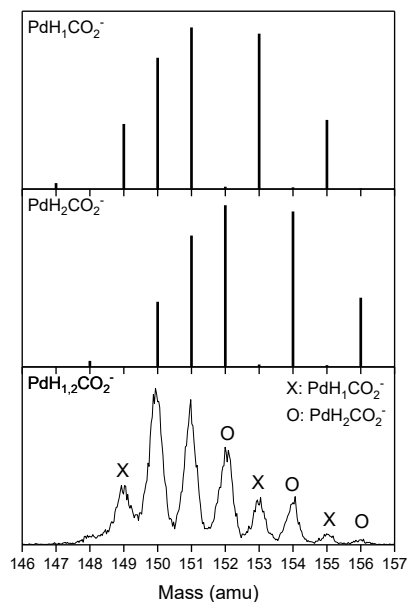


Figure 2. Simulated and experimental mass spectra of the reaction products.

With a zoomed-in analysis of the adduct mass region, we identified $\text{PdH}_1\text{CO}_2^-$ and $\text{PdH}_2\text{CO}_2^-$.

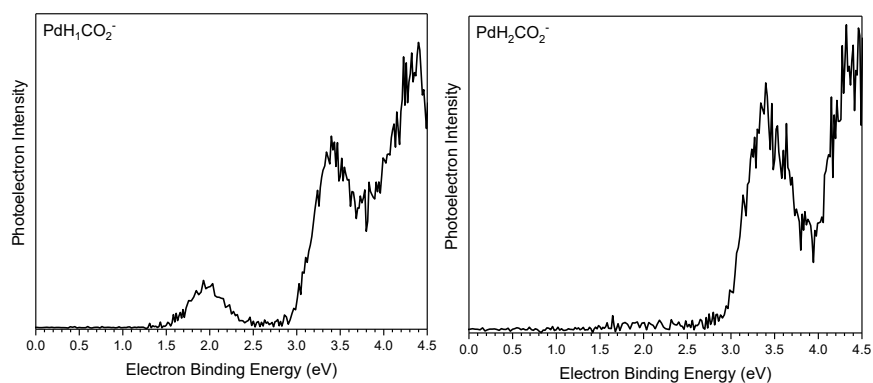


Figure 3. Photoelectron spectra of $\text{PdH}_{1,2}\text{CO}_2^-$.

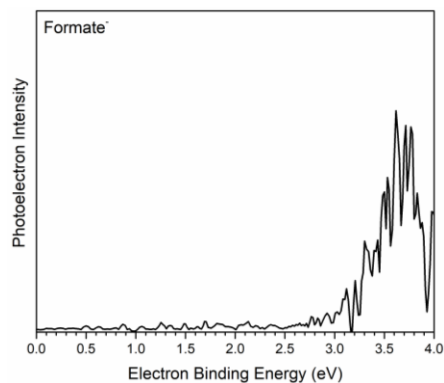


Figure 4. Photoelectron spectrum of formate.

Calculations have shown that the PdHCO_2^- can be a mixture of $\text{Pd}(\text{HCOO}^-)$, i.e., formate adduct, and $\text{HPd}(\text{CO}_2^-)$, i.e., CO_2 chemisorbed to HPd^- . The identify of formate product is verified by photoelectron spectroscopy.

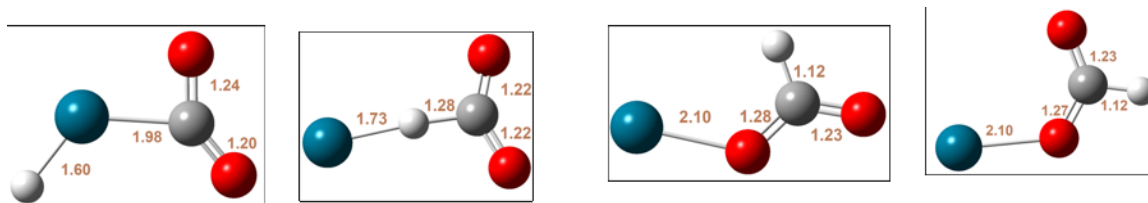


Figure 5. Calculated structures of PdHCO_2^- .

Table 1. Calculated relative energy and vertical detachment energies of PdHCO_2^- .

	Iso 1	Iso 2	Iso 3	Iso 4
E_{rel}	0 eV	1.20 eV	0.83 eV	0.84 eV
VDE B3lyp/def2-QZVP	3.50 eV	N/A	2.37 eV	2.10 eV
VDE CCSD(T)	3.20 eV	N/A	2.44 eV	2.14 eV

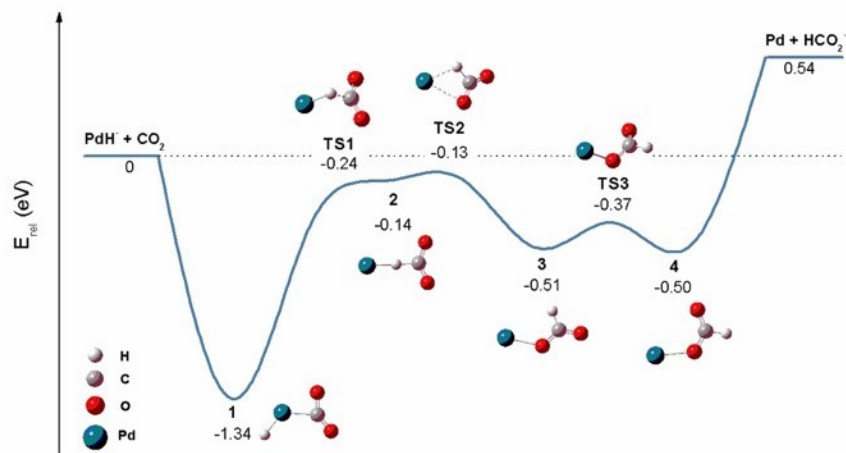


Figure 6. Calculated reaction pathway for $\text{PdH}^- + \text{CO}_2$.

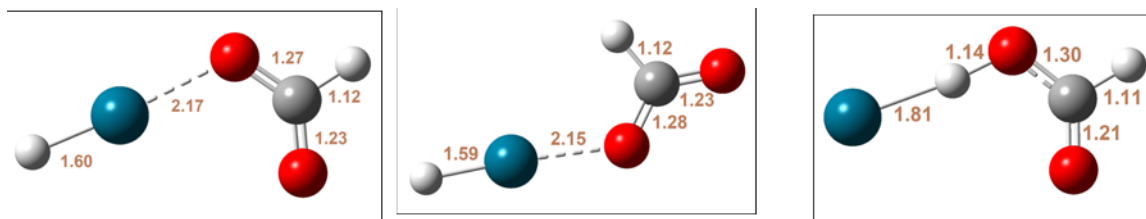


Figure 7. Calculated structures of $\text{PdH}_2\text{CO}_2^-$.

Table 2. Calculated relative energy and vertical detachment energies of PdHCO_2^- .

	Iso 1	Iso 2	Iso 3
E_{rel} (eV)	0	0.03	1.34
VDE (eV)	3.32	3.69	1.29
VDE + excitation energies (eV)	4.33 4.34 4.48 4.63	4.68 4.72	2.672 2.673 2.89 2.90 3.03 3.17

VI.10 Tertiary Systems: Tandem Molecular Activation by Single Atomic Anions

In previous studies, we have demonstrated that single platinum atomic anions can activate small molecules, including H_2O , CO_2 , and CH_4 . In the cases of H_2O and CH_4 activation, we observed activation products containing hydride, hydroxyl group, or methyl group. These complexes can be utilized to further activate other small molecules for purposes such as CO_2 hydrogenation, C-C coupling, and more.

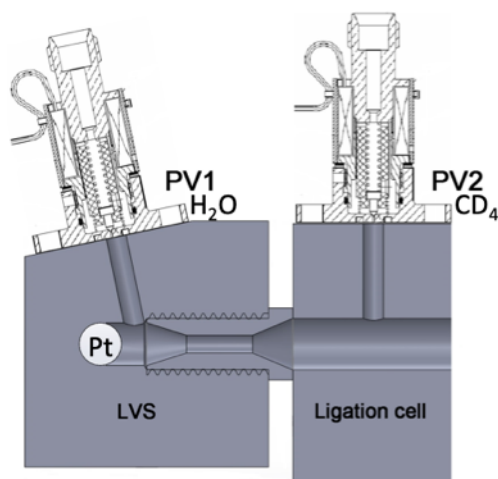


Figure 1. Source setup for tandem H_2O and methane activation by platinum anions

Tandem Activation of Water and Methane by Single Platinum Atomic Anions

Gaoxiang Liu, Isuru Ariyaratna, Sandra M. Ciborowski, Evangelos Miliordos, and

Kit H. Bowen

In this study, we integrated our previous results on methane and water activation by single platinum atomic anions, aiming to convert methane to methanol.

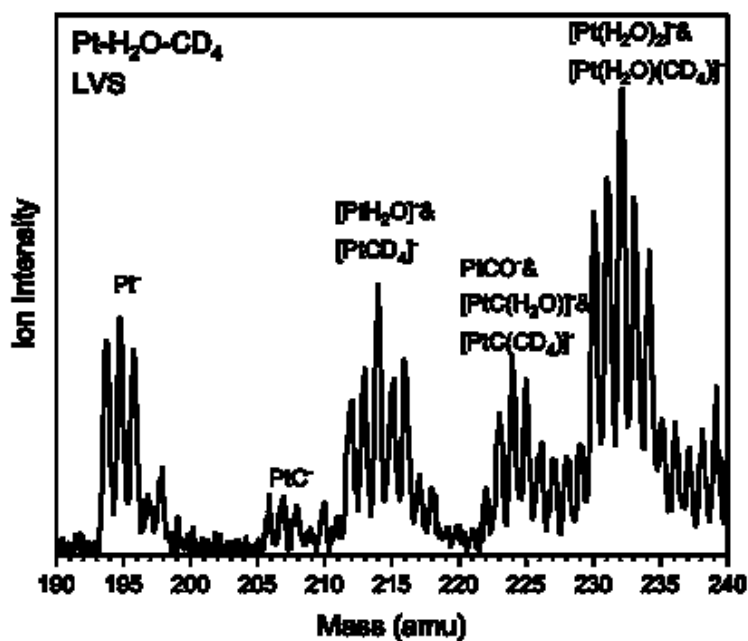


Figure 1. Mass spectrum of the tertiary reactions between Pt^- , H_2O , and deuterated methane CD_4 .

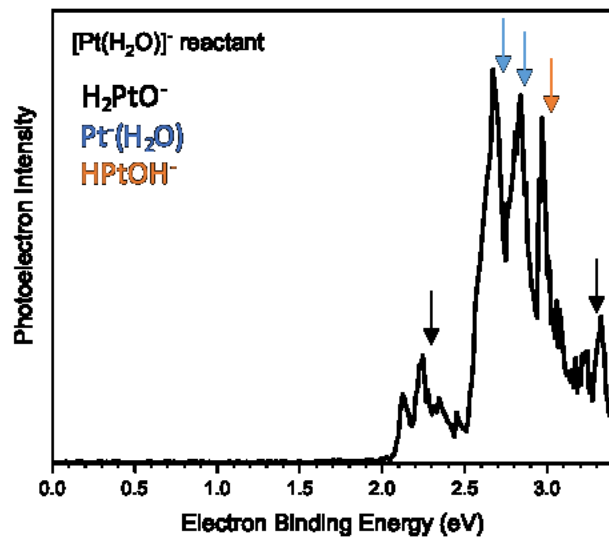


Figure 2. The photoelectron spectrum of the $[\text{Pt}(\text{H}_2\text{O})]^-$ complex which was used to react with methane. The spectrum suggests three forms of $[\text{Pt}(\text{H}_2\text{O})]^-$, $\text{Pt}^-(\text{H}_2\text{O})$, HPtOH^- , and H_2PtO^- , coexisted.

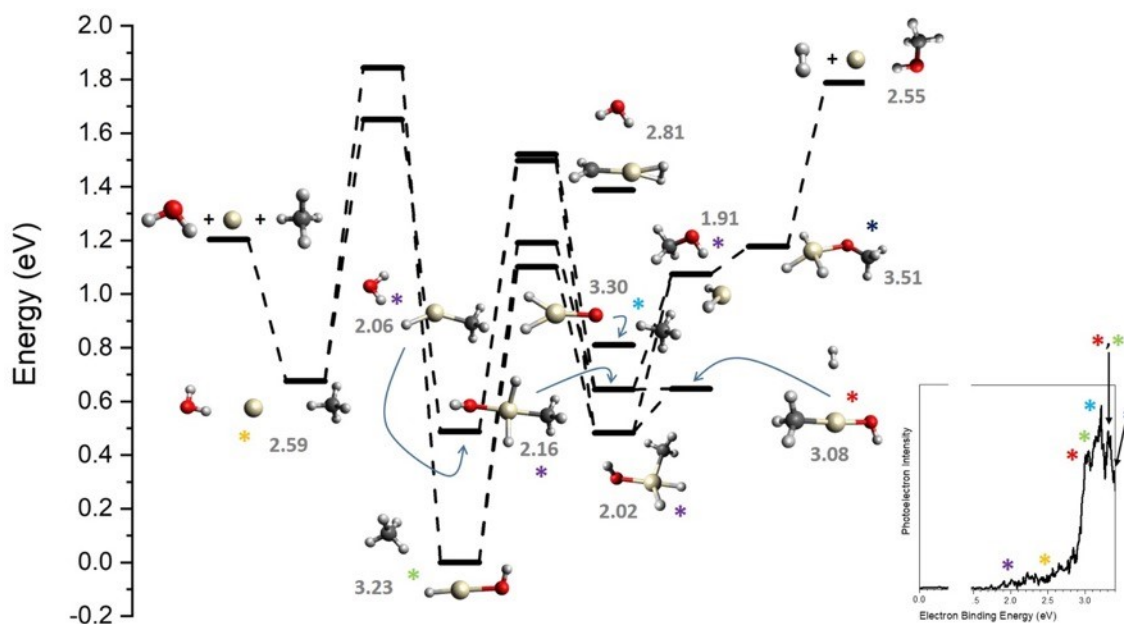


Figure 3. Calculated reaction pathway for $\text{Pt}^--\text{H}_2\text{O}-\text{CH}_4$. The inset is the photoelectron spectrum of $[\text{Pt}(\text{H}_2\text{O})(\text{CD}_4)]^-$.

CO₂ Activation and Hydrogenation by Platinum Activated Methane

Gaoxiang Liu, Isuru Ariyaratna, Sandra M. Ciborowski, Zhaoguo Zhu, Evangelos Miliordos, and Kit H. Bowen

The co-conversion of methane and carbon dioxide to value-added chemicals represents an important subject in C1-chemistry of both energy and environmental interests, but it is very challenging due to the inherent stability of both CH₄ and CO₂. Dry reforming of methane (DRM) with CO₂ has been developed for generation of syngas (CO + H₂) that can be converted to desired products by either alcohols synthesis or Fischer-Tropsch processes. However, such indirect route is highly energy intensive. The design of catalysts that can achieve the direct co-conversion of CH₄ and CO₂ thus becomes appealing driven by the economical consideration.

In this study we took the advantage of our previous success in methane and CO₂ activation by atomic platinum anions, and CO₂ hydrogenation by platinum hydrides, and for the first time accomplished the direct conversion of methane with carbon dioxide mediated by single atomic anions.

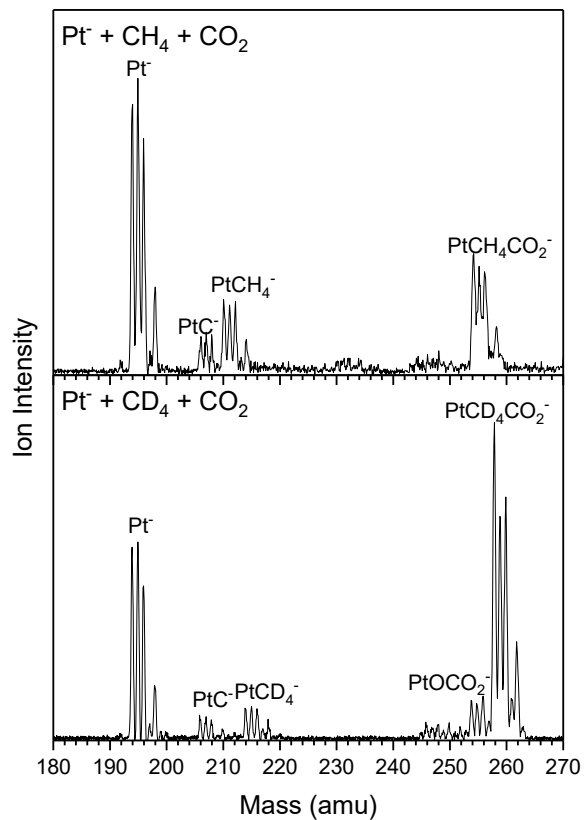


Figure 1. Mass spectra of the $\text{Pt}^- + \text{CH}_4 + \text{CO}_2$ and $\text{Pt}^- + \text{CD}_4 + \text{CO}_2$ reactions.

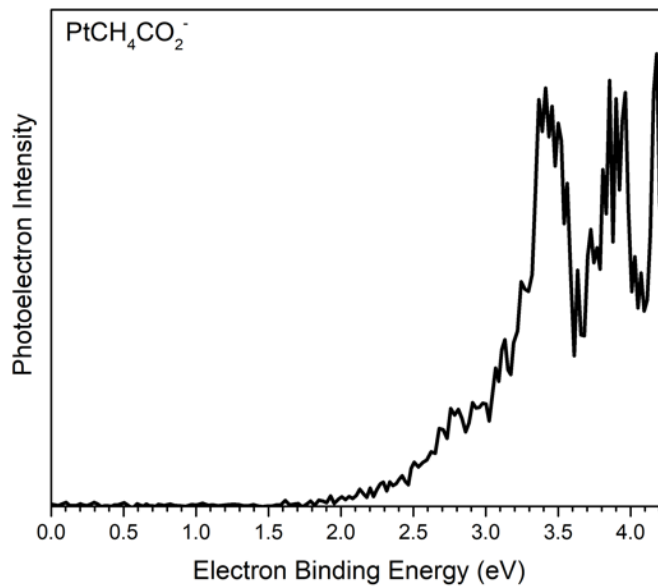


Figure 2. Photoelectron spectrum of the reaction products $\text{PtCH}_4\text{CO}_2^-$.

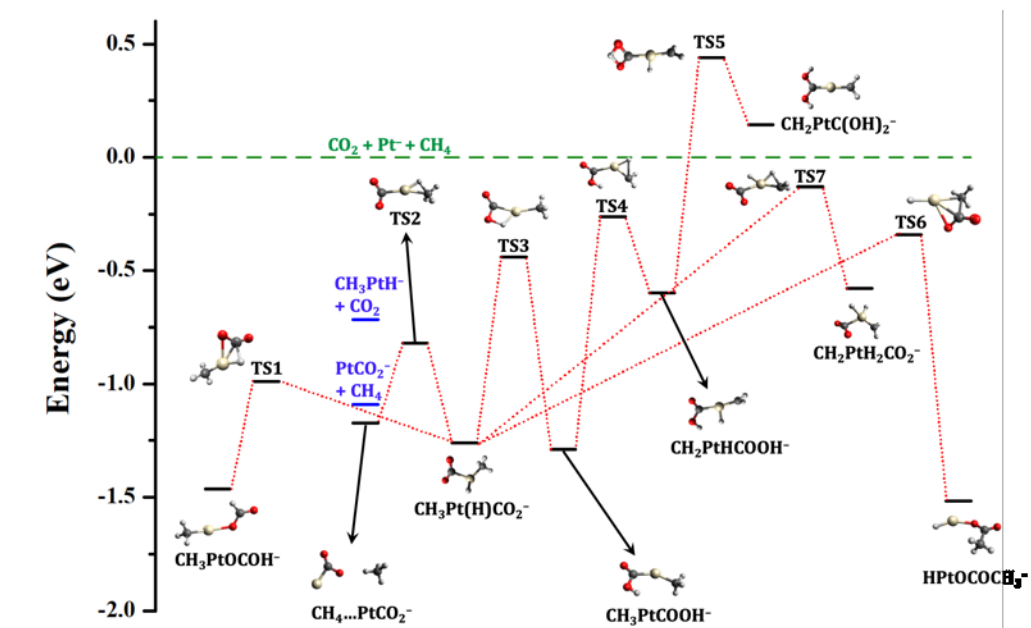
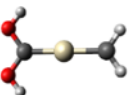
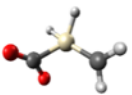
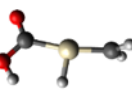
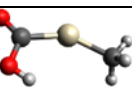
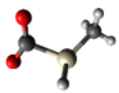
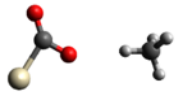
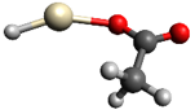
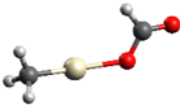


Figure 3. Calculated reaction pathway for the reaction $\text{Pt}^- + \text{CO}_2 + \text{CH}_4$.

Table 1. Calculated vertical detachment energies for the isomers of $\text{PtCH}_4\text{CO}_2^-$.

Structure	VDE to triplet	VDE to singlet
 $\text{CH}_2\text{PtC}(\text{OH})_2^-$	4.64	1.98
 $\text{CH}_2\text{PtH}_2\text{CO}_2^-$	4.47	2.96
 $\text{CH}_2\text{PtHCOOH}^-$	4.07	2.83
 $\text{CH}_3\text{PtCOOH}^-$	3.46	2.50

 $\text{CH}_3\text{Pt}(\text{H})\text{CO}_2^-$	4.02	2.71
 $\text{CH}_4 \dots \text{PtCO}_2^-$	3.62	2.84
 HPtOCOCH_3^-	5.27	3.86
 $\text{CH}_3\text{PtOCOH}^-$	3.81	3.88

Simulating Electrochemistry at the Molecular Level: Ni, Pd, Pt-H₂O-CO₂

Gaoxiang Liu, Isuru R. Ariyaratna, Sandra M. Ciborowski, Zhaoguo Zhu, Evangelos Miliordos, and Kit H. Bowen

The electrochemical reduction of CO₂ has been regarded as the promising strategy to convert CO₂ into value-added products. However, the extremely complicated environments of electrochemical reactions makes unravelling their mechanisms very difficult. With the aid from state-of-the-art calculations, gas-phase experiments provide an ideal arena for addressing many challenging topics and to probe mechanistic aspects of a chemical process in an unperturbed fashion at a strictly molecular level. Water activation and CO₂ hydrogenation are two important reactions for generating clean energy and alleviating global warming. Recently, we have demonstrated that single platinum atomic anion can activate either H₂O or CO₂ molecules. For H₂O activation, we verified the existence of the activated intermediate HPtOH⁻. In this work, we integrated these two important activation processes together: the platinum/water binary intermediate, HPtOH⁻, was used to hydrogenate the other molecule, CO₂. Their tertiary anionic intermediate, [Pt(H₂O)(CO₂)]⁻, was observed in the mass spectrum. In addition to the intermediate, we also observed the CO₂ hydrogenation product, formate.

Without adding CO₂ into the reaction cell, the products made by the reactions between Pt⁻ and H₂O are PtO⁻, Pt(H₂O)⁻ and their corresponding solvated complexes, the same as our published results. After adding CO₂ into the reaction cell, PtCO₂⁻ and Pt(H₂O)(CO₂)⁻

are formed.

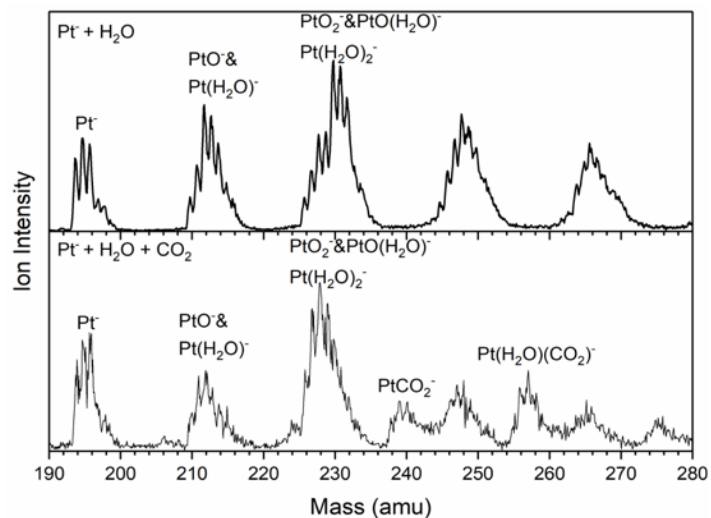


Figure 1. Mass spectra of the $\text{Pt}^- + \text{H}_2\text{O}$ reaction and the $\text{Pt}^- + \text{H}_2\text{O} + \text{CO}_2$ reaction.

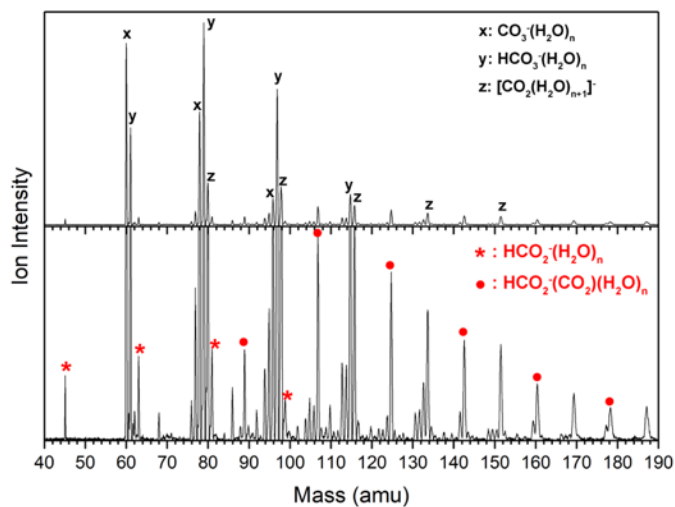


Figure 2. Mass spectra of low-mass products of the $\text{Pt}^- + \text{H}_2\text{O} + \text{CO}_2$ reaction.

HCOO^- (formate), HCO_3^- , CO_3^- and their solvation complexes are observed after adding CO_2 into the reaction cell. The intensity of HCOO^- related peaks are weaker than the

others.

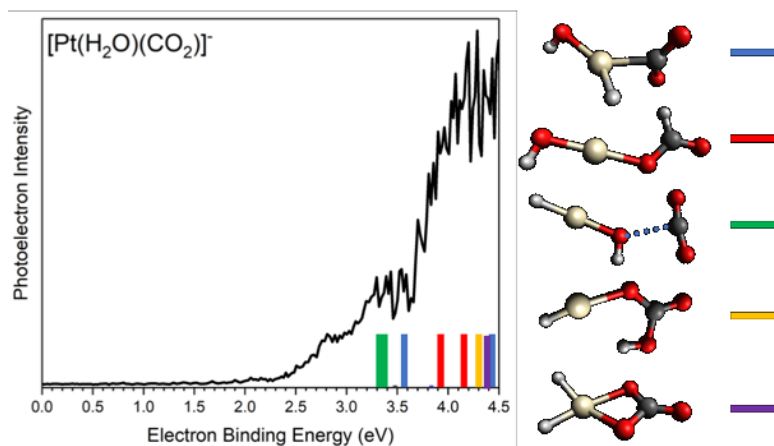


Figure 3. Photoelectron spectrum and calculated structures of $[\text{Pt}(\text{H}_2\text{O})(\text{CO}_2)]^-$. The colored sticks represent the vertical detachment energy of the corresponding structure.

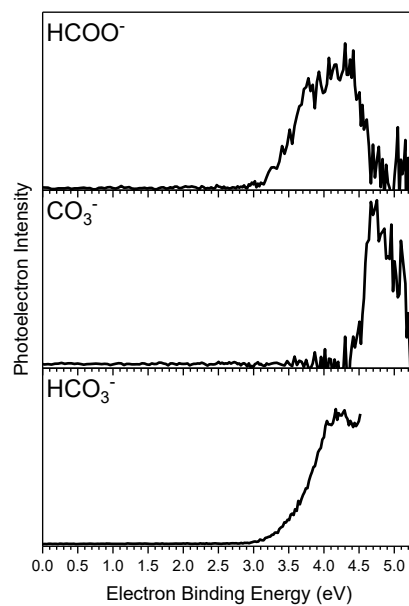


Figure 4. Photoelectron spectra of low-mass species.

The identities of these reaction products are verified by PES. These PES are in agreement

with previous published results

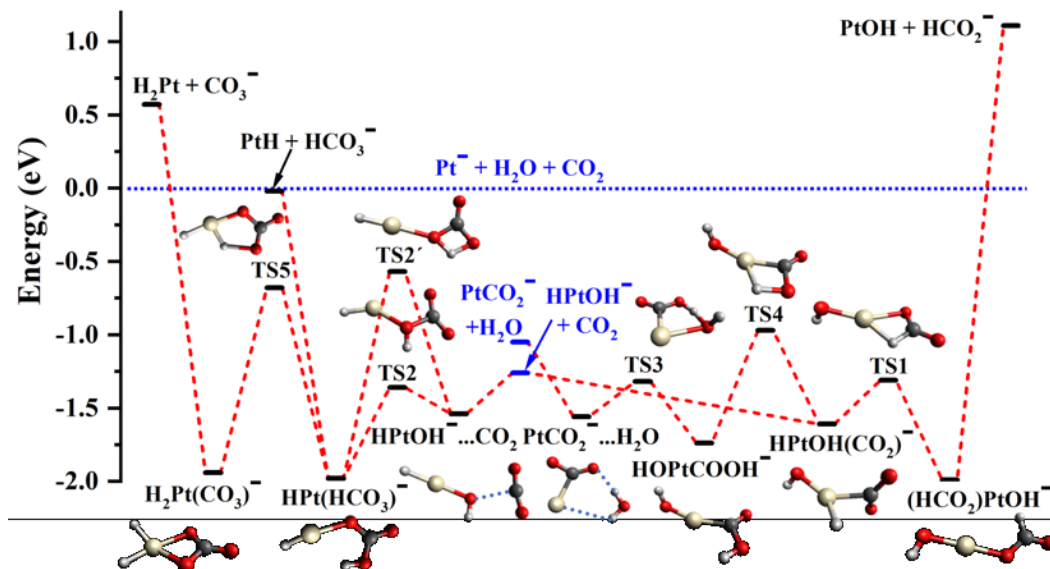
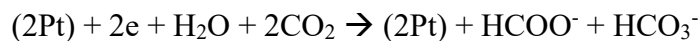


Figure 5. Calculated reaction pathway for $\text{Pt}^- + \text{H}_2\text{O} + \text{CO}_2$.

The step-by-step reactions in our experiments are thus:

1. $\text{Pt} + \text{e}^- \rightarrow \text{Pt}^-$
2. $\text{Pt}^- + \text{H}_2\text{O} \rightarrow \text{HPtOH}^-$
3. $\text{HPtOH}^- + \text{CO}_2 \rightarrow \text{PtOH} + \text{HCOO}^-$
4. $\text{HPtOH}^- + \text{CO}_2 \rightarrow \text{PtH} + \text{HCO}_3^-$
5. $\text{PtOH} + \text{PtH} \rightarrow 2\text{Pt} + \text{H}_2\text{O}$ (not observed but this reaction is exothermic, it might have happened but we are unable to observe them)

Adding and balancing the above reactions we get the overall reaction as:



In the overall reaction the Pt acts as a catalyst.

The overall reaction observed here is exactly the classical electrochemical reduction of CO₂ as happened on Pt electrodes. Therefore, our gas-phase experiments bisect the electrochemical process into molecular level reactions.

VI.11 Decomposition of Hydroxylamine by Iridium Cluster Anions

Gaoxiang Liu, Sandra M. Ciborowski, Jerry Boatz, Steven Chambreau, and Kit H.

Bowen

The Airforce research lab is very interested in using iridium clusters to catalyze the decomposition of ionic liquids, which serves as the monopropellants for space aircraft.

We investigated this topic in the gas phase, aiming to provide a molecular level insight into the decomposition process.

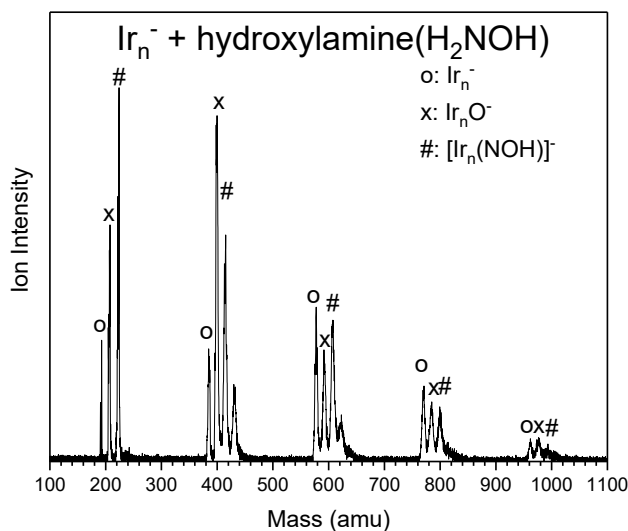


Figure 1. Mass spectrum of the reactions between Ir_n^- and hydroxylamine.

The addition of hydroxylamine resulted in a new series of peaks which are 31 amu heavier than their corresponding Ir_n^- peaks. Noted that the mass of hydroxylamine is 33 amu. Therefore, this suggests when Ir cluster anions react with hydroxylamine,

dehydrogenation happens. This reaction pattern is true for all Ir_n^- observed ($n=1-5$). The series denoted by “x” are determined as Ir oxide cluster anions, Ir_nO^- .

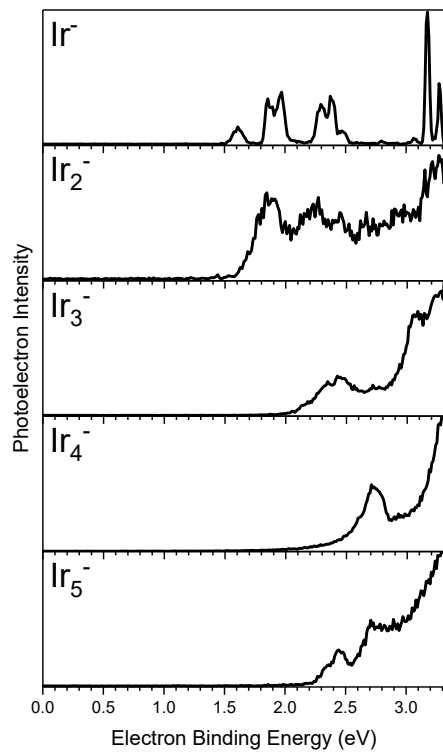


Figure 2. Photoelectron spectra of Ir_n^- , $n=1-5$.

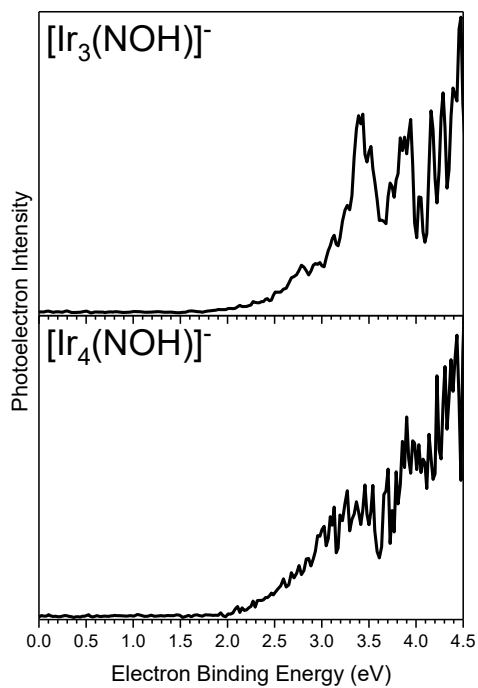


Figure 3. Photoelectron spectra the reaction products, $[\text{Ir}_{3,4}(\text{NO})]^-$.

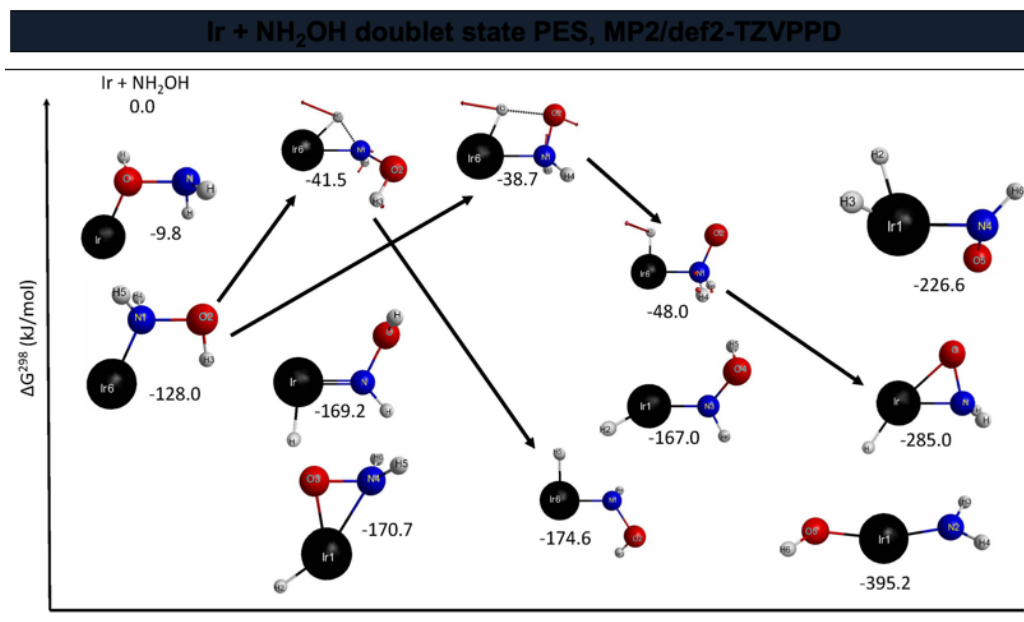


Figure 4. Calculated reaction pathway of the reaction $\text{Ir}^- + \text{NH}_2\text{OH}$.

VI.12 Photoelectron Spectroscopic Study of Dipole-bound and Valence-bound Nitromethane Anions Formed by Rydberg Electron Transfer

Gaoxiang Liu, Sandra M. Ciborowski, Jacob D. Graham, Allyson M. Buytendyk, and Kit H. Bowen

Department of Chemistry, Johns Hopkins University, 3400 N. Charles Street, Baltimore, MD 21218, USA

Abstract

The existence of close-lying dipole- and valence-bound states in the nitromethane anion makes this simple molecule an ideal model for studying the coupling of these two electronically different states. In this work, the dipole- and valence-bound nitromethane anions were generated by Rydberg electron transfer and characterized by anion photoelectron spectroscopy. The dipole-bound state was confirmed based on its strong dependence on the Rydberg level, its signature sharp peak in the photoelectron spectra, and its prominent anisotropy in the photoelectron imaging.

Introduction

Dipole-bound anions can be formed by the interaction of electrons with highly polar neutral molecules or clusters.¹⁻⁴ The formation of dipole-bound states is thought to be

the initial step of the electron attachment process to many polar molecules. Such dipole-bound states are often referred to as the “doorway” or “stepping stone” states.⁵⁻
¹⁴ Within this context, considerable efforts have been devoted to studying anions with energetically-close dipole-bound and valence-bound states, through which a deep understanding can be acquired on the coupling of the two closely spaced yet electronically very different states.¹⁵⁻¹⁷

Nitromethane represents a prototype of such anions; this simple molecule possesses close-lying dipole-bound and valence-bound states and thus serves as a suitable model system for understanding the formation of and the transition between dipole- and valence-bound anions in more complicated systems. The coupling between both anionic states of nitromethane has been widely researched both by experiment and by calculations.¹⁶⁻²⁷ The nitromethane anion, CH_3NO_2^- , can be formed through Rydberg electron transfer (RET) from rare gas and alkali atoms and by collisions with highly energetic alkali atoms.^{15,22} While nitromethane has a sufficiently large dipole moment (3.46 D) to sustain a dipole-bound anion, RET experiments show that the Rydberg state range in which electron attachment occurs is considerably broader than that of a typical dipole-bound anion, thus suggesting a coupling between the dipole-bound and valence-bound states.¹⁵ Anion photoelectron spectroscopy measures the electron affinity of nitromethane as 172 meV and reveals a long vibrational progression,

indicative of a valence bound anion with substantial difference in the equilibrium structures of the anion and the neutral.^{15,23,24} Time-resolved photoelectron imaging of iodide-nitromethane (I^- - CH_3NO_2) confirms the rapid conversion of the dipole-bound state of CH_3NO_2^- to the valence-bound state, which supports an electron attachment process via the “doorway” dipole-bound state.²⁵ Its vibrational features have also been demonstrated by autodetachment spectroscopy.^{28,29}

The coupling between the dipole-bound and valence-bound states of nitromethane, which fulfills a low-energy crossing picture, leads to the fragility of its dipole-bound anion.¹⁷ As a result, the dipole-bound nitromethane anion has only been found under restricted conditions, and previous characterizations of this dipole-bound state are controversial. Field detachment of nitromethane anions made by RET yields complex curves, hindering an exact interpretation of its dipole-bound state.¹⁵ Anion photoelectron spectra of nitromethane anions lack the signature of a dipole-bound anion, which should be a sharp photoelectron peak occurring at a low electron binding energy.^{15,23,26} Only one photoelectron spectroscopic study shows a transition tentatively assigned to the dipole-bound state. This assignment, however, is not yet conclusive; this transition is weak and broad, and the suppression of this feature due to Ar tagging is more indicative of a hot band.²⁴

Recently, we introduced our specialized Rydberg electron transfer/anion photoelectron spectroscopy (RET-aPES) apparatus and demonstrated it as the ideal tool to prepare dipole-bound anions, as well as to acquire a more comprehensive picture of their energetics.³⁰⁻³³ In this work, we present a photoelectron spectroscopic study of nitromethane anions made by Rydberg electron transfer over a wide range of Rydberg levels. The dipole-bound state is confirmed by a signature sharp transition at low electron binding energy in the photoelectron spectra. The strong Rydberg level dependence of its formation and the anisotropy of its photoelectron imaging further corroborate the assignment of the dipole-bound state.

Experimental Methods

The details of our RET-aPES apparatus are described elsewhere.³⁰⁻³³ Briefly, anion photoelectron spectroscopy is conducted by crossing a mass-selected beam of negative ions with a fixed-frequency photon beam and energy-analyzing the resultant photodetached electrons. This technique is governed by the energy-conserving relationship, $h\nu = \text{EKE} + \text{EBE}$, where $h\nu$, EKE, and EBE are the photon energy, the electron kinetic energy, and the electron binding (transition) energy, respectively. Electron kinetic energies were measured using a velocity-map imaging (VMI) spectrometer. Mass-selected anions were crossed with 1064 nm, linearly polarized photons in an electric field. The resultant photodetached electrons were accelerated

along the axis of the ion beam toward a position-sensitive detector coupled to a CCD camera. The two-dimensional image formed from the sum of the electrons was reconstructed into a portion of the three-dimensional distribution via the BASEX³⁴ method. Photoelectron spectra are calibrated against the well-known spectrum of NO⁻.³⁵

Nitromethane anions were generated by a Rydberg electron transfer (RET) source. Neutral nitromethane molecules were expanded using a pulsed valve with 10 psig of helium backing gas. The anions were formed when the neutral molecules collided with a thermally-expanded beam of potassium atoms, which had been excited to specific nd Rydberg states, where n represents the principal quantum number of the Rydberg K atoms, in two steps using two dye lasers. One dye laser pumped the potassium atoms to the $^2P_{3/2}$ state with 766.7 nm light, while the other was tuned to reach Rydberg levels between $12d$ and $19d$. The anions were then extracted using a time-of-flight mass spectrometer and mass-selected, and their electrons were photodetached and energy-analyzed with VMI spectroscopy.

Results and Discussions

Figure 1 presents the representative photoelectron image and spectrum of nitromethane anions made by charge transfer with Rydberg potassium atoms at the

16d Rydberg level. The photoelectron spectrum exhibits long vibrational progressions that are consistent with the well-documented photoelectron spectra of valence-bound CH_3NO_2^- .¹⁵ Based on previous studies, here, we assign the transition at around 0.10 eV as a vibrational hot band and the transition at 0.184 ± 0.015 eV as the vibrational 0-0 origin transition, i.e., the electron affinity peak. The most prominent feature observed here is a sharp photoelectron peak located at very low electron binding energy (EBE), which is the signature of dipole-bound anions. This sharp transition peaks at 14 meV. We assign this peak as the origin of the transition between dipole-bound CH_3NO_2^- and its corresponding neutral. Therefore, the vertical detachment energy (VDE) of dipole-bound CH_3NO_2^- is 14 meV. Due to the close similarity between the structures of the dipole-bound anion and its neutral counterpart, the anion's VDE value is almost identical to the value of its corresponding neutral's electron affinity. The current result is thus consistent with the dipole electron affinity of 12 ± 3 meV acquired by field ionization.¹⁵ The velocity mapping imaging study of CH_3NO_2^- also corroborates the observation of the dipole-bound state. In the photoelectron image, a discernable outer ring can be observed with an anisotropy that significantly differs from the inner rings of the photodetached valence-bound electrons. The anisotropy parameters, β , of the photodetached valence electrons are calculated to be around zero, while the β value of the outermost photoelectron ring is calculated as 1.41 ± 0.17 . This drastic difference suggests that this outermost ring

originates from a different electronic state than the ground electronic state of the nitromethane anion. The large β value is consistent with an outgoing p wave, which results from photodetachment of an s -character orbital with nearly zero angular momentum.²⁴ The dipole-bound state can be regarded as a spatially diffuse s -character orbital. Therefore, the matter wave of photodetached dipole-bound electrons should have p character, being consistent with the photoelectron imaging result.

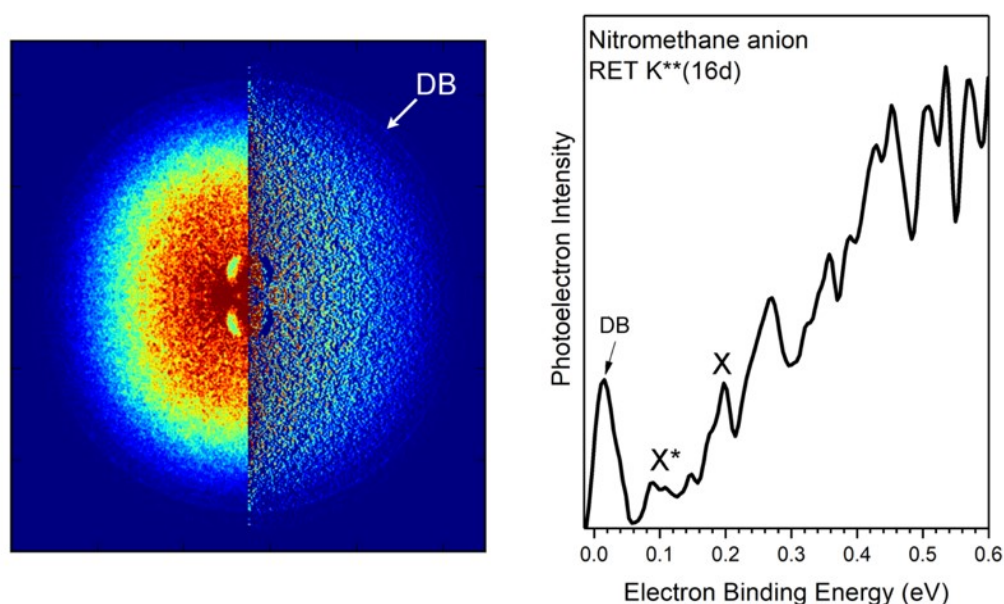


Figure 1 Photoelectron image and anion photoelectron spectrum of CH_3NO_2^- made by Rydberg electron transfer at the $\text{K}^{**}(16d)$ Rydberg level. The hot bands are marked as X^* and the electron affinity peak is marked as X . DB denotes the dipole-bound feature.

The dependence of the dipole-bound feature on Rydberg level was also investigated. Figure 2 presents the photoelectron spectra of nitromethane anions made at different

Rydberg levels, $K^{**}(nd)$. The valence-bound features in all spectra are quite similar. The sharp peak at low EBE shows a strong dependence on the level of the Rydberg K atoms. The Rydberg level range from $12d$ to $19d$ was chosen because it had been previously determined to facilitate the formation of dipole-bound nitromethane anions; ^{15,21} here, signal from the dipole-bound anion is discernable at Rydberg levels between $14d$ and $17d$, with a maximum intensity at $n = 16$. Such dependence is another signature of dipole-bound anions, as electron attachment into a dipole-bound state is expected to occur over a narrow range of relatively low principal quantum numbers, n , via resonance charge transfer. To be more specific, the d Rydberg electron transfer to the dipole-bound state can be explained by the curve crossings between the diabatic potential curves of the covalent pair $K^{**}(nd)/CH_3NO_2$ and of the formed ion pair $K^+/CH_3NO_2^-$ (dipole-bound state). To promote strong negative ion production, the Rydberg level, n , is tuned such that when the first curve crossing between the covalent and the ionic potentials happens, the orbital of the Rydberg electron overlaps with the orbital of the dipole-bound anion, and the energy of the Rydberg electron is close to the potential energy barrier associated with the combined core ion and dipole potentials. Thereby, the electron efficiently transfers into the dipole-bound well. As n becomes too large, the first curve crossing occurs at a larger distance; the overlap between the Rydberg electron wave function and the dipole-bound orbital thus decreases, dissipating the electron transfer possibility. When n gets too small, the

electron can transfer readily to the target molecule but will quickly decay back into the Rydberg orbital rather than maintain binding there.²¹

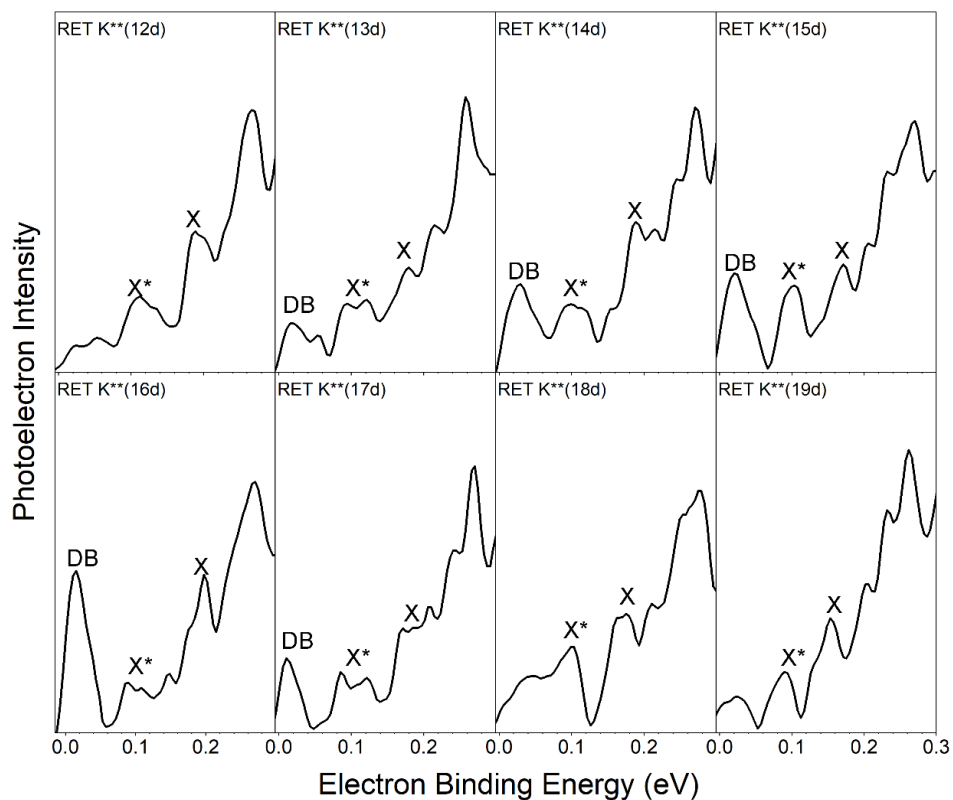


Figure 2 Photoelectron spectra of nitromethane anions formed by Rydberg electron transfer over $12d - 19d$ Rydberg levels. The hot bands are marked as X^* and the electron affinity peaks are marked as X . DB denotes the dipole-bound features.

Conclusion

In this contribution, we present a combined RET-aPES experiment on nitromethane anions made at different Rydberg levels. The acquired photoelectron image and

spectra have confirmed the presence of the dipole-bound nitromethane anion. This study represents an example of applying the RET-aPES method to reveal the energetics of dipole-bound anions and their coupling with associated valence-bound states.

References

1. K. D. Jordan, *Acc. Chem. Res.* **12**, 36–42 (1979).
2. J. Simons, and K. D. Jordan, *Chem. Rev.* **87**, 535–555 (1987).
3. G. Gutowski, P. Skurski, A. I. Boldyrev, J. Simons, and K. D. Jordan, *Phys. Rev. A: At., Mol., Opt. Phys.* **54**, 1906–1909 (1996).
4. J. Simons, *J. Phys. Chem. A* **112**, 6401–6511 (2008).
5. C. Desfrancois, B. Baillon, J. P. Schermann, S. T. Arnold, J. H. Hendricks, and K. H. Bowen, *Phys. Rev. Lett.* **72**, 48–51 (1994).
6. S. J. Xu, J. M. Nilles, and K. H. Bowen, *J. Chem. Phys.* **119**, 10696–10701 (2003).
7. I. Dabkowska, J. Rak, M. Gutowski, J. M. Nilles, S. T. Stokes, D. Radisic, and K. H. Bowen, *J. Chem. Phys.* **120**, 4351–4357 (2004).
8. T. Sommerfeld, *J. Phys. Chem. A* **108**, 9150–9154 (2004).
9. T. Sommerfeld, *J. Chem. Phys.* **126**, 124301–124305 (2007).
10. R. A. Bachorz, W. Klopper, M. Gutowski, X. Li, and K. H. Bowen, *J. Chem. Phys.* **129**, 054309 (2008).
11. S. N. Eustis, D. Radisic, K. H. Bowen, R. A. Bachorz, M. Haranczyk, G. Schenter, and M. Science **319**, 936–939 (2008).
12. L. Chomicz, M. Zdrowowicz, F. Kasprzykowski, J. Rak, A. Buonaugurio, Y. Wang, and K. H. Bowen, *J. Phys. Chem. Lett.* **4**, 2853–2857 (2013).
13. J. Kelly, S. Xu, J. Graham, M. Nilles, D. Radisic, A. Buonaugurio, K. H. Bowen, N. Hammer, and G. Tschumper, *J. Phys. Chem. A* **118**, 11901–11907 (2014).
14. A. M. Buytendyk, A. M. Buonaugurio, S. J. Xu, M. Nilles, K. H. Bowen, N. Kirnosov, and L. Adamowicz, *J. Chem. Phys.* **145**, 024301 (2016)
15. R. N. Compton, H. S. Carman, C. Desfrancois, H. Abdoul-Carime, J. P. Schermann, J. H. Hendricks, S. A. Lyapustina, and K. H. Bowen, *J. Chem. Phys.* **105**, 3472–3478 (1996).
16. J. H. Hendricks, S. A. Lyapustina, H. L. de Clercq, and K. H. Bowen, *J. Chem. Phys.* **108**, 8–11 (1998).
17. J. P. Rogers, C. S. Anstöter, and J. R. R. Verlet, *Nat. Chem.* **10**, 341–346 (2018).
18. G. L. Gutsev, and R. J. Bartlett, *J. Chem. Phys.* **105**, 8785 (1996).
19. F. Lecomte, S. Carles, C. Desfrancois, and M. A. Johnson, *J. Chem. Phys.* **113**, 10973 (2000).
20. T. Sommerfeld, *Phys. Chem. Chem. Phys.* **4**, 2511–2516 (2002).

21. L. Suess, R. Parthasarathy, and F. B. Dunning, *J. Chem. Phys.* **119**, 9532 (2003).
22. P. W. Harland, and C. E. Redden, *J. Am. Chem. Soc.* **128**, 4773-4778 (2006).
23. D. J. Goebbert, K. Pichugin, and A. Sanov, *J. Chem. Phys.* **131**, 164308 (2009).
24. C. L. Adams, H. Schneider, K. M. Ervin, and J. M. Weber, *J. Chem. Phys.* **130**, 074307 (2009).
25. M. A. Yandell, S. B. King, and D. M. Neumark, *J. Chem. Phys.* **140**, 184317 (2014).
26. C. J. M. Pruitt, R. M. Albury, and D. J. Goebbert, *Chem. Phys. Lett.* **659**, 142–147 (2016).
27. M. Kelley, S. Buathong, and F. B. Dunning, *J. Chem. Phys.* **146**, 184307 (2017).
28. J. M. Weber, W. H. Robertson, and M. A. Johnson, *J. Chem. Phys.* **115**, 10718 (2001).
29. H. Schneider, K. M. Vogelhuber, F. Schinle, J. F. Stanton, and J. M. Weber, *J. Phys. Chem. A* **112**, 7498 (2008)
30. E. F. Belogolova, G. Liu, E. P. Doronina, S. Ciborowski, V. F. Sidorkin, and K. H. Bowen, *J. Phys. Chem. Lett.* **9**, 1284-1289 (2018)
31. S. M. Ciborowski, G. Liu, J. D. Graham, A. M. Buytendyk, K. H. Bowen, *Eur. Phys. J. D* **72**, 139 (2018).
32. S. M. Ciborowski, R. M. Harris, G. Liu, C. J. Martinez-Martinez, P. Skurski, and K. H. Bowen, *J. Chem. Phys.* **150**, 161103 (2019).
33. G. Liu, S. M. Ciborowski, J. D. Graham, A. M. Buytendyk, and Kit H. Bowen, *J. Chem. Phys.*, in revision.
34. V. Dribinski, A. Ossadtchi, V. A. Mandelshtam, H. Reisler, *Rev. Sci. Instrum.* **73**, 2634-2642 (2002).
35. J. Hendricks, H. de Clercq C. B. Freidhoff, S. T. Arnold, J. G. Eaton, C. Fancher, S. A. Lyapustina, J. T. Snodgrass, K. H. Bowen, *J. Chem. Phys.* **116**, 7926-7938 (2002).

VI.13 Excess Electrons Bound to H₂S Trimer and Tetramer Clusters

*Gaoxiang Liu*¹, Manuel Díaz-Tinoco², Sandra M. Ciborowski¹, J. Vincent Ortiz^{2*}, Kit H. Bowen^{2*}

¹*Department of Chemistry, Johns Hopkins University Baltimore, MD 21218, USA*

²*Department of Chemistry and Biochemistry, Auburn University Auburn, AL 36849, USA*

Abstract

The hydrogen sulfide trimer and tetramer anions, (H₂S)₃⁻ and (H₂S)₄⁻, were generated by Rydberg electron transfer and studied via a synergy between velocity-map imaging anion photoelectron spectroscopy and high-level quantum chemical calculations. The sharp peaks at low electron binding energy in their photoelectron spectra and their diffuse Dyson orbitals are evidence of them both being dipole-bound anions. While the dipole moments of the neutral (H₂S)₃ and (H₂S)₄ clusters are small, the excess electron induces structural distortions that enhance the charge-dipolar attraction and facilitate the binding of diffuse electrons.

Introduction

As the fundamental species to many areas in physical sciences, solvated electrons play

a critical role in radiobiological chemistry¹, atmospheric aerosol chemistry², DNA damage³, and in theoretical studies as the simplest quantum solute.⁴ In condensed phase and gas phase, numerous studies have been conducted on the hydrated electron,⁵ and to a lesser extent, on solvated electrons in ammonia⁶, carbon dioxide⁷, alcohols⁸, and acetonitrile⁹. Despite the large body of work on solvated electrons, many problems still remain open. Possibly the most intriguing one is the nature of the microscopic solvation environment: how does the solvated electron interact with the surrounding molecules, and how will this interaction change upon environment variation?¹⁰

These questions have been widely addressed by experimental and theoretical studies of excess electrons in clusters, which have provided molecular-level insight to the properties of condensed-phase solvated electron species.^{11,12} The excess electrons in water clusters¹³⁻²², as well as in clusters of other polar or nonpolar molecules such as NH₃,²³ HF,²⁴ acetonitrile,²⁵ methanol,²⁶ amides²⁷, and aromatic molecules²⁸, have been subject to extensive research activity. One of the key findings is that the solvated electrons, i.e., internally-bound electrons, are common in large clusters of polar solvent, while the dipole-bound electrons, i.e., surface-bound electrons, dominate for small polar clusters.^{11,12} For example, in small water cluster anions, (H₂O)_n⁻ (n= 2~7), the most abundant anions observed are dipole-bound anions with the excess electron

localized in the vicinity of a water monomer with two free OH groups.¹³⁻¹⁶

Hydrogen sulfide (H₂S) has identical valence electron count and is structurally similar to H₂O. A major difference in their physical properties is their polarity: the dipole moment of H₂S (0.97 D) is significantly smaller than that of H₂O (1.85 D). Such difference leads to a weaker intermolecular dipole-dipole interaction among H₂S molecules.²⁹ Since H₂S and H₂O are electrically dissimilar but electronically and structurally alike, the research of excess electrons in H₂S clusters can serve as an ideal case-control study for understanding how electron binding is affected upon polarity change of the microsolvation environment. The anions of H₂S clusters, however, have evaded both experimental and theoretical investigations.

In this work, we employed our recently developed Rydberg electron transfer-anion photoelectron spectroscopy (RET-aPES) apparatus³⁰⁻³² to prepare and characterize H₂S cluster anions. We found that only H₂S trimer and tetramer clusters can bind an excess electron, while other H₂S clusters undergo dissociative electron attachment. The photoelectron spectra, which were measured via velocity-map imaging (VMI), reveal signature of dipole-bound electron in H₂S trimer and tetramer anions. High-level *ab initio* calculations reproduced the experimentally determined VDE values for (H₂S)₃⁻ and (H₂S)₄⁻. It is shown that the interaction between an excess electron and H₂S trimer or tetramer induces structural changes to the neutral clusters, which alter

their electrostatic potentials to bind a diffuse excess electron.

Methods

Experimental methods

Rydberg electron transfer (RET) provides a fragile-anion friendly environment in which to form previously inaccessible diffuse and otherwise weakly bound electron states. In RET, an electronically excited Rydberg atom transfers its outer electron to a target neutral cluster during their collision, resulting in an ion pair which separates into atomic cation and cluster anion products. RET is a slow-electron attachment process in which the receding positive ion plays a uniquely stabilizing role. As a result, Rydberg electron transfer provides an unusually gentle, highly quantum state-specific, laser-tunable, anion formation environment. In a typical RET experiment, atoms are optically pumped to specific Rydberg states (n^*) at the point where they collide with a beam of neutral target molecules. In the present case, the target is a beam of neutral H₂S clusters, formed in the supersonic expansion of 5% H₂S/He mixed gas from a pulse valve.³³ To generate high intensities of product anions, we use alkali (K) atoms and two pulsed dye lasers. One laser optically pumps to the ²P_{3/2} level of the potassium atoms, while the second laser selectively excites that population to the ns and nd Rydberg levels of interest. Several Rydberg levels, i.e., $n^* = 12d-15d$, were surveyed, and the most intense ion signal occurred at the $n^* = 14d$ Rydberg level. Beams of

Rydberg-excited K atoms and neutral target molecules cross between the ion extraction grids of our time-of-flight mass analyzer/selector. There, H₂S cluster anions were formed by RET and accelerated into a flight tube, along which they are mass-selected, prior to being photodetached.

Anion photoelectron spectroscopy is conducted by crossing a beam of negative ions with a fixed-frequency photon beam and energy-analyzing the resultant photodetached electrons. This technique is governed by the energy-conserving relationship, $h\nu = \text{EBE} + \text{EKE}$, where $h\nu$ is the photon energy, EBE is the electron binding energy, and EKE is the electron kinetic energy. The electron energies of the photodetached electrons are measured using a velocity-map imaging (VMI) anion photoelectron spectrometer, which has been described previously. There, mass-selected anions are crossed with 1064 nm linearly polarized photons from a Nd:YAG laser. The resultant photodetached electrons are then accelerated along the axis of the ion beam toward a position-sensitive detector, which is coupled to a CCD camera. The basis set expansion (BASEX)³⁴ Abel transform method is used to reconstruct the two-dimensional image, formed by the sum of these electrons, into the three-dimensional distribution. Our resulting anion photoelectron spectrum is calibrated relative to the well-known photoelectron spectrum of NO⁻.³⁵

Computational methods

Geometry optimizations on $(\text{H}_2\text{S})_3^-$ and $(\text{H}_2\text{S})_4^-$ were executed with the coupled-cluster, single, doubles and perturbative triples, or CCSD(T), method³⁶ and the doubly augmented 6-311+²⁺²G(2df,p) basis-set.³⁷⁻³⁹ Exponents of the doubly augmented basis were obtained by multiplying the most diffuse exponent of each angular momentum from the initial basis-set, 6-311++G(2df,p), by 0.3. The abundance of diffuse functions requires that the accuracy criterion of two-electron repulsion integrals be set to 10^{-20} a.u.⁴⁰ BDT1⁴¹⁻⁴⁴ electron-propagator calculations of vertical detachment energies (VDEs) were performed with augmented, correlation-consistent (aug-cc-pVDZ or aug-cc-pVTZ) basis sets.⁴⁵⁻⁴⁷ Double, triple and quadruple augmentation of the basis sets (aug², aug³ and aug⁴, respectively) is defined by exponents obtained by successively multiplying the most diffuse exponent of each angular momentum by 0.3. VEDEs also were inferred from total energy differences at the Δ CCSD(T) level. All pole strengths are above 0.85. Dyson orbitals expressed as a linear combination of approximate Brueckner orbitals in BDT1 calculations are dominated by a single, pseudo-canonical orbital in every case. All calculations were performed with Gaussian 16⁴⁸ except the BDT1 electron-propagator calculations, which employed GDV.⁴⁹ Plots of molecular structures and Dyson orbitals were generated with GaussView.⁵⁰

Results and Discussion

The mass spectrum of H₂S trimer and tetramer cluster anions made by RET is presented in the bottom panel of Figure 1, alongside with the simulated isotope patterns of S⁻(H₂S)_{2,3} and (H₂S)_{3,4}⁻ in the top panels. The peaks at 100 and 134 amu suggest the existence of S⁻(H₂S)₂ and S⁻(H₂S)₃, in which S⁻ come from the dissociative electron attachment of H₂S. The peaks at 104 and 138 amu confirm the formation of (H₂S)₃⁻ and (H₂S)₄⁻, as only (H₂S)₃⁻ and (H₂S)₄⁻ have isotopes respectively at these two masses. The two mass peaks in the middle, i.e., at 102 and 136 amu, are mixed peaks of S⁻(H₂S)₂/(H₂S)₃⁻ and S⁻(H₂S)₃/(H₂S)₄⁻, respectively. No anions are observed smaller than 90 amu. At larger mass up to 500 amu, S⁻(H₂S)_n are the major products (Figure 2), implying that dissociative electron attachment prevails in larger H₂S clusters. Therefore, under our experimental conditions, an excess electron can be attached only to (H₂S)₃ and (H₂S)₄. Note that this is surprisingly different to (H₂O)_n⁻ clusters, where (H₂O)₃⁻ and (H₂O)₄⁻ are the “missing species”¹³ due to their negative electron affinity (EA),⁵¹ and can only form via an indirect electron attachment process.⁵²

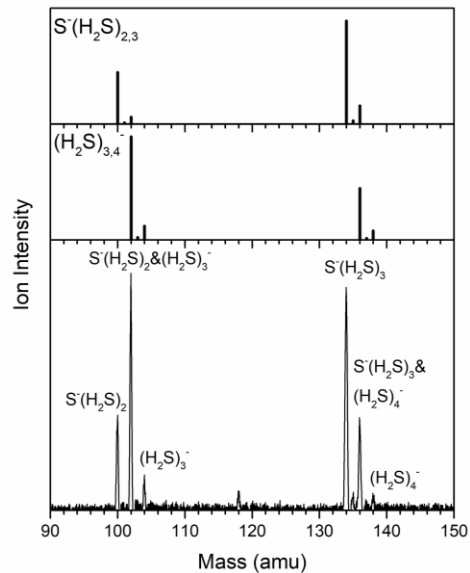


Figure 1 Simulated isotope patterns of $S^-(H_2S)_{2,3}$ and $(H_2S)_{3,4}^-$ (top two panels) and experimental mass spectrum made by Rydberg electron transfer at $n^* = 14d$ (bottom panel).

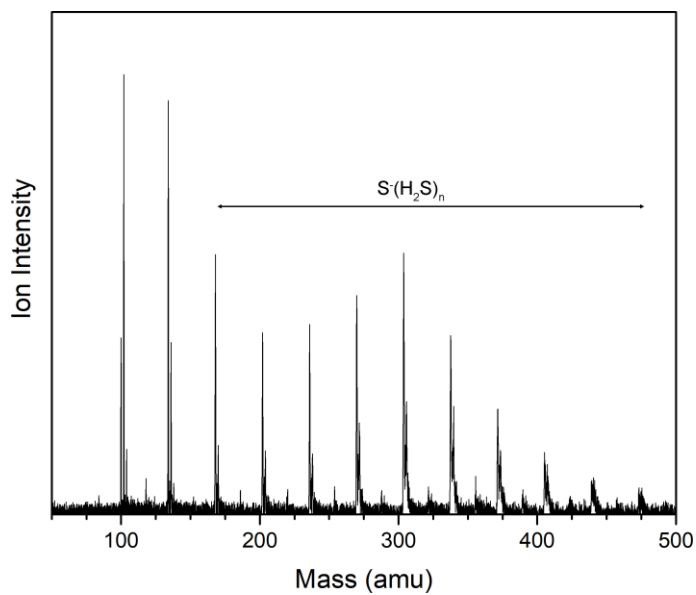


Figure 2 Experimental mass spectrum showing the larger-mass anion products made by Rydberg electron transfer at $n^* = 14d$.

Figure 3 presents the anion photoelectron spectra of $(\text{H}_2\text{S})_3^-$ and $(\text{H}_2\text{S})_4^-$ with their corresponding photoelectron images embedded. Each spectrum consists of a major, sharp peak at low electron binding energy (EBE), strongly implying that $(\text{H}_2\text{S})_3^-$ and $(\text{H}_2\text{S})_4^-$ are dipole-bound anions. For $(\text{H}_2\text{S})_3^-$, the EBE peak is centered at 29 meV; for $(\text{H}_2\text{S})_4^-$, the EBE peak is centered at 115 meV. We assign these two peaks as the origins of the transitions between the cluster anions and their corresponding neutral clusters. Therefore, the vertical detachment energy (VDE) values for $(\text{H}_2\text{S})_3^-$ and $(\text{H}_2\text{S})_4^-$ are 29 and 115 meV, respectively. In addition to the major peak, each spectrum also contains a weaker peak at higher EBE side that is separated from the center of the strong peak by 0.34 eV. These peaks are assigned as the vertical detachment to an excited H_2S vibration mode.

The photoelectron VMI image embedded in Figure 3 reveals significant anisotropy in both the H_2S trimer and tetramer anions. The anisotropy parameters, β , for the photodetached electrons were each calculated to be around 1.7, which is close to the theoretical upper limit. A large β value is consistent with an outgoing p wave, which means that photodetachment occurred from an s -orbital with nearly zero angular momentum. Since both dipole-bound anions have spatially diffuse excess electron states, their excess electrons can be viewed as possessing s -orbital character, consistent with the observed anisotropy.

We also performed the experiment on our nozzle-ion source/PES apparatus.⁵³ The $(\text{H}_2\text{S})_4^-$ photoelectron spectrum (Figure 3c) taken by this apparatus is consistent with the one taken by the RET-aPES apparatus, and shows an improved signal-to-noise ratio. $(\text{H}_2\text{S})_3^-$, however, was not observed with the nozzle-ion/PES apparatus as it was detached by the strong electric fields from multiple lenses along the ion path inside it.

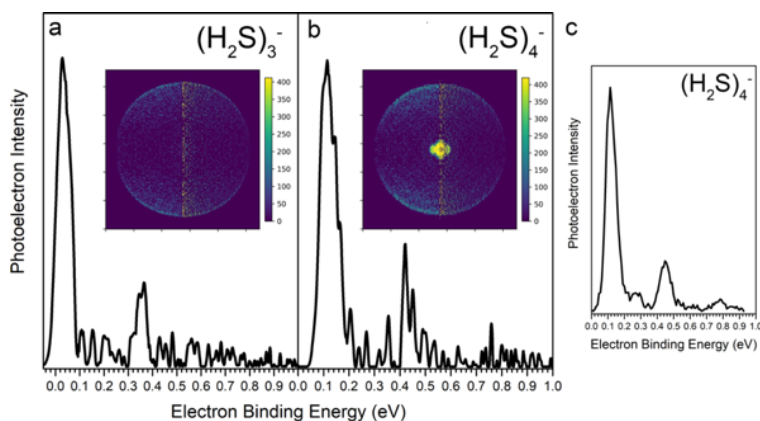


Figure 3 Photoelectron spectra of $(\text{H}_2\text{S})_3^-$ and $(\text{H}_2\text{S})_4^-$. (a) and (b) are obtained with the RET-aPES apparatus; (c) is obtained with the nozzle-ion source/PES apparatus.

The small size of the observed H_2S cluster anions enables applying high-level ab initio calculations on their structures and energetics. Figure 4 presents the optimized structures and the Dyson orbitals of $(\text{H}_2\text{S})_3^-$. The two optimized structures have C_{2v} and C_3 symmetry, respectively. Based on CCSD(T)/aug³-cc-pVTZ level of theory, the C_{2v} structure is higher in energy than the C_3 structure by 0.048 eV. In the C_{2v} structure, a central H_2S molecule has H bridges to two equivalent H_2S molecules, with all of the H nuclei oriented toward the red contour of the Dyson orbital of electron detachment. In the C_3 structure, equivalent sulfur nuclei and three hydrogens form a ring below

which lie three hydrogens that are oriented toward the red contour that pertains to the Dyson orbital of electron detachment. Both structures of $(\text{H}_2\text{S})_3^-$ exhibits positive VDE only when the basis set is saturated with diffuse basis functions. Triple augmentation suffices for this purpose. After extra diffuse augmentations, there is little difference between results generated with augmented double and triple ζ basis sets. BDT1 results for VDEs are in agreement with $\Delta\text{CCSD(T)}$ to within a few meV at basis saturation. The predicted VDEs are 21 and 66 meV respectively for the C_3 and C_{2v} structures. The former result, based on the BDT1 results with quadruple diffuse functions and corresponding to the more stable structure, is in excellent agreement with the observed value, 29 meV.

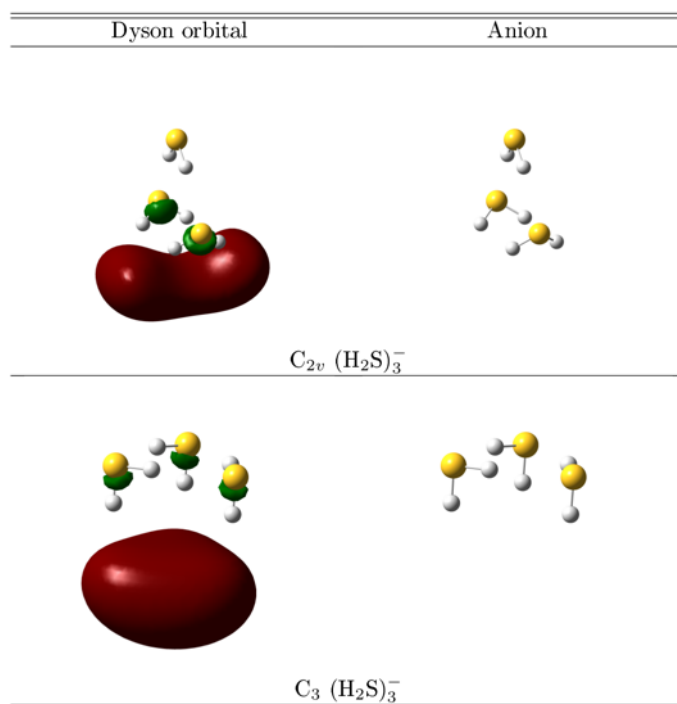


Figure 4 Dyson orbitals and structures for $(\text{H}_2\text{S})_3^-$.

Contours of the Dyson orbitals of both isomers indicate that the least bound electron is spread over a volume that lies outside S-H bonds that are oriented to stabilize the extra negative charge. The shapes of the red contours are influenced respectively by the propinquity of three or four H nuclei in the C_3 and C_{2v} structures. Green contours within S-H bonds indicate orthogonalization to occupied, valence orbitals and delocalization over a larger volume that encloses the molecules in plots of lower contours. The short distance between the majority of the extra negative charge and the nearby H nuclei indicates the importance of electrostatic attraction in stabilizing the extra negative charge. At such distances, exchange and correlation effects are also important.

Table 1 Calculated vertical detachment energies at different levels of theories for $(H_2S)_3^-$.

Expt. VDE	$(H_2S)_3^-$ structure	Basis set	Theo. VDE	
			Δ CCSD(T)	BDT1
0.029	C_3	aug-cc-pVDZ	-0.328	-0.324
		aug ² -cc-pVDZ	-0.040	-0.036
		aug ³ -cc-pVDZ	0.011	0.014
		aug ⁴ -cc-pVDZ	0.018	0.021
		aug-cc-pVTZ	-0.243	-0.252
		aug ² -cc-pVTZ	-0.026	-0.029
		aug ³ -cc-pVTZ	0.013	0.013
	C_{2v}	aug-cc-pVDZ	-0.211	-0.206
		aug ² -cc-pVDZ	0.027	0.032

aug ³ -cc-pVDZ	0.059	0.064
aug ⁴ -cc-pVDZ	0.058	0.066
aug-cc-pVTZ	-0.138	-0.148
aug ² -cc-pVTZ	0.037	0.034
aug ³ -cc-pVTZ	0.060	0.059

Four optimized structures, labelled by their point groups, are found for (H₂S)₄⁻. The C₄, C_s¹, C_s² and S₄ (wherein μ=0) clusters are shown in Figure 2. The structures are sensitive to basis sets and to the level of theory; perturbative triples have significant influence on the results. The C₄ structure has the lowest energy at the highest level of theory, ΔCCSD(T)/aug³-cc-pVTZ, with relative energies for C_s¹, C_s² and S₄ structures being 0.041, 0.027 and 0.024 eV, respectively. All four anions are bound with respect to neutrals when the basis-set is saturated with diffuse functions (see Table 3). BDT1 electron-propagator results for VDEs (53, 126, 100 and 25 meV, respectively, for the C₄, C_s¹, C_s² and S₄ clusters) are in close agreement with CCSD(T). Results for the two C_s structures are in much closer agreement with experiment value of 115 meV than those for the more symmetric geometries.

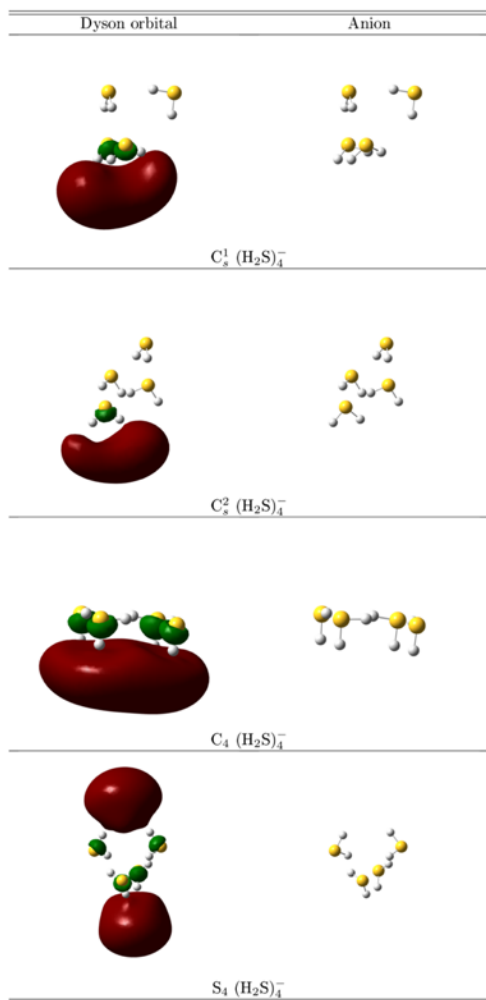


Figure 5 Dyson orbitals and structures of $(H_2S)_4^-$

Table 3 Calculated vertical detachment energies for $(H_2S)_4^-$.

Expt. VDE	$(H_2S)_4^-$		Theo. VDE	
	structure	Basis set	Δ CCSD(T)	BDT1
0.119	C ₄	aug-cc-pVDZ	-0.224	-0.219
		aug ² -cc-pVDZ	0.020	0.024
		aug ³ -cc-pVDZ	0.052	0.057
		aug-cc-pVTZ	-0.148	-0.156

	aug ² -cc-pVTZ	0.030	0.028
	aug ³ -cc-pVTZ	0.053	0.053
C _s ¹	aug-cc-pVDZ	-0.070	-0.064
	aug ² -cc-pVDZ	0.111	0.117
	aug ³ -cc-pVDZ	0.126	0.134
	aug-cc-pVTZ	-0.010	-0.021
	aug ² -cc-pVTZ	0.118	0.113
	aug ³ -cc-pVTZ	0.126	0.126
	C _s ²	aug-cc-pVDZ	-0.154
aug ² -cc-pVDZ		0.077	0.082
aug ³ -cc-pVDZ		0.101	0.107
aug-cc-pVTZ		-0.081	-0.091
aug ² -cc-pVTZ		0.085	0.082
aug ³ -cc-pVTZ		0.101	0.100
S ₄	aug-cc-pVDZ	-0.238	-0.238
	aug ² -cc-pVDZ	-0.009	-0.008
	aug ³ -cc-pVDZ	0.024	0.028
	aug-cc-pVTZ	-0.167	-0.182
	aug ² -cc-pVTZ	0.002	-0.004
	aug ³ -cc-pVTZ	0.027	0.025

The latter result can be explained with the aid of Figure 6, which shows that both C_s clusters have an anchoring molecule that binds two, out-of-plane molecules. (Only one of the two latter molecules is visible for C_s² in Figure 3; the anchor is at the top right corner in both cases.) In C_s¹, the anchor also binds an in-plane monomer, but in C_s², the two out-of-plane molecules bind it. A path with a low energy barrier

between the two minima entails the movement of the monomer on the left of both halves of Figure 3. This fluxionality gives an entropic advantage to the C_s structures over the more ordered C_4 and S_4 alternatives. (An anchor molecule that symmetrically binds two other molecules also is present in the C_{2v} structure of $(H_2S)_3^-$.) The observed VDE therefore is associated with the fluxional, C_s structures.

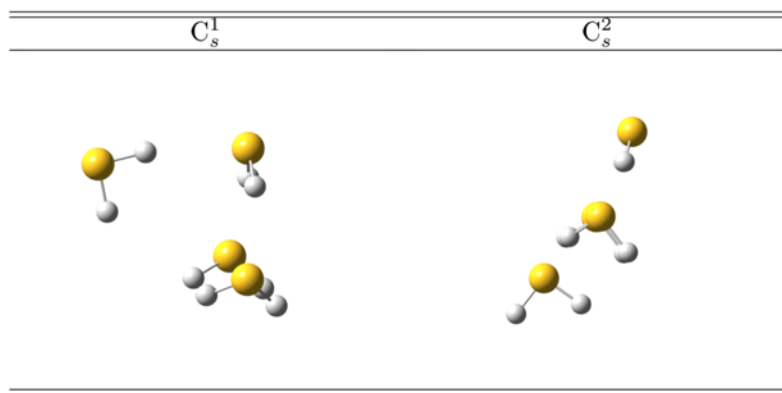


Figure 6 Fluctuation between C_s^1 and C_s^2 structures for $(H_2S)_4^-$

Dyson orbitals of electron detachment are close to five or six H nuclei, respectively, in the C_s^1 and C_s^2 structures. Volumes enclosed by the corresponding red contours of Figure 2 span regions outside nearby S-H bonds. Orthogonalization to occupied, valence orbitals results in the smaller, green contours and implies delocalization over a larger volume. The C_4 Dyson orbital resembles that of C_3 $(H_2S)_3^-$, but with a higher symmetry axis. A symmetric pattern of delocalization results in the S_4 case.

The dipole moments of the optimized neutral $(H_2S)_3$ and $(H_2S)_4$, which were

calculated in a previous study with MP2/aug-cc-pVTZ^{29b} and verified by us in this study with coupled cluster theory, are not large enough to bind an excess electron to their dipole field. The dipole moments of the uncharged (H₂S)₃ and (H₂S)₄ clusters calculated at the geometries of the anions, on the other hand, turn out sufficiently large (Table 4). This suggests that the excess electron causes nuclear rearrangements to the H₂S clusters to enable the electrostatic binding of the diffuse electron. The short distances between the extra electron's largest amplitudes and the nearest protons and indicates the importance of the neutral cluster's electrostatic potential, as well as exchange and electron correlation, in stabilizing the extra negative charge.

Table 4 Calculated dipole moments at CCSD/aug²-cc-pVTZ level of theory for neutral (H₂S)₃ at the optimized neutral structure and at the optimized anion structure.

The dipole moments are given in Debye.

	$\mu_{neutral}$	Anion geometry	μ_{anion}
(H ₂ S) ₃	0.56	C ₃	1.93
(H ₂ S) ₄	1.39	C _s ¹	3.49
		C _s ²	4.37

Summary

To summarize, we have prepared and characterized the dipole-bound anions of (H₂S)₃ and (H₂S)₄ with our specialized RET-aPES apparatus. The interaction between the excess electrons and neutral H₂S trimer and tetramer induces structural distortions in

the cluster frameworks, which enhance their dipole moments and facilitate the binding of diffuse electrons. This study has furthered our understanding on solvated electrons in clusters.

References

1. E. Alizadeh and León Sanche, *Chem. Rev.*, 2012, **112**, 5578.
2. F. Arnold, *Nature*, 1981, **294**, 732.
3. J. Gu, J. Leszczynski and H. F. Schaefer III, *Chem. Rev.*, 2012, **112**, 5603.
4. L. Turi and P. J. Rossky, *Chem. Rev.*, 2012, **112**, 5641.
5. (a) J. Savolainen, F. Uhlig, S. Ahmed, P. Hamm and P. Jungwirth, *Nat. Chem.*, 2014, **6**, 697. (b) K. R. Siefertmann, Y. Liu, E. Lugovoy, O. Link, M. Faubel, U. Buck, B. Winter and B. Abel *Nat. Chem.*, 2010, **2**, 274. (c) D. Luckhaus, Y. Yamamoto, T. Suzuki and R. Signorell, *Sci. Adv.* 2017, **3**, e1603224. (d) J. M. Herbert and Marc P. Coons, *Annu. Rev. Phys. Chem.*, 2017, **68**, 447.
6. (a) W. Weyl, *Ann. Phys.*, 1864, **199**, 350. (b) J. Lindner, A. N. Unterreiner and P. Vöhringer, *Chem. Phys. Chem.*, 2006, **7**, 363. (c) F. A. Uribe, T. Sawada and A. J. Bard, *Chem. Phys. Lett.*, 1983, **97**, 243. (d) E. Zurek, P. P. Edwards and R. A. Hoffmann, *Angew. Chem., Int. Ed.* 2009, **48**, 8198.
7. Z. Wang, J. Liu, M. Zhang, R. I. Cukier and Y. Bu, *Phys. Rev. Lett.*, 2012, **108**, 207601.
8. (a) C. Silva, P. K. Walhout, P. J. Reid and P. F. Barbara, *J. Phys. Chem. A*, 1998, **102**, 5701. (b) M. J. Tauber, C. M. Stuart and R. A. Mathies, *J. Am. Chem. Soc.*, 2004, **126**, 3414. (c) A. Thaller, R. Laenen and A. Laubereau, *J. Chem. Phys.*, 2006, **124**, 024515. (d) A. T. Shreve, M. H. Elkinsa and D. M. Neumark, *Chem. Sci.*, 2013, **4**, 1633.
9. (a) C. Xia, J. Peon, and B. J. Kohler, *Chem. Phys.* 2002, **117**, 8855. (b) I. A. Shkrob and J. Sauer, *J. Phys. Chem. A*, 2002, **106**, 9120. (c) S. C. Doan and B. J. Schwartz, *J. Phys. Chem. Lett.*, 2013, **4**, 1471.
10. (a) R. E. Larsen, W. J. Glover and B. J. Schwartz, *Science*, 2010, **329**, 65. (b) L. Turi, and A. Madarász, *Science*, 2011, **331**, 1387.
11. R. M. Young and D. M. Neumark, *Chem. Rev.*, 2012, **112**, 5553.
12. A. W. Castleman and K. H. Bowen, *J. Phys. Chem.*, 1996, **100**, 12911.
13. J. V. Coe, G. H. Lee, J. G. Eaton, S. T. Arnold, H. W. Sarkas, C. Ludewigt, H. Haberland, D. R. Worsnop and K. H. Bowen, *J. Chem. Phys.*, 1990, **92**, 3980.
14. J. R. Roscioli, N. I. Hammer and M. A. Johnson, *J. Phys. Chem. A*, 2006, **110**, 24.
15. N. I. Hammer, J. W. Shin, J. M. Headrick, E. G. Diken, J. R. Roscioli, G. H. Weddle and M. A. Johnson, *Science*, 2004, **306**, 675.
16. T. Sommerfeld and K. D. Jordan, *J. Am. Chem. Soc.*, 2006, **128**, 5828.

17. H. M. Lee, S. Lee and K. S. Kim, *J. Chem. Phys.*, 2003, **119**, 187.
18. J. R. R. Verlet, A. E. Bragg, A. Kammrath, O. Cheshnovsky and D. M. Neumark, *Science*, 2005, **307**, 93.
19. L. Turi, W. S. Sheu, P. J. Rossky, *Science*, 2005, **309**, 914.
20. L. A. Posey, P. J. Campagnola, M. A. Johnson, G. H. Lee, J. G. Eaton and K. H. Bowen, *J. Chem. Phys.*, 1998, **91**, 6536.
21. H. Haberland and K. H. Bowen, in *Clusters of Atoms and Molecules*, ed., H. Haberland (Springer-Verlag: Heidelberg, 1993), 134-153.
22. G. H. Lee, S. T. Arnold, J. G. Eaton, H. W. Sarkas, K. H. Bowen, C. Ludewigt and H. Haberland, *Z. Phys. D.*, 1991, **20**, 9.
23. (a) H. W. Sarkas, S. T. Arnold, J. G. Eaton, G. H. Lee and K. H. Bowen, *J. Chem. Phys.*, 2002, **116**, 5731. (b) I. R. Lee, W. Lee and A. H. Zewail, *Chem. Phys. Chem.* 2008, **9**, 83. (c) T. Sommerfeld, *J. Phys. Chem. A*, 2008, **112**, 11817.
24. M. Gutowski, C. S. Hall, L. Adamowicz, J. H. Hendricks, H. L. de Clercq, S. A. Lyapustina, J. M. Nilles, S.-J. Xu and K. H. Bowen, *Phys. Rev. Lett.*, 2002, **88**, 143001.
25. (a) T. Takayanagi, T. Hoshino, K. Takahashi, *Chem. Phys.*, 2006, **324**, 679. (b) M. Mitsui, N. Ando, S. Kokubo, A. Nakajima and K. Kaya, *Phys. Rev. Lett.*, 2003, **91**, 153002.
26. A. Kammrath, Jan R. R. Verlet, G. B. Griffin and Daniel M. Neumark, *J. Chem. Phys.*, 2006, **125**, 171102.
27. (a) T. Maeyama, K. Yoshida and A. Fujii, *J. Phys. Chem. A*, 2012, **116**, 3771. (b) M. Seydou, A. Modelli, B. Lucas, K. Konate, C. Desfrancois and J.P. Schermann, *Eur. Phys. J. D*, 2005, **35**, 199. (c) T. Maeyama, Y. Negishi, T. Tsukuda, I. Yagia and N. Mikami, *Phys. Chem. Chem. Phys.*, 2006, **8**, 827.
28. M. Mitsui, A. Nakajima and K. J. Kaya, *Chem. Phys.*, 2002, **117**, 9740.
29. (a) A. Das, P. K. Mandal, F. J. Lovas, C. Medcraft, N. R. Walker, E. Arunan, *Angew. Chem. Int. Ed.*, 2018, **57**, 15199. (b) Y. N. Kalugina, D.A. Shuchugashev, V.N. Cherepanov, *Chem. Phys. Lett.*, 2018, **692**, 184.
30. S. M. Ciborowski, R. M. Harris, G. Liu, C. J. Martinez-Martinez, P. Skurski, and K. H. Bowen, 2019, *J. Chem. Phys.*, **150**, 161103.
31. S. M. Ciborowski, G. Liu, J. D. Graham, A. M. Buytendyk and K. H. Bowen, *Eur. Phys. J. D*, 2018, **72**, 139.
32. E. F. Belogolova, G. Liu, E. P. Doronina, S. Ciborowski, V. F. Sidorkin and K. H. Bowen, *J. Phys. Chem. Lett.*, 2018, **9**, 1284.
33. X. Zhang, G. Liu, S. Ciborowski and K. Bowen, *Angew. Chem. Int. Ed.* 2017, **56**, 9897.
34. V. Dribinski, A. Ossadtchi, V. A. Mandelshtam and H. Reisler, *Rev. Sci. Instrum.* 2002, **73**, 2634.
35. J. H. Hendricks, H. L. De Clercq, C. B. Freidhoff, S. T. Arnold, J. G. Eaton, C. Fancher, S. A. Lyapustina, J. T. Snodgrass and K. H. Bowen, *J. Chem. Phys.*, 2002, **116**, 7926.
36. K. Raghavachari, G.W. Trucks, J.A. Pople and M. Head-Gordon, *Chem. Phys. Lett.*, 1989, **157**, 479-483.
37. R. Krishnan, J.S. Binkley, R. Seeger and J.A. Pople, *J. Chem. Phys.*, 1980, **72**, 650.

38. T. Clark, J. Chandrasekhar, G.W. Spitznagel and P.v.R. Schleyer, *J. Comput. Chem.*, 1983, **4** 294.
39. A.D. McLean and G.S. Chandler, *J. Chem. Phys.* 1980, **72**, 5639.
40. M. Czapla, J. Simons and P. Skurski, *Phys. Chem. Chem. Phys.*, 2018, **20**, 21739.
41. J. V. Ortiz, *Chem. Phys. Lett.*, 1998, **296**, 494.
42. J. V. Ortiz. *Chem. Phys. Lett.*, 1998, **297**, 193.
43. J.V. Ortiz, *Wiley Interdisciplinary Reviews: Computational Molecular Science*, 2013, **3**, 123.
44. J. V. Ortiz, *Annual Reports in Computational Chemistry*, **13**, 139-182, Elsevier, 2017.
45. T. H. Dunning, *J. Chem. Phys.*, 1989, **90**, 1007.
46. R.A. Kendall, T.H. Dunning and R.J. Harrison, *J. Chem. Phys.*, 1992, **96**, 6796.
47. D.E. Woon and T.H. Dunning, *J. Chem. Phys.*, 1993, **98**, 1358.
48. M.J. Frisch, G.W. Trucks, H.B. Schlegel, G.E. Scuseria, M.A. Robb, J.R. Cheeseman, G. Scalmani, V. Barone, G.A. Petersson, H. Nakatsuji, X. Li, M. Caricato, A.V. Marenich, J. Bloino, B.G. Janesko, R. Gomperts, B. Mennucci, H.P. Hratchian, J.V. Ortiz, A.F. Izmaylov, J.L. Sonnenberg, D. Williams-Young, F. Ding, F. Lipparini, F. Egidi, J. Goings, B. Peng, A. Petrone, T. Henderson, D. Ranasinghe, V.G. Zakrzewski, J. Gao, N. Rega, G. Zheng, W. Liang, M. Hada, M. Ehara, K. Toyota, R. Fukuda, J. Hasegawa, M. Ishida, T. Nakajima, Y. Honda, O. Kitao, H. Nakai, T. Vreven, K. Throssell, J. Montgomery, J.A., J.E. Peralta, F. Ogliaro, M.J. Bearpark, J.J. Heyd, E.N. Brothers, K.N. Kudin, V.N. Staroverov, T.A. Keith, R. Kobayashi, J. Normand, K. Raghavachari, A.P. Rendell, J.C. Burant, S.S. Iyengar, J. Tomasi, M. Cossi, J.M. Millam, M. Klene, C. Adamo, R. Cammi, J.W. Ochterski, R.L. Martin, K. Morokuma, O. Farkas, J.B. Foresman and D.J. Fox, *Gaussian 16*, Gaussian, Inc., Wallingford CT, 2016.
49. M. J. Frisch, G. W. Trucks, H. B. Schlegel, G. E. Scuseria, M. A. Robb, J. R. Cheeseman, G. Scalmani, V. Barone, G. A. Petersson, H. Nakatsuji, X. Li, M. Caricato, A. V. Marenich, J. Bloino, B. G. Janesko, R. Gomperts, B. Mennucci, H. P. Hratchian, J. V. Ortiz, A. F. Izmaylov, J. L. Sonnenberg, D. Williams-Young, F. Ding, F. Lipparini, F. Egidi, J. Goings, B. Peng, A. Petrone, T. Henderson, D. Ranasinghe, V. G. Zakrzewski, J. Gao, N. Rega, G. Zheng, W. Liang, M. Hada, M. Ehara, K. Toyota, R. Fukuda, J. Hasegawa, M. Ishida, T. Nakajima, Y. Honda, O. Kitao, H. Nakai, T. Vreven, K. Throssell, J. A. Montgomery, Jr., J. E. Peralta, F. Ogliaro, M.J. Bearpark, J. J. Heyd, E. N. Brothers, K. N. Kudin, V. N. Staroverov, T. A. Keith, R. Kobayashi, J. Normand, K. Raghavachari, A. P. Rendell, J. C. Burant, S. S. Iyengar, J. Tomasi, M. Cossi, J. M. Millam, M. Klene, C. Adamo, R. Cammi, J. W. Ochterski, R. L. Martin, K. Morokuma, O. Farkas, J. B. Foresman and D. J. Fox, *Gaussian Development Version, Revision I.14+*, Gaussian, Inc., Wallingford CT, 2018.
50. R. Dennington, T.A. Keith and J.M. Millam, *GaussView, Version 6*, Semichem Inc., Shawnee Mission, KS, 2016.
51. H. M. Lee, S. B. Suh, P. Tarakeshwar and K. S. Kim, *J. Chem. Phys.*, 2005, **122**, 044309.
52. (a) N. I. Hammer, J. R. Roscioli, M. A. Johnson, E. M. Myshakin, and K. D. Jordan, *J. Phys. Chem. A*, 2005, 109, 11526. (b) J. W. Shin, N. I. Hammer, J. M. Headrick and M.

- A. Johnson, *Chem. Phys. Lett.*, 2004, **399**, 349.
53. S. N. Eustis, D. Radisic, K. H. Bowen, R. A. Bachorz, M. Haranczyk, G. Schenter, and M. Gutowski, *Science*, 2008, **319**, 936.

VI.14 Solvated Electrons in Formic Acid Trimer and Tetramer

Gaoxiang Liu, Xinxing Zhang, Sandra M. Ciborowski, Maciej Gutowski, and Kit H.

Bowen

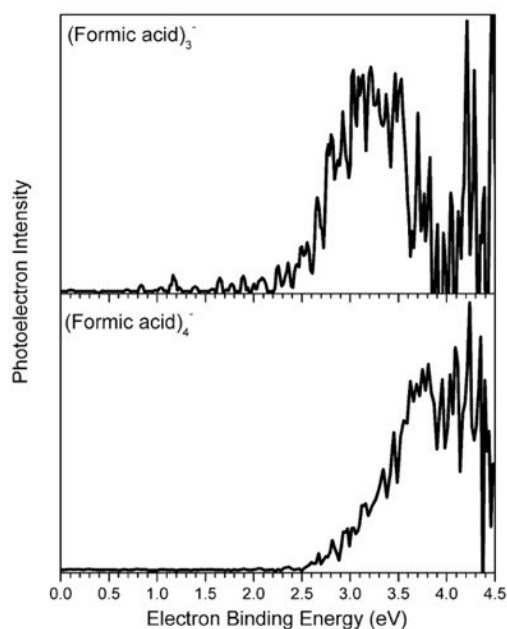


Figure 1. Photoelectron spectra of formic acid trimer and tetramer anions.

This is the first independent project that I accomplished in this lab. According to Maciej Gutowski, electron-induced proton transfer (EIPT) occurs in formic acid trimer and tetramer anions. His calculations have been going on for at least five years

☹️.

VI.15 Methane Solvated Cyanide: The Titan Clusters

Gaoxiang Liu, Sandra M. Ciborowski, and Kit H. Bowen

Astrophysicists detected a series of clusters spaced at 16 amu on the Titan atmosphere with their low-resolution space mass spectrometer. While their mass spectra suggest the species as methane solvated cyanide, $\text{CN}^-(\text{CH}_4)_n$, they are not confident about if it is realistic to solvate a polar anion with a unipolar solvent. In this project, we confirmed that $\text{CN}^-(\text{CH}_4)$ does exist.

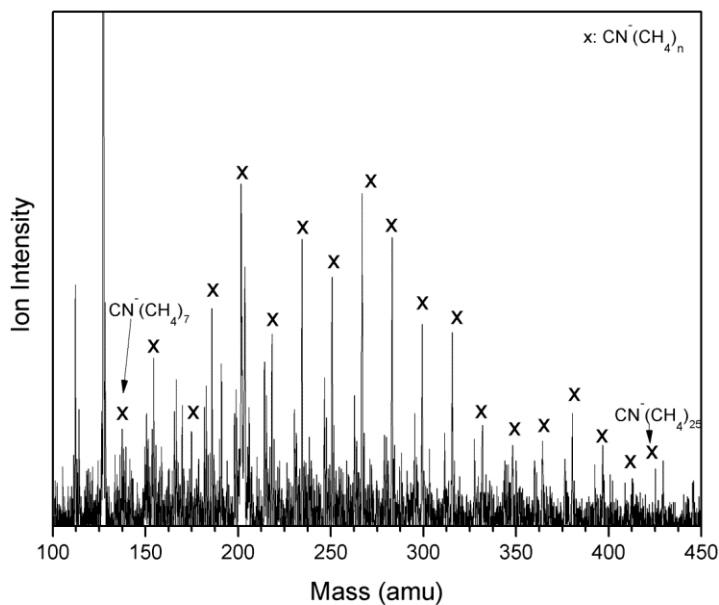


Figure 1. Mass spectrum of $\text{CN}^-(\text{CH}_4)_n$.

The astrophysicists were right about one thing, that is, $\text{CN}^-(\text{CH}_4)_n$ were indeed not

trivial to make. One common way to get CN^- is through the dissociative electron attachment to $-\text{CN}$ group containing molecules. Such molecules, however, are highly polar, and they naturally solvate the as-prepared CN^- much better than the nonpolar CH_4 . Therefore, one needed to figure out a way to generate CN^- without mixing any polar molecules in the expansion beam. Our approach was to coat a layer of tetracyanocyclohexan (TCCH) onto a copper rod, hit the rod with a laser to generate CN^- from TCCH, and mix it with a supersonically expanding He/methane beam.

VI.16 Electron Induced Proton Transfer

Electron Induced Proton Transfer in Hydrogen Halide-Ammonia Dimer

Gaoxiang Liu, Zhaoguo Zhu, Sandra M. Ciborowski, Kit H. Bowen

It is well-established that when electron attaches to neutral hydrogen halide-ammonia dimer, EIPT occurs and triggers the proton to relocate from hydrogen halide to ammonia. That is, $\text{HX} \cdots \text{NH}_3 + e^- \rightarrow \text{X}^- \cdots \text{NH}_4^0$. The NH_4^0 is the Rydberg radical made from the excess electron association with the NH_4^+ . Previous experiments, however, have only observed the spectroscopic feature of NH_4^0 . The feature of X^- was not seen due to a limitation in PES photon energy. We revisited these systems with Rydberg electron transfer to prepare the anionic complexes and a much higher PES photon energy for photoelectron spectroscopy. The observed feature of X^- puts a conclusion to this unfinished business.

NH₃-HCl

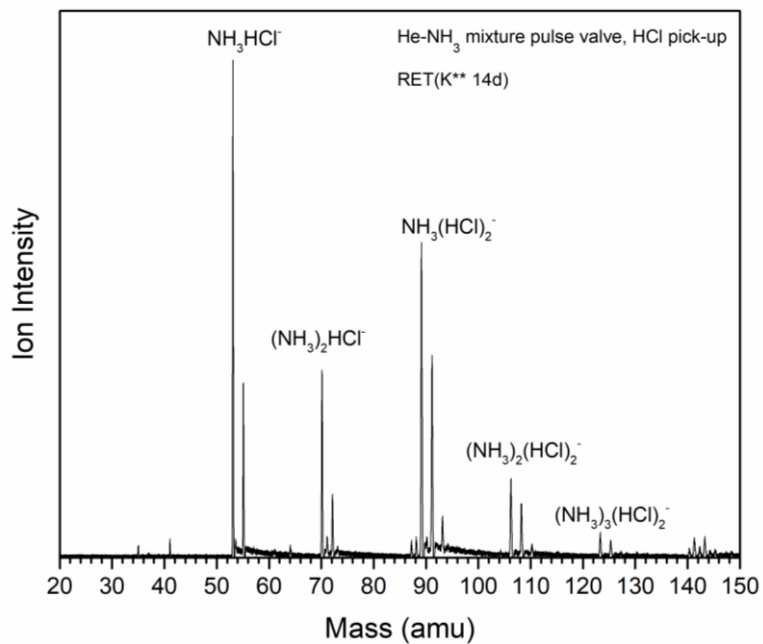


Figure 1. Mass spectrum of NH₃-HCl clusters made by RET.

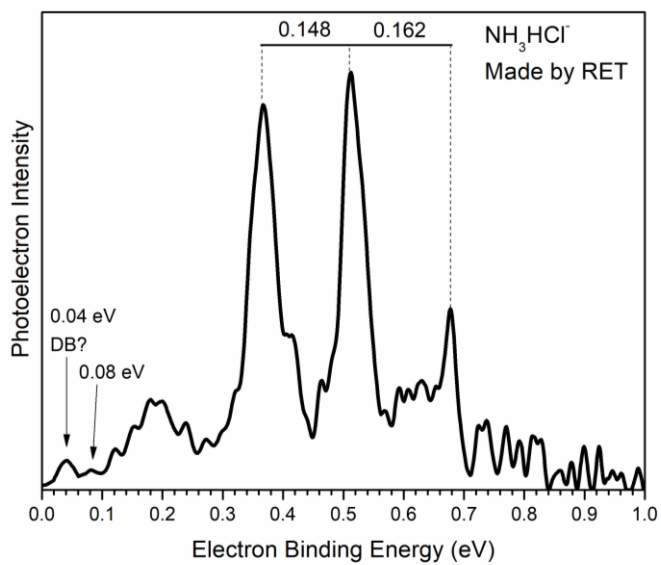


Figure 2. Photoelectron spectrum of $(\text{NH}_3\text{HCl})^-$ taken with 1.165 eV photon.

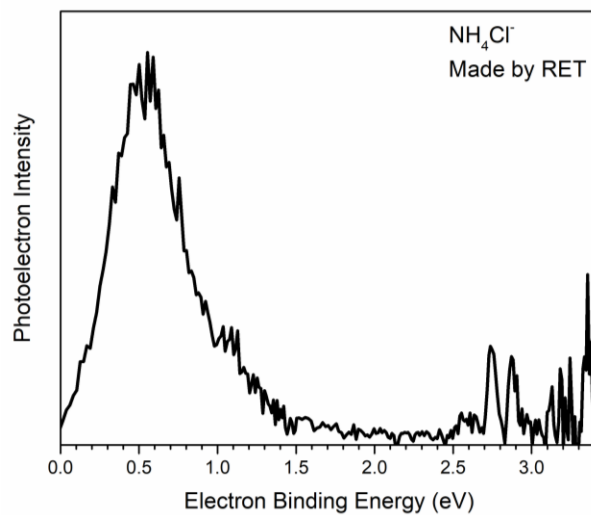


Figure 3. Photoelectron spectrum of $(\text{NH}_3\text{HCl})^-$ taken with 3.495 eV photon.

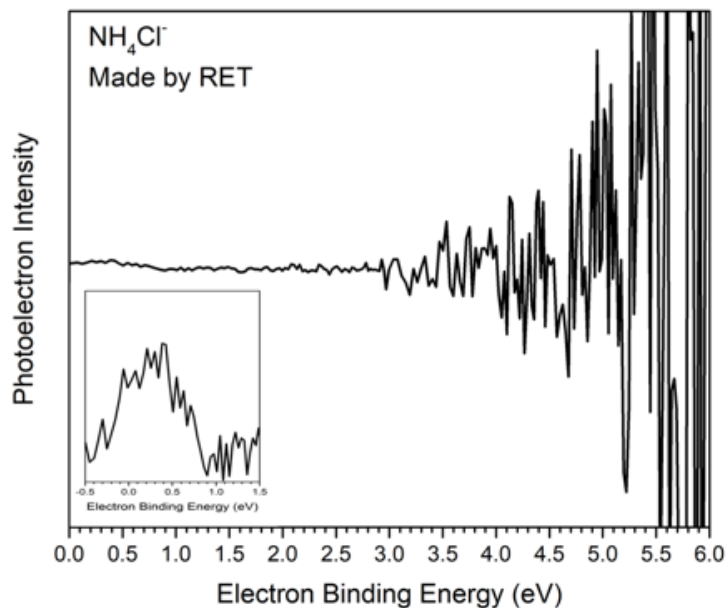


Figure 4. Photoelectron spectrum of $(\text{NH}_3\text{HCl})^-$ taken with 6.42 eV photon. No obvious feature at high electron binding energy can be observed. According to Vincent Ortiz, the energy needed to photodetach the Cl^- moiety may be higher than the photon energy of ArF excimer laser.

NH₃-HBr

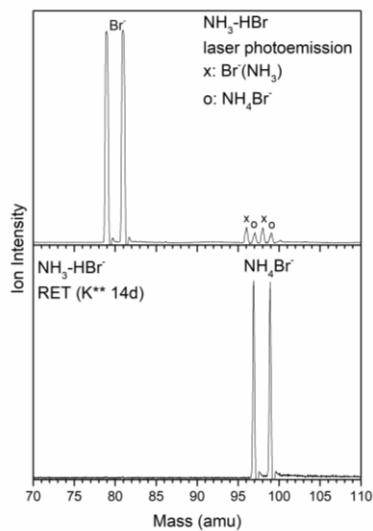


Figure 5. Mass spectra of NH₃-HBr made by laser photoemission (top) and RET (bottom).

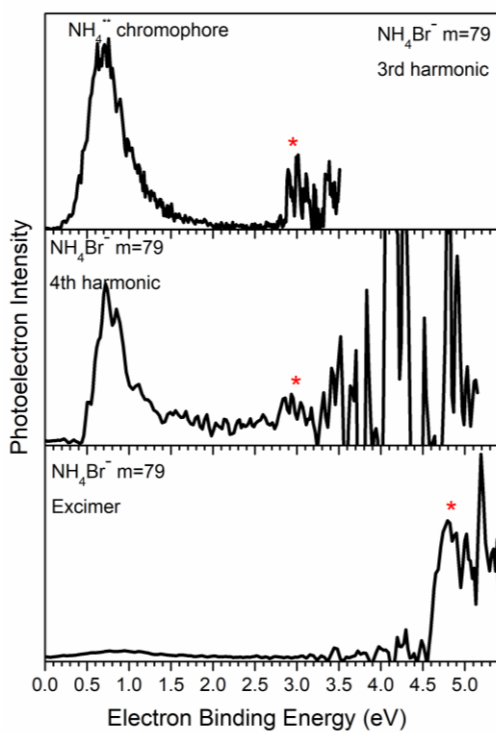


Figure 6. Photoelectron spectra of NH₄Br⁻ taken with 1.165, 3.495, and 6.42 eV

photon.

Electron-Induced Proton Transfer in Ammonia Clusters

Gaoxiang Liu, J. Vincent Ortiz, and Kit H. Bowen

The nature of solvated electrons has long been a source of fascination. It has been widely accepted that excess electrons in solvent are stabilized in cavities surrounded by the solvent molecules. The stabilization is primarily formed of physical interactions such as electrostatic forces, dispersions, correlations, and so on. Chemistry, which is here defined as chemical bond breakage and formation, is rarely observed in solvated electron systems. While this popular cavity model is often assumed to describe the status of the excess electrons in ammonia clusters as well, our anion photoelectron spectra of unusually small ammonia cluster anions suggest that EIPT plays a major role.

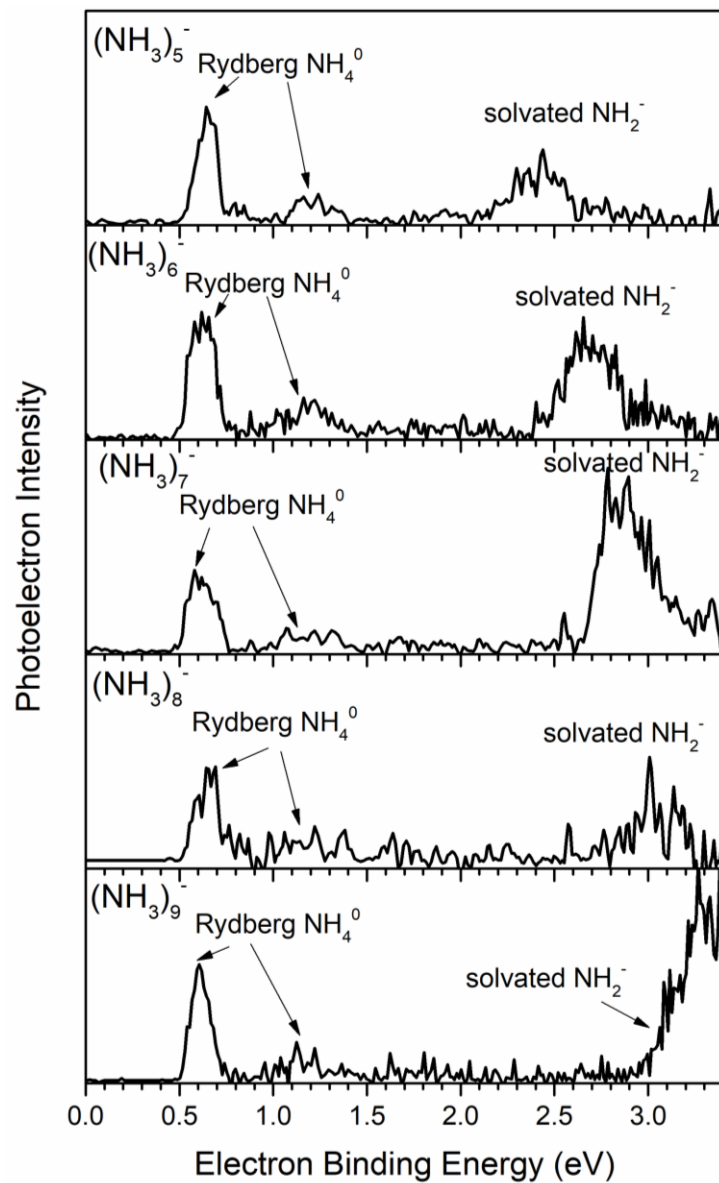


Figure 7. Photoelectron spectra of $(\text{NH}_3)_{5-9}^-$.

VI.17 Xenon Cluster Anions

Gaoxiang Liu, Moritz Blankenhorn, Rachel Harris, and Kit H. Bowen

We have already studied correlation-bound, quadrupole-bound, and dipole-bound anions as well as multiple Rydberg anions. We now propose to extend the systems for study to polarizability-bound cluster anions. Polarizability-bound anions are anions where the excess electrons in these species are bound by electron-induced dipole interactions. We propose to focus on xenon cluster anions, Xe_n^- , as prototypical examples of such species. Calculations predicted the smallest Xe_n^- cluster anion to be stable at $n \sim 6$. Haberland reported observing Xe_n^- cluster anions in mass spectra, although these results were not reproduced by others and were questioned by some. Over the past thirty years, generations of graduate students in Bowen's lab have put tremendous efforts in making Xe_n^- cluster anions, but none of them was successful. It was not until recently that we finally made a breakthrough. In this study, we successfully prepared a series of Xe_n^- cluster anions and measured their photoelectron spectra. The photoelectron spectra show two electron binding energy (EBE) transitions. The one at lower EBE corresponds to the polarizability- or correlation-bound electrons that were predicted in several theoretical papers. The nature of the higher EBE one is still being investigated. Photoelectron spectra are still being collected by the time the dissertation is finished.

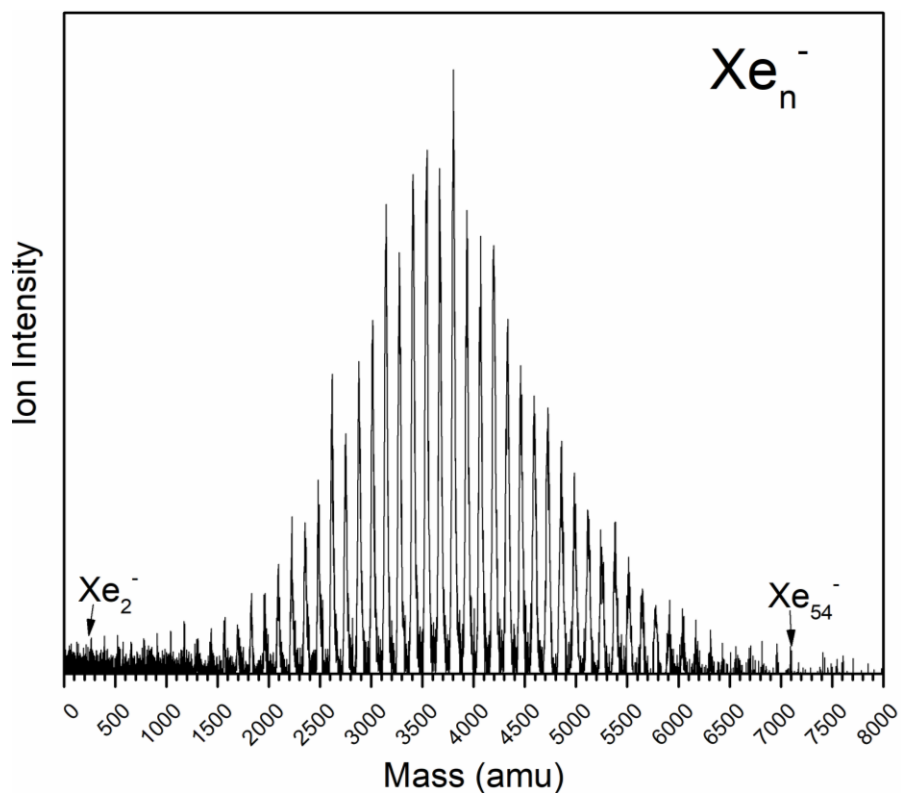


Figure 1. Mass spectrum of Xe_n^- made by laser photomission source. The source of electrons is an ultrapure (99.999%) aluminum rod.

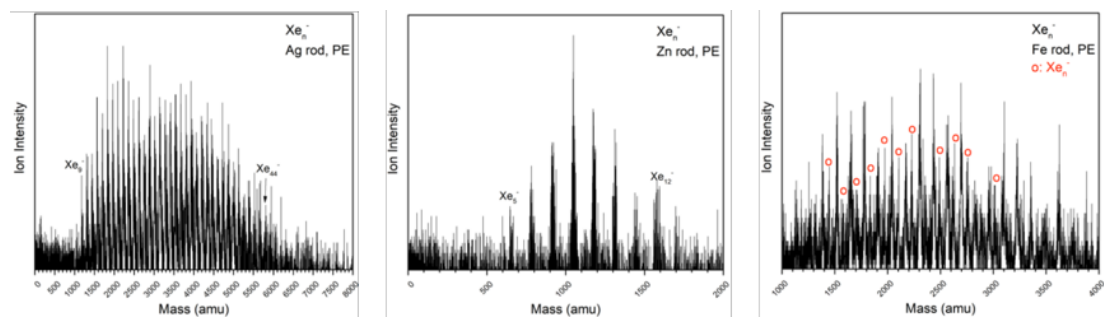


Figure 2. Mass spectra of Xe_n^- made with different photoelectron emitters, silver, zinc, and iron rods, showing that the generation of Xe_n^- is independent from the rod material. This verifies that the prepared Xe_n^- are real Xe_n^- rather than Xe_n solvated anions made from the rods.

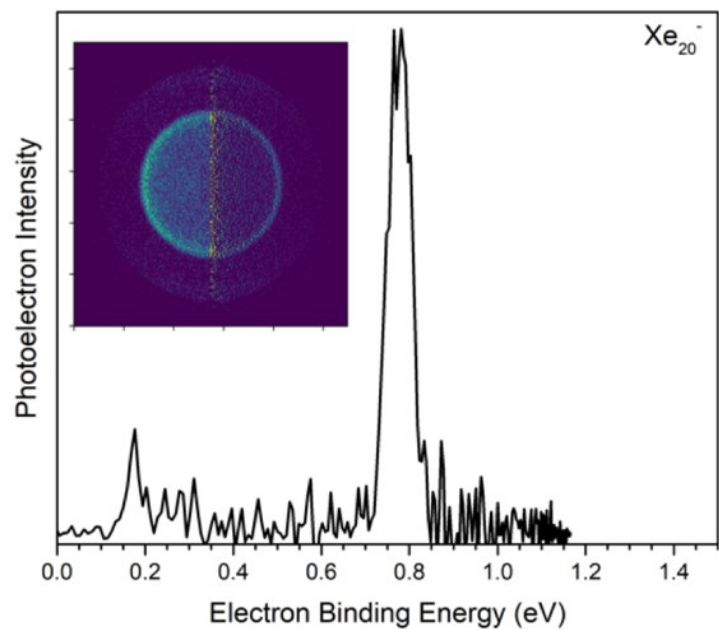


Figure 3. Photoelectron spectrum and image of Xe_{20}^- . The EBE of the two peaks are 0.177 and 0.781 eV.

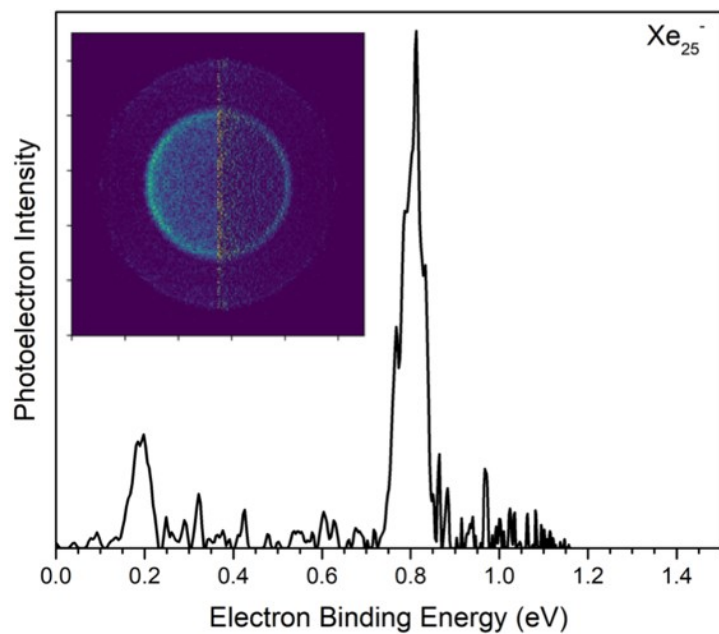


Figure 4. Photoelectron spectrum and image of Xe_{25}^- . The EBE of the two peaks are

0.193 and 0.813 eV.

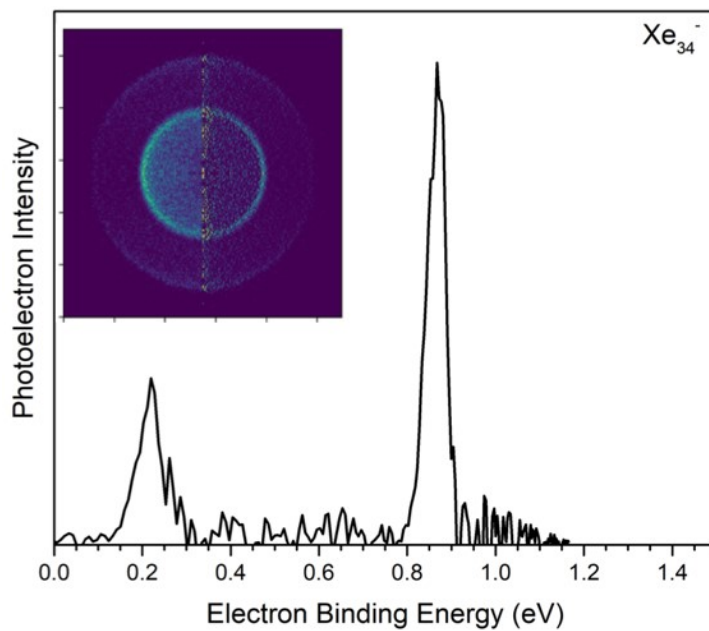


Figure 5. Photoelectron spectrum and image of Xe_{25}^- . The EBE of the two peaks are 0.220 and 0.867 eV.

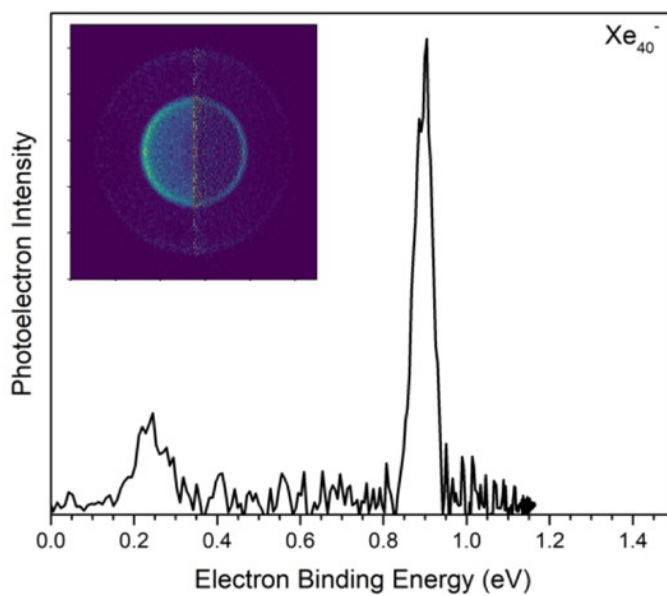


Figure 6. Photoelectron spectrum and image of Xe_{40}^- . The EBE of the two peaks are

0.245 and 0.904 eV.

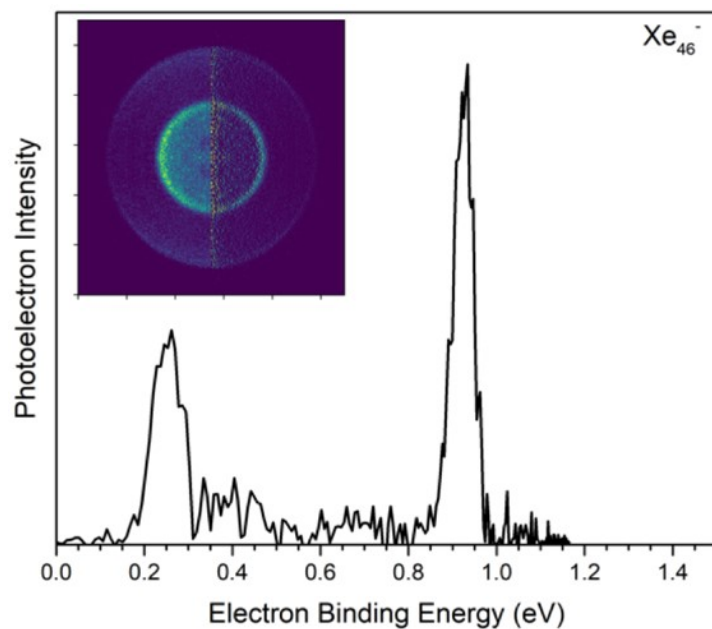


Figure 7. Photoelectron spectrum and image of Xe_{46}^- . The EBE of the two peaks are 0.252 and 0.911 eV. Vibrational progression is observed for the higher EBE peak, which is suggestive of the vibrational energy levels of the Xe excimer moiety.

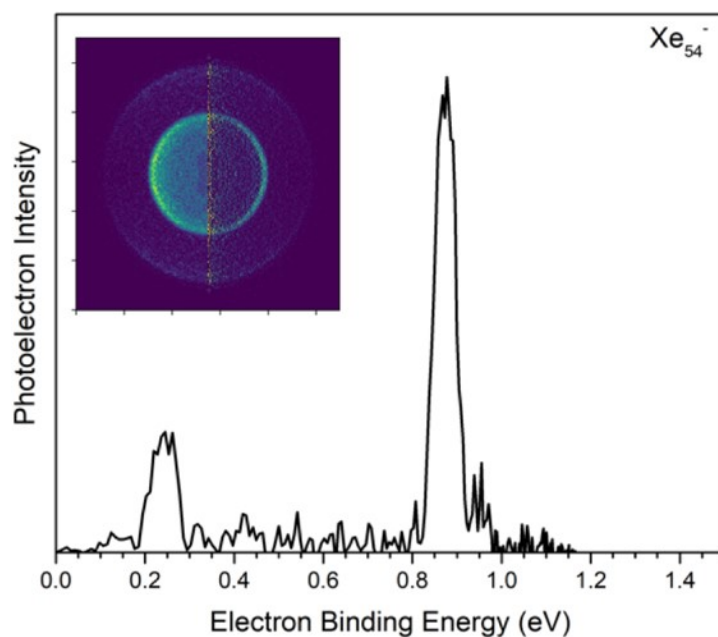


Figure 8. Photoelectron spectrum and image of Xe_{54}^- . The EBE of the two peaks are 0.253 and 0.886 eV.

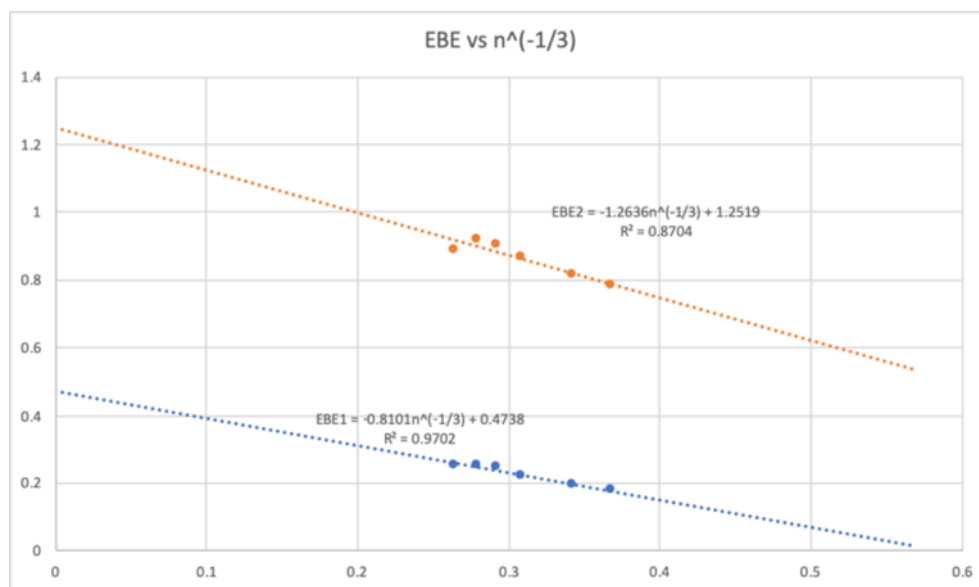


Figure 9. Fitting of the electron binding energy of the two peaks versus $n^{-1/3}$, n being the size of Xe cluster anions. According to the fitting, when n approaches ∞ , the EBE is 0.474 eV; when EBE is 0 eV, the corresponding n is ~ 5 .

VI.18 VMI Imaging Data Analysis Software Update

A Python program that can process the VMI data with the PyAbel library (<https://pyabel.readthedocs.io/en/latest/abel.html>) was written. This newer program can perform raw image symmetrization, inverse Abel transition, calibration, anisotropy analysis, generation of VMI images, and many more. The installation of the PyAbel library is necessary for the first time of using this program, whose procedure could be found in the provided link.

```
from __future__ import division

from __future__ import print_function

from __future__ import unicode_literals

import numpy as np

import abel

import os

import pdb

import matplotlib.pyplot as plt
```

```

#####
# CHANGE THE PRESENT WORKING DIRECTORY TO THE DATA FOLDER
FIRST #
#####

# Load image as a numpy array - numpy handles .gz, .bz2

filename = input("The name of the symmetrized image, no.dat: ")

IM = np.loadtxt(filename+".dat")

# use scipy.misc.imread(filename) to load image formats (.png, .jpg, etc)

# Symmetrize raw image

quadrants = abel.tools.symmetry.get_image_quadrants(IM,True,(0,1)) # get an array
of averaged and symmetrized quadrants

ImageSym = abel.tools.symmetry.put_image_quadrants(quadrants,(rows,cols)) # use
the 4 quadrants to make the symmetrized image

IM = ImageSym

rows, cols = IM.shape # image size

```

```

IM_t = IM.transpose()

rows_t,cols_t = IM_t.shape

IM_t_up = IM_t[0:rows_t//2]

IM_t_down = IM_t[rows_t//2:rows_t-1]

# centerline = IM_t[rows_t-1].transpose()

IM_t = np.concatenate([IM_t_up,IM_t_down])

IM = IM_t.transpose()

rows, cols = IM.shape # New image size

# Image center should be mid-pixel, i.e. odd number of columns

# The original

if cols % 2 != 1:

print ("even pixel width image, make it odd and re-adjust image center")

IM = abel.tools.center.center_image(IM, center="slice")

rows, cols = IM.shape # new image size

r2 = rows//2 # half-height image size

```

```

c2 = cols//2 # half-width image size

# Change the method parameter to use different algorithm for the inverse Abel
# transition. Available choices: basex, hansenlaw, onion_peeling, onion_bordas
# At this moment, it seems that the Basex gives the best resolution. However,
# if the fine structures are caused by noise, than using HansenLaw may be a
# better choice

AIM = abel.Transform(IM, method=input('choose your Abel transition method: '),
direction="inverse",
symmetry_axis=None).transform

# PES - photoelectron speed distribution -----

print('Calculating speed distribution:')

r, speed = abel.tools.vmi.angular_integration(AIM)

# normalize to max intensity peak

speed /= speed[200:].max() # exclude transform noise near centerline of image

# plots of the analysis

```



```

fig = plt.figure(figsize=(15, 4))

ax1 = plt.subplot(131) # Image

ax2 = plt.subplot(132) # Speed distribution

ax3 = plt.subplot(133) # PES

# join 1/2 raw data : 1/2 inversion image

vmax = IM[:, :c2-100].max()

AIM *= vmax/AIM[:, c2+100:].max()

JIM = np.concatenate((IM[:, :c2], AIM[:, c2:]), axis=1)

# Prettify the plot a little bit:

# Plot the raw data

im1 = ax1.imshow(JIM, origin='lower', aspect='auto', vmin=0, vmax=vmax)

fig.colorbar(im1, ax=ax1, fraction=.1, shrink=0.9, pad=0.03)

ax1.set_xlabel('x (pixels)')

ax1.set_ylabel('y (pixels)')

ax1.set_title('VMI, inverse Abel: {:d}x{:d}'\

.format(rows, cols))

```

```

# Plot the 1D speed distribution

ax2.plot(speed)

ax2.axis(xmax=280, ymin=-0.05, ymax=1.2)

ax2.set_xlabel('radial pixel')

ax2.set_title('speed distribution')

# Convert 1D speed distribution to photoelectron spectrum

##### Your calibration file here, no data points limit #####

# This array is the radial positions

caliRadial = [241.0, 224.5, 214.0, 0.0]

# This array is the EBE

caliEBE = [0.012, 0.172, 0.248, 1.165]

##### End of calibration file input #####

c = np.polyfit(caliRadial,caliEBE,2)

speedX = range(len(speed))

EBEX = np.polyval(c, speedX)

# Plot the photoelectron spectrum

```

```
ax3.plot(EBEX, speed)

ax3.axis(xmax=1.165, xmin=-0.01, ymin=-0.01)

ax3.set_xlabel('Electron Binding Energy (eV)')

ax3.set_ylabel('Photoelectron Intensity')

# Save a image of the plot

plt.savefig(filename, dpi=300)

# Save the EBE file for Origin

np.savetxt(filename+".ebe",np.transpose([EBEX,speed]),delimiter='\t')

# Show the plots

plt.show()
```

VII. Curriculum Vitae

Gaoxiang Liu

Department of Chemistry, Johns Hopkins University
Email: gliu17@jhu.edu Cell Phone: (+1) 443-509-5911

EDUCATION

Johns Hopkins University , United States	2019
Ph.D. Candidate, Chemistry Advisor: Dr. Kit H. Bowen	
Johns Hopkins University , United States	2016
Master of Arts, Chemistry	
Fudan University , China	2013
Bachelor of Science, Chemistry	

PUBLICATIONS

21. **G. Liu**, V. Chauhan, A. Aydt, S. Ciborowski, A. Pinkard, Z. Zhu, X. Roy, S. Khanna, and K. H. Bowen
Ligand Effect on the Electronic Structure of Metal Chalcogenide Clusters: A Combined Experimental and Theoretical Study
J. Phys. Chem. C **2019**, published online.
20. **G. Liu**, S. M. Ciborowski, C. R. Pitts, J. D. Graham, A. M. Buytendyk, T. Lectka, and K. H. Bowen
Observation of the Dipole- and Quadrupole-Bound Anions of 1,4-Dicyanocyclohexane
Phys. Chem. Chem. Phys. **2019**, *21*, 18310-18315.
19. **G. Liu**, S. Ciborowski, J. Graham, A. Buytendyk, and K. H. Bowen
The Ground State, Quadrupole-Bound Anion of Succinonitrile Revisited
J. Chem. Phys. **2019**, *151*, 101101.
Highlighted in *AIP Scilight*
“Direct Evidence for the Ground state, Quadrupole-bound Anion of Succinonitrile”
18. **G. Liu**, N. Fedik, C. Martinez-Martinez, S. Ciborowski, X. Zhang, A.

- Boldyrev, and K. H. Bowen
Realization of Lewis Basic Sodium Anion in the NaBH_3^- Cluster
Angew. Chem. Int. Ed. **2019**, *131*, 13927-13931.
17. X. Zhang, **G. Liu**, S. Ciborowski, W. Wang, C. Gong, Y. Yao, and K. H. Bowen
Spectroscopic Measurement of a Halogen Bond Energy
Angew. Chem. Int. Ed. **2019**, *58*, 11400-11403.
Highlighted in *X-mol*
16. **G. Liu**, Z. Zhu, S. M. Ciborowski, I. R. Ariyaratna, E. Miliordos, and K. H. Bowen
Selective Activation of the C-H Bond in Methane by Single Platinum Atomic Anions
Angew. Chem. Int. Ed. **2019**, *58*, 7773-7777 (VIP Paper).
15. **G. Liu**, A. Pinkard, S. M. Ciborowski, V. Chauhan, Z. Zhu, A. P. Aydt, S. N. Khanna, X. Roy, and K. H. Bowen
Tuning the Electronic Properties of Hexanuclear Cobalt Sulfide Superatoms via Ligand Substitution
Chem. Sci. **2019**, *10*, 1760-1766.
14. **G. Liu**, S. M. Ciborowski, Z. Zhu, Y. Chen, and K. H. Bowen
The Metallo-Formate Anions, $\text{M}(\text{CO}_2)^-$, $\text{M} = \text{Ni}, \text{Pd}, \text{Pt}$, formed by Electron-Induced CO_2 Activation
Phys. Chem. Chem. Phys. **2019**, *21*, 10955-10960 (2019 HOT PCCP article).
13. **G. Liu**, S. M. Ciborowski, Z. Zhu, and K. H. Bowen
Activation of Hydroxylamine by Single Gold Atomic Anions
Int. J. Mass Spectrom. **2019**, *435*, 114-117.
12. S. Ciborowski, R. Harris, **G. Liu**, C. Martinez-Martinez, P. Skurski, and K. H. Bowen
The Correlation Bound Anion of *p*-Chloroaniline
J. Chem. Phys. **2019**, *150*, 161103.
11. E. F. Belogolova[§], **G. Liu**[§] (§equal contribution), E. P. Doronina, S. M. Ciborowski, V. F. Sidorkin, and K. H. Bowen
Dipole-Bound Anions of Intramolecular Complexes
J. Phys. Chem. Lett. **2018**, *9*, 1284-1289.

10. **G. Liu**, E. Miliordos, S. M. Ciborowski, M. Tschurl, U. Boesl, U. Heiz, X. Zhang, S. S. Xantheas, and K. H. Bowen
Water Activation and Splitting by Single Metal-Atom Anions
J. Chem. Phys. **2018**, *149*, 221101.
9. S. M. Ciborowski, **G. Liu**, J. D. Graham, A. M. Buytendyk, and K. H. Bowen
Dipole-Bound Anions: Formed by Rydberg Electron Transfer (RET) and Studied by Velocity Map Imaging, Anion Photoelectron Spectroscopy (VMI-aPES)
Eur. Phys. J. D **2018**, *72*, 139.
8. **G. Liu**, S. M. Ciborowski, and K. H. Bowen
Photoelectron Spectroscopic and Computational Study of Pyridine-Ligated Gold Cluster Anions
J. Phys. Chem. A **2017**, *121*, 5817-5822.
7. P. J. Robinson, **G. Liu**, S. Ciborowski, C. Martinez-Martinez, J. R. Chamorro, X. Zhang, T. M. McQueen, K. H. Bowen, and A. N. Alexandrova
Mystery of Three Borides: Differential Metal-Boron Bonding Governing Superhard Structures
Chem. Mater. **2017**, *29*, 9892-9896.
6. X. Zhang, **G. Liu**, S. M. Ciborowski, and K. H. Bowen
Stabilizing otherwise Unstable Anions with Halogen Bonding
Angew. Chem. Int. Ed. **2017**, *56*, 9897-9900.
Highlighted in *X-mol*
5. X. Zhang, **G. Liu**, K. Meiwes-Broer, G. Ganteför, and K. H. Bowen
CO₂ Activation and Hydrogenation by PtH_n⁻ Cluster Anions
Angew. Chem. Int. Ed. **2016**, *55*, 1-5.
Highlighted in *X-mol*
4. F. Buendía, M. R. Beltrán, X. Zhang, **G. Liu**, A. Buytendyk, and K. H. Bowen
Ab initio and Anion Photoelectron Study of Au_nRh_m⁻ (n = 1-7, m = 1-2) Clusters
Phys. Chem. Chem. Phys. **2015**, *17*, 28219-28227.
3. M. Rezaee, Y. Wang, X. Zhang, **G. Liu**, K. H. Bowen, A. M. Bayer, M. D. Best, and R. N. Compton
Negative Ion Properties of *trans* 2,2',6,6'-Tetrafluoroazobenzene: Experiment and Theory
J. Chem. Phys. **2015**, *143*, 114303.

2. X. Zhang, **G. Liu**, G. Ganteför, K. H. Bowen, and A. N. Alexandrova
PtZnH₅⁻, A σ -Aromatic Cluster
J. Phys. Chem. Lett. **2014**, *5*, 1596-1601.
1. **G. Liu**, S. Wang, Y. Nie, Y. Zhang, and Y. Tang
Electrostatic-Induced Synthesis of Tungsten Bronze Nanostructures with
Excellent Photo-to-thermal Conversion Behavior
J. Mater. Chem. A **2013**, *1*, 10120-10129 (Front Cover).

ORAL PRESENTATIONS

3. “Adventures in Photoelectron Spectroscopy: Electronic Structures, Chemical Bonding, Molecular Activation, and Electron-Molecule Interactions”
ACS Fall 2019 National Meeting, San Diego, USA, 2019
2. “Revealing the Nature of Chemical Bonding with Anion Photoelectron Spectroscopy”
Division of Younger Chemists Committee Invited Talk
ACS Spring 2019 National Meeting, Orlando, USA, 2019.
1. “Hardness of Transition Metal Boride Materials”
ACS Fall 2018 National Meeting, Boston, USA, 2018

SERVICE TO THE PROFESSION

Journal Reviewer

Phys. Chem. Chem. Phys., Inorg. Chem., Sci. Adv.

SKILLS

Experimental

Spectroscopy, Velocity-Map Imaging, Ion/Laser Optics, Mass Spectrometry, Vacuum Technique

Computational

Quantum Chemistry Simulation, Programming

TEACHING EXPERIENCE

Johns Hopkins University

Teaching

Assistant

Physical Chemistry Lab	2014
General Chemistry and General Chemistry Lab	2013-2014

HONORS AND AWARDS

Johns Hopkins University

The Sarah and Adolph Roseman Achievement Award	2018
--	------

Fudan University

Wangdao Scholarship	2013
Chemistry Departmental Award	2010-2013
Samsung Scholarship	2010